DESIGN PRINCIPLES FOR HIGH-PERFORMANCE O_2 REDUCTION REACTION USING NOVEL MATERIALS

Ph.D. Thesis

By

ASHOK SINGH

DISCIPLINE OF PHYSICS

INDIAN INSTITUTE OF TECHNOLOGY INDORE

MARCH 2025

DESIGN PRINCIPLES FOR HIGH-PERFORMANCE O_2 REDUCTION REACTION USING NOVEL MATERIALS

A THESIS

Submitted in partial fulfillment of the
requirements for the award of the degree
of
DOCTOR OF PHILOSOPHY

by
ASHOK SINGH

DISCIPLINE OF PHYSICS
INDIAN INSTITUTE OF TECHNOLOGY INDORE
MARCH 2025

INDIAN INSTITUTE OF TECHNOLOGY INDORE

I hereby certify that the work which is being presented in the thesis entitled **DESIGN PRINCIPLES FOR HIGH-PERFORMANCE O_2 REDUCTION REACTION USING NOVEL MATERIALS** in the partial fulfillment of the requirements for the award of the degree of **DOCTOR OF PHILOSOPHY** and submitted in the **DEPARTMENT/SCHOOL OF PHYSICS, INDIAN INSTITUTE OF TECHNOLOGY INDORE**, is an authentic record of my own work carried out during the time period from August 2021 to March 2025 under the supervision of Dr. Srimanta Pakhira, Associate Professor, Department of Physics, Indian Institute of Technology Indore.

The matter presented in this thesis has not been submitted by me for the award of any other degree of this or any other institute.

03/07/2025

signature of the student with date

ASHOK SINGH

This is to certify that the above statement made by the candidate is correct to the best of my/our knowledge.

Dr. Srimanta Pakhira, Ph.D.
Associate Professor
Department of Physics and
Centre for Advanced Electronics
Indian Institute of Technology Indore, M.P., India

03.07.2025

Signature of Thesis Supervisor with date

Dr. SRIMANTA PAKHIRA

ASHOK SINGH has successfully given his Ph.D. Oral Examination held on **03/07/2025**.

Dr. Srimanta Pakhira, Ph.D.
Associate Professor
Department of Physics and
Centre for Advanced Electronics
Indian Institute of Technology Indore, M.P., India

03.07.2025

Signature of Thesis Supervisor with date

Dr. SRIMANTA PAKHIRA

ACKNOWLEDGEMENTS

I would like to express my deepest gratitude to my parents for their sacrifices, guidance, love, and support throughout my journey. Thank you for standing by me during the challenges and celebrating the triumphs, for teaching by example how to value people, for allowing me the freedom to explore my passions, and for always trusting and encouraging my curiosity without limitations.

I would like to express my heartfelt gratitude to my thesis advisor, Professor Srimanta Pakhira, for giving me an opportunity to be a part of his vibrant academic research group, for countless joyful celebrations of life and science with boundless enthusiasm, and for scientific and dynamic discussions. His genuine passion, exceptional mentorship, authenticity, and the supportive and familial atmosphere he cultivated in his research group have been a constant source of inspiration. His tireless curiosity, steadfast work ethic, and generous encouragement, as well as his thoughtful and carefully measured feedback, have been instrumental in my professional and academic growth. I am honored to have had the privilege of working alongside him and grateful for the opportunity to have learned from him.

I would like to thank my Ph.D. Student Progress Committee (PSPC) members Professor Somaditya Sen and Professor Suman Mukhopadhyay, for their thoughtful evaluations, constructive feedback, insightful suggestions during the annual progress reviews, and the time and effort they dedicated to assessing my work and providing encouragement. I would like to extend my heartfelt gratitude to the experimental collaborators with whom I had the privilege of working throughout my research journey. Their expertise, dedication, and willingness to share insights have been instrumental in bridging the gap between theory and experiment. I am deeply appreciative of their support, patience, and invaluable contributions, which have greatly enhanced the depth and impact of my research.

I would also like to extend my sincere appreciation to my laboratory mates for their collaboration, support, and valuable discussions. Our discussions, debates, and shared experiences have greatly enhanced my research and made the laboratory environment a stimulating and enjoyable place.

I would like to thank my amazing friends for their emotional support, love, and motivation. Their presence and words of encouragement have been the driving force behind the journey of completing this thesis and helped me maintain a healthy work-life balance.

Lastly, I would like to express my gratitude to everyone who has directly or indirectly contributed to the completion of this thesis. Your support and encouragement have meant the world to me.

Thank you

To my beloved parents

SYNOPSIS

Introduction: The relentless pace of industrialization, population growth, and global development have led to rising energy demand, predominantly met by fossil fuels like oil, coal, and natural gas, which account for over 80% of global energy consumption. In 2022, coal demand increased by 0.6%, reaching its highest consumption since 2014, and coal production rose by over 7% compared to 2021. The high and practically unchanged share of fossil fuel in the rapidly increasing energy consumption has the consequence of the rapid depletion of fossil fuel resources and emission of CO_2 pollutant gas, surging to an unprecedented 39.3 gigatons CO_2 emission in 2022[1]. The systematic representation of the trend of global carbon emissions by year and global energy consumption from different energy resources in 2022 has been shown in Figures 1a and 1b, respectively.

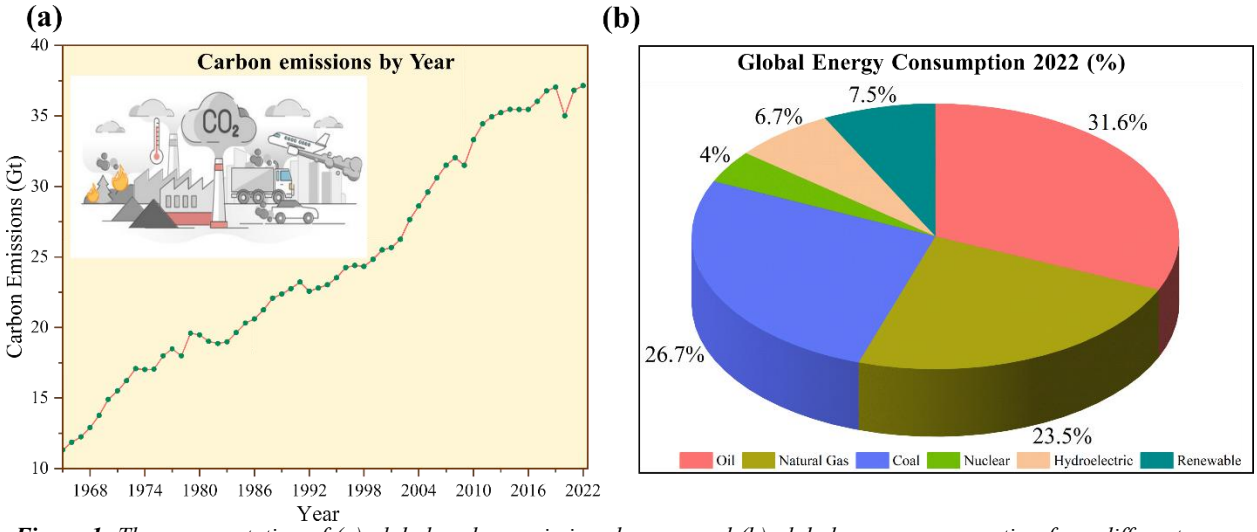

Figure 1. *The representation of (a) global carbon emissions by year and (b) global energy consumption from different energy resources.*

In this view, academic and industrial researchers have made numerous efforts to increase the share of renewable energies, energy efficiency, and fuel switching. These scenarios have stimulated the development of novel energy storage and conversion devices (fuel cells, batteries, and supercapacitors), of which fuel cells have received tremendous attention due to their wide range of applications. They span power devices that include stationery, transport, and small-scale portable electronics. In the fuel cells, the H_2 dissociation occurs at the anode, while at the cathode, O_2 reduction occurs, transforming chemical energy into electricity. Oxygen reduction reaction (ORR) is an important process involved in energy conversion and storage devices, significantly determining the performance, service level, and operating life of these devices[2]. However, the ORR at the cathode produces many negative effects on the fuel cell system performance and

commercialization owing to its sluggish kinetics and diversity of the reaction pathways. Thus, the ORR electrocatalysts dominate overall performance and become the main descriptor of the efficiency of renewable energy conversion and storage devices. To date, conventional platinum (Pt) is still regarded as the best ORR electrocatalyst in both acid and alkaline electrocatalyst. However, Pt has a high price, and it is prone to poisoning by CO (an intermediate product of electro-oxidizing alcohol fuels), and limited availability of Pt constraints the possibility of using and commercializing devices whose operation is based on ORR[2]. Therefore, one of the main challenges in fuel cell research and development is obtaining more economical, appropriate, alternate electrocatalysts without compromising the activity and durability. Electrocatalysts should have high electronic conductivity, large specific surface area, good stability, tunable morphology and functionality, electroactive properties, and be cost-effective. The two-dimensional transition metal dichalcogenides (TMDs) and carbon-based material (graphene, carbon nanotube (CNT), amorphous carbon) can fulfill these requirements and have become two representative types of non-noble materials electrocatalysts for ORR. For example, recently, Pumera et al. experimentally presented a systematic study dealing with the effects of four different dopants represented by V, Ti, Mn, and Fe on the catalytic activity of layered MoS_2 and WS_2 toward ORR and hydrogen evolution reaction (HER). They demonstrated that the doping of Fe and Mn on MoS_2 can boost its catalytic performance towards the ORR[3]. Recently, Tian et al. performed systematic density functional theory (DFT) calculations to probe the ORR performance of a series of sulfur-based TMDs (TM= Ti, Zr, Hf, V, Nb, Ta, W, Re, and Pt) in different phase structures (2H, 1T, and 3R). They evaluated that the Ni or Co-doped sulfur-based TMDs act as a feasible ORR electrocatalyst with overpotentials (0.32-0.55V) compared to the state-of-the-art Pt-based electrocatalyst[4]. Other emerging electrocatalysts are carbon-based materials, particularly carbon nanotubes (CNTs), which have markedly influenced the development of fuel cells. For example, Zhu et al. fabricated the cobalt and nitrogen co-doped carbon nanotubes (Co@N-CNTs) and studied their electrocatalytic activity towards ORR. They showed that Co@N-CNTs exhibit excellent ORR electrocatalytic activity due to the synergetic effect of Co species and N-doping[5]. Recently, Niu et al. studied the electrocatalytic activity of CoNi nanoparticles (NPs) encapsulated within the apical domain of NCNT (CoNi@NCNT/NF) and reported that the CoNi@NCNT/NF exhibits an excellent catalytic performance toward both ORR and OER[6].

Motivation and objectives of the thesis: Our primary motivation is to tackle the challenge of activating the electrocatalytically inert basal planes of transition metal dichalcogenides (TMDs) and the outer surfaces of carbon nanotubes (CNTs), which is essential for enhancing the catalytic

performance of TMDs and CNTs materials towards ORR. Our primary motivation lies in the potential to manipulate the electronic structure and electronic properties of these materials to significantly improve their electrocatalytic activity in electrochemical reactions. We aim to provide insights into the rational designing of well-defined electrocatalytic structures to understand the structure-activity relationship. Additionally, our goal is to explore, identify, and address the critical active sites that drive the ORR process and determine the most favorable paths for the O_2 reduction reaction. We are particularly motivated to conduct an extensive investigation into diverse pathways of the ORR, which is essential for optimizing catalytic efficiency and selectivity. This detailed understanding will enable us to establish fundamental principles that can guide the development of more effective electrocatalysts in the field of sustainable energy technologies.

The main objectives of the thesis are:

(a) Synergistic Niobium (Nb) Doped Two-Dimensional Zirconium Diselenide: An Efficient Electrocatalyst for O_2 Reduction Reaction

(b) Unraveling the Electrocatalytic Activity of Platinum-Doped Zirconium Disulfide Towards Oxygen Reduction Reaction

(c) Revealing the Mechanism and Activity of O_2 Reduction Reaction of Co Nanocluster Encapsulated by Carbon Nanotube

(d) Exploring the Active Site and Catalytic Activity of N-Coordinated Ni_2 Dual-Atom Catalysts for Oxygen Reduction Reaction

The comprehensive details of rising energy demands, environmental challenges associated with fossil fuel consumption, and the critical role of ORR electrocatalysts in advancing fuel cell technology are thoroughly discussed in Chapter 1 of this thesis. Chapter 1 also provides an in-depth analysis of the ORR pathways, a detailed explanation of catalysts and electrocatalysts, as well as discussions on the advancements of non-noble catalysts.

Computational details: The electronic structure, ground state energy calculations, structural and electronic properties, and the ORR activity descriptor parameters have been achieved by employing the CRYSTAL17 suite code. We have employed a hybrid B3LYP-D3 density functional theory (DFT) based method implemented in the CRYSTAL17 code for our calculations. The full geometry optimization (internal coordinates and lattice parameters were optimized) has been adopted to obtain the ground state electronic structure using the Broyden–Fletcher–Goldfarb–

Shanno (BFGS) algorithm implemented in the CRYSTAL17 suite code. The structures are considered to be relaxed when $3x10^{-5}$ a.u. in the root-mean-square values (RMS) of force and $1.2x10^{-4}$ a.u. in the RMS values of atomic displacement are simultaneously achieved for the atomic position and lattice constant optimization, respectively. The self-consistent field (SCF) calculations were achieved when the total energy difference between successive SCF cycles was less than 10^{-6} a.u. These convergence thresholds were maintained consistently throughout all the calculations in the present calculation. In the CRYSTAL17 code, Kohn-Sham (KS) orbitals are expressed in terms of localized atomic-like functions, which are, in turn, expended in a linear combination of Gaussian-type orbitals (GTOs) with fixed coefficients. The expansion coefficients and exponents of GTOs define a basis set for a given atom[7]. The adsorption energy and Gibbs free energy are used as descriptors of the ORR activity of TMDs and CNTs and have been calculated using the computational hydrogen electrode (CHE) model. In this technique, the chemical potential (μ) of the proton-electron pair in an electrocatalytic step was referenced to that of the dihydrogen molecule using the standard hydrogen electrode (SHE). Accordingly, at a potential of 0V vs. SHE, the sum of $\mu(H^+)$ and $\mu(e^-)$ is set equal to half of the chemical potential of molecular hydrogen, $1/2\ \mu(H_2)$[8]. The electronic band structure and density of states (DOS) were plotted in this thesis by using GNUPLOT and Python codes developed by our group. The Γ-centered Monkhorst-pack grid has been used for sampling the reciprocal space in the first Brillouin zone[9]. The VESTA software is employed for modeling, manipulating, and visualizing the structures used in the present thesis[10].

Chapter 2 of this thesis provides an in-depth exposition of our computational methodologies. This includes a detailed discussion of the CRYSTAL17 suite code, including the input scripts and a comprehensive description of the Gaussian-type basis sets. Furthermore, Chapter 2 provides a thorough exposition of the procedures for geometry optimization and achieving self-consistent field (SCF) convergence. This detailed presentation is designed to provide a rigorous understanding of the computational framework and its application to our study of electrocatalytic materials.

Summary of objective (a): The main goal of this objective, "**Synergistic Niobium Doped Two-Dimensional Zirconium Diselenide: An Efficient Electrocatalyst for O_2 Reduction Reaction**" is the determination of the electrocatalytic O_2 reduction activity of monolayer Nb-doped Zirconium Diselenide (Nb-$ZrSe_2$) TMDs towards electrochemical ORR. Specifically, we aim to answer the following questions: (1) How does the doping of Nb alter the structural and electronic

properties of the 2D monolayer $ZrSe_2$? (2) Does the 2D monolayer Nb-$ZrSe_2$ material act as an efficient ORR electrocatalyst? (3) If yes, which ORR path will it follow to reduce the O_2?

To address these research questions, we first computationally designed the doped system, i.e., Nb-$ZrSe_2$, by substituting one Zr atom with the transition metal Nb per 2x2 supercell of the 2D monolayer pristine $ZrSe_2$ TMD. The 2D monolayer Nb-$ZrSe_2$ system has been fully relaxed

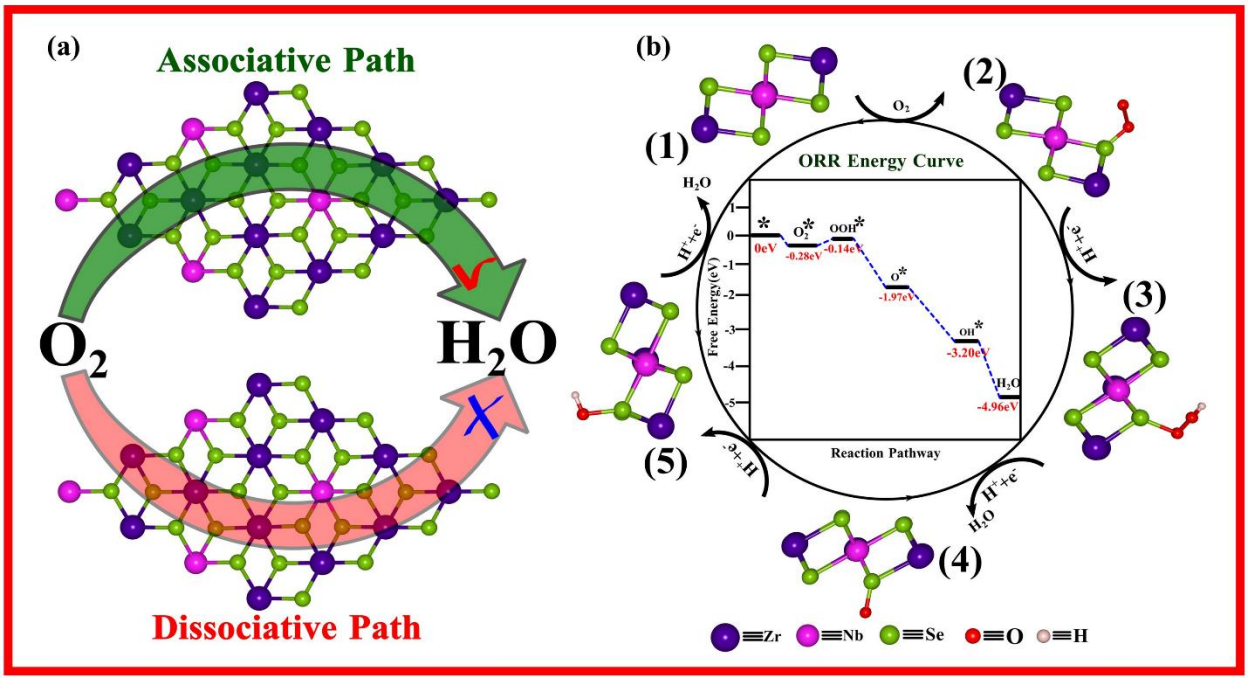

Figure 2. *(a) Schematic representation of the oxygen reduction reaction (ORR) pathways on Nb-$ZrSe_2$, illustrating the associative (green arrow) and dissociative (red arrow) routes. The associative pathway (green arrow) is indicated as the favorable path for the ORR. (b) the potential energy surface for the associative ORR pathway highlights the free energy changes at each reaction step.*

with respect to both atomic coordinates and cell parameters by using the DFT-D3 method. The analysis of the electronic properties of pristine 2D monolayer $ZrSe_2$ demonstrated that a single layer of $ZrSe_2$ in two-dimensional form exhibits semiconducting behavior characterized by a band gap of 1.48 eV. On the other hand, the 2D monolayer Nb-$ZrSe_2$ material has zero band gap, indicating the metallic nature of the 2D monolayer Nb-$ZrSe_2$. The good conductivity of 2D monolayer Nb-$ZrSe_2$ material can play a crucial role in facilitating the movement of electrons in the mechanism of ORR, and 2D monolayer Nb-$ZrSe_2$ could act as an excellent catalyst towards ORR. The analysis of the electrocatalytic activity of Nb-$ZrSe_2$ and the selectivity of the favorable ORR path have been examined by computing the adsorption energy of the ORR intermediate species involved in both associative and dissociative pathways. The adsorption energy of the key intermediates suggests that the dissociative ORR path would be the less favorable path to reduce the O_2 molecule to water as compared to that of the associative path. In addition, the study of Gibbs

free energy of intermediate ORR species suggests that the associative path would be energetically favorable path. The equilibrium structure of the 2D monolayer Nb-$ZrSe_2$ electrocatalyst and potential energy surface (PES) with the reaction coordinates of the associative path based on the change of Gibbs free energy have been represented in Figures 2a and 2b, respectively. A detailed exploration and analysis of the electrocatalytic properties of Nb-$ZrSe_2$ have been provided in Chapter 3 of the thesis. The results presented in this section correspond to the following article:

A. Singh, S. Pakhira, Synergistic Niobium Doped Two-Dimensional Zirconium Diselenide: An Efficient Electrocatalyst for O_2 Reduction Reaction, ACS Phys. Chem Au 4 (2024), 40–56. DOI: https://pubs.acs.org/doi/10.1021/acsphyschemau.3c00035.

Summary of objective (b): The primary motivation of the objective "**Unraveling the Electrocatalytic Activity of Platinum-Doped Zirconium Disulfide Towards Oxygen Reduction Reaction**" is to understand the ORR electrocatalytic activity of the two-dimensional sulfur-based TMDs. A detailed ORR reaction mechanism has been studied with the aim of in-

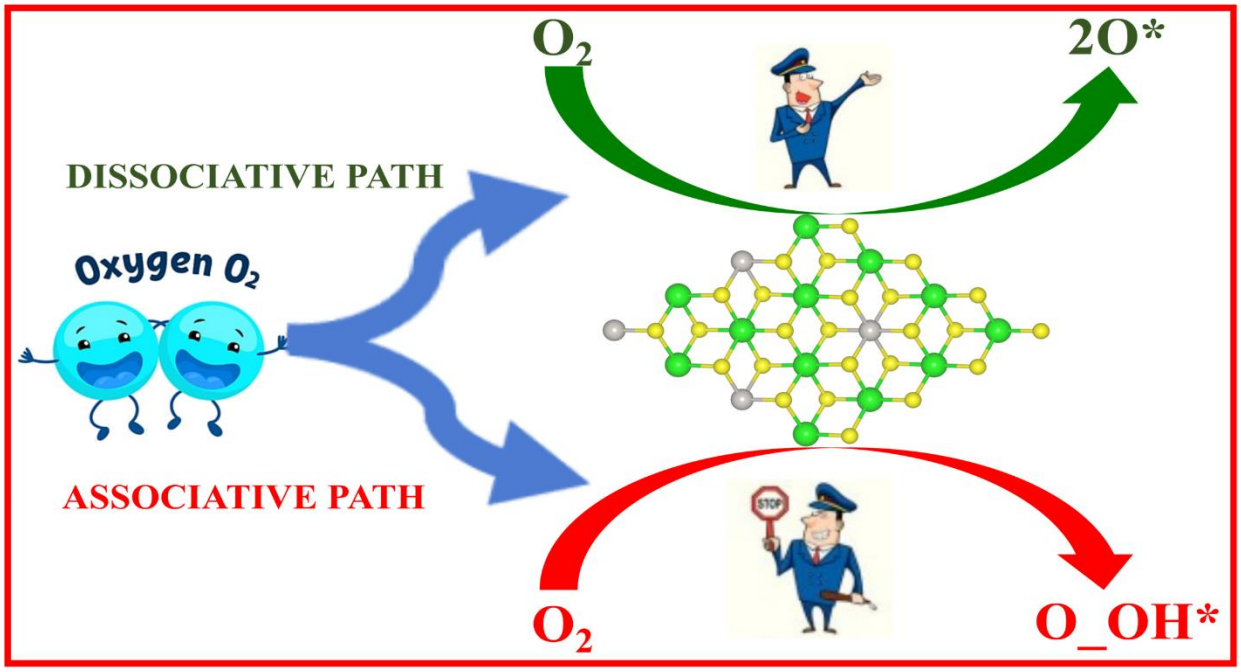

Figure 3. *Schematic representation of the oxygen reduction reaction (ORR) pathways on Pt-ZrS_2, illustrating the dissociative (green arrow) and associative (red arrow) routes. The dissociative pathway (green arrow) is indicated as the favorable path for the ORR.*

depth understating the process and being able to design a novel TMD-based electrocatalyst toward ORR. In addition to proposing different ORR reaction mechanisms, special efforts are made to clearly identify the effect of metal doping on the structural and electronic properties with the catalytic activity of the 2D sulfur-based TMDs. In this section, we propose an intriguing 2D

monolayer Pt-doped Zirconium disulfide (Pt-ZrS_2) as an effective electrocatalyst for ORR by using the first principle-based dispersion corrected density functional (DFT-D3) method. We have started the study by computationally designing the 2D monolayer ZrS_2 and 2D monolayer Pt-ZrS_2. The designing process is followed by relaxing the designed systems to get the minimum energy electronic structure of the 2D monolayer ZrS_2 and 2D monolayer Pt-ZrS_2. We have explored the electronic properties, i.e., band structure, electronic band gap, density of states, and position of the Fermi energy level of the presented systems by employing the same DFT-D3 method. The present computations found that the position of the Fermi level of the 2D monolayer ZrS_2 is at -7.14 eV, and it has an indirect band gap of 2.13 eV (in the Γ-M direction). The electronic band gap of 2D monolayer Pt-ZrS_2 material was found to be 1.95 eV with the position of the Fermi level at -6.73 eV, indicating the semiconducting nature of the 2D monolayer Pt-ZrS_2. The present study reveals that the electronic band gap has been significantly reduced by an amount of 0.18 eV due to the Pt doping in the pristine 2D monolayer ZrS_2. The analysis of the potential of the 2D monolayer Pt-ZrS_2 as an ORR electrocatalyst and the study of the ORR path selectivity have been done based on the adsorption energy of the ORR intermediates species on the catalytic active site of 2D monolayer Pt-ZrS_2. This study indicates that the 2D monolayer ZrS_2 is a promising ORR electrocatalyst with outstanding catalytic activity and a high $4e^-$ reduction pathway selectivity. The 2D monolayer Pt-ZrS_2 electrocatalyst structure has been shown in Figure 3. A detailed and systematic analysis of this study has been provided in Chapter 4 of this thesis. The results presented in this section correspond to the following article:

A. Singh, S. Pakhira, Unraveling the Electrocatalytic Activity of Platinum Doped Zirconium Disulfide Towards Oxygen Reduction Reaction, Energy Fuels, 37(2023), 567-579. DOI: https://doi.org/10.1021/acs.energyfuels.2c02831.

Summary of objective (c): The main goals of the objective of the titled work, "**Revealing the Mechanism and Activity of O_2 Reduction Reaction of Co Nanocluster Encapsulated by Carbon Nanotube**", are as follows: (i) exploring the exact role of the Co nanoparticle cluster, which is encapsulated inside the single-wall carbon nanotube (SWCNT), (ii) study the different ORR mechanisms on the surface of the Co nanoparticle encapsulated single-wall carbon nanotube (Co@SWCNT), (iii) proposing the thermodynamically and energetically feasible ORR mechanism for the reduction of O_2 on the surface of the Co@SWCNT. To address the above research objectives, we adopted a periodically repeated unit cell of SWCNT. We utilized an armchair Co@SWCNT with (6,6) chiral symmetry in our current investigation. A Co nanoparticle

cluster (Co_4) has been encapsulated in the channel of the SWCNT, i.e., the system of interest in this work is Co@SWCNT. In the present study, we have defined the catalytic active site as the carbon atom situated on the surface of the SWCNT, forming a Co-C bond with the encapsulated Co nanoparticle. The electronic band structure of the SWCNT reveals that certain energy bands intersect the Fermi energy level, but the electron density near the Fermi level is excessively low. This observation indicates the semi-metallic nature of the SWCNT. When a Co nanoparticle is encapsulated inside the SWCNT, it results in a substantial electron density in proximity to the Fermi level. The electronic characteristics of the Co@SWCNT reveal the metallic nature of the Co@SWCNT and indicate the potential application of the Co@SWCNT as an electrocatalyst toward ORR. In order to access the catalytic activity and effectiveness of the Co@SWCNT in facilitating the ORR, we conducted theoretical and computational calculations to determine the adsorption energy of the intermediate species of the surface of the Co@SWCNT. The value of

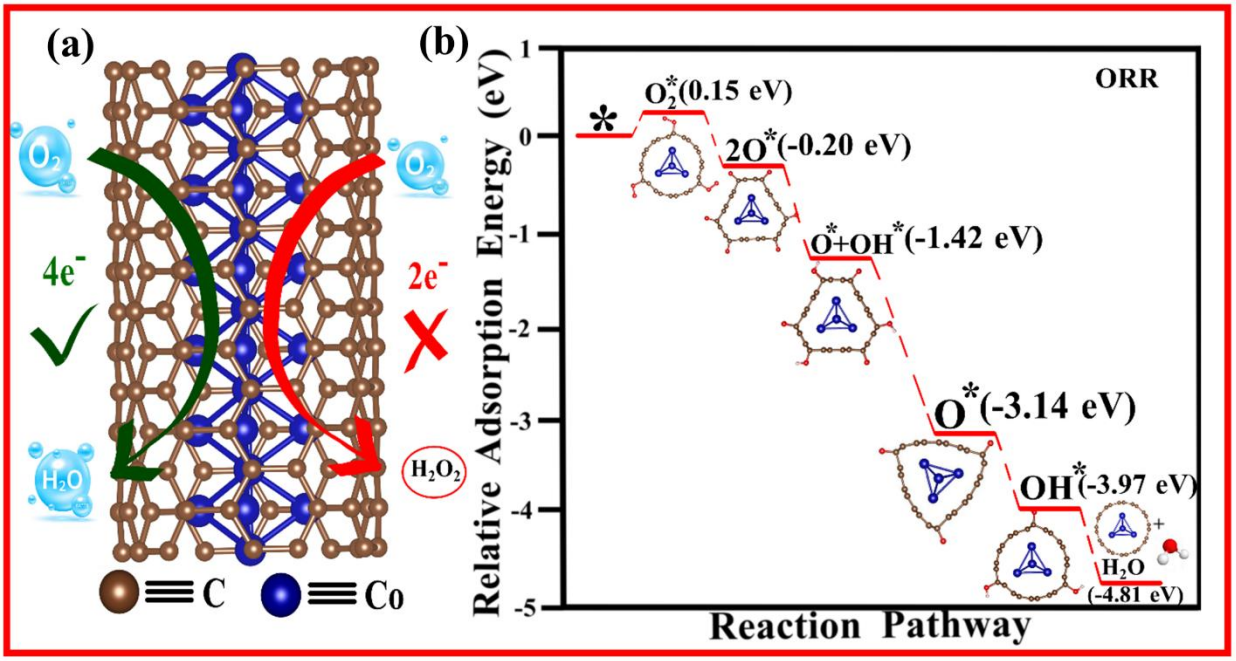

Figure 4. *(a) Schematic representation of the oxygen reduction reaction (ORR) pathways on Co@SWCNT, illustrating the four-electron (green arrow) and two-electron (red arrow) routes. The four-electron pathway (green arrow) is indicated as the favorable path for the ORR. (b) Potential energy surface for the four-electron dissociative ORR pathway, highlighting the relative adsorption energy changes at each reaction step.*

adsorption energy of 2O species was determined to be -0.35 eV, and for the OOH species was determined to be -3.59 eV. By comparing the values of the above key intermediate species, it was found that the $4e^-$ dissociative pathway would be the more favorable path for the reduction of the O_2 on the surface of the Co@SWCNT. The equilibrium structure of the Co@SWCNT electrocatalyst and the ORR reaction PES has been represented in Figure 4a and 4b, respectively.

This theoretical analysis based on the CHE model reveals that the Co@SWCNT is a promising ORR electrocatalyst with exceptional catalytic activity and high $4e^-$ reduction pathway selectivity. A detailed study of the ORR catalytic activity of the Co@SWCNT has been provided in Chapter 5 of this thesis. The results presented in this section correspond to the following article:

A. Singh, S. Pakhira Revealing the Mechanism and Activity of O_2 Reduction Reaction of Co Nanocluster Encapsulated by Carbon Nanotube, Energy Fuels, 38 (2024), 11837–11851. DOI: https://doi.org/10.1021/acs.energyfuels.4c01355.

Summary of objective (d): The primary objectives of the work **"Exploring the Active Site and Catalytic Activity of N-Coordinated Ni_2 Dual-Atom Catalysts for Oxygen Reduction Reaction"** are as follows: (1) to explore the catalytic performance and active site characteristics of nitrogen-coordinated nickel dual-atom (Ni_2) catalysts anchored on carbon nanotubes (CNT) towards ORR, (2) what is the effect of dual-metal doping on the structural and electronic properties of CNT and (3) could Ni_2 dual-atom catalyst exhibit superior catalytic activity toward the ORR?

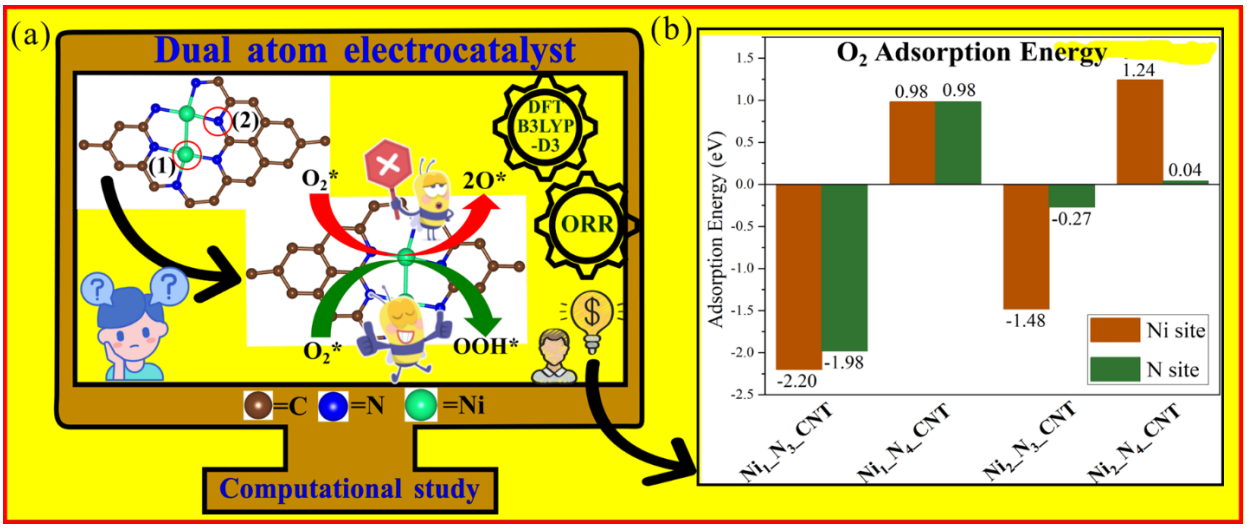

Figure 5. *(a) Schematic representation of the oxygen reduction reaction (ORR) pathways on Ni_2_N_3_CNT, illustrating the four-electron associative (green arrow) and four-electron dissociative (red arrow) routes. The four-electron associative pathway (green arrow) is indicated as the favorable path for the ORR. (b) O_2 adsorption energy on the Ni and N site for each single and duel metal configuration.*

To tackle the above interesting questions, we computationally designed all the experimentally synthesized Ni_2 dual and Ni_1 single atoms anchored on NCNT catalysts and investigated their ORR catalytic activity by employing the first principles-based DFT method. We have considered four catalyst configurations comprising two single-atom systems, namely Ni_1_N_3_CNT and Ni_1_N_4_CNT, and two dual-atom systems, referred to as Ni_2_N_3_CNT and Ni_2_N_4_CNT. For each configuration, we have investigated favorable active sites for ORR (nickel and nitrogen sites),

structural stability, electronic properties, adsorption behavior of key ORR intermediate species on two possible active sites (Ni and N). Among all models, the Ni_2_N_3_CNT system emerged as the most promising catalyst, with the Ni site identified as the dominant active site for ORR as represented in Figure 5a. Electronic band structure and density of states analysis confirmed the metallic character of Ni_2_N_3_CNT, enabling efficient electron transport necessary for catalytic activity. The adsorption energy calculations of key ORR intermediates (O_2*, O*, OH*, H_2O) revealed moderate binding energies at the Ni site, which supports optimal activation and desorption behavior required for catalytic turnover as represented in Figure 5b. Thermodynamic analysis based on the computational hydrogen electrode (CHE) model indicated that the four-electron associative pathway is the most favorable mechanism for O_2 reduction on the Ni_2_N_3_CNT surface as shown in Figure 5a. All ORR steps are exergonic, and the final desorption of H_2O is facile, suggesting that Ni_2_N_3_CNT can sustain continuous catalytic cycling with high efficiency. Overall, this study reveals that Ni_2 dual-atom catalysts, particularly the Ni_2_N_3_CNT configuration, demonstrate excellent catalytic activity, strong ORR selectivity, and potential to serve as viable substitutes for Pt-based catalysts in fuel cell systems. These findings are discussed in detail in Chapter 6 of this thesis and correspond to the following published article:

A. Singh, S. Pakhira Exploring the Active Site and Catalytic Activity of N-Coordinated Ni_2 Dual-Atom Catalysts for Oxygen Reduction Reaction, ACS Appl. Energy Mater., 8 (2025), 1544−1560. DOI: https://doi.org/10.1021/acsaem.4c02649.

Conclusions: In conclusion, this thesis has explored the innovative design of electrocatalysts using advanced computational methods to enhance the oxygen reduction reaction (ORR), a key process in energy conversion and storage technologies. By focusing on materials such as niobium-doped zirconium diselenide, platinum-doped zirconium disulfide, and cobalt-encapsulated carbon nanotubes, the research has provided new insights into mechanisms and pathways of ORR, the structure-activity relationships and identified promising ORR pathways for improving electrocatalytic efficiency. The findings underscore the potential of these materials to serve as cost-effective alternatives to traditional noble metal catalysts, contributing significantly to the advancement of sustainable energy solutions. This work sets the stage for future research to further enhance the efficiency and commercial viability of electrocatalysts in fuel cells and other energy applications.

References:

[1] www.energyinst.org/statistical-review/home.

[2] C. Zhang, X. Shen, Y. Pan, Z. Peng, A review of Pt-based electrocatalysts for oxygen reduction reaction, Front. Energy. 11 (2017) 268–285.

[3] V. Urbanová, P. Lazar, N. Antonatos, Z. Sofer, M. Otyepka, M. Pumera, Positive and negative effects of dopants toward the electrocatalytic activity of MoS_2 and WS_2: experiments and theory, ACS Appl. Mater. Interfaces. 12 (2020) 20383–20392.

[4] S. Tian, Q. Tang, Activating transition metal dichalcogenide monolayers as efficient electrocatalysts for the oxygen reduction reaction via single atom doping, J. Mater. Chem. C. 9 (2021) 6040–6050.

[5] Y. G. Zhu, C. Q. Shang, Z. Y. Wang, J. Q. Zhang, M. Y. Yang, H. Cheng, Z. G. Lu, Co and N co-modified carbon nanotubes as efficient electrocatalyst for oxygen reduction reaction, Rare Met. 40 (2021) 90-95.

[6] W. Niu, S. Pakhira, K. Marcus, Z. Li, J. L. Mendoza-Cortes, Y. Yang, Apically dominant mechanism for improving catalytic activities of N-doped carbon nanotube arrays in a rechargeable zinc-air battery, Adv. Energy Mater. 8 (2018) 1800480.

[7] R. Dovesi, A. Erba, R. Orlando, C. M. Zicovich-Wilson, B. Civalleri, L. Maschio, M. Rérat, S. Casassa, J. Baima, S. Salustro, B. Kirtman, Quantum-mechanical condensed matter simulations with CRYSTAL, Wiley Interdiscip. Rev. Comput. Mol. Sci. 8 (2018) e1360.

[8] J. K. Nørskov, J. Rossmeisl, A. Logadottir, L. Lindqvist, J. R. Kitchin, T. Bligaard, H. Jónsson, Origin of the overpotential for oxygen reduction at a fuel-cell cathode, J. Phys. Chem. B. 108 (2004) 17886–17892.

[9] H. J. Monkhorst, J. D. Pack, Special points for Brillonin-zone integrations, J. Mater. Chem. A. 13 (1976) 5188– 5192.

[10] K. Momma, F. Izumi, VESTA 3 for three-dimensional visualization of crystal, volumetric and morphology data, J. Appl. Crystallogr. 44 (2011) 1272–1276.

LIST OF PUBLICATIONS

Publications included in the thesis:

1. A. Singh, S. Pakhira, Synergistic Niobium Doped Two-Dimensional Zirconium Diselenide: An Efficient Electrocatalyst for O_2 Reduction Reaction, ACS Phys. Chem Au 4 (2024) 40-56. DOI: https://pubs.acs.org/doi/10.1021/acsphyschemau.3c00035.

2. A. Singh, S. Pakhira, Unraveling the Electrocatalytic Activity of Platinum Doped Zirconium Disulfide Towards Oxygen Reduction Reaction, Energy Fuels, 37 (2023) 567-579, DOI: https://doi.org/10.1021/acs.energyfuels.2c02831.

3. A. Singh, S. Pakhira, Revealing the Mechanism and Activity of O_2 Reduction Reaction of Co Nanocluster Encapsulated by Carbon Nanotube, Energy Fuels, 38 (2024) 11837-11851. DOI: https://doi.org/10.1021/acs.energyfuels.4c01355.

4. A. Singh, S. Pakhira, Exploring the Active Site and Catalytic Activity of N-Coordinated Ni_2 Dual-Atom Catalysts for Oxygen Reduction Reaction, ACS Applied Energy Materials, 8 (2025) 1544–1560. DOI: https://doi.org/10.1021/acsaem.4c02649 .

Publications other than thesis:

1. Kshirsagar S. D., Shelake S. P., Biswas B., Singh A., Pakhira S., Sainath A. V. S., Pal U., In Situ Decoration of 2D-MoS_2/ZIF-67 Type II Heterojunction for Enhanced Hydrogen Production Under Simulated Sunlight, Catalysis Today 445 (2025) 115056. DOI: https://doi.org/10.1016/j.cattod.2024.115056.

2. S. Mishra, S. Sapru, S. N. Upadhyay, A. Singh, S. Pakhira, A. K. De, Elucidating the Structure-Property Relationship and Ultrafast Exciton/Charge Carrier Dynamics of Layered $Cs_4CuSb_2Cl_{12}$ Double-Perovskite Microcrystals, J. Phys. Chem. C, 127 (2023), 1881-1890. DOI: https://doi.org/10.1021/acs.jpcc.2c07045.

3. S. N. Upadhyay, V. B. Sardar, A. Singh, V. Kumar, S. Pakhira, Elucidating the Oxygen Reduction Reaction Mechanism on the Surfaces of 2D Monolayer $CsPbBr_3$ Perovskite, Phys. Chem. Chem. Phys., 24 (2022) 28283-28294. DOI: https://doi.org/10.1039/D2CP03432H.

4. H. K. Beere, S. Pakhira, P. Yadav, A. Singh, S. N. Upadhyay, P.B. Naik, N. S. Kotrappanavar, D. Ghosh, Realizing Favorable Synergism Towards Efficient Hydrogen Evolution Reaction with Heterojunction Engineered Cu_7S_4/CuS_2/NiS_2 and Functionalized Carbon Sheet Heterostructures, Adv. Mater. Interfaces, 9 (2022) 2201478. DOI: https://doi.org/10.1002/admi.202201478.

TABLE OF CONTENTS

LIST OF FIGURES

LIST OF TABLES

ACRONYMS

μ	:	Chemical potential
η	:	Theoretical overpotential
2D Nb-$ZrSe_2$	:	Two-dimensional single-layer Nb-doped zirconium diselenide
AIMD	:	*Ab initio* molecular dynamics
AO	:	Atomic orbital
B3LYP	:	3 parameter BLYP hybrid functional
BFGS	:	Broyden–Fletcher–Goldfarb–Shanno
BLYP	:	Becke-Lee-Yang-Parr
CB	:	Conduction band
CPD	:	Carbonized polymer dot
CNT	:	Carbon nanotube-based
Co@N-CNT	:	Nitrogen-doped CNT encapsulated Co nanoparticle
Co@SWCNT	:	Cobalt nanoparticle-encapsulated single-wall carbon nanotubes
CGTO	:	Contracted Gaussian-type orbital
CHE	:	Computational hydrogen electrode
CIF	:	Crystallographic information file
COFs	:	Covalent organic frameworks
DAC	:	Dual-atom catalyst
DFT	:	Density functional theory
DFT-D	:	DFT with a semiempirical dispersion correction
DOSs	:	Total density of states
DZ	:	Double zeta
ECPs	:	Effective core potentials
E_F	:	Fermi energy level
E_g	:	Electronic band gap

ER	:	Eley–Rideal
FE	:	Finite element
GGA	:	Generalized gradient approximation
GTO	:	Gaussian-type orbital
HER	:	Hydrogen evolution reaction
HF	:	Hartree-Fock
HK	:	Hohenberg-Kohn
HOR	:	Hydrogen oxidation reaction
HSE	:	Heyd-Scgseria-Enzerhof
IUCr	:	International Union of Crystallography
KMC	:	Kinetic Monte Carlo
KS	:	Kohn-Sham
LCAO	:	Linear combination of atomic orbitals
LDA	:	Local density approximation
L-H	:	Langmuir-Hinshelwood
MABs	:	Metal-air batteries
MC	:	Monte Carlo
MD	:	Molecular dynamics
MM	:	Molecular mechanics
MOFs	:	Metal-organic frameworks
N-SWCNT	:	Nitrogen-doped single-wall carbon nanotubes
OER	:	Oxygen evolution reaction
ORR	:	Oxygen reduction reaction
PBE	:	Perdew-Burke-Ernzerhof
PBE0	:	Hybrid PBE functional
PDOS	:	Partial density of states
PEMFC	:	Proton Exchange Membrane Fuel Cells

PES	:	Potential energy surface
PGM	:	Pt group metals
PGTO	:	Primitive Gaussian-type orbital
PSB	:	Powell symmetric Broyden
Pt-ZrS_2	:	Pt-doped 2D monolayer zirconium disulfide
PW86	:	Perdew-Wang 1986 functional
PW91	:	Perdew-Want 1991 functional
QM/MM	:	Hybrid quantum mechanics/molecular mechanics model
RFO	:	Rational function optimization
RMS	:	Root-mean-square
RRHO	:	Rigid-rotor-harmonic oscillator
SAC	:	Single-atom catalyst
SCF	:	Self-consistent field
SHE	:	Standard hydrogen electrode
SO	:	Spin-orbital
STO	:	Slater-type orbital
SWCNT	:	Single-wall carbon nanotube
TM	:	Transition metal
TMDs	:	Transition metal dichalcogenides
TS	:	Transition state
TZ	:	Triple zeta
TZVP	:	Triple-ζ valence polarized
UL	:	ORR limited potential
VB	:	Valence band
vdW	:	Van der Waals materials
VESTA	:	Visualization for electronic structural analysis
ZPE	:	Vero-point energy

CHAPTER 1

Foundations of Electrocatalysis: Mechanisms, Materials, and Strategies

This chapter discusses about the escalating global energy demands driven by industrialization and population growth, highlighting the dependence on fossil fuels and the resulting environmental impacts such as CO_2 emissions and climate change. The chapter argues for the exploration of efficient, scalable alternative renewable energy resources, particularly electrochemical energy conversion devices. The chapter provides a comprehensive overview of fuel cells, detailing the hydrogen oxidation and oxygen reduction reactions (ORR), and elucidates the complex multielectron processes involved in ORR. Additionally, the chapter traces the historical evolution of catalysis, from early empirical observations to modern theoretical frameworks, and classifies various types of catalysis while highlighting the role of electrocatalysts in enhancing reaction rates through surface interactions and electron transfer processes. The chapter emphasizes the importance of heterogeneous catalysts in electrocatalysis, where reactions occur on the surface of the catalyst, involving adsorption and desorption of intermediates. This chapter reviews advancements in electrocatalysts toward ORR, highlighting challenges with Pt-based and expensive metal electrocatalysts. This chapter also explores innovative approaches like alloying and non-precious metal catalysts to enhance ORR efficiency and reduce Pt dependence, highlighting the significant progress in the field to enhance fuel cell performance and sustainability. This chapter explores the theoretical and computational design of cost-effective two-dimensional transition metal dichalcogenides (TMDs) as highly efficient electrocatalysts toward ORR in fuel cells. The chapter

examines the structural and electronic properties of these catalysts, exploring ORR mechanisms and pathways, particularly through metal atom doping.

1.1 Introduction: The monotonic growth of industrialization, human population, and global civilization is directly proportional to the ever-increasing energy demand. The most convenient energy sources are fossil fuels (e.g., oil, coal, natural gas), which cover more than 80% of global energy consumption, as shown in the bar chart in Figure 1.1b. The coal demand has been expanded by 0.6% in 2022, surging to its highest consumption rate since 2014. Additionally, global coal production was surged by more than 7% in comparison to 2021. In the year 2022, coal retrained its prominent status as the primary fuel source for global power generation, maintaining a consistent presence at approximately 35.4%, exhibiting a marginal decrease from 35.8% in 2021, as shown in the bar chart in Figure 1.2. Concurrently, natural gas-fired power generation remained steady throughout 2022, holding a proportionate share of roughly 23%[1,2]. Our energy consumption is expected to double in the year of 2100 compared to the recent year. The high and practically unchanged share of fossil fuels in the rapidly increasing energy consumption has the consequence of the rapid depletion of fossil fuel resources and environmental damage due to the emission of pollutant gases (mainly CO_2 and CO). Notably, the emissions resulting from energy consumption contributed significantly, composing a substantial 87% proportion of the total global emissions.

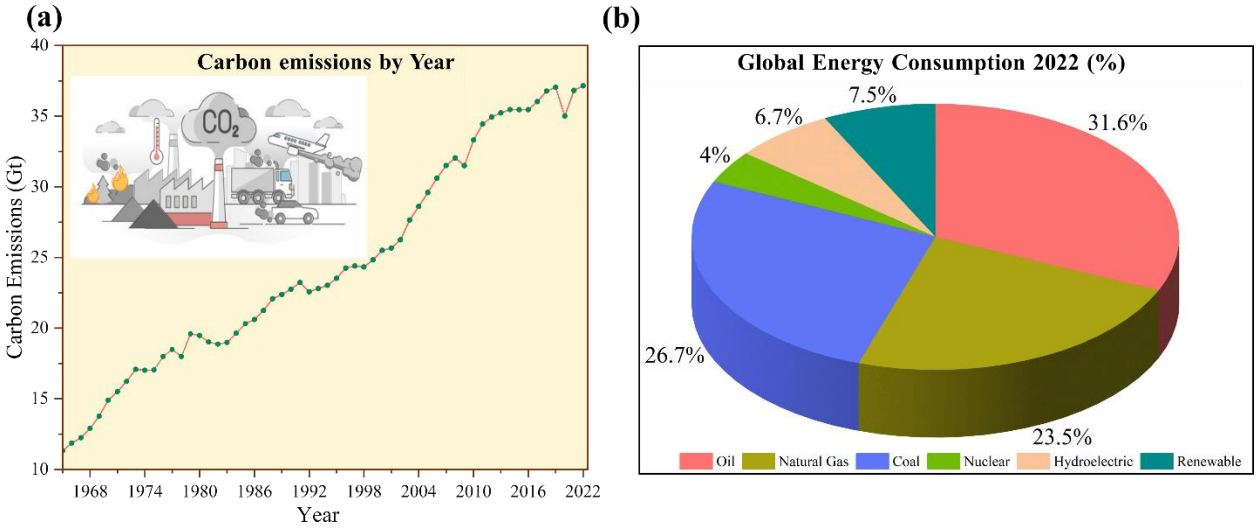

Figure 1.1. *The representation of (a) global carbon emissions by year and (b) global energy consumption by different energy resources.*

The CO_2 stems from energy utilization, industrialization process, flaring, and methane persistently ascended, surging to an unprecedented 39.3 gigatons of CO_2 emission in 2022, as shown in Figure 1.1a[2–4]. These excessive emissions of pollutant gases lead to climate change and global warming, which are significant threats to all life forms. The central goal in this scenario is to develop strong growth and access to renewable energy resources with novel technology. Renewable energy is intensely penetrating global energy, achieving a 7.5% contribution to primary energy consumption in 2022, as shown in the pie chart in Figure 1.1b. The expansion of renewable energy in terms of power generation was 14% of the total generation in 2022, just below the 16% growth rate observed in the previous year, as shown in the pie chart in Figure 1.2[1,2]. This small percentage of renewable energy growth comes from only wind and solar energy. The growth of solar and wind power is not the answer because the expansion of wind and solar energy has a very small impact on fossil fuel demand. The failure in the process of expansion and commercialization of such sustainable energy resources (wind, solar, and hydro) is associated with some severe limitations[5–9]: (1) Intermittency:- solar and wind energy depends on the weather conditions. They are intermittent, and making them a consistent power supply is difficult. (2) Storage capabilities:- storing excess energy generated during peak limit for

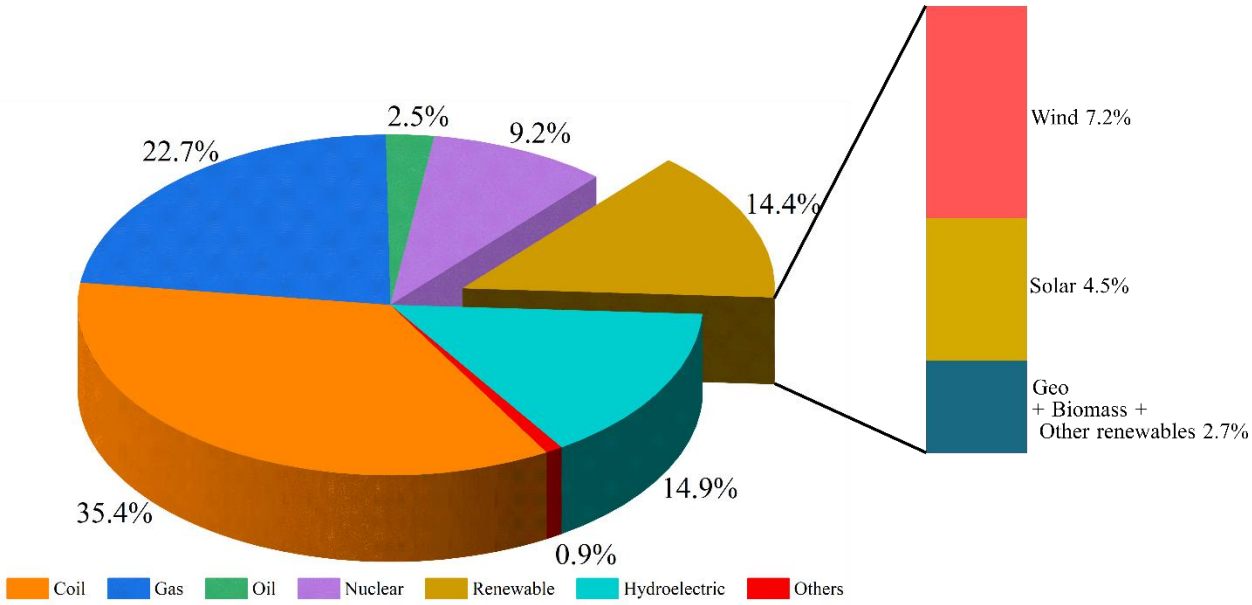

Figure 1.2. *The contribution of the different energy sources in terms of power generation.*

use when the sun is not shining and the wind is not blowing is a significant challenge. (3) Land use: land usage presents another specific challenge, with both solar farms and wind turbines

requiring substantial acreage for effective deployment. This necessarily provides land use conflicts and environmental concerns, especially in densely populated areas. (4) Initial cost: the initial set-up cost for solar panels and wind turbines can be high, although the cost has decreased over time. Additionally, integrating these sustainable sources into the existing energy grid may require substantial infrastructure upgrades. These limitations hinder their seamless, widespread commercialization and highlight the need for alternative renewable energy resources. Thus, exploring dependable, efficient, and scalable alternatives is very much required for sustainable power generation. One promising strategy is electrochemical energy conversion, which uses electrochemical methods and electrochemical reactions to convert small molecules in the atmosphere into valuable added products. These electrochemical methods mainly include water cycle reactions, nitrogen cycle reactions, and carbon cycle reactions. Among all core reactions, water cycle reactions have received widespread attention for clean energy production and conversion. The electrolyzer and fuel cells are the two essential electrochemical devices in the water cycle process. For electrolyzer cells, the hydrogen evolution reaction (HER) and oxygen evolution reaction (OER) occur at the cathode and the anode, producing gases hydrogen and oxygen, respectively, by spilling water into its components. The hydrogen and oxygen produced in the electrolyzer are used to produce energy in the case of the fuel cells through the oxygen reduction reaction (ORR) and hydrogen oxidation reaction (HOR) at the cathode and anode of the fuel cell, respectively. The optimal technological loop for the water cycle involves water splitting via HER and OER to produce fuel, followed by power generation through ORR and HOR in fuel cells[10–12].

1.2 Objective: This thesis mainly concentrates on the theoretical and computational discovery and development of efficient and cost-effective two-dimensional materials-based and carbon nanotube-based (CNT) electrocatalysts through high-throughput computing methods for ORR occurring at the cathode side of fuel cells. The main objectives of the thesis are listed below.

(1) The first objective of this thesis is to design and explore cost-effective, layered two-dimensional (2D) transition metal dichalcogenides (TMDs) as electrocatalysts, focusing on understanding their fundamental structural and electronic properties to optimize their performance for energy conversion processes.

(2) The second objective is to study the structural properties, electronic properties, and catalytic active sites with the electrocatalytic performances toward ORR after engineering the basal plane of the 2D TMDs, mainly by introducing the substitutional metal atom doping on the 2D TMDs materials.

(3) The third objective is to study the electrochemical properties of carbon-based materials, particularly carbon nanotubes (CNTs) as electrocatalysts, particularly focusing on how encapsulating metal clusters within the CNTs alters their structural, electronic, and catalytic properties to boost their efficiency toward ORR.

(4) The fourth objective is to conduct a comprehensive study of ORR mechanisms on the surface of the 2D TMDs materials and CNTs, exploring various reaction pathways and their implications for enhancing catalytic efficiency with high selectivity in energy conversion systems.

1.3 Fundamentals of Fuel Cells: A fuel cell represents an electrochemical apparatus that systematically and efficiently transforms the chemical energy of externally provided fuel and oxidant into electrical energy. The core elements of the fuel cell are two electrodes, namely the anode and cathode, and a proton exchange membrane which comprises a polymer electrolyte in direct contact with an anode and cathode on opposite sides as represented in Figure 1.3b. The capacity of the membrane is to facilitate the conduction of the proton and maintain isolation between the fuel and oxidant, thereby preventing the mixing of the two gases. Hydrogen fuel undergoes decomposition at the anode, yielding the protons and electrons. Proton traverses the membrane to the cathode while electrons navigate the external circuit to the cathode, generating an electrical current. At the cathode, electrons reunite with protons, harmonizing with O_2 to produce water as a reaction byproduct, which is then expelled from the cell. The procedure of the water-splitting cycle has been represented in Figure 1.3a-b. The cleavage of the hydrogen molecule is relatively straightforward at the anode, but more robust oxygen molecules possess a greater challenge for splitting at the cathode, resulting in notable activation loss. Thus, the effective performance of the fuel cells relies on the membrane characteristics, design, and efficiency of electrocatalytic materials as well as influential parameters like temperature. The fuel cells have the capability to generate power ranging from a fraction of a watt to several hundred kilowatts, making them suitable for different applications from stationary power systems to vehicles of varying

sizes[13,14]. The fuel cell operations are governed by two electrochemical reactions: HOR at the anode and ORR at the cathode. The specific reactions are articulated as follows:

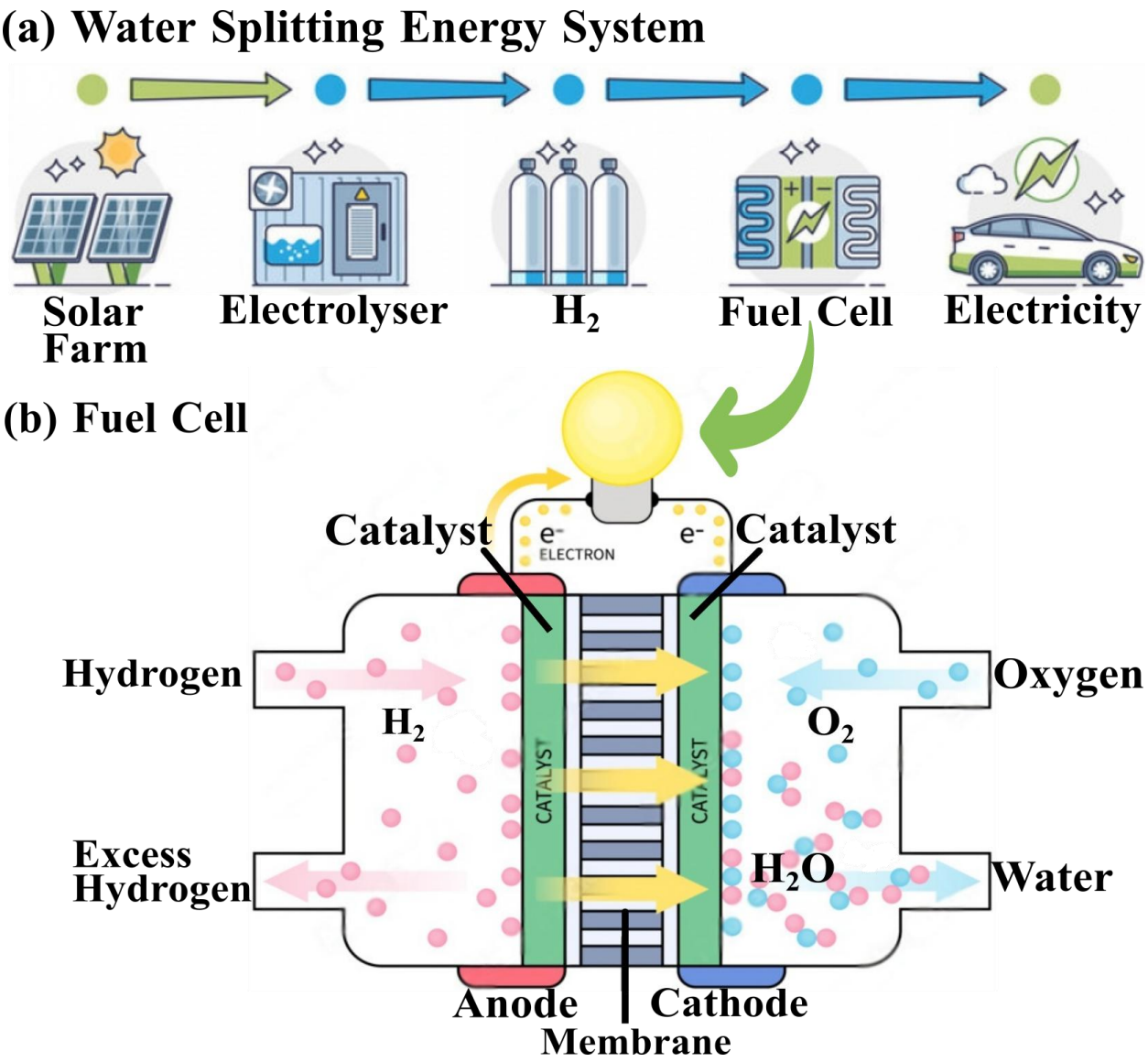

***Figure 1.3**. Schematic depiction of (a) the electrocatalytic water splitting process and (b) the fuel cell components.*

Anode reaction:- The hydrogen molecule undergoes electron detachment separating proton and electron.

$$H_2 \longrightarrow 2H^+ + 2e^- \ldots\ldots\ldots\ldots\ldots\ldots\ldots\ldots\ldots\ldots (1)$$

This corresponds to the anode potential E^o of 0.00 V versus standard hydrogen electrode (SHE) under standard conditions.

Cathode reaction:- The cathode reaction involves the reduction of oxygen in the formation of water.

$$2H^+ + 2e^- + \frac{1}{2}O_2 \longrightarrow H_2O \ldots\ldots\ldots\ldots\ldots\ldots\ldots\ldots\ldots\ldots\ldots\ldots (2)$$

This corresponds to the cathodic potential E^o of 1.23 V versus SHE under the standard conditions. Consequently, the comprehensive reaction governing the fuel cell is expressed as:

$$H_2 + \frac{1}{2}O_2 \longrightarrow H_2O \ldots\ldots\ldots\ldots\ldots\ldots\ldots\ldots\ldots\ldots\ldots\ldots\ldots\ldots (3)$$

The HOR is straightforward, whereas ORR involves several sequences and parallel steps. In this thesis, we have explored and studied ORR mechanisms and the different reduction pathways involved in the subject reaction.

1.4 O_2 Reduction Reaction: The ORR holds paramount significance in energy conversion devices such as fuel cells. The mechanism of the electrochemical ORR is indeed complex and can be based on several factors, including the electrode material, catalysts, and electrolytes. Therefore, understanding the ORR mechanism is crucial for improving the efficiency of the electrochemical devices. The ORR can be characterized as the multielectron process that involves several ORR intermediate species. In fuel cell operation, the cathodic reduction of oxygen presents two distinctive routes in acidic media. The first involves a $4e^-$ reduction or transfer pathway, where O_2 adsorbs to the catalytic surface and undergoes reduction to produce water. Conversely, the $2e^-$ transfer pathway involves the formation of an intermediate hydrogen peroxide, which can either undergo addition reduction to form water or chemically decompose, generating both water and oxygen as end products[15–18].

Pathway (a): $4e^-$ pathway

$$O_2 + 4H^+ + 4e^- \longrightarrow 2H_2O \qquad (E^o = 1.229\ V)$$

Pathway (b): $2e^-$ pathway

$$O_2 + 2H^+ + 2e^- \longrightarrow H_2O_2 \qquad (E^o = 0.67\ V)$$

Followed by either the reduction of hydrogen peroxide

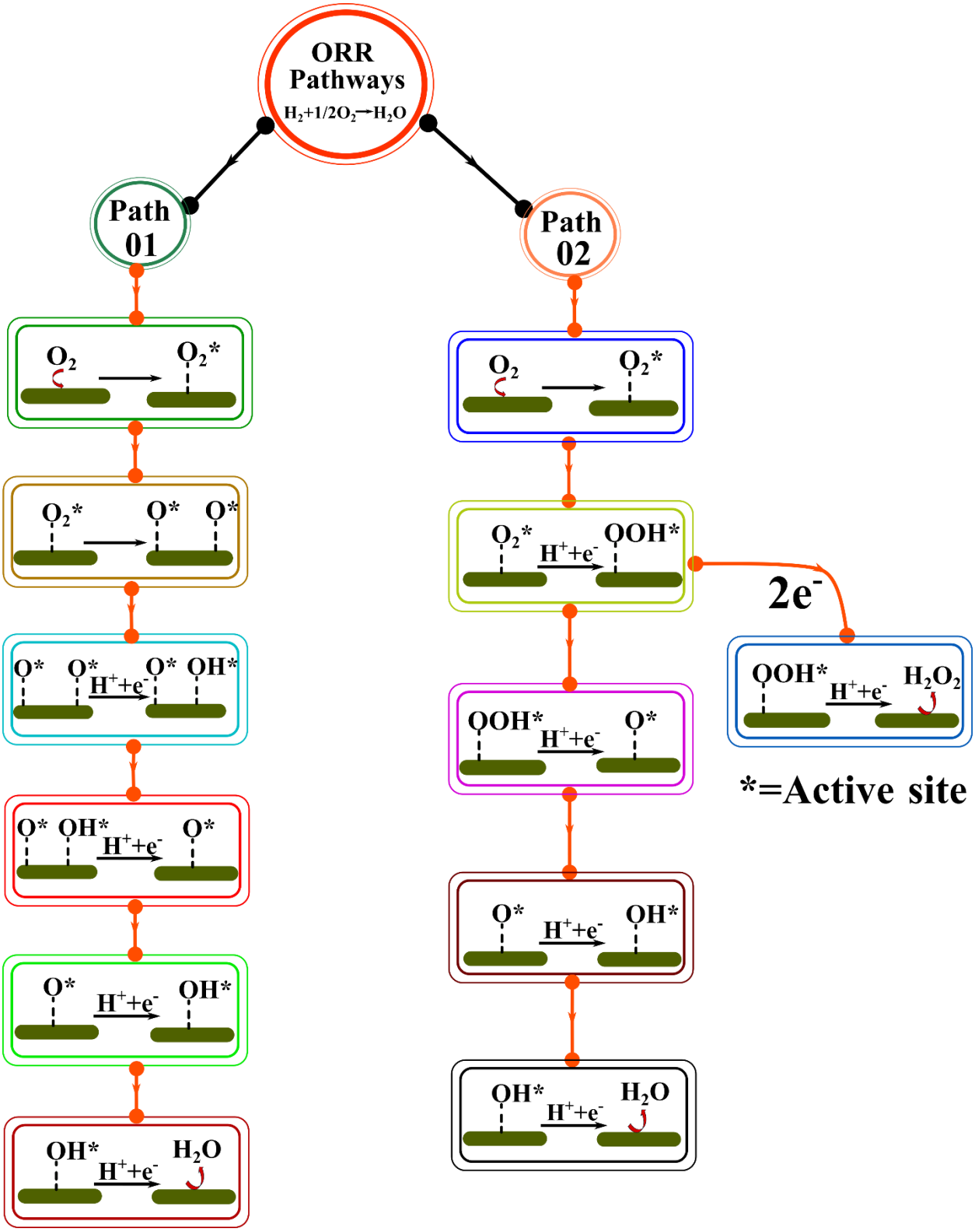

Figure 1.4. *Schematic illustration of the possible routes for electrocatalytic O_2 reduction reaction (ORR).*

$$H_2O_2 + 2H^+ + 2e^- \longrightarrow 2H_2O \qquad (E^o = 1.77\ V)$$

Or by the decomposition of peroxide

$$2H_2O_2 \longrightarrow 2H_2O + O_2$$

Based on the cleavage of the O-O bond and establishment of the O-H bond, the $4e^-$ reduction pathway can be further divided into two different pathways.

Pathway (a1): The initial reaction path is known as the associative pathway. The initial step involves the adoption of the O_2 molecule at the reaction active site in the associative reaction pathway, which is denoted by O_2*, a crucial step for subsequent steps. Once adsorbed, the further oxygen atom on the surface engages in a reaction with an H^+ and e^-, yielding the OOH* intermediate. In the subsequent steps, the release of the water molecule happens, leading to the formation of O* by the reaction of OOH* with an H^+ and e^-. In the final two steps, the oxygen molecule (O*) undergoes successive reduction through a pair of proton-coupled electron transfers, ultimately resulting in the production of another water molecule. The whole reaction steps can be expressed as follows:

$$O_2 \longrightarrow O_2^*$$

$$O_2^* + H^+ + e^- \longrightarrow OOH^*$$

$$OOH^* + H^+ + e^- \longrightarrow O^* + H_2O$$

$$O^* + H^+ + e^- \longrightarrow OH^*$$

$$OH^* + H^+ + e^- \longrightarrow H_2O + *$$

Pathway (a2): Dissociative pathway:- in contrast to the associative mechanism, the dissociative ORR pathway takes a distinctive turn following the adsorption of O_2 onto the reaction site. In the route, the adsorbed O_2 undergoes a bond-breaking process after the adsorption on the reaction site, leading to the formation of two distinct oxygen atoms adsorbed at two different reaction sites. Subsequently, one of these adsorbed oxygen atoms goes to a series of two consecutive reduction steps by reaction with the proton-coupled electron pair. These reduction steps convert the adsorbed oxygen atom into the first water molecule. The final two reaction steps mirror those observed in

the associative pathway. Through the pair of proton-coupled electron transfers, the remaining oxygen species on the reaction site undergo a reduction process, ultimately resulting in the product of another water molecule. The whole reaction steps can be expressed as follows:

$$O_2 + * \longrightarrow O_2^*$$

$$O_2^* \longrightarrow 2O^*$$

$$2O^* + H^+ + e^- \longrightarrow O^* + OH^*$$

$$O^* + OH^* + H^+ + e^- \longrightarrow O^* + H_2O$$

$$O^* + H^+ + e^- \longrightarrow OH^*$$

$$OH^* + H^+ + e^- \longrightarrow * + H_2O$$

where * represents the electrocatalytic active reaction site. The graphical representation of various paths of the ORR has been shown in Figure 1.4. This thesis includes the exploration of better electrocatalysts for ORR and understanding the above ORR processes on the surface of the electrocatalysts to endeavor effective and efficient electrocatalysts.

1.5 The Evolution of Catalysis: A Historical Perspective: Although the concept of catalysis has been recognized since ancient times, a unified theoretical framework only has emerged much later. The earliest recorded use of an organic catalyst dates back to 1552, when Valenius Codus demonstrated the conversion of alcohol into ether using sulfuric acid. For centuries, civilizations attributed the transformation of substances took place for mysterious reasons related to mythology and spirituality. At the dawn of the 19th century, following centuries of speculative ideas and empirical observations about chemical transformations, Swedish chemist Jöns J. Berzelius formally introduced the concept of catalytic forces and catalysis. He is widely recognized for coining the term "catalysis" and describing the decomposition of compounds driven by catalytic forces[19–21]. After a period of empirical evidence, in 1884, J. H. Vantie Hoff described the formal dependence of the reaction rate on temperature $k=Ae^{-Ea/RT}$, while S. Arrhenius, in 1895, understood the physical basis of this empirical relationship, and the equation is now attributed to Arrhenius. The Arrhenius equation describes E_a as the activation energy of the reaction (kJ/mol), R as the gas constant (8.34 J/K·mol), T as the absolute temperature, and A as the frequency factor,

representing the collision frequency. As per Arrhenius, only collisions between molecules that are properly oriented in space and possess energy greater than the activation energy can lead to the formation of products[19]. In 1897-1898, Wilhelm Ostwald provided a detailed account of the state of knowledge on catalysis, identifying it as a kinetic phenomenon. He defined a catalyst as "A catalyst is a material that changes the rate of the chemical reaction without appearing in the final product." Ostwald also highlighted how certain foreign substances can accelerate reaction rates without being consumed in the process. His groundbreaking work on catalysis, along with his contributions to understanding chemical equilibria and reaction rates, earned him the Nobel Prize in 1909[20,22]. Meanwhile, a pioneering chemist, Paul Sabatier, introduced a groundbreaking molecular perspective on catalysis known as the "Sabatier principles". This concept links catalytic activity to the free energy involved in the interaction between the catalyst and reactants. According to this model, the highest catalytic activity is achieved when the adsorption strength is at an optimal level. Additionally, the Sabatier principle offers a kinetic framework for understanding the catalytic cycle and its corresponding elementary reaction steps, including adsorption, surface diffusion, surface reaction, and desorption. In 1912, Paul Sabatier was awarded the Nobel Prize in Chemistry for his pioneering work on hydrogenation, particularly his studies on the hydrogenation of ethylene and carbon monoxide using nickel and cobalt catalysts[23–25]. A remarkable step in catalysis took place in 1918 when methane was produced on an industrial scale using a metal (iron) catalyst by the Haber-Bosch process[26]. Afterward, H. S. Tayor, in 1925, focused main attention on the concept of the active sites and proposed that total catalytic solid surface would not be equally active in effective chemical reactions, but there would be heterogeneity in the catalytic efficiency of the solid surface catalyst[27]. In a short time, due to the development of new characterization techniques and computational methods, great progress has been made in the field of catalysts, catalytic materials, and catalytic materials at the electronic level. However, the rational designing of efficient catalysts is still a long-standing challenge in terms of cost-effectiveness and mass production.

1.6 Exploring the Accelerated World of Catalysis: Types and Mechanisms: Catalysis is a chemical process in which a substance called a catalyst is employed to lower the activation energy barrier of a reaction, thereby accelerating the reaction rate without altering the equilibrium state. A catalyst functions by increasing the speed at which the reaction approaches equilibrium without being substantially consumed in the process, influencing only the reaction kinetics. It has no

impact on the thermodynamics or the equilibrium composition of the reaction. In contrast, reactions proceeding without a catalyst occur at a slower rate because of the high activation energy of the path to achieve the product from reactants. But, in the presence of a catalyst, the efficiency or rate of the particular reaction increases substantially because a catalyst provides an

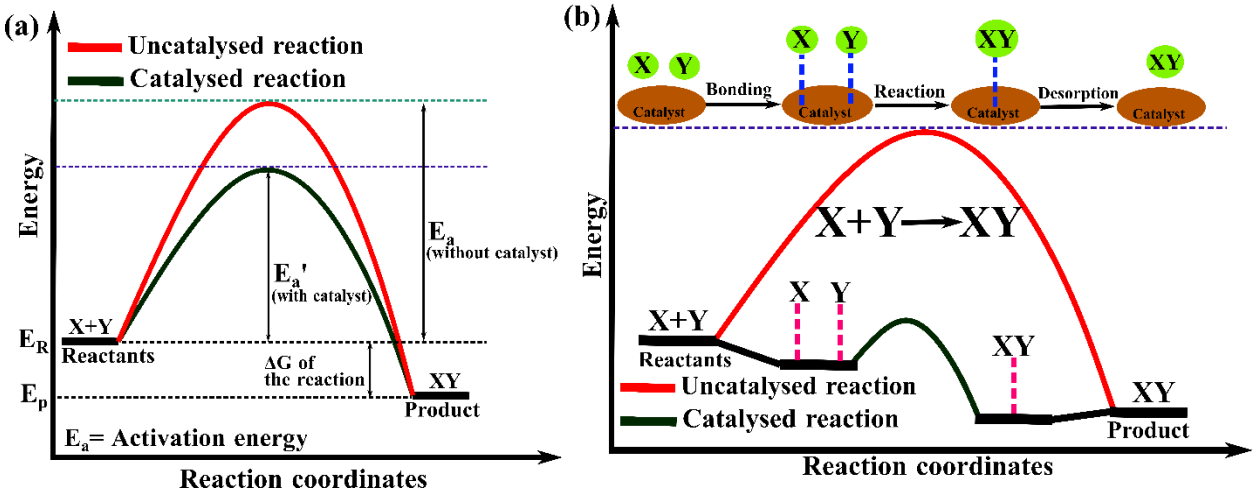

Figure 1.5. *The representation of (a) the catalysts provides an alternative mechanism by providing a different transition state and lowering the activation energy and (b) the sequence of elementary steps of a catalytic reaction.*

alternative route with a lower activation energy, as shown in Figure 1.5a. It is essential to clarify that a catalyst does not directly lower the activation energy of a reaction but instead offers an alternative pathway with a lower energy requirement, making the process more efficient. The catalysis is mainly categorized into three parts: (1) Homogeneous catalysis: in homogeneous catalysis, both reactants and products are in the same phase (i.e., solid, liquid, or gas) as the catalyst itself. Most of the homogeneous catalytic processes are carried out in the liquid phase. (2) Heterogeneous catalysis: The catalysis process in which the catalyst is in a different phase from the reactants and products phase. In heterogeneous catalysis, a solid catalyst catalyzes reactions of molecules in gas or solution. In heterogeneous catalysts, only certain sites on the catalytic surface actually participate in the chemical reaction, and these sites are called chemically active sites on the catalytic surface. (3) Biocatalysis: Biocatalysis is a biological process that relies on enzymes, which are complex protein macromolecules, to serve as catalysts. Enzymes are natural catalysts and can be considered large proteins with structures of very shape-specific active sites[27,28]. To comprehend the catalytic process, let us examine a reaction between two reactant molecules, X and Y, forming the product XY, as illustrated in Figure 1.5b. Initially, molecules X and Y bind to the catalyst. The two reactant molecules, X and Y, then react within the complex to give a product

XY, which is also bonded to the catalyst. In the final stage, XY detaches from the catalyst, restoring the catalyst to its original state and completing the reaction cycle. The role of the catalyst in accelerating the reaction can be understood by analyzing the potential energy diagram in Figure 1.5b, which compares catalytic and non-catalytic pathways. Figure 1.5b is simply the familiar way to visualize the Arrhenius equation that the reaction proceeds when X and Y collide with sufficient energy to overcome the activation barrier (E_a or E_a'). The change in the Gibbs free energy between the reactant X and Y and the product XY is ΔG, as shown in Figure 1.5a. The comparison of catalytic (black color) and non-catalytic (red color) reactions is represented in Figure 1.5b which demonstrates that in the presence of the catalyst (indicated in black), the reaction begins with the binding of reactants X and Y to the catalyst, a process that is exothermic and results in a decrease in free energy. This complex formation occurs spontaneously during the subject reaction. Then, the reaction between X and Y is followed while they are bonded to the catalyst. This step is associated with the activation energy (E_a') of the reaction. This step shows that the activation energy is significantly lowered as compared to the uncatalyzed reaction. Finally, the product XY separated from the catalyst in the last step of the catalyzed reaction. Thus, the catalyst provides an alternative reaction pathway that is much more energetically favorable, which is energetically much more favorable, as represented in Figure 1.5b by the black color. The activation energy for the catalyzed reaction is significantly lower than for the uncatalyzed one, resulting in a faster reaction rate for the catalyzed process[27,28].

1.7 Electrocatalysis and Electrocatalyst: The electrochemical reactions are processes in which charge is transferred across the interface between the electrode and the electrolyte. An electrocatalyst is a material that accelerates the electrochemical reactions (or charge transfer during electrochemical reactions), which consist of an electron transfer oxidation or reduction process, and this phenomenon is called electrocatalysis. In other words, an electrocatalyst facilitates the movement of electrons between the electrode and the reactants, driving a chemical process defined by a half-reaction. During electrocatalytic reactions, the transport of both the electron (e^-) and ion at the electrode surface simultaneously leads to the breaking and forming of chemical bonds. The electrocatalysts are usually heterogeneous catalysts (solid phase), which means that the reactions take place on the surface of the catalyst and the adsorption/desorption of reaction intermediate steps on the surface of the electrocatalyst. The electrocatalyst typically functions as the interface between the electrode and electrolyte medium or as the electrode itself. Redox reactions such as

OER, ORR, HER, and others occur at the electrodes of energy storage devices. HER, ORR, and OER are integral to the development of clean and sustainable energy technologies, including water-splitting devices, transition metal-air batteries (MABs), and fuel cells. However, these electrochemical processes face several challenges[29]. Electrocatalysts play a key role in enhancing reaction rates, such as improving oxygen reduction in fuel cells for energy conversion, oxygen evolution in transition metal-air batteries for energy storage, and hydrogen evolution in water splitting for hydrogen fuel production. Noble metals like Ir (iridium), Pd (palladium), Pt (platinum), and metal oxides are often used as electrocatalysts in these processes[30,31]. However, electrocatalysts based on noble metals present several issues, including susceptibility to gas poisoning, poor stability, high cost, limited selectivity, and scarce availability, all of which hinder the commercialization of these energy technologies[32,33]. To reduce the reliance on expensive metals and their oxides, researchers have focused on developing metal-free and Pt-free catalysts that are efficient for O_2 reduction reactions, O_2 evolution reactions, hydrogen evolution reactions (HER), and other electrochemical processes. The key characteristics of ideal electrocatalysts include (1) high catalytic activity, (2) large surface area, (3) excellent electrical conductivity, (4) long-term stability, and (5) cost-effectiveness with durability.

In this thesis, the main focus will be on the design and development of efficient and effective electrocatalysts for electrochemical ORR at the cathode of the fuel cell. Here, the electrocatalytic reactions are studied based on the Langmuir-Hinshelwood mechanism (L-H) and Eley–Rideal (ER) reaction mechanisms[34,35]. We basically focused on the transition metal dichalcogenides (TMDs) and carbon-based electrocatalysts for the oxygen reduction reaction.

1.8 Advancements in Electrocatalysts for Oxygen Reduction Reaction: The continued reliance on conventional fuels, particularly in transportation and power generation, is driving harmful climate change due to greenhouse gas emissions. To address this, high-capacity energy sources such as metal-air batteries and fuel cells have been developed to meet the growing demand for clean energy in transportation applications as well as the usage of renewable energies. The future of green energy calls for the development of efficient renewable energy conversion and storage devices. The fuel cells can convert chemical energy into electricity and are regarded as one of the most promising energy technologies. However, achieving optimal practical efficiency and widespread commercial applications of the fuel cells is challenging due to the slow kinetics of the

ORR at the cathode of the fuel cells. The difficulty of oxygen reduction is due to the particularly high energy of the O=O bond (498 KJ/mole) and the kinetically slow activation. At present, precious platinum (Pt) is the most efficient electrocatalyst with prominent high activity. However, the scaling up of the Pt electrocatalysts-based fuel cells faces some major challenges, including scarcity, susceptibility to carbon monoxide poisoning, and exorbitant cost of the Pt noble metal electrocatalyst[36–38]. To achieve optimal fuel cell performance, significant focus has been placed on improving the slow kinetics of the ORR at the cathode, which necessitates nearly eight times more Pt loading (~0.4 mg/cm^{-2}) compared to the anode of the fuel cell[39,40]. Since Pt is a scarce and expensive metal, extensive research has been focused on reducing its usage in the cathode or finding a cost-effective, abundant, and efficient alternative to replace it entirely to enable the large-scale application of fuel cells. A facile and effective way is to form alloys and compounds of precious metals with Pt group metals and other metals to reduce the loading of the precious Pt metal without compromising the catalytic activity of the electrocatalysts[41,42]. Cui et al. represented the Pt alloys, namely Pt_3M alloys (M= Ni, Co, Fe, V, Ti, Sc) supported on O-doped graphene, showing high ORR activity with a significantly lower precious Pt metal loading[43]. Sun et al. studied the catalytic activity of the Pt-Cu alloys toward ORR through experimental and theoretical methods. They reported that Pt-Cu alloys have shown an enhanced ORR activity than the commercial benchmark Pt/C electrocatalyst[44]. Duan et al. proposed that hierarchical nanoporous PtTi alloys exhibit excellent electrocatalytic performance for ORR[45]. Wang et al. developed FePt alloys with experimental and DFT methods and they reported the excellent catalytic activity of the FePt toward ORR[46]. In this series, numerous Pt alloys with Pt group and other metals electrocatalysts have been investigated as ORR through the combination of theory and experiment[47–49]. Furthermore, metal oxides, nitrides, carbides, and sulfides have been extensively studied as electrocatalysts for ORR and demonstrated excellent electrocatalytic activity towards ORR[50–54]. However, all the metal-based electrocatalysts are interlinked with some serious challenges, including their high cost, insufficient stability, and scarcity in the earth's crust, which are critical barriers to large-scale practical applications. To realize the large-scale applications of renewable energy, it is significant to explore and develop an earth-abundant, cheap, highly stable, and highly active electrocatalyst for ORR. Since the discovery of graphene, various 2D materials have been synthesized experimentally and theoretically studied their properties with the applications. Moreover, they are widely used in different fields, such as catalysts,

electrochemical energy storage devices, photocatalysis, electronics, optoelectronics, spintronics, and so on[55,56]. The 2D graphene-based materials have attracted significant interest as effective ORR catalysts due to their excellent conductivity, affordability, and large surface area[57]. In addition, other carbon-based heterostructures with high electronic conductivity and uniformly distributed active sites have been extensively studied as potential ORR electrocatalysts[58]. Building on the success of graphene, there has been growing exploration of other 2D materials, such as 2D metal-organic frameworks (MOFs), 2D covalent organic frameworks (COFs), hexagonal boron nitrides, MXenes, and 2D transition metal dichalcogenides (TMDs) for their potential usage as ORR electrocatalysts[56]. In the past few years, 2D TMDs have represented a promising candidate for electrocatalysis due to their vast properties and their capabilities to accept electrons and protons. Several applications, such as solar cells, electronics, biomass, electrocatalysis, and batteries, have emerged due to the extensive range of properties of the TMDs[59]. Various 2D TMDs have been synthesized experimentally and theoretically and studied as an application of electrocatalysts for various electrochemical reactions, such as HER and ORR, due to various superior properties such as high thermal stability, high oxidative resistance, earth abundance, and unique electronic structure[59]. MoS_2 is one of the rising TMDs in the quest for an alternative electrocatalyst for electrochemical reactions. Jaramillo et al. determined the active site and catalytic activity of the MoS_2 towards ORR and proposed that the electrocatalytic activity measurements for HER correlated linearly with the number of edge sites on the MoS_2 electrocatalysts[60]. Tsai investigated various layered TMDs electrocatalysts using density functional theory (DFT) and reported that the optimal hydrogen binding is not achievable for stable basal planes, whereas it is possible for the edge sites of the TMDs[61]. Tiaet al. performed systematic DFT calculations to examine the ORR performance of a series of sulfur-based TMDs (TM = Ti, Zr, Hf, V, Nb, Ta, W, Re, and Pt) in different phase structures (2H, 1T and 1T')[62]. It is found that the surface S layers (basal plane) of pristine TMDs are catalytically inactive for the ORR and are limited by weak O_2 activation. Both experimental and theoretical studies have demonstrated that only the edge side of the 2D TMDs possesses high electrocatalytic activity toward electrochemical reactions, while the basal plane of defect-free TMDs is catalytically inert. In other words, edges of TMDs have shown to be catalytic active unless flakes of small sizes are used, and their concentrations are naturally relatively low[62,63]. Thus, the possible activation of the basal plane of TMDs has been created to increase the electrocatalytic activity of the 2D TMDs

by various strategies such as defect engineering, doping engineering, phase engineering, heterostructure, strain engineering, and so on[64]. Doping stands out as one of the most effective strategies for modifying the structure and enhancing the catalytic activity of TMD electrocatalysts. The introduction of dopant atoms often induces spin density redistribution, leading to changes in the adsorption behavior of O_2 and reaction intermediates. This, in turn, enhances the efficiency of the ORR near the dopant atoms on the material's surface. For instance, Xio et al. theoretically demonstrated that Co/Ni-doped 2H-MoS_2 functions as exceptional ORR electrocatalysts by effectively activating O_2[65]. Experimentally, Pumera et al. showed that Fe and Mn doping on MoS_2 improved its catalytic performance for ORR[65]. Zhang et al. revealed that the ORR activity of N and P-doped MoS_2 monolayer originated from spin density changes introduced by the dopant atoms[65].

Along the line of exploration of inexpensive electrocatalysts, carbon-based materials are another active area of modern electrocatalytic science. In particular, graphene and carbon nanotubes (CNTs) have garnered significant attention for ORR applications due to their outstanding electronic conductivity, large specific surface area, and excellent thermal and mechanical properties[66]. Remarkably, integrating heteroatoms and metal clusters into these carbon-based materials can significantly boost their ORR performance by modulating O_2 adsorption, refining catalytic sites, and optimizing the reaction mechanism of the catalyst[67]. Jiao et al. predicted the electrocatalytic performance of a series of graphene doped with nonmetal elements. They synthesized and predicted the ORR performance of graphene doped with N, B, O, S, and P with the help of experimental and theoretical data. This combined experimental and theoretical study revealed that the electrocatalytic performance of the non-metal-doped graphene is comparable with or much better than that of the state-of-the-art Pt catalysts[68]. Recent studies have demonstrated that nitrogen-coordinated transition metals, such as Mn, Fe, and Co, incorporated into graphene exhibit significant ORR catalytic activity[69]. Liu et al. reported that the Fe/N-doped graphene offers promising catalytic properties for ORR[70]. Yu et al. successfully synthesized both undoped and nitrogen-doped single-wall carbon nanotubes (N-SWCNT) using straightforward plasma techniques. Their findings revealed that N-SWCNT displayed excellent electrocatalytic activity for ORR in acidic solutions, with a notable reduction in overpotential compared to undoped CNTs, achieving a value of around 0.52[71]. Furthermore, recent research has shown that heteroatom doping with elements such as N, O, B, S, and P into CNTs induces

charge redistribution on their surface, thereby significantly enhancing their ORR performance [72]. Recently, the use of non-precious metal clusters encapsulated within carbon nanotubes as ORR electrocatalysts has gained intense attention because of the comparable catalytic activity to the Pt-based catalysts but also because of its long-term durability in electrochemical reaction environments. In this kind of electrocatalyst, the encapsulated metal cluster can activate O_2 on the outer carbon surface while the encapsulated metal clusters are protected by the carbon layer from being leached in the electrochemical reaction environment[73]. Wang et al. synthesized nitrogen-doped CNT encapsulated Co nanoparticle (Co@N-CNT) and studied the electrocatalytic activity of the Co@N-CNT. They demonstrated that the Co@N-CNT exhibits good electrocatalytic activity and high stability towards ORR in both alkaline and acidic solutions[74]. Liu et al. described the synthesis of transition metal (Fe, Co, and Ni) nanoparticles encapsulated within nitrogen-doped carbon nanotubes (M/N-CNT, where M = Fe, Co, Ni) through a solid-state thermal reaction. They highlighted the application of these materials as electrocatalysts for both ORR and OER. The optimized Co/N-CNT catalyst demonstrated outstanding bifunctional catalytic performance for ORR and OER, showcasing high efficiency, excellent selectivity, and remarkable long-term durability[75]. Furthermore, Deng et al. designed Fe nanoparticle encapsulated CNT and studied its catalytic activity towards ORR through experimental and theoretical calculations. They demonstrated that the electron transfer from the Fe particle to the CNT activated the CNT for ORR and possessed a good electrocatalytic activity towards ORR[76].

In this endeavor, a vast number of 2D TMDs and carbon-based materials have been investigated for the ORR. Although tremendous progress has been made in the field of TMDs and carbon-based materials electrocatalysts, in terms of knowledge, we are quite lagging in the practical uses of the cost-effective electrocatalyst. A clear understanding of the fundamental properties of materials can assist us in accelerating the functionality of the designed catalysts. Given the continued interest in TMDs and carbon-based materials for electrocatalytic applications such as ORR, it is important to make a depth profile analysis of the electrocatalytic behavior of the 2D TMDs and carbon-based materials family and explore effective strategies to modulate the catalytic activity of the 2D TMDs and carbon-based materials. In practice, the ORR electrochemical reaction is performed at the surface of the materials. In the present thesis work, we have mainly explored some interesting 2D TMD surfaces and carbon-based materials and their properties and electrocatalytic activity by modulating their structure strategically. Furthermore, we

explored the electrochemical ORR mechanism and gained the adsorption and desorption process of the reactants, intermediate reaction species, and product during the ORR using the first principle DFT-based methods.

1.9 Transition Metal Dichalcogenides (TMDs): The TMDs lie in the domain of the two-dimensional van der Waals materials (vdW). TMDs represent a category of compounds characterized by the chemical formula MX_2, where the transition metal is denoted by M, hails from group IV (such as Ti, Zr, Hf, and so on) or group V (Ta, V, so on) or group VI (Mo, W, so on), while X designated the chalcogenides atoms (Se, S, Te, so on). The TMDs are the layered material, and in the composition of these crystals, a single layer is composed of transition metal (M) atoms positioned between two layers of the chalcogen atoms (X), creating an X-M-X configuration. The atoms within the layer are bonded by covalent bonds, whereas the connection between the adjacent layers is facilitated by comparatively weaker van der Waals interactions to form bulk crystals. The interlayer coupling through the weak vdW interactions demonstrates a notable ease of mechanical exploitation into the monolayer. On the other hand, the covalent bond between the M and X atoms within the same plane significantly contributes to the mechanical strength of the TMD crystals[77–79].

To differentiate the polytype of layered TMDs materials, an adapted version of Ramsdell's convention, introduced in 1963, has gained prominence and earned endorsement for "International Union of Crystallography (IUCr)". The TMDs are classified into multiple phases by the stacking sequence of the X-M-X layer and the metal coordination with the chalcogen atoms. The most common stable polytype phases of the layered TMDs are the 2H-MX_2, 1T-MX_2, and 3R-MX_2 phases, as represented in Figure 1.6a-c. In this nomenclature, the first number signifies the number of X-M-X layers required to describe the primitive unit cell and latter defines the symmetry (e.g., trigonal (T), hexagonal (H), and rhombohedral (R)) of the TMD[79–81]. In each case, transition metal atoms are coordinated six-fold by chalcogen atoms.

(a) 2H-MX_2 Phase: In this phase of TMDs, two layers of the X-M-X are used to constitute a unit cell, and H represents the hexagonal symmetry, with the upper and lower chalcogen triangles identical in orientation and does not have inversion symmetry as highlighted in Figure 1.6a. In the 2H phase, the transition metal is coordinated with six chalcogen atoms in a trigonal prismatic

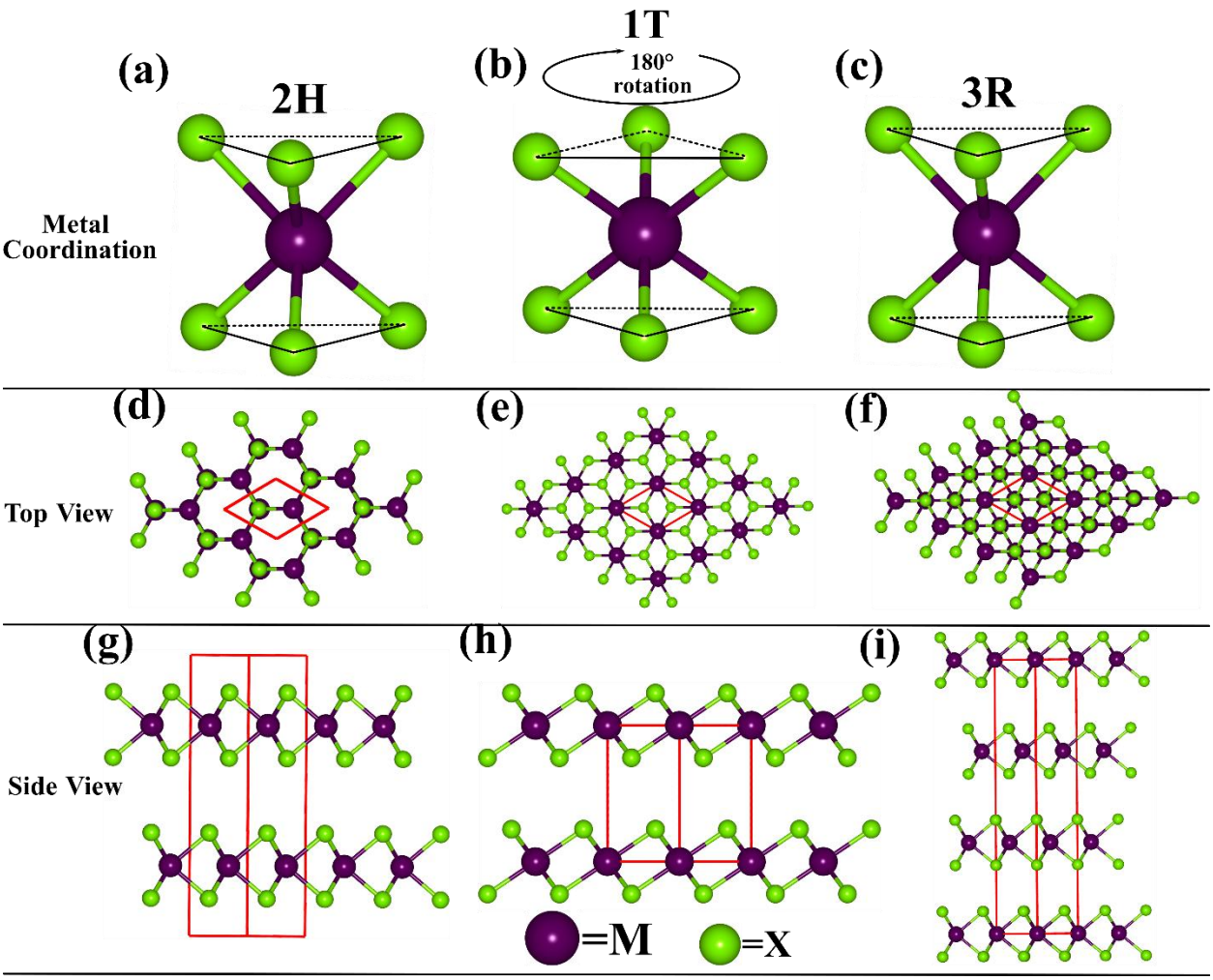

Figure 1.6. *Schematic of metal coordination in different phases (a) 2H phase, (b) 1T phase, (c) 3R phase of transition metal dichacogenides material and the top view of layer stacking sequence in (d) 2H phase, (e) 1T phase, (f) 3R phase and side view of layer stacking sequence in (g) 2H phase, (h) 1T phase, and (i) 3R phase of transition metal dichacogenides materials.*

arrangement. This phase can exist in two variations with distinct stacking sequences: $2H_a$, which follows an AbA CbC stacking pattern, and $2H_c$, which exhibits a CaC and AcA stacking configuration, where uppercase letters denote chalcogen atoms and lowercase letters represent metal atoms. In the $2H_a$ sequence, a metal atom is positioned directly above the atom in the subsequent layer. In contrast, in the $2H_c$ arrangement, each metal atom is aligned above two chalcogen atoms from the layer below, as illustrated in Figure 1.6g. The top view of the 2H phase TMDs has been illustrated in Figure 1.6d. The MoS_2, $MoSe_2$, WS_2, WSe_2 etc., are the key examples of the 2H phase of the TMDs[79–81].

(b) 1T-MX_2 Phase: This phase consists of one layer of X-M-X to form the unit cell of this phase of TMDs and has a trigonal symmetry. In this phase, the lower triangle of the chalcogen atoms is

inverted with respect to the upper triangle of the chalcogen atoms, which then has an inverted symmetry, as highlighted by a line in Figure 1.6b. The transition metal (TM) atom is octahedrally coordinated with six chalcogen atoms in the 1T phase of the TMDs, as shown in Figure 1.6b. This phase follows the AbC stacking sequence in the X-M-X layer where uppercase represents the chalcogen atoms and lowercase represents the transition metal atom. Within the layer, the chalcogens in the two sheets occupy different positions (A and C), as shown in Figure 1.6h. The ZrS_2, $ZrSe_2$, and TaS_2 are a few examples of the 1T phase of the TMDs[79–81].

(c) 3R-MX_2 Phase: This is the third popular polytype of TMDs and contains three X-M-X layers per unit cell stack in the rhombohedral symmetry. In 3R phase TMDs, the transition metal atom coordinated with six chalcogen atoms in a trigonal prismatic fashion, as highlighted in Figure 1.6c. The 3R phase has the stacking sequence AbA CaC BaB, where the upper case represents the chalcogen atom and the lower case represents the transition metal atom. In the 3R phase, all the monolayers are oriented parallel to each other, unlike the 2H phase of the TMDs, as shown in Figure 1.6i[79–81].In TMDs, the Bravais lattice is hexagonal, as in the graphene, with a_1 and a_2 being the in-plane primitive unit vectors, as shown in Figure 1.7a. Consequently, the first Brillouin zone is also hexagonal, with b_1 and b_2 in-plane reciprocal primitive unit vectors. The first Brillouin zone of the monolayer is shown by a dotted area in Figure 1.7b, showing the high symmetry points Γ, M, K, Γ[82,83].

1.10 Electronic Properties of TMDs: The electronic properties of TMDs (MX_2) are influenced by their elemental composition and the coordination of the transition metal (M) with the chalcogen atoms (X). The transition metals in MX_2 typically exhibit either octahedral or trigonal prismatic coordination. The energy levels of the atomic orbitals in these materials lead to the formation of bonding and antibonding bands from the interactions between the chalcogen and metal atoms. In contrast, the d states are not significantly impacted by the M-X interaction and reside between the bonding and antibonding levels. In particular, the electronic properties of TMDs are defined by the non-bonding d-orbitals of the transition metal atom lying between bonding and antibonding orbitals of M-X. The octahedral coordination in the 1T phase of the TMDs leads to dz^2, dx^2-y^2 (e_g) (two-fold) and d_{xy}, d_{yz}, d_{zx} (t_{2g}) (three-fold) crystal field splitting of the d-orbital of transition metal as shown in Figure 1.7e-f. In contrast, for the 2H phase, crystal field splitting of the d-orbitals leads to the formation of the d_z^2, d_{xy}, d_x^2-$_y^2$ (two-fold), and d_{xz}, d_{yz} (two-fold) under the trigonal prismatic

crystal field splitting as represented in Figure 1.7c-d[79,80]. Based on the occupancy of the d orbitals, TMDs can possess either semiconducting or metallic characteristics. The 1T phase generally shows metallic characteristics, while the 2H phase of the TMDs shows semiconducting behavior. Group 4 TMDs (defined as d0 transition metal) tend to favor the 1T phase, while both octahedral and trigonal prismatic phases are observed in group 5 TMDs (d^1). Group 6 TMDs (d^2) primarily adopt the 2H geometry, and group 7 TMDs (d^3) typically exhibit a distorted octahedral structure. Group 10 TMDs (d^6) generally form an octahedral structure[79,80].

1.11 Key Advantages of TMDs for Oxygen Electrocatalytic Reactions: The 2D monolayer TMDs have been synthesized using techniques like liquid exfoliation, micromechanical cleavage, and sulfurization of suitable materials via chemical vapor depositions on various substrates. The 2D monolayer exhibits many distinctive properties than their bulk counterpart, which makes them a potential candidate as an electrocatalyst for electrochemical reactions (ORR). The 2D TMDs have the following properties:

(1) The Layered Structure and Excellent Stability: In layered TMDs bulk materials, the structural arrangements involve numerous covalently bonded 2D planes interlinked by relatively weak van der Waals forces. When subjected to a small external force, these van der Waals interactions can be easily surpassed, leading to material fracture and perception of weakness. On the other hand, the 2D monolayer TMDs have only strong in-plane bonding, contributing to the overall strength of the 2D monolayer TMDs at the atomic scale. Thus, stable monolayer TMDs electrocatalysts are more likely to have a longer lifespan and exhibit sustained electrocatalytic activity.

(2) Higher Surface-to-Volume Ratio: The surface area-to-volume ratio of a material plays a significant role in determining its exposure to the surrounding environment. This ratio holds particular importance because the surface of the catalyst takes part in the electron transfer, intermediate species adsorptions, and catalytic activation. This enhancement exposes a greater number of surface atoms to reaction species, elevating the likelihood of active sites engaging with the reaction intermediate species. Thus, increased contact between material surface and reactants accelerates reaction rates, rendering 2D materials inherently more reactive as compared to their bulk counterpart. This ratio in TMDs increases as the atomic layer number decreases; thus, this

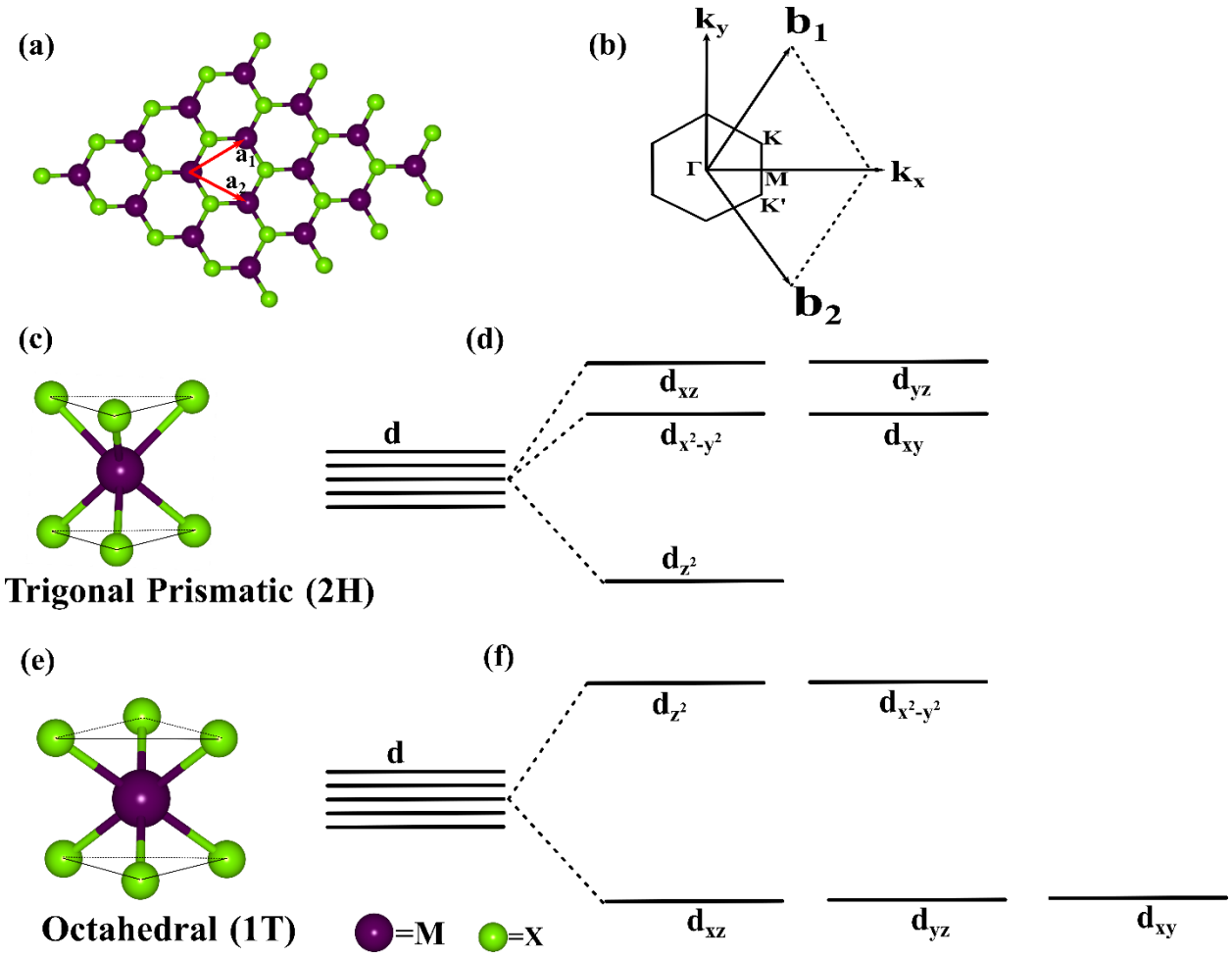

Figure 1.7. *The representation of (a) the hexagonal lattice vectors in ordinal coordinates, (b) the first Brillouin zone of the hexagonal lattice, (c) metal coordination in the 2H phase, (d) the crystal field splitting of d orbitals in the 2H phase, (e) metal coordination in 1T phase, and (f) the crystal field splitting of d orbitals in 2H phase.*

ratio attains a maximum at the monolayer configuration of TMDs. Thus, the high surface-to-volume ratio of 2D monolayer TMDs makes them potential candidates for maximizing catalytic efficiency for electrochemical reactions.

(3) Excellent Charge Transport and Conductivity: The efficiency of the electrocatalyst is equally influenced by the electron dynamics among the active site, electrode, and electrochemical reaction species. The 2D monolayer TMDs mostly possess semiconducting and metallic characteristics. This high conducting nature of the 2D monolayer TMDs increases the electron transfer during the electrochemical reaction process. This property thus minimizes the energy losses and maximizes the overall efficiency of the electrocatalytic 2D monolayer TMDs material.

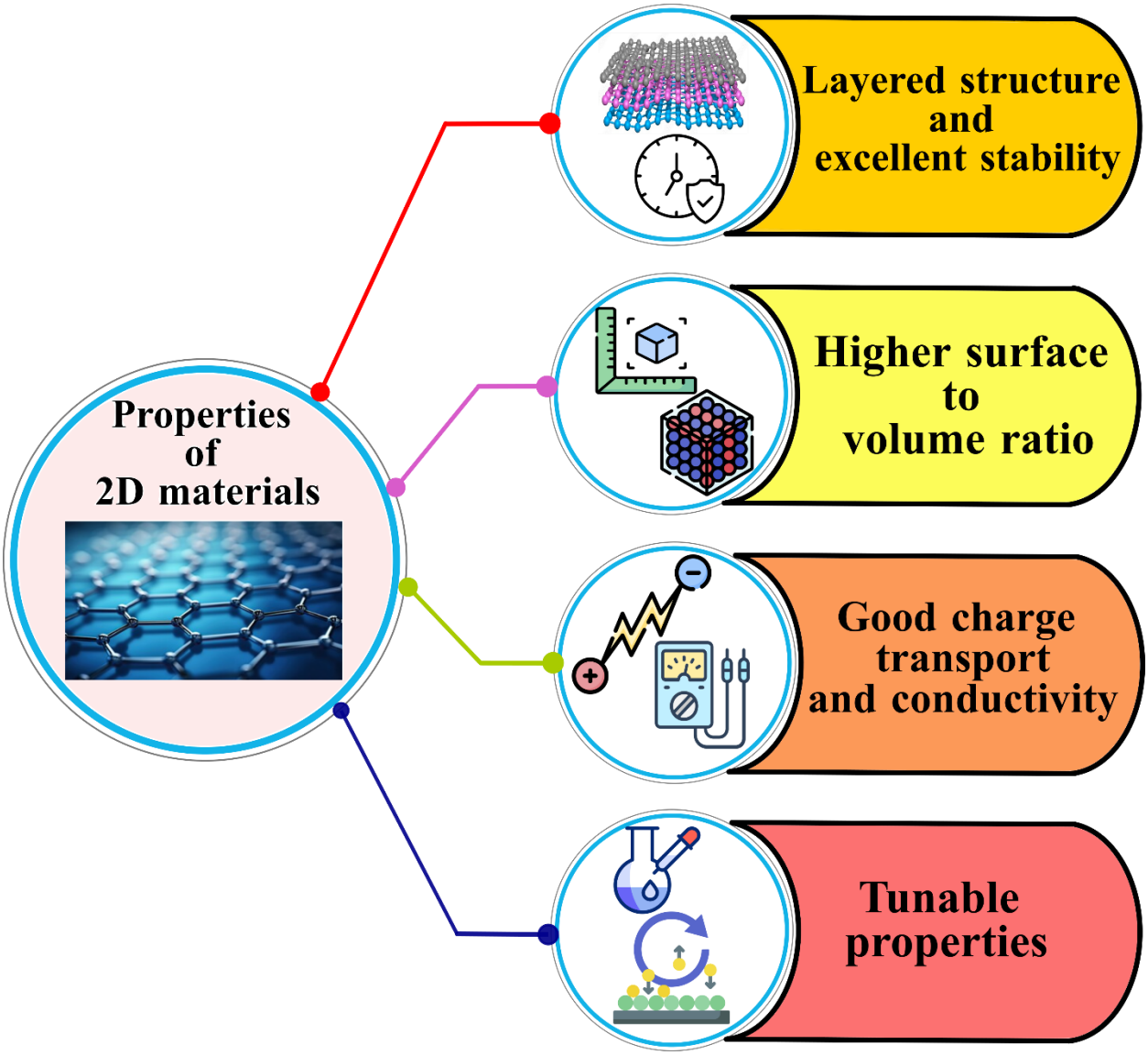

Figure 1.8. *Illustration of the suitable properties of the 2D materials, which makes them a promising candidate for ORR electrocatalysts.*

(4) Tunable Structural, Electronic, and Catalytic Properties: The 2D monolayer TMDs offer excellent opportunities to adjust material properties for achieving the desired activity, selectivity, and electronic structure for particular electrochemical reactions. It is important to highlight here that the basal plane of most 2D monolayer TMDs catalysts exhibits catalytic inertness in most electrochemical reactions, and the edges are catalytic active. However, this characteristic does not undermine the merit of 2D TMDs because the electrocatalytic activity of these materials can be tuned through different methodologies, including doping, strain engineering, intercalation, defect

engineering, alloying, and so forth. The important properties of the TMDs, which make them suitable candidates as electrocatalysts for ORR, have been summarized in Figure 1.8.

1.12 Carbon Nanotubes (CNTs): The discovery of carbon nanotubes has been a topic of ongoing debate regarding its true origins. In 1952, two distinguished researchers, Redushkevich and Lukyanovich, published a clear image showing 50 carbon nanotubes in the Journal of Chemistry in the Soviet Union. Later, in 1979, John Abrahamson provided further evidence for the existence of carbon nanotubes in the 14th biennial carbon conference held at Pennsylvania State University, USA[84]. Although there was a large number of evidence of the existence of carbon nanotubes, the excitement associated with the carbon nanotube was created by Sumio Lijima in 1991 through his literature attributed to the discovery of hollow, nanometer-sized tubes composed of graphite carbon. Lijima reported multi-walled carbon nanotubes in the insoluble arc-burning graphite rods, followed by their single-wall counterparts. Iijima is recognized for the discovery of carbon nanotubes, as his findings in 1991 brought global attention to their existence, inspiring the scientific community[85]. His work sparked significant interest in carbon nanotubes, which have since been explored for various applications owing to their outstanding mechanical and electrochemical properties. Today, carbon nanotubes continue to present a broad range of potential applications.

A carbon nanotube can be conceptualized as a graphene sheet or multiple graphene sheets rolled into a cylindrical shape, as illustrated in Figure 1.9a-d. These nanotubes consist of a highly organized network of sp^2 hybridized carbon atoms arranged in hexagonal patterns, with each carbon atom forming covalent bonds with three neighboring carbon atoms as depicted in Figure 1.9b. The carbon nanotube can be classified based on two criteria: (1) based on the number of cylindrical wall layers and (2) based on the chirality[86].

(1) Based on the Number of Layers: CNTs can be classified based on the number of graphene layers they contain. Here are the primary classifications:

(a) Single-Wall Carbon Nanotube: The structure of a single-wall carbon nanotube can be visualized as a rolled tubular sheet of graphite layer (called graphene layer), or we can say carbon nanotube made up by rolling a graphene layer into a seamless cylinder as shown in Figure 1.9c. The diameter of the single-wall carbon nanotube typically ranges from 0.4 nm to 3 nm.

(b) Multiwall Carbon Nanotubes: The multiwall carbon nanotube consists of multiple layers of graphene sheet rolled up into concentric cylinders, as represented in Figure 1.9d. The multiwall

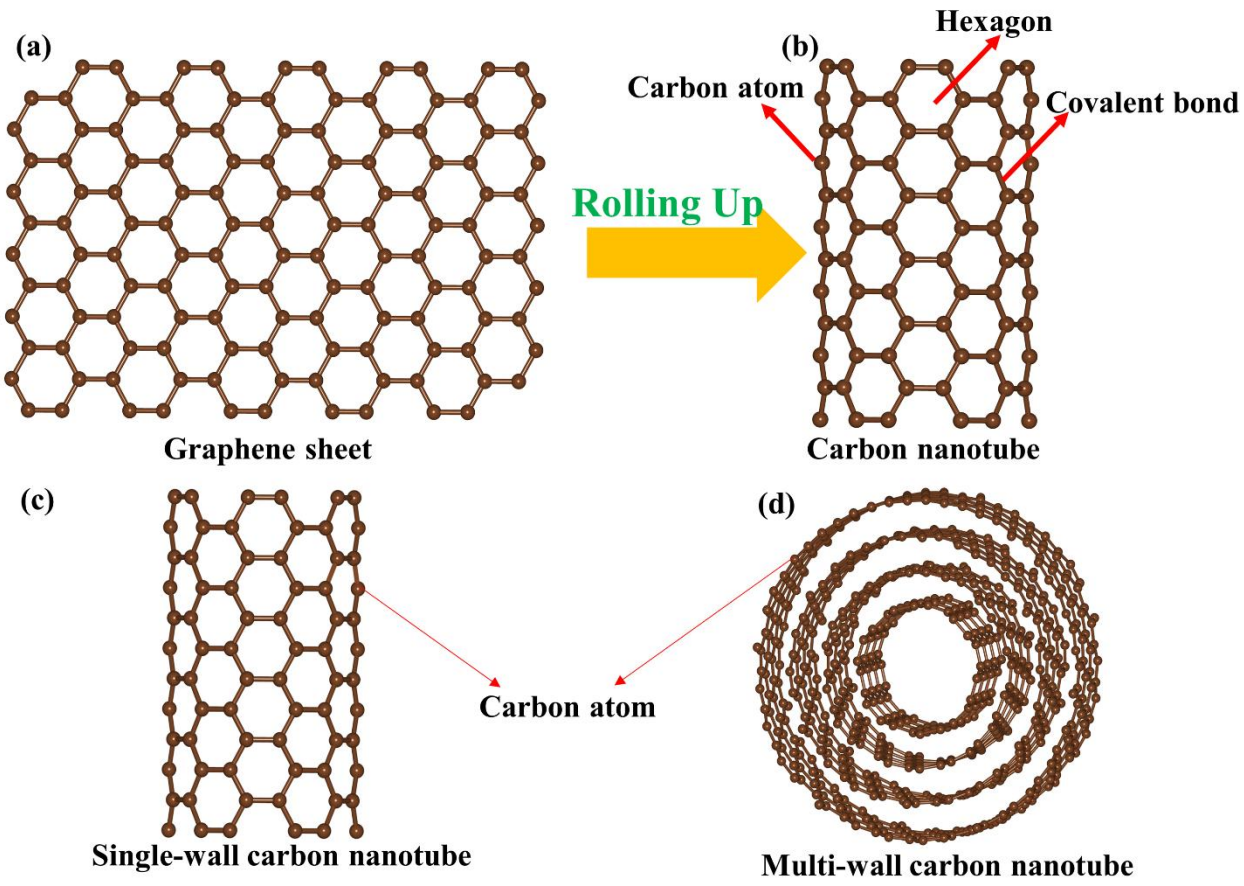

Figure 1.9. *Schematic representation of (a) graphite sheet, (b) carbon nanotube made up by rolling the graphite sheet, (c) single wall carbon nanotube, (d) multi-wall carbon nanotube.*

carbon nanotube can have a diameter ranging from a few nanometers to several tens of nanometers.

(2) Based on the Chirality: In this criterion of the classification, the type of carbon nanotubes depends on how the graphene sheet is oriented on rolling. This can be specified by a vector called a chiral vector, which defines how the is rolled up. Figure 1.10a shows a graphene layer, where the basis vectors of the graphene sheet a_1 and a_2 are represented with the inter angle of 60°. The chiral vector is determined by the two integers (n,m). For a carbon nanotube of given chiral indices (n,m), its chiral vector is:

$$\vec{c} = (n, m) = n\overrightarrow{a_1} + m\overrightarrow{a_2}$$

Which has a magnitude $c = a_0(n^2 + m^2 + nm)^{\frac{1}{2}}$ and defines the circumference of the carbon nanotube. The diameter d of the carbon nanotube is

$$d = \frac{c}{\pi} = \frac{a_0}{\pi}\sqrt{n^2 + m^2 + nm}$$

The direction of the carbon nanotube axis is perpendicular to the chiral vector, as shown in Figure 1.10a, represented by $\vec{T}$. The chiral vector has to be a lattice vector of the graphene. Three types of nanotube structures are considered by rolling a graphene sheet with different orientations about the axis as follows:

(a) The Armchair Structure: Armchair nanotubes have (n,n), meaning that the integers n and m are equal. The name armchair comes from the appearance of the edge of the nanotubes, which resembles the shape of the armchair, as shown in Figure 1.10b. These nanotubes possess metallic character and have the chiral vector $\vec{c} = n(\overrightarrow{a_1} + \overrightarrow{a_2})$.

(b) Zig-Zag Structure: The Zig-zag nanotube has the form (n,0) or (0,m), indicating that one of the integers is zero. The name zig-zag comes from the edge pattern of nanotubes, which looks like a zig-zag, as shown in Figure 1.10c. The zig-zag nanotubes can either be metallic or semiconducting, depending on the structure. The chiral vector of the zig-zag nanotube is $\vec{c} = n\overrightarrow{a_1}$ for (n,0) or $\vec{c} = m\overrightarrow{a_2}$ for (0,m).

(c) Chiral Structure: Chiral carbon nanotubes have the form (n,m), where (n≠m) and m≠0. The chiral nanotube exhibits a helical structure that does not fall into the categories of armchair or zig-zag. Chiral nanotubes can also be either metallic or semiconducting, depending on the values of the n and m. The chiral vector for the carbon nanotube is

$$\vec{c} = n\overrightarrow{a_1} + m\overrightarrow{a_2}$$

The representation of a chiral carbon nanotube has been shown in Figure 1.10d. Understanding the chirality of carbon nanotubes is essential for tailoring their properties for specific appreciations. We have employed the (6,6) carbon nanotube in this thesis to understand the electrocatalytic activity of the carbon nanotubes toward ORR.

1.13 Key Advantages of CNTs for Oxygen Electrocatalytic Reactions: Carbon nanotubes have several properties that make them sightly suitable for use as electrocatalysts, especially in applications such as ORR.

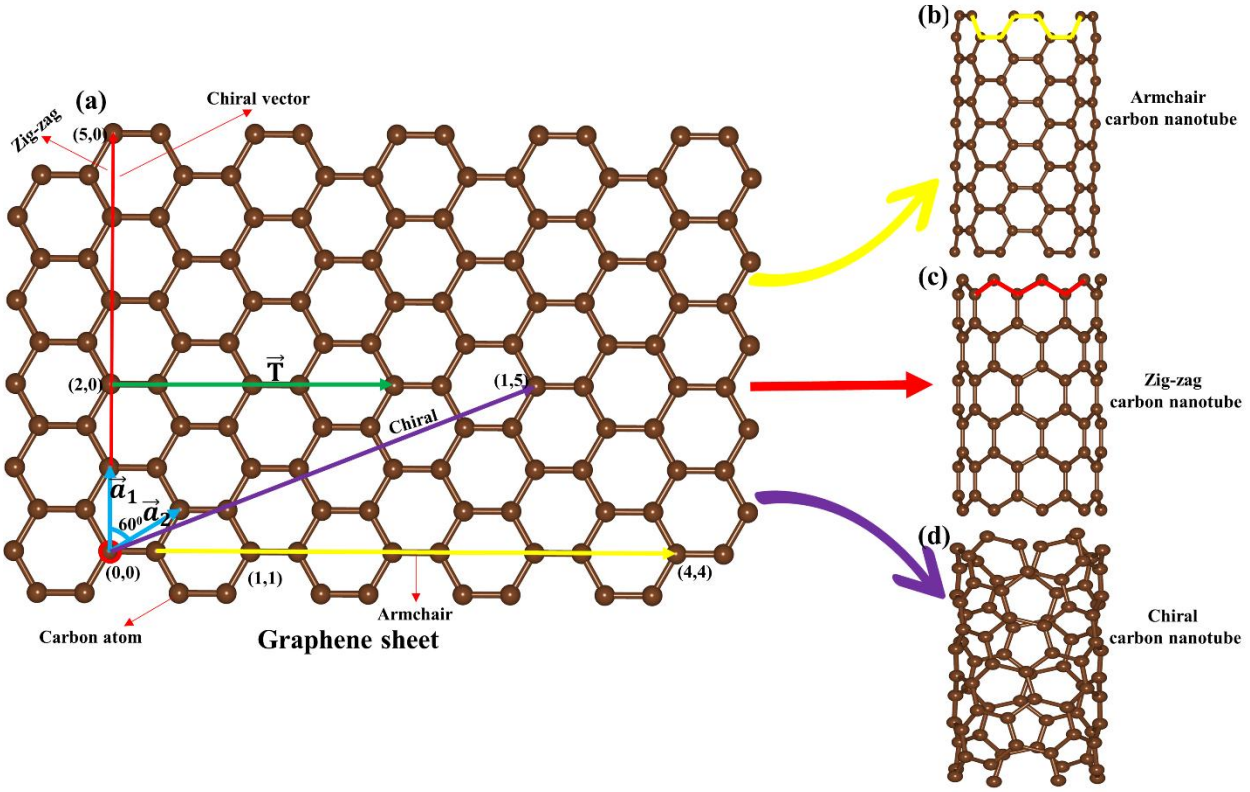

Figure 1.10. *Representation of (a) chiral vector and the depiction of (b) armchair, (c) zig-zag, and (d) chiral single wall carbon nanotube.*

(1) High Electronic Conductivity: The CNTs have excellent electronic conductivity due to their unique electronic structure. The continuous sp^2-hybridized carbon structure brings CNTs excellent electrical conductivity of over 1×10^5 Sm^{-1}. The sp^2 hybridization of carbon atoms in CNTs results in delocalized π electrons, which facilitate efficient electron transfer. CNTs with particular combinations of the n and m can be semiconducting or metallic. Armchair nanotubes are metallic, while others can be metallic and semiconducting. This property is crucial for electrocatalysts, as it ensures that electrons can move quickly to the active sites where the catalytic reaction occurs[87].

(2) Large Surface Area: The unique tubular structure of CNTs endows them with an exceptionally high surface area, with single-wall CNTs theoretically achieving 1315 m^2/g. This large surface area provides abundant active sites for catalytic reaction, allowing for greater

interaction between the catalyst and reactants. Additionally, it enhances the loading capacity for catalytic materials like metal or metal oxides, improving overall catalytic performance[88].

(3) Exceptional Mechanical, Thermal, and Chemical Stability: The sp^2 C-C covalent bond found in the hexagonal lattice of graphite is regarded as one of the strongest chemical bonds in nature. Consequently, CNTs, made entirely of carbon atoms by wrapping graphene sheets into cylindrical structures, are expected to exhibit extraordinary mechanical properties. Both theoretical and experimental studies have demonstrated that CNTs possess an exceptionally high elastic modulus exceeding 1 TPa (compared to diamond's 1.2 TPa) and are reported to be 10 to 100 times stronger than the strongest steel while being much lighter. CNTs also exhibit outstanding thermal stability, with the ability to withstand temperatures as high as 7500°C under normal conditions and 2800°C in a vacuum. Additionally, they serve as excellent thermal conductors due to the strength of their atomic bonds. CNTs, with a graphitized closed structure, have minimal dangling bonds and defects, granting them excellent stability and corrosion resistance in various electrolytes. These exceptional properties of CNTs maintain their structure integrity under harsh electrochemical conditions and physical stresses, contributing to long-term stability and durability[89].

(4) Facile Functionalization: Despite CNTs's exceptional properties, the defect-free CNTs with homogenous Π electron cloud are inert for ORR. The surface of the CNTs does not have much electrochemical activity toward electrochemical reactions. The modification of CNTs with other materials makes them the ultimate candidate as an efficient electrocatalyst for electrochemical reactions such as ORR. The properties of CNTs can be adjusted through both covalent and noncovalent modifications, including doping with heteroatoms like nitrogen and sulfur, attaching functional groups, encapsulating metal clusters, and adsorbing molecules. These modifications do not significantly alter the structural integrity of the CNTs, allow for the fine-tuning of their electronic properties, and further enhance the overall catalytic performance and selectivity[90].

1.14 References:

[1] https://www.bp.com/en/global/corporate/energy-economics.html.

[2] https://www.energyinst.org/statistical-review/home.

[3] https://www.iea.org/energy-system/fossil-fuels.

[4] https://ourworldindata.org/co2-emissions.

[5] H. Sharma, P. Kumar, N. Pal, P. K. Sadhu, Problems in the accomplishment of solar and wind energy in India, Problems of Sustainable Development 13 (2018) 41-48.

[6] Q. Hassan, S. Algburi, A. Z. Sameen, H. M. Salman, M. Jaszczur, A review of hybrid renewable energy systems: Solar and wind-powered solutions: Challenges, opportunities, and policy implications, Results Eng. 20 (2023) 101621.

[7] T. A. Hamed, A. Alshare, Environmental impact of solar and wind energy-A review, J. Sustain. Dev. Energy, Water Environ. Syst. 10 (2022) 1-23.

[8] G. E. Halkos, E. C. Gkampoura, Reviewing usage, potentials, and limitations of renewable energy sources, Energies 13 (2020) 2906.

[9] A. M. Bagher, M., Vahid, M. Mohsen, D. Parvin, Hydroelectric energy advantages and disadvantages, American Journal of Energy Science 2(2015) 17-20.

[10] E. B. Agyekum, C. Nutakor, A. M. Agwa, S. Kamel, A critical review of renewable hydrogen production methods: factors affecting their scale-up and its role in future energy generation, Membranes 12 (2022), 173.

[11] M. P. Browne, Z. Sofer, M. Pumera, Layered and two-dimensional metal oxides for electrochemical energy conversion, Energy Environ. Sci. 12 (2019) 41-58.

[12] S. Aslam, S. Rani, K. Lal, M. Fatima, T. Hardwick, B. Shirinfar, N. Ahmed, Electrochemical hydrogen production: sustainable hydrogen economy, Green Chem. 25 (2023) 9543-9573.

[13] L. Giorgi, Fuel Cells: Technologies and Applications, The Open Fuel Cells Journal, 6 (2013) 1-20.

[14] G. R. Molaeimanesh, F. Torabi, (2023) Fuel cell fundamentals, Third ed., John Wiley & Sons, Inc., Hoboken, New Jersey, USA, pp 1-583 (9781119114208).

[15] A. Kulkarni, S. Siahrostami, A. Patel, J. K. Nørskov, Understanding catalytic activity trends in the oxygen reduction reaction, Chem. Rev. 118 (2018) 2302-2312.

[16] H. Singh, S. Zhuang, B. Ingis, B. B. Nunna, E. S. Lee, Carbon-based catalysts for oxygen reduction reaction: A review on degradation mechanisms, Carbon N. Y. 151 (2019) 160-174.

[17] J. Quílez-Bermejo, E. Morallón, D. Cazorla-Amorós, Metal-free heteroatom-doped carbon-based catalysts for ORR. A critical assessment about the role of heteroatoms, Carbon N. Y. 165 (2020) 434-454.

[18] R. Ma, G. Lin, Y. Zhou, Q. Liu, T. Zhang, G. Shan, M. Yang, J. Wang, A review of oxygen reduction mechanisms for metal-free carbon-based electrocatalysts, Npj Comput. Mater. 5 (2019) 78.

[19] A. H. Zewail, Femtochemistry: Recent progress in studies of dynamics and control of reactions and their transition states, J. Phys. Chem. 100 (1996) 12701-12724.

[20] B. Lindström, L. J. Pettersson, A brief history of catalysis, Cattech. 7 (2003) 130-138.

[21] J. Wisniak, The History of Catalysis. From the beginning to Nobel prizes, Educ. Quim. 21 (2010) 60-69.

[22] G. Ertl, Wilhelm Ostwald: Founder of physical chemistry and Nobel laureate 1909, Angew. Chemie - Int. Ed. 48 (2009) 6600-6606.

[23] H. Ooka, J. Huang, K. S. Exner, The Sabatier principle in electrocatalysis: basics, limitations, and extensions, Front. Energy Res. 9 (2021) 1-20.

[24] J. Kari, J. P. Olsen, K. Jensen, S. F. Badino, K. B. R. M. Krogh, K. Borch, P. Westh, Sabatier principle for interfacial (Heterogeneous) enzyme catalysis, ACS Catal. 8 (2018) 11966-11972.

[25] M. Piumetti, A brief history of the science of catalysis-i: From the early concepts to single-site heterogeneous catalysts. Chim. Oggi. 32 (2014) 22-27.

[26] B. Friedrich, Fritz Haber: Chemist, Nobel Laureate, German, Jew. By Dietrich Stoltzenberg., Angew. Chem. Int. Ed. 44 (2005) 3957-3961.

[27] J. K. Nørskov, F. Studt, F. Abild-Pedersen, T. Bligaard, (2014) Fundamental concepts in heterogeneous catalysis, First ed., John Wiley & Sons, Inc., Hoboken, New Jersey, USA, pp 1-196 (9781118892114).

[28] I. Chorkendorff, J. W. Niemantsverdriet, (2017) Concepts of modern catalysis and kinetics, 3rd ed., Wiley, Weinheim, Berlin, pp 1-505 (978-3-527-33268-7).

[29] R. K. Gupta, P. Banoth, C. Kandula P, (2022) Noble metal-free electrocatalysts: New trends in electrocatalysts for energy applications, First ed., American Chemical Society, United States, pp 1-278 (9780841297340).

[30] F. Ahmad, K. E. Kainat, U. Farooq, A comprehensive review on materials having high oxygen reduction reaction (ORR) activity, J. Chem. Rev. 4 (2022) 374-422.

[31] C. Goswami, K. K. Hazarika, P. Bharali, Transition metal oxide nanocatalysts for oxygen reduction reaction, Mater. Sci. Energy Technol. 1 (2018) 117-128.

[32] H. A. Gasteiger, S. S. Kocha, B. Sompalli, F. T. Wagner, Activity benchmarks and requirements for Pt, Pt-alloy, and non-Pt oxygen reduction catalysts for PEMFCs, Applied Catalysis B: Environmental 56 (2005) 9-35.

[33] R. Borup, J. Meyers, B. Pivovar, Y. S. Kim, R. Mukundan, N. Garland, D. Myers, M. Wilson, F. Garzon, D. Wood, P. Zelenay, K. More, K. Stroh, T. Zawodzinski, J. Boncella, J. E. McGrath, M. Inaba, K. Miyatake, M. Hori, K. Ota, Z. Ogumi, S. Miyata, A. Nishikata, Z. Siroma, Y. Uchimoto, K. Yasuda, K.I. Kimijima, N. Iwashita, Scientific aspects of polymer electrolyte fuel cell durability and degradation, Chem. Rev. 107 (2007) 3904-3951.

[34] V. Bratan, A. Vasile, P. Chesler, C. Hornoiu, Insights into the redox and structural properties of CoOx and MnO_x: fundamental factors affecting the catalytic performance in the oxidation process of VOCs, Catalysts 12 (2022) 1134.

[35] G. Ertl, Reactions at well-defined surfaces, Surf. Sci. 299-300 (1994) 742-754.

[36] J. A. Keith, G. Jerkiewicz, T. Jacob, Theoretical investigations of the oxygen reduction reaction on Pt(111), ChemPhysChem 11 (2010) 2779-2794.

[37] Z. Duan, G. Wang, Comparison of reaction energetics for oxygen reduction reactions on Pt(100), Pt(111), Pt/Ni(100), and Pt/Ni(111) surfaces: A first-principles study, J. Phys. Chem. C. 117 (2013) 6284-6292.

[38] J. K. Nørskov, J. Rossmeisl, A. Logadottir, L. Lindqvist, J. R. Kitchin, T. Bligaard, H. Jónsson, Origin of the overpotential for oxygen reduction at a fuel-cell cathode, J. Phys. Chem. B. 108 (2004) 17886-17892.

[39] M. K. Debe, Electrocatalyst approaches and challenges for automotive fuel cells, Nature 486 (2012) 43-51.

[40] H. A. Gasteiger, J. E. Panels, S. G. Yan, Dependence of PEM fuel cell performance on catalyst loading, J. Power Sources 127 (2004) 162-171.

[41] Y. Bing, H. Liu, L. Zhang, D. Ghosh, J. Zhang, Nanostructured Pt-alloy electrocatalysts for PEM fuel cell oxygen reduction reaction, Chem. Soc. Rev. 39 (2010) 2184-2202.

[42] H. Wang, R. Wang, S. Sui, T. Sun, Y. Yan, S. Du, Cathode design for proton exchange membrane fuel cells in automotive applications, Automot. Innov. 4 (2021) 144-164.

[43] C. Cui, M. Sun, X. Zhu, J. Han, H. Wang, Q. Ge, Oxygen reduction reaction catalyzed by Pt_3M (M = 3d transition metals) supported on O-doped graphene, Catalysts 10 (2020) 156.

[44] J. Sun, J. Shi, J. Xu, X. Chen, Z. Zhang, Z. Peng, Enhanced methanol electro-oxidation and oxygen reduction reaction performance of ultrafine nanoporous platinum-copper alloy: Experiment and density functional theory calculation, J. Power Sources 279 (2015) 334-344.

[45] H. Duan, Q. Hao, C. Xu, Hierarchical nanoporous PtTi alloy as highly active and durable electrocatalyst toward oxygen reduction reaction, J. Power Sources 280 (2015) 483-490.

[46] D. Y. Wang, H. L. Chou, C. C. Cheng, Y. H. Wu, C. M. Tsai, H. Y. Lin, Y. L. Wang, B. J.

Hwang, C. C. Chen, FePt nano dendrites with high-index facets as active electrocatalysts for oxygen reduction reaction, Nano Energy 11 (2015) 631-639.

[47] Z. Tang, W. Wu, K. Wang, Oxygen reduction reaction catalyzed by noble metal clusters, Catalysts 8 (2018) 65.

[48] A. Byeon, W. C. Yun, J. M. Kim, J. W. Lee, Non-precious metal catalysts for two-electron oxygen reduction reaction, ChemElectroChem 10 (2023) e202300234.

[49] Z. Duan, G. Wang, Comparison of reaction energetics for oxygen reduction reactions on Pt (100), Pt (111), Pt/Ni (100), and Pt/Ni (111) surfaces : A first-principles study, J. Phys. Chem. C 117 (2013), 6284-6292.

[50] A. Farhan, M. Murad, W. Qayyum, A. Nawaz, M. Sajid, S. Shahid, M. A. Qamar, Transition-metal sulfides with excellent hydrogen and oxygen reactions: A mini-review, J. Solid State Chem. 329 (2024) 124445.

[51] R. Zeng, Y. Yang, X. Feng, H. Li, L. M. Gibbs, F. J. DiSalvo, H. D. Abruña, Nonprecious transition metal nitrides as efficient oxygen reduction electrocatalysts for alkaline fuel cells, Sci. Adv. 8 (2022) 35-37.

[52] Z. G. Yang, H. M. Xu, T. Y. Shuai, Q. N. Zhan, Z. J. Zhang, K. Huang, C. Dai, G. R. Li, Recent progress in the synthesis of transition metal nitride catalysts and their applications in electrocatalysis, Nanoscale 15 (2023) 11777-11800.

[53] Y. Xue, S. Sun, Q. Wang, Z. Dong, Z. Liu, Transition metal oxide-based oxygen reduction reaction electrocatalysts for energy conversion systems with aqueous electrolytes, J. Mater. Chem. A 6 (2018) 10596-10626.

[54] M. A. Abdelkareem, T. Wilberforce, K. Elsaid, E. T. Sayed, E. A. M. Abdelghani, A. G. Olabi, Transition metal carbides and nitrides as oxygen reduction reaction catalyst or catalyst support in proton exchange membrane fuel cells (PEMFCs), Int. J. Hydrogen Energy 46 (2021) 23529-23547.

[55] P. Kumbhakar, J. S. Jayan, A. Sreedevi Madhavikutty, P. R. Sreeram, A. Saritha, T. Ito, C.

S. Tiwary, Prospective applications of two-dimensional materials beyond laboratory frontiers: A review, IScience 26 (2023) 106671.

[56] T. Li, T. Jing, D. Rao, S. Mourdikoudis, Y. Zuo, M. Wang, Two-dimensional materials for electrocatalysis and energy storage applications, Inorg. Chem. Front. 9 (2022) 6008-6046.

[57] M. Zhang, H. Tao, Y. Liu, C. Yan, S. Hong, J. Masa, A. W. Robertson, S. Liu, J. Qiu, Z. Sun, Ultrasound-assisted nitrogen and boron codoping of graphene oxide for efficient oxygen reduction reaction, ACS Sustain. Chem. Eng. 7 (2019) 3434-3442.

[58] S. P. Mbokazi, T. Matthews, M. P. Chabalala, C. T. Selepe, K. Mugadza, S. S. Gwebu, L. Mekuto, N. W. Maxakato, Recent progress on carbon-based electrocatalysts for oxygen reduction reaction: insights on the type of synthesis protocols, performances and outlook mechanisms, ChemElectroChem 10 (2023) e202300290.

[59] W. Choi, N. Choudhary, G. H. Han, J. Park, D. Akinwande, Y. H. Lee, Recent development of two-dimensional transition metal dichalcogenides and their applications, Mater. Today 20 (2017) 116-130.

[60] T. F. Jaramillo, K. P. Jørgensen, J. Bonde, J. H. Nielsen, S. Horch, I. Chorkendorff, Identification of active edge sites for electrochemical H_2 evolution from MoS_2 nanocatalysts, Science 317 (2007) 100-102.

[61] C. Tsai, K. Chan, J.K. Nørskov, F. Abild-Pedersen, Theoretical insights into the hydrogen evolution activity of layered transition metal dichalcogenides, Surf. Sci. 640 (2015) 133-140.

[62] S. Tian, Q. Tang, Activating transition metal dichalcogenide monolayers as efficient electrocatalysts for the oxygen reduction reaction via single atom doping, J. Mater. Chem. C. 9 (2021) 6040–6050.

[63] B. Mohanty, M. Ghorbani-Asl, S. Kretschmer, A. Ghosh, P. Guha, S. K. Panda, B. Jena, A. V. Krasheninnikov, B. K. Jena, MoS_2 Quantum dots as efficient catalyst materials for the oxygen evolution reaction, ACS Catal. 8 (2018) 1683-1689.

[64] H. Xia, Z. Shi, C. Gong, Y. He, Recent strategies for activating the basal planes of transition metal dichalcogenides towards hydrogen production, J. Mater. Chem. A. 10 (2022) 19067-19089.

[65] B. B. Xiao, P. Zhang, L. P. Han, Z. Wen, Functional MoS_2 by the Co/Ni doping as the catalyst for oxygen reduction reaction, Appl. Surf. Sci. 354 (2015) 221-228.

[66] D. M. Sun, C. Liu, W. C. Ren, H. M. Cheng, A review of carbon nanotube- and graphene-based flexible thin-film transistors, Small 9 (2013) 1188-1205.

[67] D. Yu, E. Nagelli, F. Du, L. Dai, Metal-free carbon nanomaterials become more active than metal catalysts and last longer, J. Phys. Chem. Lett. 1 (2010) 2165-2173.

[68] Y. Jiao, Y. Zheng, M. Jaroniec, S. Z. Qiao, Origin of the electrocatalytic oxygen reduction activity of graphene-based catalysts: A roadmap to achieve the best performance, J. Am. Chem. Soc. 136 (2014) 4394-4403.

[69] K. Qu, Y. Zheng, S. Dai, S. Z. Qiao, Graphene oxide-polydopamine derived N, S-codoped carbon nanosheets as superior bifunctional electrocatalysts for oxygen reduction and evolution, Nano Energy 19 (2016) 373-381.

[70] W. Liang, J. Chen, Y. Liu, S. Chen, Density-functional-theory calculation analysis of active sites for four-electron reduction of O_2 on Fe/N-doped graphene, ACS Catal. 4 (2014) 4170-4177.

[71] D. Yu, Q. Zhang, L. Dai, Highly efficient metal-free growth of nitrogen-doped single-walled carbon nanotubes on plasma-etched substrates for oxygen reduction, J. Am. Chem. Soc. 132 (2010) 15127-15129.

[72] X. Liu, L. Dai, Carbon-based metal-free catalysts, Nat. Rev. Mater. 1 (2016) 16064.

[73] Y. Hu, J. O. Jensen, W. Zhang, L. N. Cleemann, W. Xing, N. J. Bjerrum, Q. Li, Hollow spheres of iron carbide nanoparticles encased in graphitic layers as oxygen reduction catalysts, Angew. Chemie - Int. Ed. 53 (2014) 3675-3679.

[74] X. Wang, F. Zhang, Y. Liu, Z. Wang, Nitrogen-doped carbon nanotubes encapsulated cobalt nanoparticles hybrids for highly efficient catalysis of oxygen reduction reaction, J. Electrochem. Soc. 165 (2018) J3052-J3058.

[75] Y. Liu, H. Jiang, Y. Zhu, X. Yang, C. Li, Transition metals (Fe, Co, and Ni) encapsulated in nitrogen-doped carbon nanotubes as bi-functional catalysts for oxygen electrode reactions, J. Mater. Chem. A. 4 (2016) 1694-1701.

[76] D. Deng, L. Yu, X. Chen, G. Wang, L. Jin, X. Pan, J. Deng, G. Sun, X. Bao, Iron encapsulated within Pod-like carbon nanotubes for oxygen reduction reaction, Angew. Chem. Int. Ed. 52 (2013) 371-375.

[77] S. Manzeli, D. Ovchinnikov, D. Pasquier, O. V. Yazyev, A. Kis, 2D transition metal dichalcogenides, Nat. Rev. Mater. 2 (2017) 17033.

[78] R. Lv, H. Terrones, A. L. Elías, N. Perea-López, H. R. Gutiérrez, E. Cruz-Silva, L. P. Rajukumar, M. S. Dresselhaus, M. Terrones, Two-dimensional transition metal dichalcogenides: Clusters, ribbons, sheets and more, Nano Today 10 (2015) 559-592.

[79] M. Samadi, N. Sarikhani, M. Zirak, H. Zhang, H. L. Zhang, A. Z. Moshfegh, Group 6 transition metal dichalcogenide nanomaterials: Synthesis, applications and future perspectives, Nanoscale Horizons 3 (2018) 90-204.

[80] A. Kuc, Low-dimensional transition-metal dichalcogenides, Chem. Modell. 2014, 11, 1-29.

[81] X. Yin, C. S. Tang, Y. Zheng, J. Gao, J. Wu, H. Zhang, M. Chhowalla, W. Chen, A. T. S. Wee, Recent developments in 2D transition metal dichalcogenides: Phase transition and applications of the (quasi-)metallic phases, Chem. Soc. Rev. 50 (2021) 10087-10115.

[82] W. Wei, Y. Dai, C. Niu, B. Huang, Controlling the electronic structures and properties of in-plane transition-metal dichalcogenides quantum wells, Sci. Rep. 5 (2015) 17578.

[83] L. Mouchliadis, S. Psilodimitrakopoulos, G. M. Maragkakis, I. Demeridou, G. Kourmoulakis, A. Lemonis, G. Kioseoglou, E. Stratakis, Probing valley population imbalance in transition metal dichalcogenides via temperature-dependent second harmonic

generation imaging, Npj 2D Mater. Appl. 5 (2021) 1-9.

[84] J. Chen, S. Wei, H. Xie, A brief introduction of carbon nanotubes: history, synthesis, and properties, J. Phys. Conf. Ser. 1948 (2021) 012184.

[85] S. Iijima, Helical microtubules of graphite carbon, Nature 354 (1991) 56-58.

[86] N. Gupta, S. M. Gupta, S. K. Sharma, Carbon nanotubes: synthesis, properties and engineering applications, Carbon Lett. 29 (2019) 419-447.

[87] T. H. Kim, J. F. Wendelken, A.P. Li, G. Du, W. Li, Probing electrical transport in individual carbon nanotubes and junctions, Nanotechnology 19 (2008) 485201.

[88] M. E. Birch, T. A. Ruda-Eberenz, M. Chai, R. Andrews, R. L. Hatfield, Properties that influence the specific surface areas of carbon nanotubes and nanofibers, Ann. Occup. Hyg. 57 (2013) 1148-1166.

[89] S. Ogata, Y. Shibutani, Ideal tensile strength and band gap of single-walled carbon nanotubes, Phys. Rev. B 68 (2003) 1-4.

[90] A. Hirsch, Functionalization of single-walled carbon nanotubes, Angew. Chem. Int. Ed. 41 (2002) 11.

CHAPTER 2

Theoretical Methods and Computational Frameworks

This chapter provides a comprehensive exploration of the advanced computational methodologies and theoretical frameworks employed in the multiscale modeling of electrocatalytic materials. The chapter elaborates on the methods used to simulate and predict the properties and performance of electrocatalytic materials, emphasizing the integration of first principle electronic structural methods. The Hartree potential and Hartree-Fock approximations are explored, highlighting iterative self-consistent field (SCF) methods and the role of spin-orbitals (SO) in considering exchange interactions and electron spin. Additionally, the chapter discusses about the Density Functional Theory (DFT) methods, emphasizing the Hohenberg-Kohn theorems, the significance of electron density as a function, and the Kohn-Sham equations that revolutionized computational chemistry. The chapter includes a comprehensive discussion on theoretical descriptors and theoretical models for catalytic surfaces, such as cluster and periodic slab models, to provide insights into catalytic activity and material properties. This chapter provides an overview of the CRYSTAL17 suite code, a sophisticated tool designed for ab initio electronic structure calculations of crystalline solids and periodic systems. The chapter meticulously details the input script of CRYSTAL17, which contains different blocks, specific keywords, and numerical parameters to control the type of calculations. Additionally, we incorporate the importance of basis sets, highlighting their critical role in defining electronic wavefunctions and ensuring precise simulations, with particular emphasis on optimized sets for periodic systems. Furthermore, we discuss the geometry optimization process, which is crucial for determining the most stable structure of materials. Finally we describe the instruments used in our

computational studies and theoretical findings.

2.1 Multiscale Modeling: Computational science is a branch of science whose major goal is to describe a certain system by creating equations with the help of mathematical approximations and investigate the desired properties of the system from the computer programs from the more or less exact model of the particular system. In short, the computer tries to imitate the real system, and computer simulations are driven by mathematical models. Computer simulations based on certain theoretical and mathematical descriptions can be compared with the measurements of real systems to evaluate theory and experiments. One can test the accuracy of the theory and support the findings of experiments by performing simulations on the same system. Moreover, computational techniques complement the experimental techniques in different ways. For example, extreme conditions that are hard or even impossible to prepare in a laboratory, such as very high temperatures and pressure, can be tested in computer simulations. Computational methods offer a viable alternative for studying unstable compounds that are difficult or risky to examine experimentally. While simulations may have certain limitations, they are typically more cost-effective and time-efficient than experimental approaches. They can provide valuable predictions regarding the properties, performance, and behavior of a system under various conditions. Currently, these techniques are extensively used in diverse fields, including physics, chemistry, materials science, biology, medicine, and mathematics, as well as economics, psychology, social sciences, and engineering.

Physical phenomena that dictate material properties and processes inherently occur across various length and time scales, each characterized by different levels of complexity. The time scale refers to the duration required for a phenomenon to respond to specific external conditions, while the length scale pertains to the size of the objects involved in the process. Multiscale modeling involves developing a mathematical framework that breaks a complex problem into a series of interconnected subproblems across different scales. These scales can be organized based on the characteristics of systems and the intended application of the model. Essentially, multiscale modeling seeks to predict material properties and system behavior at one level by integrating information or models from different lengths and time scales. Figure 2.1 illustrates the connection between macroscale, mesoscale, and microscale computational approaches across various length and time scales. In material simulations, four key characteristics of length scales can be identified

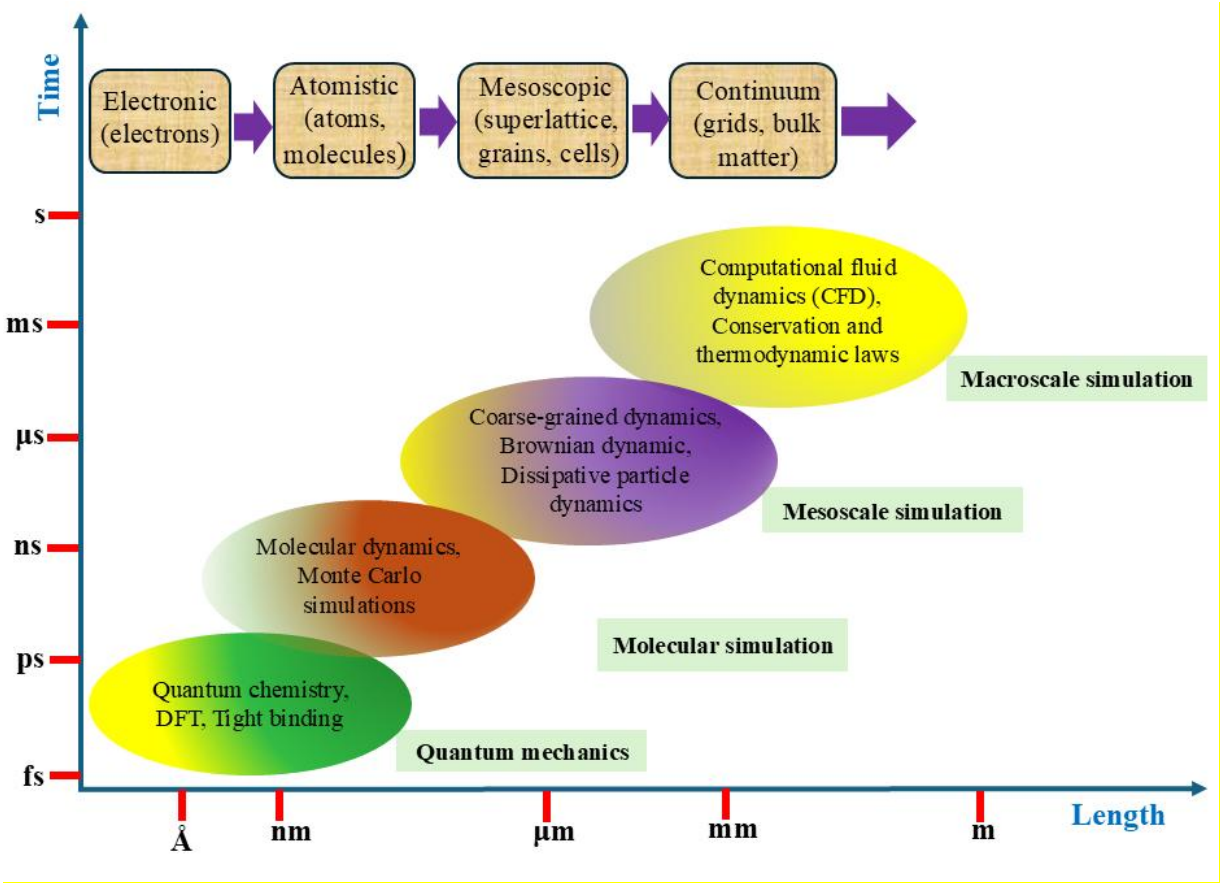

Figure 2.1. *Illustration of multiscale modeling, which provides a fundamental insight into different categories of methods to design the materials and study material information available from distinct lengths and time scales.*

and distinguished as follows[1,2]:

(1) The quantum scale (~ 10^{-9} m to a few nanometers): At this scale, electrons dominate as the key players, with interactions between electrons and protons being central. To treat the electrons explicitly, many-body structural theories, Density Functional Theory (DFT), and quantum chemistry methods are used.

(2) The atomic scale (~ 10^{-6} m to a few micrometers): This scale focuses on atoms and clusters of atoms, where their interactions are described by classical interatomic potentials. For the atomic scale, molecular dynamics (MD) and Monte Carlo (MC) simulations are usually performed employing classical interatomic potential.

(3) The mesoscopic scale (~ 10^{-4} m to hundreds of micrometers): In this scale, lattice defects such as dislocations, grain boundaries, and other microstructural elements are the players. On the

mesoscopic scale, lattice kinetic Monte Carlo (KMC) and mean field microkinetic modeling methods are used to find the average dynamic properties.

(4) The macroscopic scale (~ 10^{-3} m to centimeters and beyond): This scale addresses phenomena like flow, mass transfer, and heat transfer. It involves continuum fields such as density, velocity, temperature, displacement, and stress. The finite element (FE) method is widely employed to study the large-scale elastic properties of materials, while continuum Navier-Stokes and phase-field equations are used for fluid dynamics analysis.

Before initiating the simulation, it is crucial to identify the specific phenomena and properties of interest. This ensures that the chosen model is appropriately tailored to address the problem at hand. In this present thesis, the first principle electronic structural methods are used for calculations and design of electrocatalytic material for the ORR.

2.2 Methods: Materials are made up of electrons and nuclei, with their properties at the nanoscale governed by the principles of quantum mechanics. In this framework, the behavior of quantum particles is described by the non-relativistic Schrödinger equation. The state of a quantum system is represented by the wavefunction $\psi(r_1, r_2, \dots\dots\dots r_i, \dots R_1, R_2 \dots\dots\dots R_I \dots\dots\dots)$, where r_i and R_I are the position of the ith electron and Ith nucleus. While the wavefunction ψ itself has no direct physical interpretation, its square, $|\psi(r_1, r_2, \dots\dots\dots r_i, \dots R_1, R_2 \dots\dots\dots R_I \dots\dots\dots)|^2$ defines the probability of simultaneously finding electron number 1 at point r_1, electron number 2 at point r_2 and so on. For the system having only one electron $|\psi(r)|^2 dr$ determines the probability of finding the electron in the volume dr at the point r.

Here, we are interested in the time-independent Schrödinger's equation and the solution of the time-independent Schrödinger's equation. For a many-body system the solution of the Schrödinger's equation gives the information about the physical and chemical properties at the nanoscale range. The time-independent Schrödinger's equation of a system having N electrons and M nucleus can be expressed as,

$$\left[-\sum_{i}^{N}\frac{\hbar^2}{2m_e}\nabla_i^2-\sum_{I}^{M}\frac{\hbar^2}{2M_I}\nabla_I^2+\frac{1}{2}\sum_{i\neq j}^{N}\frac{e^2}{4\pi\epsilon_0}\frac{1}{|r_i-r_j|}+\frac{1}{2}\sum_{I\neq J}^{M}\frac{e^2}{4\pi\epsilon_0}\frac{Z_IZ_J}{|R_I-R_J|}-\sum_{iI}^{NM}\frac{e^2}{4\pi\epsilon_0}\frac{Z_I}{|r_i-R_I|}\right]\psi=E_{total}\psi \quad (1)$$

where ψ represents the many body wavefunctions, ħ, m_e, and M_I, are the Plank constants, masses of the electrons, and masses of the nucleus, respectively.

First term: $-\sum_i^N\frac{\hbar^2}{2m_e}\nabla_i^2$ represents the kinetic energy of the n electrons.

Second term: $-\sum_I^M\frac{\hbar^2}{2M_I}\nabla_I^2$ represents the kinetic energy of the M nuclei.

Third term: $\frac{1}{2}\sum_{i\neq j}^N\frac{e^2}{4\pi\epsilon_0}\frac{1}{|r_i-r_j|}$ represents the Coulomb repulsion between electrons. The factor half is included in order to count only one contribution per pair.

Fourth term: $\frac{1}{2}\sum_{I\neq J}^M\frac{e^2}{4\pi\epsilon_0}\frac{Z_IZ_J}{|R_I-R_J|}$ represents the Coulomb repulsion between nuclei. The factor half is included in order to count only one contribution per pair.

Fifth term: $-\sum_{iI}^{NM}\frac{e^2}{4\pi\epsilon_0}\frac{Z_I}{|r_i-R_I|}$ represents the Colomb attraction between the electron and nuclei.

The Equation (1) in the atomic unit can be expressed as,

$$\left[-\sum_{i}^{N}\frac{\nabla_i^2}{2}-\sum_{I}^{M}\frac{\nabla_I^2}{2}+\frac{1}{2}\sum_{i\neq j}^{N}\frac{1}{|r_i-r_j|}+\frac{1}{2}\sum_{I\neq J}^{M}\frac{Z_IZ_J}{|R_I-R_J|}-\sum_{iI}^{NM}\frac{Z_I}{|r_i-R_I|}\right]\psi=E_{total}\psi \quad (2)$$

This form of Schrödinger's equation is commonly applied in first-principles material modeling. In practice, obtaining an exact solution for many-body systems is not feasible, as analytical solutions are only possible for simpler systems, such as a hydrogen atom (H) or a single-electron system. However, by incorporating certain approximations and assumptions, a fairly accurate description of the total energy of the many-body system can be achieved, which enables the investigation of the properties of the many-body system[3–5].

2.3 Born–Oppenheimer Approximation: The Born–Oppenheimer approximation is based on separating the dynamics of the nuclei and electrons to describe electron motion. This approximation is grounded in the fact that the mass of the nuclei (M_I) is significantly larger than that of the electrons (m_e) (the mass of a proton is about 1836 times higher than m_e as compared to an electron). In this approximation, electrons are treated as if they move within a fixed external potential created by the nuclei. The nuclei are considered stationary relative to the electrons, meaning their kinetic energy is assumed to be zero, and the interactions between them are considered constant regardless of their configuration. Adding a constant to an operator has no effect on the eigenstate but only shifts the eigenvalue. Using this approximation, the total wavefunction can be expressed as a simple product of the nuclear and electronic wavefunctions. In mathematical expressions:

$$\psi(r_1, r_2, \dots\dots\dots r_i, \dots R_1, R_2 \dots\dots\dots R_I \dots\dots\dots) = \psi_{elec}(r_1, r_2, \dots\dots\dots r_i; R) * \psi_{nuclei}(R_1, R_2 \dots\dots\dots R_I \dots\dots\dots)$$

The electronic wavefunction $\psi_{elec}(r_1, r_2, \dots\dots\dots r_i; R)$ depends explicitly on the electronic coordinates and parametrically on the nuclei coordinates. The concept of parametric dependence means that, for different arrangements of the nuclei, ψ_{elec} is a different function of electronic coordinates. The electronic Hamiltonian describes the motion of the N electrons in the field of the M point charges can be expressed as,

$$\widehat{H} = -\sum_{i}^{N} \frac{\nabla_i^2}{2} + \frac{1}{2}\sum_{i \neq j}^{N} \frac{1}{|r_i - r_j|} - \sum_{iI}^{NM} \frac{Z_I}{|r_i - R_I|} \qquad (3)$$

From this point forward, we will focus on the electronic Hamiltonian and electronic wavefunction as our primary concern will be the electronic problem, i.e., electronic structure theory[3–5].

2.4 The Hartree Approximations: Despite the Born-Oppenheimer approximation, obtaining an exact solution to the Schrödinger equation is only possible for the simplest systems, such as the hydrogen atom. The challenge arises from the need to account for 3N variables due to electron-electron interactions. As a result, solving the N-electron system remains impractical and necessitates additional approximations.

The Hartree approximation is the simplest technique used to approximate the ground state wavefunction of many electrons system. The Hartree approximation is an independent electron approximation that assumes that electrons are not correlated with each other individually, and each electron experiences an interaction with an average field representing the electrons, including itself. This approximation of neglecting the dynamic electron correlation is called mean field approximation. Utilizing this approximation, the wave function of many electrons system can be described by the product of the one electron wavefunction (known as orbital $\phi_i(r_i)$). The product of the one electron wavefunctions $\phi_i(r_i)$ is called Hartree product and can be represented as:

$$\psi(r_1 r_2 r_3 \dots\dots r_N) = \phi_1(r_1)\phi_2(r_2)\phi_3(r_3) \dots\dots \phi_N(r_N) \qquad (4)$$

The independent particle Hamiltonian can be expressed as,

$$H_0(r) = -\frac{1}{2}\nabla^2 + V_n(r) \qquad (5)$$

The density associated with each independent electron can be expressed as,

$$\rho_i(r) = |\phi_i(r)|^2$$

The total density of many-electron systems is:

$$\rho_{total}(r) = \sum_{i=1}^{N} \rho_i(r_i) = \sum_{i=1}^{N} |\phi_i(r)|^2$$

However, if we want to write the density to which the kth electron will interact, we must exclude its own density from the total density:

$$\eta_k(r) = \rho_{\text{total}}(r) - \rho_k(r) = \left[\left(\sum_{i=1}^{N} \rho_i(r)\right) - |\phi_k(r)|^2\right] = \sum_{i=1, i\neq k}^{N} |\phi_i(r)|^2 \qquad (6)$$

The electron density can be used to determine the electrostatic field generated by the electrons. Suppose we need to evaluate the interaction of an electron located at point r with the electron density of the rest of the electrons. The electrostatic potential can be written as:

$$V_H(r) = \int \frac{\eta_k(r')}{|r - r'|} dr'$$

This is called Hartree potential.

The independent particle Hamiltonian and Hartree potential term contract the one electronic Hamiltonian and can be expressed as,

$$H_{ele} \simeq \sum_{i=1}^{N} (H_0(r_i) + V_H^i(r_i))$$

The Schrodinger equation for any electron system can now be written into N-independent one-electron equations:

$$\left[-\frac{1}{2}\nabla^2 + V_n(r) + V_H(r)\right]\phi_i(r) = \epsilon_i\phi_i(r) \qquad (7)$$

Where ϵ_i is the energy of the ith electron, and the total energy of the many electrons system can be expressed as,

$$E = \sum_{i=1}^{N} \epsilon_i - \frac{1}{2}\sum_{i\neq j} (ii|jj)$$

To solve the equation (7), the iterative method is used, which is called self-consistent field approximations. The chart of the iterative method is shown in Figure 2.2.

In the beginning, we start from an approximate orbital $\phi_i(r)$. Then, the Hartree potential will be found using the electrostatic Gauss's or Poison's equations. Then, we improve the orbital $\phi_i(r)$ by solving the N Schrödinger one electron system. In the following iteration, these updated orbitals serve as the starting point. When no further changes are observed in the orbitals between successive iterations, we can conclude that the self-consistent field orbitals have converged[3–5].

2.5 Spin-Orbitals: We define the spatial distribution of electrons by using the spatial orbitals $\phi_i(r)$, which is the function of position vector r. However, the electrons have a spin degree of freedom in addition to their spatial coordinates. Hence, to describe an electron, it is necessary to specify its spin in addition to the spatial orbitals. A complete set for describing the spin of an electron consists of two orthonormal functions noted as $\alpha(\omega)$ and $\beta(\omega)$ i.e., spin up (↑) and spin down (↓). A spin-orbital $(\chi(r))$ is a wave function for an electron that describes both its spatial

distribution and its spin. For each spatial orbital $\chi(r)$, one can form two different spin orbitals by multiplying the

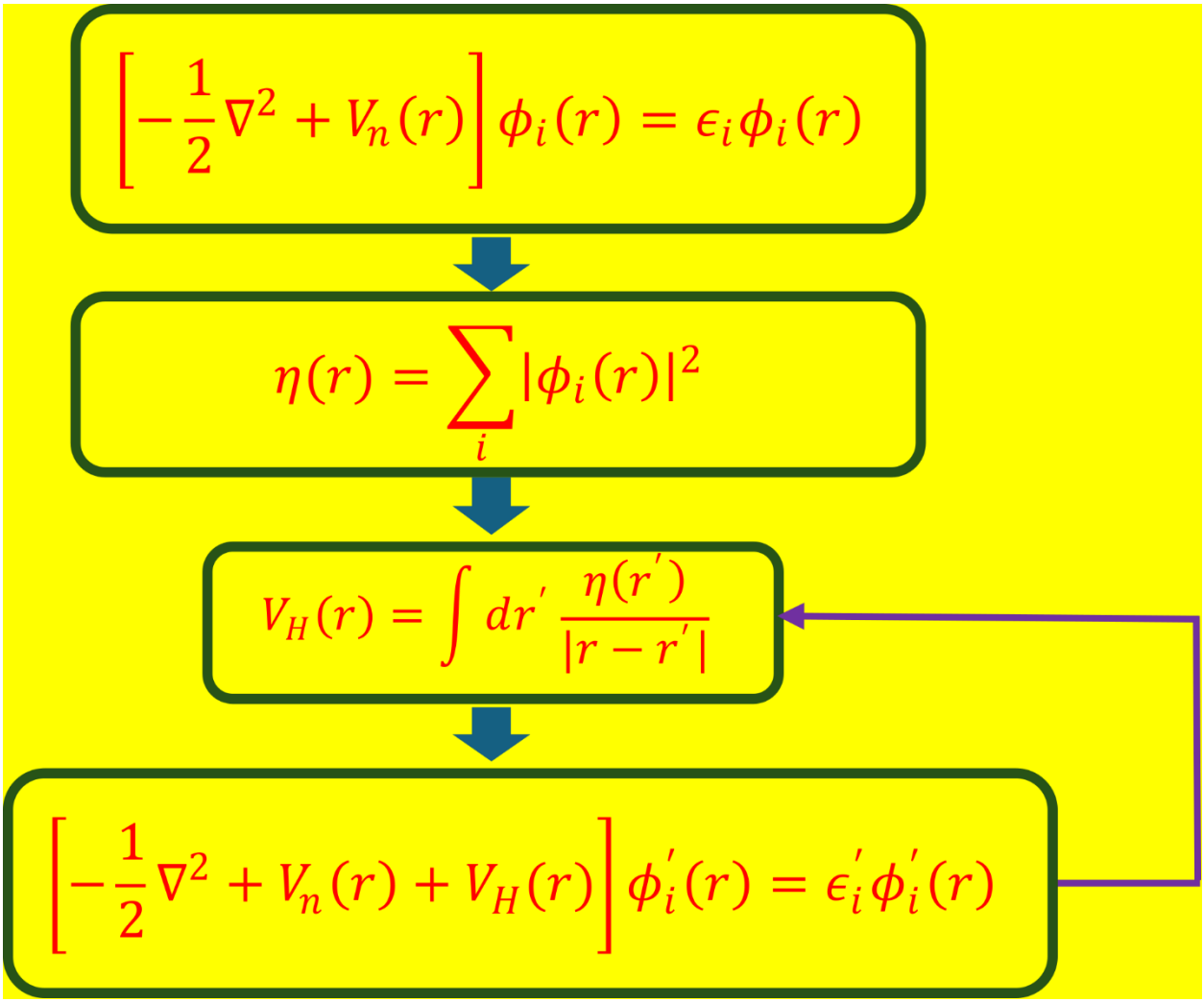

Figure 2.2. *Representation of the flow chart of Hartree iterative procedure to find the solution of the many electrons Hartree equation.*

spatial orbital by $\alpha(x)$ and $\beta(x)$ spin function

$$\chi(r) = \{\phi(r)\alpha(\omega)\ or\ \phi(r)\beta(\omega)\}$$

The spin-orbital follows the orthonormal condition $\int dr\chi_i^{\dagger}(r)\chi_i(r) = \delta_{ij}$. The many electron wavefunction in terms of the spin orbitals $(\chi(r))$ can be written as

$$\psi = \chi_1(r_1)\chi_2(r_2)\chi_3(r_3) \dots\dots \chi_i(r_i)\chi_j(r_j) \dots . \chi_N(r_N)$$

This is called the Hartree product. The Hartree wave function distinguishes electron one is occupying the spin-orbital χ_1 and electron two is occupying χ_2 etc. Thus, this wavefunction violates the fact that electrons are indistinguishable. Another drawback of Hartree approximation is that the form of the wavefunction does not hold the antisymmetric nature of the fermions. The antisymmetric nature requires that the electronic wavefunction should change the sign with respect to the interchange of the space and spin coordinates of any two electrons.

2.6 Hartree-Fock Approximation: In the Hartree-Fock (HF) approximation, the improvement in energy calculations has been done by incorporating the exchange effect. In this approximation, the product of one-electron wavefunction (spin-orbital) is replaced by the linear combination of the spin-orbital. The many electron wavefunctions are constructed as a single Slater with a single electron state as an element of the determinant.

$$\psi(r_1, r_2 \dots \dots .. r_N) = \frac{1}{\sqrt{N!}} \begin{vmatrix} \chi_1(r_1) & \chi_2(r_1) & \dots \dots \dots & \chi_N(r_1) \\ \chi_1(r_2) & \chi_2(r_2) & \dots \dots \dots & \chi_N(r_2) \\ \vdots & \vdots & \vdots & \vdots \\ \vdots & \vdots & \vdots & \vdots \\ \vdots & \vdots & \vdots & \vdots \\ \chi_1(r_N) & \chi_2(r_N) & \dots \dots \dots & \chi_N(r_N) \end{vmatrix}$$

Where $\frac{1}{\sqrt{N!}}$ is the normalization factor. The slater determinants meet all the requirements:

(1) Satisfy the antisymmetric principle: The rows are labeled by electrons, and the columns are labeled by spin orbitals. Interchanging the coordination of two electrons changes the sign of the determinant.

(2) Satisfy the Pauli exclusion principle: No more than one electron can occupy the same spin-orbital. If two electrons occupy the same spin-orbital, it results in two identical columns in the determinant, causing the determinant to become zero.

As a result of this approximation, an extra term known as the exchange energy, commonly known as Fock exchange, must be added to the equation (7), which comes from the exchange of electronic coordinated in the expanded determinant wavefunction. The exchange energy can be expressed as,

$$-\frac{1}{2}\iint \chi_i(r_1)\chi_j^{\dagger}(r_1)\frac{1}{|r_1 - r_2|}\chi_j(r_2)\chi_i^{\dagger}(r_2)dr_1 dr_2$$

This operator in the one-electron Schrödinger's equation for electron i in the field of the other electrons can be expressed as,

$$-\int dr' \frac{\chi_j^{\dagger}(r')\chi_j(r)}{|r-r'|}\chi_i^{\dagger}(r')$$

Thus, incorporating the exchange energy, the mean-field equation can now be written as:

$$\left[-\frac{1}{2}\nabla^2 + V_n(r) + V_H(r)\right]\chi_i(r) - \int dr' \frac{\chi_j^{\dagger}(r')\chi_i(r')}{|r-r'|}\chi_j(r)$$

$$= \epsilon_i \chi_i(r) \qquad (8)$$

The Hartree-Fock approximations give qualitatively reasonable results for atoms. However, it fails for solids because it neglects correlation and screening, which is crucial for solids. The difference between Hartree energy and exact ground state energy is called the exchange-correlation energy[3–5].

2. 7 Functional and Functional Derivatives: A function accepts a number as input and produces a number as output, mapping one number to another. On the other hand, a functional takes a function as input and produces a number as output, mapping a function to a number.

$$Function = y(x) = x^2 \xrightarrow{yields} y(x=2) = 4$$

$$Functional = F[y(x)] = \int_0^1 y(x)dx \xrightarrow{yields} F[y = x^2] = \frac{1}{3}$$

The ordinary differential dy measures how y changes as a result of a variation x → x+dx of the variable x. The derivative formed in terms of the ordinary differential, $\frac{dy}{dx}$ measure the first order change of y upon change of x, i.e., the slope of the function y(x) at x.

$$y(x+dx) = y(x) + \frac{df}{dx}dx + O(dx^2)$$

$$y(x+dx) - y(x) = \frac{df}{dx}dx \ \ (upto\ first\ order)$$

Similarly, for a fixed-point x, the functional variation δF measure how the value of F at this point changes as a result of variation in the functional form y(x). The functional derivative measures the order change in a functional upon a functional variation of its arguments.

$$F[y(x) + \delta y(x)] = F[y(x)] + \int [\frac{\partial F}{\partial y} \delta x]\, dx + O(\delta x^2)$$

$$F[y(x) + \delta y(x)] - F[y(x)] = \int \left[(\frac{\partial F[y(x)]}{\partial y(x)}) \delta y(x) \right] dx \quad (upto\ first\ order)$$

Therefore, the functional derivative helps us understand how a functional varies in response to variations in the form of the function it depends on.

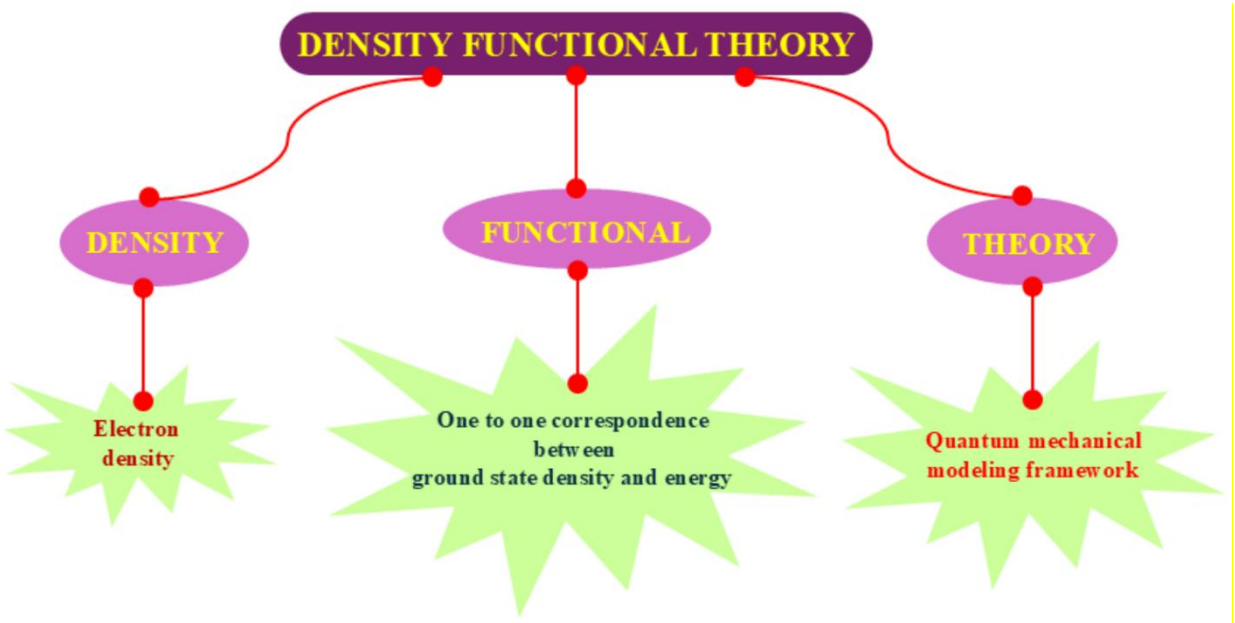

Figure 2.3. *Scheme highlighting the significance of each word in the density functional theory.*

2. 8 Density Functional Theory: Density Functional Theory (DFT) is a framework that describes the energy of electrons as a functional of their density, meaning the total energy depends on the electron density. The significance of the DFT has been summarized in Figure 2.3. The functional of electron density implies a one-to-one correspondence between energy and electron density. DFT has proven to be a highly effective method for determining the structure of atoms, molecules, and solids. The foundation of DFT is the electron density, designated by the $\eta(r)$ which is the number of electrons per unit volume in a given state.

$$\eta(r) = N \int \ldots\ldots \int |\psi(r, r_2 \ldots\ldots r_N)|^2 dr dr_2 \ldots\ldots dr_N$$

By integrating this function, it is possible to get the total number of electrons. The wavefunction methods utilize a complicated wavefunction to describe a system that, in principle, contains a 3N degree of freedom, and in DFT, the density is a function of only three space coordinates, which greatly simplifies the many-body problem. Thus, in DFT, the solution of the Schrodinger equation becomes computationally feasible even for large systems. The foundation of DFT is the Hohenberg and Kohn theorem (HK) and Sham equations. Walter Kohn was awarded a Nobel Prize in chemistry in 1998 for his contribution to the foundation of the DFT. The two fundamental theorems based on the electron density in external potential $V_{ext}(r)$ are as follows[3–7]:

Ist theorem: According to the HK theorem, for any system of interacting particles, with a nondegenerate ground state, the external potential $V_{ext}(r)$ is, to within a constant, a unique functional of the electron density $\eta(r)$. This theorem provides a direct mapping of the $\eta(r)$ to the energy of the system. If the $\eta(r)$ uniquely defines the $V_{ext}(r)$, it thus determines the Hamiltonian, and hence the wavefunction. Let us consider the ground state of the system of electrons with the wavefunction ψ^1, Hamiltonian H^1, and the external potential $V^2_{ext}(r)$. Let us consider the ground state of another system of electrons with Hamiltonian H^2, external potential $V^2_{ext}(r)$, and gives rise to the wavefunction ψ^2. Let us consider that both wavefunctions give the same electron density $\eta(r)$.

The wavefunction ψ^1 minimizes the ground state energy of Hamiltonian H^1:

$$E^1 = \langle \psi^1 | H^1 | \psi^1 \rangle = T[n(r)] + U_{ee}[\eta(r)] + \int V^1_{ext}(r)\eta(r)dr$$

The wavefunction ψ^2 minimized the ground state energy of Hamiltonian H^2:

$$E^2 = \langle \psi^2 | H^2 | \psi^2 \rangle = T[\eta(r)] + U_{ee}[\eta(r)] + \int V^2_{ext}(r)\eta(r)dr$$

According to variational principle:

$$E^1 < \langle \psi^1 | H^1 | \psi^1 \rangle = \langle \psi^2 | H^2 | \psi^2 \rangle + \langle \psi^2 | H^1 - H^2 | \psi^2 \rangle$$

$$E^1 < E^2 = \int \eta(r)[V_{ext}^1(r) - V_{ext}^2(r)]dr \qquad (9)$$

The same procedure can be applied to the E^2, we will arrive at the result:

$$E^2 < E^1 = \int \eta(r)[V_{ext}^2(r) - V_{ext}^1(r)]dr \qquad (10)$$

Adding equations (9) and (10), we get

$$E^1 + E^2 < E^2 + E^1$$

This creates a contradiction, as it suggests that two distinct external potentials could produce the same ground-state electron density. Thus, the external potential acting on the electrons can be expressed as a unique functional of the electron density, apart from an additive constant.

$$\mathrm{E_0[n_0(r)]} = T[\eta_0(r)] + U_{ee}[\eta_0(r)] + V_{ext}[\eta_0(r)]$$

Where $V_{ext}[\eta_0(r)] = \int V_{ext}(r)\eta_0(r)dr$

The first term $T[\eta_0(r)] + U_{ee}[\eta_0(r)]$ are universal and are more difficult to calculate, and some approximations have to be made. The $V_{ext}[\eta_0(r)]$ depends on the system and is easy to calculate for a given external potential.

IInd theorem: This principle states that the electron density, which minimizes the energy of the entire functional, corresponds to the true ground-state electron density, and the resulting minimum energy represents the ground-state energy. In other words, for a trial density $\eta(r)$ that meets the required boundary conditions, such as $\eta(r) \geq 0, \int \eta(r)dr = N$, which is associated with some external potentials V_{ext}, the energy functional is the upper bound to the true ground state energy. The exact ground-state energy can only be obtained when the precise ground-state electron density is used. This theorem arises as a direct consequence of the variational principle.

2.9 Formulation of the Kohn Sham DFT: In 1965, Kohn and Sham (KS) proposed the theoretical foundation to calculate the ground state density and energy of the system of interacting electrons with the help of the single particle scheme. The core concept of the KS method is to design a single-particle potential $V_s(r)$ such that the density of an auxiliary, non-interacting system matches the density of the actual interacting system. This approach simplifies the problem by replacing the

real system of N-interacting electrons with a hypothetical system of N-non-interacting electrons. In this auxiliary system, electrons move within an effective potential, ensuring that the ground-state density mirrors that of the real system. Since ground-state density encapsulates all the necessary information, it is theoretically possible to compute all properties of the actual system using the auxiliary one, as both share the same ground-state density. A systematic representation of the KS and real system is shown in Figure 2.4. In the interacting system, the N interacting electrons move in the field of the nuclei, and in the non-interacting system, the electrons move in the modified potential such that the real and fictitious systems have the same ground state density.

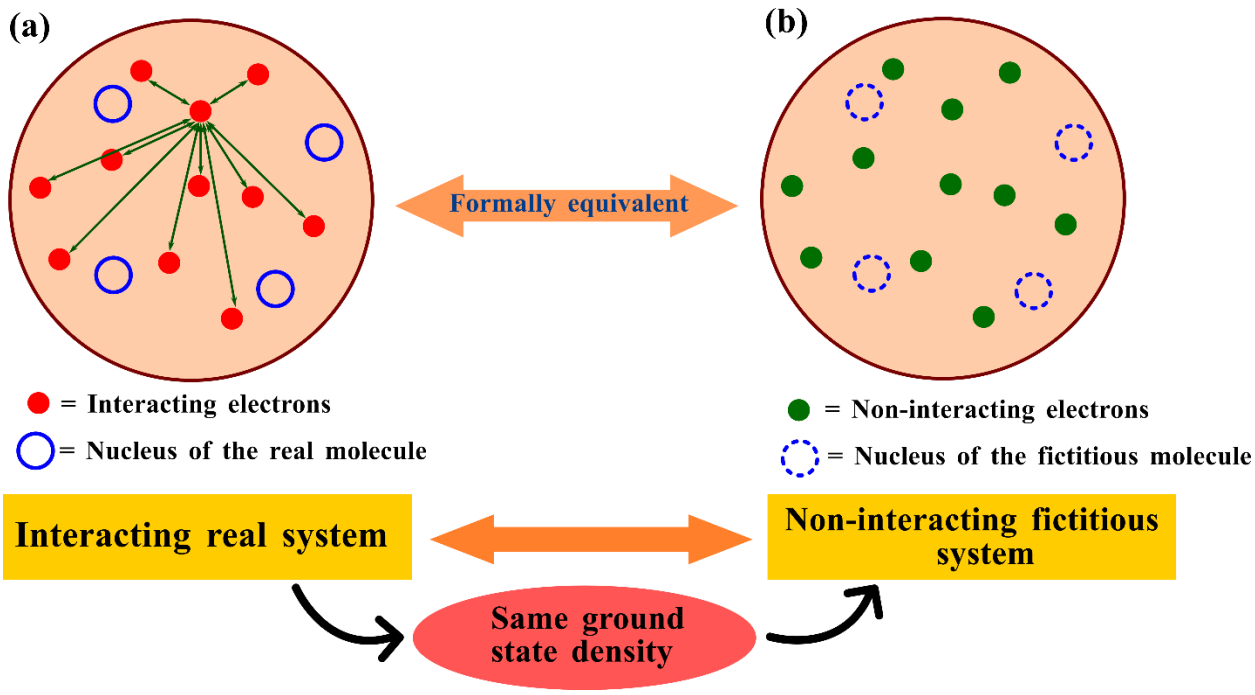

Figure 2.4. *The model representation of the (a) real interacting many-electron system and (b) the Kohn-Sham fictitious non-interacting system, which has the same ground state density as that of the interacting system.*

In the KS approximation, an expression for the density is then written in terms of the set of the N-non-interacting orbitals $\phi_i(r)$.

$$\eta(r) = \sum_{i}^{N} |\phi_i(r)|^2$$

The kinetic energy is decomposed into two parts, one represents the kinetic energy of the non-interacting particles of density $\eta(r)$ and represented as $T_s[\eta(r)]$ called correlation kinetic energy part.

$$T[\eta(r)] = T_s[\eta(r)] + T_c[\eta(r)]$$

The $T_s[\eta(r)]$is expressed in terms of the single-particle orbitals $\phi_i(r)$ called KS orbitals of a non-interacting system with the density $\eta(r)\ as$:

$$T_s[\eta(r)] = -\sum_i \int \phi_i^*(r)\frac{\nabla^2}{2}\phi_i(r)dr$$

Now, the electron-electron interaction can be split into a coulomb component and an exchange and correlation component and represented as

$$E_{HXC}[\eta(r)] = E_H[\eta(r)] + E_{XC}[\eta(r)].$$

The classical Coulomb interaction can be written as:

$$E_H[\eta(r)] = \frac{1}{2}\iint \frac{\eta(r)\eta'(r)}{|r-r'|}drdr'$$

The $E_H[\eta(r)]$ is called the Hatree energy functional, which is the classical coulomb interaction of charge densities with itself. This is the largest contribution to the $E_{HXC}[\eta(r)]$, but it should be here noted that the Hatree energy functional contains the unphysical contribution of an electron repelling itself, referred to as self-interaction energy. The $E_{XC}[\eta(r)]$ is called exchange-correlation energy functional that captures the exchange-correlation effect that is missing from the non-interacting electronic systems, which is formally defined as:

$$E_{Xc}[\eta(r)] = \left[T\big(\eta(r)\big) - T_s\big(\eta(r)\big)\right] + \left[E_{Hxc}\big(\eta(r)\big) - E_H\big(\eta(r)\big)\right] \qquad (11)$$

The role of the $E_{Xc}[\eta(r)]$ is to (1) fix the kinetic energy, (2) take into account the Pauli repulsion, (3) cancel the interaction of an electron with itself, and (4) include the remainder of the electrostatic interaction between electrons. The term $E_{Xc}[\eta(r)]$ looks smaller but has a significant contribution to the total energy functional, and this cannot be neglected, and a good approximation is important

to calculate the $E_{Xc}[\eta(r)]$term. Now, we have the expression for the energy functional, and can be expressed as,

$$E = F[\eta(r)] = -\sum_i dr\phi_i^*(r)\frac{\nabla^2}{2}\phi_i(r) + \int dr\eta(r)V_n(r) + \frac{1}{2}\iint drdr'\frac{\eta(r)\eta'(r)}{|r-r'|} + E_{XC}[\eta(r)] \qquad (12)$$

Now, if you know the $E_{XC}[\eta(r)]$, then, we can calculate the total ground state energy of the system by minimizing the energy functional $F[\eta(r)]$ relative to the electron density. The density that precisely minimizes the energy functional is the ground state electron density. This is known as HK's second theorem and can be expressed as,

$$\frac{\delta F[\eta]}{\delta\eta}|_{\eta_0} = 0 \qquad (13)$$

In order to use equation (12), the chain rule applies in the case of the functional derivative. If we apply the chain rule to the functional derivative of $F[\eta]$ with respect to any of the wavefunction ϕ_i^*, we find:

$$\frac{\delta F}{\delta\phi_i^*} = \frac{\delta F}{\delta\eta}\frac{\delta F}{\delta\phi_i^*} = \frac{\delta F}{\delta\eta}\phi_i$$

Now, from the equation (13), we see that Kohn-sham orbitals must satisfy the following conditions:

$$\frac{\delta F}{\delta\phi^*} = 0$$

Here, the electron density minimizes the total energy under the normalized condition

$$\sum_i \int \phi_i^*(r)\phi_i(r)\,dr = N$$

Which is a constraint that should be satisfied. Lagrange's method of undermining multipliers is a viable way to conduct this constraint minimization. This constraint is added to the functional multiplied by the undermined constant (μ) called Lagrange's multipliers. Thus, the Lagrange functional can be expressed as,

$$L[\eta] = F[\eta] - \sum_{ij} \epsilon_{ij}[\int \phi_i^*(\vec{r})\phi_i(\vec{r})d\vec{r} - \delta_{ij}] \quad (14)$$

The Lagrange derivative of equation (14) to search for the minimization is:

$$\frac{\delta L}{\delta \phi_i^*(r)} = 0 \quad (15)$$

Now, using equations (14) and (15), the functional derivative can be evaluated as follows:

$$-\frac{\nabla^2}{2}\phi_i(r) + \frac{\delta}{\delta\eta}\left[\int dr\eta(r)V_n(r) + \frac{1}{2}\iint dr\, dr' \frac{\eta(r)\eta'(r)}{|r-r'|} + E_{XC}[\eta(r)]\right]\phi_i(r)$$
$$= \sum_j \epsilon_{ij}\phi_j(r) \quad (16)$$

In practice, the Kohn–Sham orbitals are chosen such that the matrix ϵ_{ij} becomes diagonal, i.e.,

$$\epsilon_{ij} = \epsilon_i \delta_{ij}$$

$$\Downarrow$$

$$-\frac{\nabla^2}{2}\phi_i(r) + [V_n(r) + \int dr' \frac{\eta'(r)}{|r-r'|} + \frac{\delta E_{XC}[\eta(r)]}{\delta\eta(r)}]\phi_i(r) = \sum \epsilon_i\phi_i(r) \quad (17)$$

Thus, we obtain the Kohn-Sham equation, which can be represented as:

$$\left[-\frac{1}{2}\nabla^2 + V_n(r) + V_H(r) + V_{XC}(r)\right]\phi_i(r) = \epsilon_i\phi_i(r)$$

Or

$$\left[-\frac{1}{2}\nabla^2 + V_{KS}(r)\right]\phi_i(r) = \epsilon_i\phi_i(r) \quad (18)$$

Where $V_{KS}(r) = V_n(r) + V_H(r) + V_{XC}(r)$ called the Kohn-Sham (KS) effective potential. The $V_{XC}(r)$ is the exchange-correlation potential, which is constructed from the derivative of the exchange-correlation energy with respect to the density

$$V_{XC}(r) = \frac{\delta E_{XC}[\eta(r)]}{\delta\eta(r)}$$

The form of equations (17) and (18) is for the non-interacting electrons in the modified potential, which ensures that the ground state density is the same as the exact ground state density of the

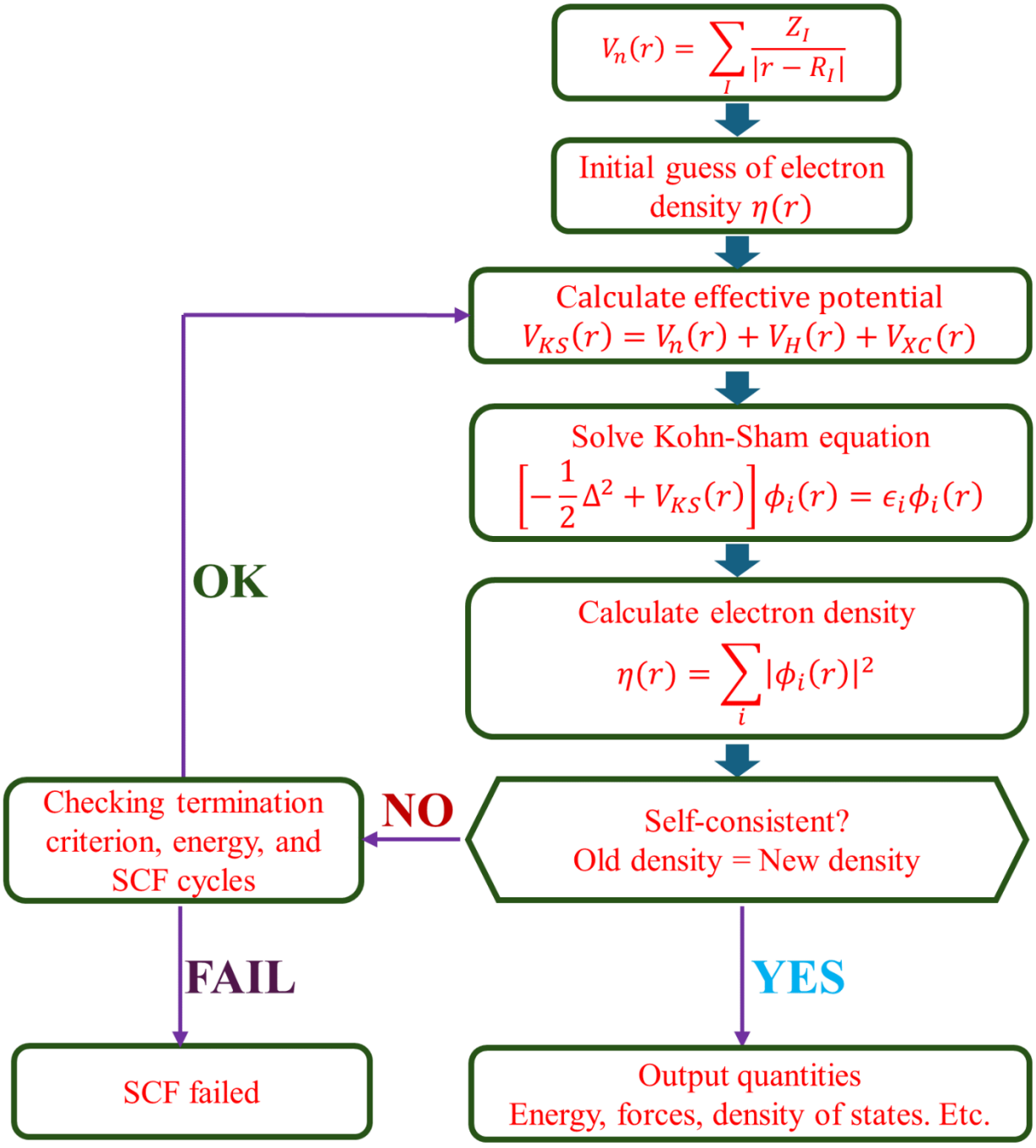

Figure 2.5. *Schematic representation of the flow chart of interactive procedure self-consistent field (SCF) calculation of the Kohn-Sham equation.*

physical system of interacting electrons. After solving the Kohn-Sham equations (17) and (18), we obtain the orbital $\phi_i(r)$ called Kohn-Sham orbitals and the eigenvalue ϵ_i called the Kohn-Sham

orbital energy. To find the solution of the Kohn-sham equations (17) and (18), we have to use the iterative method as used in the Hatree method. This procedure is done by selecting the initial guess of the electron density $\eta(r)$, calculating the corresponding $V_{KS}(r)$, constructing the Hamiltonian that depends on the $\eta(r)$, obtaining the set of Kohn-Sham orbitals $\phi_i(r)$, and eigenvalue by solving the Kohn-Sham equations (17) and (18). Then, a new electron density is constructed from the new Kohn-Sham orbitals $\phi_i(r)$ and this procedure is repeated until the convergence of the electron density $\eta(r)$, is obtained. This interactive procedure is called a self-consistent field (SCF) method, and the flow chart of the interactive procedure SCF calculation of the Kohn-Sham equation has been represented in Figure 2.5. The electron density that minimizes the energy corresponds to the ground-state density, and the resulting minimum energy represents the ground-state energy. If the exact exchange-correlation functional is available, solving the Kohn- Sham equations (17) and (18) allows for the determination of both the exact ground-state density and the true ground-state energy[3–7].

In practice, the $E_{XC}[\eta(r)]$ is approximate, and so the reliability of the calculation is dependent on the approximations used to obtain the $E_{XC}[\eta(r)]$. Various approximations are proposed to find the expression for $E_{XC}[\eta(r)]$ to accurately solve the KS single-particle equation. The approximation can be categorized into two main parts: (1) local and semi-local approximations, e.g., local density approximations, generalized gradient approximation (GGA), and meta GGA approximations, (2) non-local approximations, e.g., hybrid functionals and random phase approximations[3–8].

2.10 Local Density Approximation [LDA]: The LDA is the earliest and most widely used approximation for the exchange-correlation interaction. It assumes that the exchange-correlation energy of a system can be approximated by that of a homogeneous electron gas with the same local electron density n(r). The exact exchange-correlation energy for such a homogeneous electron gas is given by the following expression:

$$E_{XC}[\eta] = \int \eta(r)\epsilon_{XC}\,[\eta](r)dr$$

where ϵ_{Xc}^{homo} is the exchange-correlation energy per electron of the homogeneous electron gas of density n(r). Despite local approximations, LDA is remarkably successful in describing the

ground-state properties of many materials. However, it still has many limitations and net errors. The approximation is, in principle, adequate for systems with low spatial varying densities. However, an obvious problem with LDA is that it fails for non-uniform systems where the densities vary very rapidly. It is unsuccessful in predicting the accurate energetics of chemical bonds, binding energies, the heat of reaction, activation energy barrier, and description of the many properties of the d and f compounds.

2.11 GGA Approximation: in the quest for improved functional, an important breakthrough was achieved with the emergence of the GGA functionals. The GGA is the more elaborated approximation of the exchange-correlation interactions, which consists of taking into account the non-uniform characteristics of the electron density by replacing ϵ_{Xc}^{homo} by the semi-local function of the electron density and the magnitude of the gradient of the electron density. The general form of the GGA functional is

$$\epsilon_{XC}^{GGA}[\eta] = \int \eta(r)\epsilon_{XC}^{GGA}(\eta(r), |\nabla\eta(\mathrm{r})|)dr$$

The popular functional in the family of the GGA are Perdew-Wang (PW86, PW91), Backe88, Perdew-Burke-Ernzerhof (PBE), Becke- Lee-Yang-Parr (BLYP) functionals. The functionals like W96 and B88 are based on the scaling relation, and some rules, other like PBE, are parameterized by the numerical fitting procedure in order to reproduce the experimental values of some molecular properties. The BLYP is the combination of Becke's 1988 exchange functional with the 1988 correlation functional of Lee, Yang, and Parr. Generally, current GGA functionals seem to give reliable results for all main types of chemical bonds (covalent, ionic, metallic, and hydrogen bonds). For Van der Walls interactions, the common GGA and LDA functionals fail. Furthermore, both LDA and GGA approximations are known to underestimate the band gap of the semiconductors by about 30 to 80 % and to inaccurately describe the band structure of strongly correlated materials. Further extension of GGA's model has been suggested, including meta GGA's, which either contains a dependency on the orbital kinetic energy or a Laplacian (second derivative of the electron density).

2.12 Hybrid Functionals: The final class of approximations to the exchange-correlation energy are the hybrid functionals. These methods are empirically fitted and contain some percentage of

the exact exchange, i.e., the Hartree exchange term. The best example of the hybrid functionals is Backe 3 Lee Yang Parr (B3LYP) hybrid functional, which has the form:

$$E_{XC}^{B3LYP} = E_{XC}^{LDA} + 0.2(\ E_X^{HF} - E_X^{LDA}) + 0.7(E_X^{B86} - E_X^{LDA}) + 0.81(E_C^{PW91} - E_C^{LDA})$$

Where E_X^{B86} is the B88 exchange functional and E_C^{PW91} is the PW91 correlation functional. The well-known B3 functional from Becke is a three-parameter functional fitted to experimental values and contains 20% exact exchange. PBE0, Heyd-Scgseria-Enzerhof (HSE), and B3PW91 are well-known functionals in the hybrid functional family. A higher family of functionals called Hybrid meta GGA functionals, which includes parameters to relatively account in an approximate way for dispersion, the Minnesota M05 and M06 family falls in this category. Hybrid functional are the more accurate in atomization entropies, geometries, and vibrational frequencies as well as the electronic structure of the materials. In this thesis, we have employed B3LYP hybrid functionals as it is an established DFT method and has shown accurate and reliable results. The B3LYP functional offers improved accuracy for energetics, bond distances, and intermolecular interactions compared to GGA functionals. Moreover, its ability to provide a more precise description of band gaps is a significant advantage when studying the electronic structure of a system[3–8].

2.13 van der Waals Corrections: The van der Waals (vdW) named after Johannes van der Waals is distance-related interactions between atoms, molecules, surfaces, as well as intermolecular forces. These forces arise from the motion of electrons, which leads to fluctuations in multipoles and generates long-range interactions. In other words, the force is a result of electron density transit shift, where the electron density shifts move one side temporarily, generating a transit charge attraction and repelling the nearby atoms. Generally, the vdW names are given to the forces acting between permanent dipole-dipole, permanent dipole-induced dipole, and two instantaneous induced dipoles (known as London dispersion forces). Although vdW interactions are the weakest interactions of weak chemical potential, it has a big influence in describing systems such as biomolecules, physisorbed molecules on the surfaces, polymer science, and stacked layered materials. The manuscript related to this is mainly based on the layered materials (TMDs) and adsorption of the molecules (ORR species) on the slab surfaces. Thus, to perform DFT calculations up to considerable accuracy, information of the dispersion correction is needed.

It is widely recognized that widely used DFT functionals, such as LDA and GGA, fail to account for the long-range electron interactions responsible for van der Waals (vdW) forces. These dispersion interactions are considered non-local electron effects, which standard exchange-correlation functionals cannot accurately capture. Achieving a precise and efficient estimation of vdW interactions within the framework of DFT remains a complex and ongoing challenge. Grimme introduced one approach to address this, known as the DFT-D method. In the DFT-D approaches, the total energy E_{total} is calculated as the sum of the standard Kohn-Sham energy E_{KS-DFT} and the semi-empirical dispersion correction E_{disp}, so that $E_{total} = E_{KS-DFT} + E_{disp}$. The E_{KS-DFT} is the DFT electronic energy computed by a given exchange-correlation function. The empirical dispersion potential has the form $-\frac{c_6}{R^6}$ at the long distances, and a damping function is applied at the short distances to scale down the contribution from the empirical term within typical bonding distances at which the local DFT approaches perform correctly[9,10]. The general expression for the dispersion term is:

$$E_{disp} = -\frac{1}{2}\sum_{A\neq B}^{atom}\sum_{n=6,8} S_n \frac{C_n^{AB}}{R_{AB}^n} f_{dmp,6}(R_{AB}) \qquad (19)$$

Where C_n^{AB} is the nth order dispersion coefficients for the pair of atoms A and B, R_{AB} their internuclear distances, S_n is the global scaling factor depending on the exchange-correlation functional used, and $f_{dmp,n}(R_{AB})$ is the damping function serving to avoid singularities at the small R_{AB} and double counting of electrons correction at the intermediate distances.

In the DFT-D2 method, only n=6 terms are included and can be expressed as[9,11–13],

$$E_{disp}^{D2} = -\frac{1}{2}\sum_{A}^{atom}\sum_{B<A}^{atom}\left(\frac{c_6^{AB}}{R_{AB}^6}\right) f_{dmp}(R_{AB}) \qquad (20)$$

The damping function in this case is

$$f_{dmp,6}(R_{AB}) = \frac{S_6}{1 + e^{-d\left(\frac{R_{AB}}{R_0^{AB}} - 1\right)}}$$

Where R_0^{AB} is the sum of atomic VdW radii, and d determines the steepness of the damping function (d=20). The geometric mean rule is applied to estimate c_6^{AB} coefficient for pairs of distinct elements $C_6^{AB} = \sqrt{c_6^A c_6^B}$.

In the DFT-D3 approach, n=6 and n=8 terms and two-body and three-body contributions are included and can be expressed as[9,11–13],

$$E_{disp}^{D3} = E^2 + E^3$$

$$= -\frac{1}{2}\sum_{A}^{atom}\sum_{B<A}^{atom}\left[\left(\frac{c_6^{AB}}{R_{AB}^6}\right) f_{dmp,6}(R_{AB}) + \sum_{A}^{atom}\sum_{B<A}^{atom}\left[\left(\frac{c_8^{AB}}{R_{AB}^8}\right) f_{dmp,8}(R_{AB})\right]\right.$$

$$\left. -\frac{1}{6}\sum_{ABC}^{atom}\frac{c_9^{ABC}}{R_{ABC}^9} f_9^d(R_{ABC}, \theta_{ABC})\right] \qquad (18)$$

The damping functions have the following forms:

$$f_{dmp,n}(R_{AB}) = \frac{S_n}{1+6\left(\frac{R_{AB}}{S_{r,n}R_{0,AB}}\right)^{-\alpha_n}} \text{ and } f_9^d(R_{ABC}\theta_{ABC}) = \frac{(3cos\theta_a cos\theta_b cos\theta_c+1)}{1+6\left(\frac{R_{ABC}}{S_{r,n}R_{0,AB}}\right)^{-\alpha_n}}$$

Where θ_a, θ_b, θ_c are the internal angle of the triangle formed by R_{AB}, R_{BC}, R_{CA}, R_{ABC} is the geometric mean of R_{AB}, R_{BC}, R_{CA}, and $c_9^{ABC} = -\sqrt{c_6^{AB} c_6^{AC} c_6^{BC}}$.

In CRYSTAL17 suit code the BLYP, PBE, B97, B3LYP, PBE0, PW1PW, M06, HSE06, HSEsol, and LC-wPBE, D3 dispersion corrected DFT methods are available. In the present thesis, we have employed the B3LYP-D3 dispersion corrected DFT method for all the research work.

2.14 CRYSTAL17: The CRYSTAL17 package is a powerful computational tool for solid-state chemistry and physics widely used for *ab initio* electronic structure calculations on crystalline solid and periodic systems. CRYSTAL17 employs various quantum mechanical methods, including Hartree Fock (HF), Kohn Sham Hamiltonian (or DFT), and hybrid approaches to determine the ground state energy, energy gradient, electronic wavefunctions, and properties of periodic systems[9,14,15]. The key characteristic of periodic systems is their symmetry, and CRYSTAL offers a variety of symmetry operators that can be applied at each step of the calculations, greatly decreasing computational costs. The program can handle systems ranging

from zero-dimensional (molecules) to three-dimensional systems like crystals, solid solutions, and even some disordered systems. Additionally, the program includes automatic tools that make it easy to generate lower-dimensional structures, such as slabs, nanotubes, nanorods, and polymers. To perform any task using CRYSTAL17 suit code, it involves the approximation of single particle wavefunction as a linear combination of the Bloch functions. These Bloch functions are defined by using local functions (atomic orbitals), which are constructed as a linear combination of Gaussian-type functions. In CRYSTAL17, the conventional atomic number (NAT) is a key parameter used to assign a specific basis set to an atom. The real atomic number (Z) associated with an atom is determined by taking the remainder of the NAT divided by 100. For example, if NAT is 237, the real atomic number Z would be 37. It is worth noting here that atoms with identical atomic numbers but located at non-equivalent positions in the crystal structure may require different basis sets to accurately represent their electronic structure. To accommodate this, different NATs can be assigned to these atoms. For example, carbon atoms (Z=6) may be associated with different basis sets using NAT like 6, 106, and 1006, each representing different electronic configurations. Similarly, core pseudopotentials for carbon atoms can be designated using NAT, like 206 or 306. This flexibility allows the precise modeling of atoms with similar atomic numbers but distinct chemical environments or electronic states. Modeling adsorption on surfaces or defects in solids typically requires large unit cells with low symmetry, where symmetry operators offer limited computational benefits. However, CRYSTAL17 provides a massive parallel version (MPPCRYSTAL) in addition to the serial and normal parallel options (PCRYSTAL), enabling the use of hundreds or thousands of cores in parallel. This version provides excellent time and memory scalability relative to system size and the required number of CPUs. The main distinction between MPPCRYSTAL and PCRYSTAL is that, in the latter, important matrices and determinants are copied entirely to each node, while in MPPCRYSTAL, they are divided and distributed across the cores. For my PhD project, I utilized CRYSTAL17 to study surface reactions, taking full advantage of the massively parallel version implemented on a supercomputer cluster. The crystal structure is determined by the space group, by the size and shape of the unit cell (i.e., lattice parameters (a, b, c), lattice angles (α, β, γ), and by the relative positions of the atoms in the asymmetric unit. To specify the lattice parameters in the input file of the CRYSTAL17, the minimal set required for different crystal systems is tabulated in Table 2.1[9,14,15]:

Table 2.1. *The crystal system and minimal set of lattice parameters corresponding to the crystal system are required to define the crystal system in the input script of the CRYSTAL17 suite code.*

Crystal system	**A minimal set of lattice parameters required**
Cubic	a
Hexagonal	a, c
Trigonal	Rhombohedral cell a, γ Hexagonal cell a, c
Tetragonal	a, c
Orthorhombic	a, b, c
Monoclinic	a, b, c, α (a unique) a, b, c, β (b unique) a, b, c, γ (c unique
Triclinic	a, b, c, α, β, γ,

Specifying the correct unit and representation of atom coordinates in the input file of the CRYSTAL17 is essential for accurately describing the geometry and symmetry of the system under investigation. In the CRYSTAL17 input file, different units (fractional or Å) of atom coordinates are employed to define a crystal structure depending on the dimensionality and symmetry of the structure. The fractional unit representation of the atomic coordinates for the periodicity of the structure along certain axes and for non-periodic direction atomic coordinates are typically expressed in Å[9,14,15]. The unit of measure of atom coordinates and keywords to specify the system dimensionality has been summarized in Table 2.2.

Table 2.2. *The unit and representation of atom coordinates in the input file of the CRYSTAL17 for accurately describing the dimensionality, geometry, and symmetry of the system.*

Translational symmetry	**Unit of measure of coordinates**			**Keyword used**
	X	Y	Z	

3D	Fraction	Fraction	Fraction	CRYSTAL
2D	Fraction	Fraction	Å	SLAB
1D	Fraction	Å	Å	POLYMER
0D	Å	Å	Å	MOLECULE

2.15 The Input File Script of CRYSTAL17: The input file structure of the CRYSTAL17 suite code is composed of a title and three main sections (geometry block, basis set block, Hamiltonian, SCF, and computational parameters). Each block has different and specific keywords and numerical parameters to control the type of calculations. Each block is closed by the keyword END[9,14,15].

Table 2.3. *The input file structure of the CRYSTAL17 suite code to perform the DFT calculation.*

Title	
Block 1	Geometry input Standard geometry input Optional geometry optimization and editing keywords END
Block 2	Basis set input Standard basis set input Optional basis set related keywords END
Block 3	Single particle Hamiltonian and SCF control SHRINK factor Sampling in reciprocal space

Optional geometry information and SCF-related keywords
END

The input file starts with the title line, which contains the relevant information about the system of study. The title section is printed in the output file but not executed by the CRYSTAL17 suite code.

Block 1: This block begins with the appropriate keywords to define the dimensionality of the system of study, as mentioned in Table 2.3. The next line defines the symmetry of the structure defined by using the corresponding symmetry group number. The next two lines define the minimal set of lattice parameters necessary to define the Bravais lattice, as represented in Table 2.3, and the number of atoms in the asymmetric unit. The preceding lines then define the relative position of each atom in the symmetric unit cell. Each line represents the conventional atomic number followed by the coordinates of the atoms. After that, this section contains the optimization keyword to locate the equilibrium structure of the system. This geometry input block must be then closed with the END keyword. The complete block 1 looks as given in Table 2.4 (for 2D slab)[9,14,15]:

Table 2.4. *An example to explain the first block of the CRYSTAL17 input file by considering the geometry optimization of the graphene slab.*

Title: **Graphene slab B3LYP-D3 C= C_pob_TZVP_2012, Ashok_singh_18052024**	
Block 1	**Example: Graphene slab**
Dimensionality of the system	SLAB
Crystallographic information (3D only)	0 0 0 (3D only)
Symmetry group number	80
Lattice parameters	2.4560 2.4560 120.0000
Number of atoms in the asymmetric unit	2

Conventional atomic number and coordinates of the atoms	6 0.00000 0.00000 0.25000 6 0.33333 0.66667 0.25000
Geometry optimization-based keywords	OPTGEOM FULLOPTG MAXCYCLE 800
End of the geometry input sections	ENDOPT
End of the geometry block	END

Block 2: Block 2 of the input file of the CRYSTAL17 suite code is dedicated to introducing the basis set for each atom with different conventional atomic numbers. In a crystal structure, each atom is associated with the basis set through its conventional atomic number. Selecting the appropriate basis set is a key aspect of conducting ab initio calculations for periodic systems. A thorough explanation of the basis sets can be found in the basis set section. Additionally, an optimized library of basis sets tailored for periodic systems is available at https://www.crystal.unito.it/basis_sets.html. The basis set block should be closed with two line sequences 99 0 followed by the END keyword[9,14,15]. An example of a basis set block has been given in Table 2.5.

Table 2.5. *An example to explain the second block of the CRYSTAL17 input file by considering the basis set of the graphene slab.*

Basis set	**Example: Graphene slab**
	6 8 0 0 6 2.0 1.0 13575.349682 0.00022245814352

	2035.2333680 0.00172327382520
	463.22562359 0.00892557153140
	131.20019598 0.03572798450200
	42.853015891 0.11076259931000
	15.584185766 0.24295627626000
	0 0 2 2.0 1.0
	6.2067138508 0.41440263448000
	2.5764896527 0.23744968655000
	0 0 1 0.0 1.0
	0.4941102000 1.00000000000000
	0 0 1 0.0 1.0
	0.1644071000 1.00000000000000
C=C_pob_TZVP_2012	0 2 4 2.0 1.0
	34.697232244 0.00533336578050
	7.9582622826 0.03586410909200
	2.3780826883 0.14215873329000
	0.8143320818 0.34270471845000
	0 2 1 0.0 1.0
	0.5662417100 1.00000000000000
	0 2 1 0.0 1.0
	0.2673545000 1.00000000000000
	0 3 1 0.0 1.0

	0.8791584200 1.00000000000000
End of the basis set block	99 0 END

Block 3: This block of the input file includes the keywords that specify the Hamiltonian description, parameters for SCF calculations, and the computational parameters. This block starts with the determination of the single particle Hamiltonian (RHF, UHF, ROHF, DFT) followed by the desired exchange-correlation functionals. A range of functionals has been included in the CRYSTAL17 software package, ranging from simplistic local-density approximation to complex dense hybrid functionals. The van der Waals correction can be considered by Grimme's dispersion correction methods. This block then contains the keywords for defining the integrals of tolerance and shrinking factor (to generate a commensurate grid of k-points in reciprocal space). This section is then followed by specifying the SCF control parameters (maximum number of SCF cycles, the criterion on the total energy for the SCF convergence). The block 3 is then closed by the END keyword. The sample of block 3 looks as shown in Table 2.6[9,14,15]:

Table 2.6. *An example to explain the final block of the CRYSTAL17 input file, which includes the keywords for numerical accuracy and computational parameter control.*

Block 3	**Example: Graphene slab**
Choose single particle Hamiltonian	DFT
Spin polarization calculations	SPIN
Choice of the exchange-correlation functional	B3LYP-D3
Numerical accuracy and computational parameter control	XLGRID END TOLINTEG 7 7 7 7 14

	TOLDEE 7 SHRINK 0 8 4 4 1 SCFDIR BIPOSIZE 110000000 EXCHSIZE 110000000
SCF convergence control	MAXCYCLE 800 SMEAR 0.01 FMIXING 80
Population analysis	ANDERSON PPAN
End of the block 3	END

The keywords Block 1, and Block 3 can be added or removed according to the requirements of the calculations and investigation. For example, harmonic vibrational frequency calculations can be performed by including the keyword FREQCALC in the input Block 1.

2.16 Basis Set: To solve the Schrodinger or KS equations of DFT, one of the approximations is essential, which is the introduction of the basis sets. The unknown functions (one electron HF or KS orbitals) are expressed in terms of the expansion in a set of known functions that are represented by a mathematical function called the basis function. A basis function is a set of wave functions that describes the shape of the atomic orbitals (AOs). A basis set is used to create the molecular orbitals (Φ_i), and each molecular orbital is expressed in terms of the linear combination of the AOs (LCAOs). The mathematical representation of Φ_i in terms of the LCAOs is represented as:

$$\Phi_i(r) = \sum_{\alpha}^{M} C_{\alpha i}\chi_{\alpha}(r) \qquad (21)$$

Where $\Phi_i(r)$, $\chi_{\alpha}(r)$,and $C_{\alpha i}$ represents the molecular orbital, basis function, and expansion coefficient. If M→∞, then $\Phi_i(r)$ reaches the complete basis set limit and represents the exact expression of a molecular orbital, not the approximations. Unfortunately, complete basis sets tend to have an infinite number of functions and, therefore, are not practical for calculations. In practice, a finite basis set is used to represent a molecular orbital in electronic structure calculations. A larger basis set generally improves the quality of orbital representation, but the quality of a basis set ultimately depends on both its size and how well it spans the relevant space of the true wavefunction [16,17].

2.17 Types of Basis Functions: There are two types of basis functions commonly used for the representation of molecular orbital in electronic structure calculations. One is called Stater type orbital (STO), and the other is Gaussian type orbital (GTO). The STOs have the mathematical function form as:

$$S_{\xi nlm}(r,\theta,\phi) = N\, Y_{l,m}(\theta,\phi) r^{n-1} e^{-\xi r} \qquad (22)$$

Where N is a normalization constant, $Y_{l,m}(\theta,\phi)$ represents the spherical harmonic functions, and n represents the principle quantum number. STOs do not contain radial nodes, and these nodes are introduced through linear combinations of STOs. These functions were originally used for atomic and diatomic systems that demand high accuracy, as well as in semi-empirical methods that neglect three- and four-center integrals. However, from a computational standpoint, STOs present

challenges, as most of the necessary integrals for the SCF procedure need to be computed numerically, which considerably reduces the speed of the calculations. The second most used basis functions are the GTOs. The GTOs can be written in terms of the cartesian and polar coordinates. The mathematical definition of GTOs can be written as:

$$G_{\xi,l_x,l_y,l_z} = NX^{l_x}Y^{l_y}Z^{l_z}e^{-\xi r^2} \qquad (23)$$

$$G_{\xi,n,l,m}(r,\theta,\phi) = NY_{l,m}(\theta,\phi)r^{2n-2-l}\,e^{-\xi r^2} \qquad (24)$$

In the cartesian coordinate, the angular dependence of the GTOs is computed from the l_x, l_y, l_z. For example, s-orbital (l=0), p-orbital (l=1), and so on. A comparison between the STOs and GTOs shows that there are some major differences in the behavior of these two functions. (1) the behavior at r→0: the derivative of GTOs at the nucleus is equal to zero due to r^2 dependence in the exponent of the function, hence has zero slope. In contrast to GTOs, STOs have a discontinuous derive and, hence, have a cusp. Thus, GTOs represent an incorrect electronic behavior near the nucleus. (2) the behavior at r→∞: far from the nucleus, the GTOs decay rapidly as compared to the STOs. Thus, the tail of the Gaussian-type wave functions poorly represents the electronic behavior. In principle, more GTOs are required in order to achieve certain accuracy.

2.18 Properties of the Basis Functions: A basis function should satisfy the following properties:

(1) must have physical significance

(2) the coefficients are obtained variationally

(3) the chosen basis function needs to be able to approximate the actual wavefunction sufficiently well to give chemically meaningful results and should give maximum flexibility to the molecular orbitals.

2.19 Classification of Basis Set: The chemically important region is the outer orbitals (i.e., valence electrons) of an atom in performing calculations since chemical bonding involves valence orbitals. The core orbitals exhibit minimal variation depending on the chemical bonding environment, and the expansion coefficients for these inner basis functions remain relatively constant. Energy-optimized basis sets are especially sensitive to the wavefunction in the region of inner-shell electrons. The 1s electrons contribute significantly to the total energy, so minimizing

the energy typically results in an optimized basis set for the core electrons, but less so for the valence electrons. Additionally, many properties are influenced by the tail of the wavefunction, which, while technically present, plays little role in chemical behavior. A single Gaussian wavefunction is not ideal for accurately representing the spatial extent and nodal features of atomic orbitals, as it focuses more on describing the core electrons, which are energetically important but chemically insignificant. To address this issue, basis functions are expressed as sums of multiple Gaussian functions, each with different exponential parameters. This approach treats the variational coefficient of the inner basis functions as fixed, eliminating the need for it to be determined through variational methods. The 1s orbital is thus represented as a fixed combination of basis functions. In quantum chemistry, a single Gaussian function is referred to as a primitive Gaussian-type orbital (PGTO), and when these PGTOs are combined into a smaller set via fixed linear combinations, the result is known as a contracted Gaussian-type orbital (CGTO)[9]. The CGTOs can be mathematically represented as:

$$\zeta(CGTOs) = \sum_{i}^{k} \alpha_i G_i(PGTOs) \qquad (25)$$

There are various classifications of contracted GTOs, as listed below:

(1) Minimal basis set: After defining the types of functions (STOs/GTOs), the most important factor is the number of AOs used. A minimum basis set consists of a single basis function assigned to each orbital in the electronic configuration of a neutral atom. For instance, Hydrogen and Helium (with their 1s orbitals) require only a single s function or a single atomic orbital (AO) to define the 1s orbital. Similarly, elements in the first row of the periodic table need two s functions (for the 1s and 2s orbitals) and a set of p functions (for the p_x, p_y, and p_z orbitals). Therefore, the first row of elements would have five basis functions, the second row would have nine, and so on. A widely used minimal basis set is STO-nG, where the integer n indicates the number of Gaussian-type orbitals (GTOs) employed to approximate the Slater-type orbitals (STOs) for both core and valence orbitals. Examples of common minimal basis sets include STO-3G, STO-4G, and STO-5G. However, minimal basis sets lack sufficient flexibility to accurately represent orbitals since they assign only one contracted GTO to each atomic orbital. The solution to this is to use multiple functions to represent each orbital of an atom[9].

(2) Split-valence basis set: This type of basis set uses multiple basis functions to represent each valence orbital. These are referred to as split-valence basis sets because the representation of valence orbitals is divided into two or more separate basis functions. These basis sets, designed by People and coworkers and denoted b n-ijG or n-ijkG, where n represents the number of PGTOs, are used to define the core orbitals. The ijk indicates how many functions the valence orbitals are split into and how many PGTOs are used for the representation of the valence orbitals. The examples of the split-valence basis set are 3-21G, 6-031G, 6-311G, and so on. The 3-21G represents that the non-valence electrons are described by a single basis function composed of a contraction of three PGTOs. Each valence electron is described by two CGTOs. The first of these basis functions is composed of two PGTOs, and the second consists of a single PGTOs. Let us consider the example of the carbon atom (namely C-6-21G*_docesi_1990) used in the CRYSTAL17 software as given in Table 2.7[9].

The first block of Table 2.7, namely block 1, represents the basis function, which describes the non-valence core orbitals and is constructed by using six PGTOs. We observed that there are two blocks for the 2s and 2p orbitals (i.e., block 2 and block 3). The s and p orbitals share the same exponents, as shown in the first column of block 2 and block 3. From block 2 and block 3, we can observe that the first sp shell has a larger exponent than that of the second sp shell. Thus, the first sp shell has tighter PGTOs, and the second sp shell has more diffused PTGOs. Thus, the first block describes the electron density closer to the nucleus, and the second sp shell describes the electron density away from the nucleus[9].

Table 2.7. *The example and description of the split-valence basis set by considering the C-6-21G*_docesi_1990 basis set of a carbon atom.*

Block	**C-6-21G*_docesi_1990**	**Description**
	6 4	
Block 1	0 0 6 2.0 1.0 3048.0 0.001826 456.4 0.01406	This represents the s-core shell of the carbon atom, which contains six PGTOs. The first column represents the exponents, and the second column represents the s-coefficients.

	103.7 0.06876 29.23 0.2304 9.349 0.4685 3.189 0.3628	
Block 2	0 1 2 4.0 1.0 3.665 -0.3959 0.2365 0.7705 1.216 0.8606	This represents the first sp shell, which contains two PGTOs. The first column represents the exponents, and the second and third column represents the s-coefficients and p-coefficient respectively.
Block 3	0 1 1 0.0 1.0 0.1959 1.0 1.0	This represents the second sp shell, which contains two PGTOs. The first column represents the exponents, and the second and third column represents the s-coefficients and p-coefficient respectively.
	0 3 1 0.0 1.0 0.8 1.0	

(3) Double zeta (DZ) and triple zeta (TZ) basis set: These types of basis sets use double and triple CGTOs to contract the orbitals (i.e., more than one CGTOs per atomic orbital). The terms DZ and TZ do not imply whether more than one CGTOs are used for all orbitals or only for the valence orbitals. The main difference between the triple zeta (TZ) basis set and the split-valence basis set is that these basis functions do not share the same exponent for two orbitals. Therefore, these basis functions are more flexible but computationally more expensive. The example of the TZ basis set for the carbon atom used in the CRYSTAL17 suite code has been given in Table 2.8.

The first block of Table 2.8 represents the 1s core of the carbon, and block 2 describe the 2s valence orbital of carbon, and block 3, describes the 2p valance orbital of the carbon. Each atomic orbital is described by using the three CGTOs as highlighted by the blue color in Table 2.8. That is why these are called TZ basis sets[9].

Table 2.8. *The example and description of the triple zeta (TZ) basis set by considering the C_pob_TZVP_rev2 basis set of a carbon atom.*

Block	**C_pob_TZVP_rev2**		**Description**
	6 8		
Block 1	0 0 6 2.0 1.0		This represents the s-core shell of the carbon atom, which contains six PGTOs. The first column represents the exponents, and the second column represents the s-coefficients.
	13575.349682	0.00022245814352	
	2035.2333680	0.00172327382520	
	463.22562359	0.00892557153140	
	131.20019598	0.03572798450200	
	42.853015891	0.11076259931000	
	15.584185766	0.24295627626000	
Block2	0 0 2 2.0 1.0		This represents the s shell, which contains three CGTOs. The first column represents the exponents, and the second represents the s-coefficients.
	6.2067138508	0.41440263448000	
	2.5764896527	0.23744968655000	
	0 0 1 0.0 1.0		
	0.4941102000	1.00000000000000	
	0 0 1 0.0 1.0		
	0.1644071000	1.00000000000000	
Block 3	0 2 4 2.0 1.0		This represents the p shell, which contains three CGTOs. The first column represents the exponents, and the second represents the p-coefficients.
	34.697232244	0.00533336578050	
	7.9582622826	0.03586410909200	
	2.3780826883	0.14215873329000	

0.8143320818	0.34270471845000
0 2 1 0.0 1.0	
0.5662417100	1.00000000000000
0 2 1 0.0 1.0	
0.1973545000	1.00000000000000
0 3 1 0.0 1.0	
0.5791584200	1.00000000000000

(4) Polarized basis set: The basis sets, which we discussed till now, can be further modified to obtain an approximation that describes better quality of the molecular structures. The polarization function enhanced the flexibility of atoms to form a chemical bond in any direction. The polarization functions allow for a more realistic representation of electron behavior in molecules, particularly in non-uniform environments. Flexibility refers to the ability to polarize the atomic electron density, leading to a more accurate representation of a molecule's electron density. For instance, in the case of hydrogen, which typically has a spherical s orbital, bonding with a carbon atom causes the electron density to deviate from a spherical shape. By adding a p orbital, the electron density aligns more effectively in the bond's direction, indicating polarization. This flexibility is improved by including basis functions with higher angular momentum to valence split, double-zeta (DZ), and triple-zeta (TZ) basis sets. Thus, to consider the polarization, a p-type basis function can be added to the basis set with the valence s orbital (e.g., Hydrogen), and a d-type basis function can be added to the basis set with the valence p orbital (e.g., first and second-row elements of the periodic table), and a f-type basis function can be added to the basis set with the valence d orbital (e.g., transition metal). The addition of one or two asterisks to the basis set specifies the addition of the polarization function. The specification of the addition of the polarization function can also be done by naming such double zeta valence polarization (DZVP) and triple zeta valence polarization (TZVP) basis sets. E.g., 3-21G*, 6-31G*, DZVP, and TZVP. The example of the polarized basis set is given in Table 2.9, and the polarized block is highlighted by the red color (block 4) for the carbon atom[9].

Table 2.9. *The example and description of the triple zeta valence polarization basis set by considering the C_pob_TZVP_rev2 basis set of carbon atom.*

Block	C_pob_TZVP_rev2		Description
	6 8		
Block 1	0 0 6 2.0 1.0		This represents the s-core shell of the carbon atom, which contains six PGTOs. The first column represents the exponents, and the second column represents the s-coefficients.
	13575.349682	0.00022245814352	
	2035.2333680	0.00172327382520	
	463.22562359	0.00892557153140	
	131.20019598	0.03572798450200	
	42.853015891	0.11076259931000	
	15.584185766	0.24295627626000	
Block 2	0 0 2 2.0 1.0		This represents the s shell, which contains three CGTOs. The first column represents the exponents, and the second represents the s-coefficients.
	6.2067138508	0.41440263448000	
	2.5764896527	0.23744968655000	
	0 0 1 0.0 1.0		
	0.4941102000	1.00000000000000	
	0 0 1 0.0 1.0		
	0.1644071000	1.00000000000000	
Block 3	0 2 4 2.0 1.0		This represents the p shell, which contains three CGTOs. The first column represents the exponents, and the second represents the p-coefficients.
	34.697232244	0.00533336578050	
	7.9582622826	0.03586410909200	
	2.3780826883	0.14215873329000	

	0.8143320818 0.34270471845000 0 2 1 0.0 1.0 0.5662417100 1.00000000000000 0 2 1 0.0 1.0 0.1973545000 1.00000000000000	
Block 4	0 3 1 0.0 1.0 0.5791584200 1.00000000000000	This block represents the polarization of the basis set. Here, a d-type basis function has been added to the basis set of carbon atom, which gas the valence p orbital.

(5) Diffuse basis set: Diffuse functions are essential for accurately describing anions and weak interactions, such as hydrogen bonds, and for predicting properties like dipole moments and polarizability. These functions are usually introduced as an additional set of uncontracted Gaussian basis functions with the same angular momentum as the valence electrons. The inclusion of diffuse functions is indicated by a + symbol. The examples of the diffuse basis set are n-ij+G, n-ijk+G, n-ij++G, and n-ijk++G.

2.20 Basis Sets in CRYSTAL17 Suite Code: A CRYSTAL17 suite code either uses a general basis set, including s, p, d functions, or standard Pople basis sets. In CRYSTAL17, the basis set type is classified by using the code as tabulated in Table 2.10[9]:

Table 2.10. *The basis set implemented in the CRYSTAL17 suite code and their code for the use of these basis set in applications.*

Basis set code	**Basis set name**
0	General basis set
1	Pople's STO-nG basis set
2	Pople's 3(6)-21G basis set

The shell types are specified in the CRYSTAL17 code by using the shell code as listed in Table 2.11:

Table 2.11. *The basis set shell code is used to define the atomic shell in the Gaussian basis set implemented in the CRYSTAL17 suite code.*

Shell type code	Shell type	AOs	Maximum shell charge
0	s	1	2
1	sp	4	8
2	p	3	9
3	d	5	10
4	f	7	0-polarisation only

2.21 Basis Set Format of CRYSTAL17 Suite Code: The basis set in the CRYSTAL17 code has the following format as shown in Table 2.12[9]:

Table 2.12.. *The Gaussian basis set format in the CRYSTAL17 sit code.*

For each atom				
The conventional atomic number		Number of shells n_s of the atomic basis set		
For each shell				
Type of basis set	Type of shell	Number of PGTOs	Shell electronic charge	Scalar factor
For each PGTOs				
Exponent		Contraction coefficient	Contraction coefficient	

The CRYSTAL17 dataset has the following listed basis sets[9]:

Table 2.13. *The type of basis sets available in the CRYSTAL17 dataset.*

Keyword	Description
STO-3G	Pople's STO-3G minimal basis set
STO-6G	Pople's STO-6G minimal basis set
POB-DZVP	POB-double zeta valence plus polarization set for solid-state systems
POB-DZVPP	POB-double zeta valence plus double set of polarization set for solid-state systems
POB-TZVP	POB-triple zeta valence plus polarization set for solid-state systems

Where POB stands for Peintinger-Oliveira-Bredow.

The example of the format of the CRYSTAL17 basis set has been represented in Figure 2.6.

2.22 Theoretical Model: There is a strong correlation between the catalytic structure model and the catalytic activity of the material because the catalytic active sites (face, edge, and corner side) have different nearest neighbors for different structures and hence have different catalytic activity. During the electrocatalytic reaction, the adsorption of the reactants and reaction intermediates **occurs** on the surface of the catalytic material, which makes proper surface modeling an important step to enhance the accuracy of the calculation. There are two main conceptual ways to design the 2D catalytic surface: (1) the cluster model and (2) the periodic slab model.

(1) The Cluster Model: In this method, a section of the crystal is extracted with a particular size and geometry, making it possible to examine the exposed surface. The cluster model focuses on representing small, isolated clusters of atoms and molecules that mimic the active site of the catalyst. An example and the process of formation of the cluster model for the TMDs is shown in Figure 2.7. In the cluster model, the results are strongly affected by the cluster size and geometry, and the convergence of the results with respect to the increased cluster size is irregular. his issue does not arise in the periodic slab model. The in-depth description of the cluster model is out of the scope of this thesis.

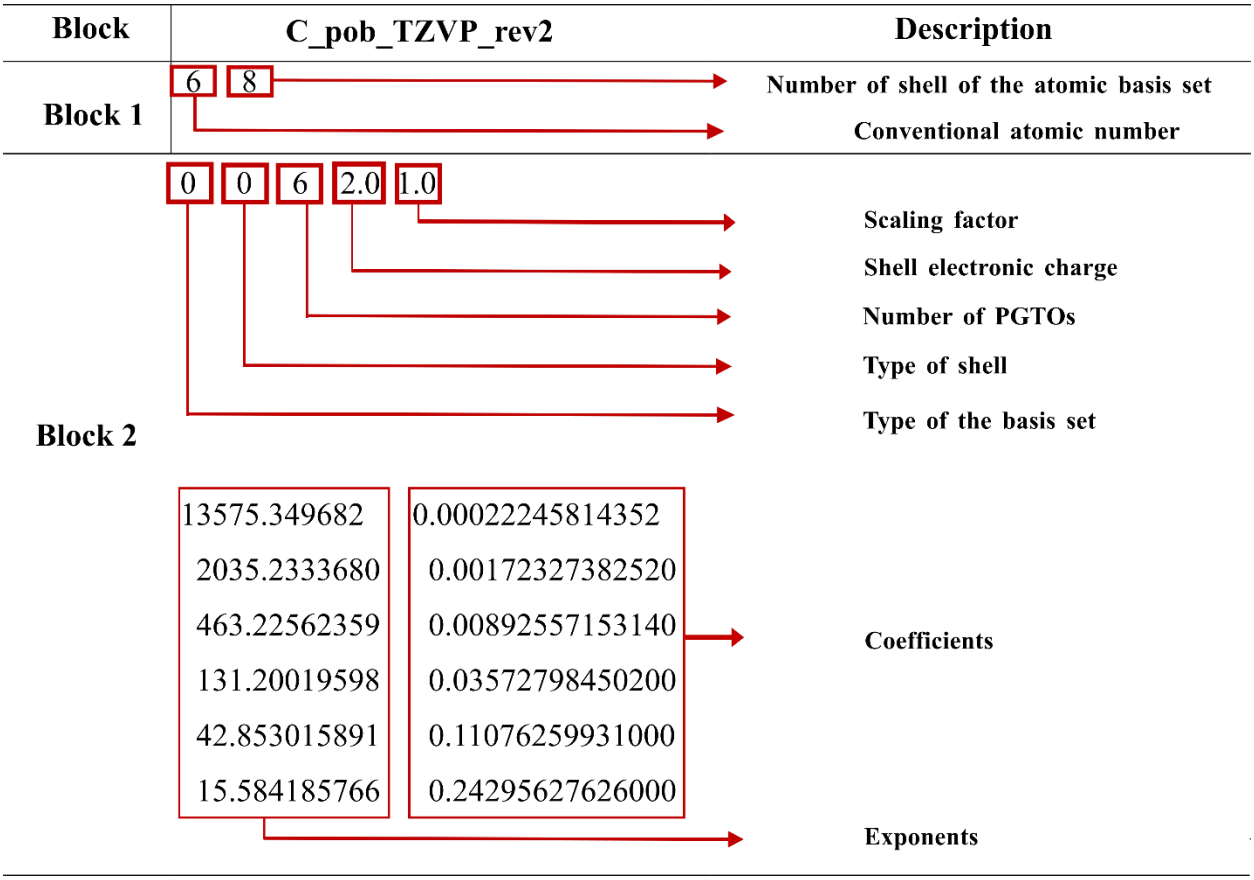

Figure 2.6. *Representation of the format of the Gaussian basis set used in the CRYSTAL17 suite code.*

(2) The Periodic Slab Model: In this model, a periodic slab is created by the cleavage along some crystallographic plane in the bulk crystal material. The process of the creation of the slab model starts with obtaining the crystallographic information file (CIF) from the experimental

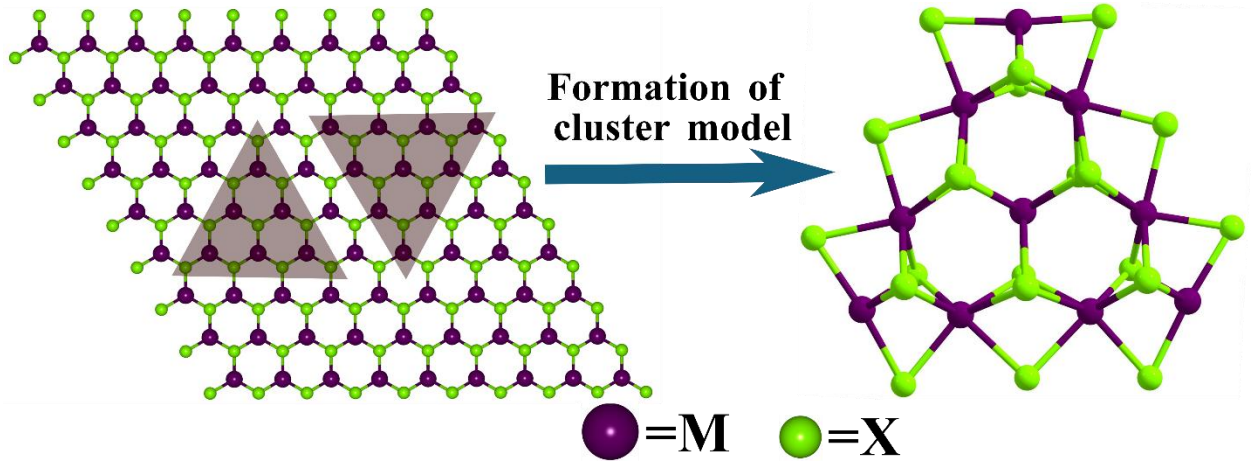

Figure 2.7. *Illustration of the procedure for the formation of the cluster model to create a catalytic surface from the bulk material.*

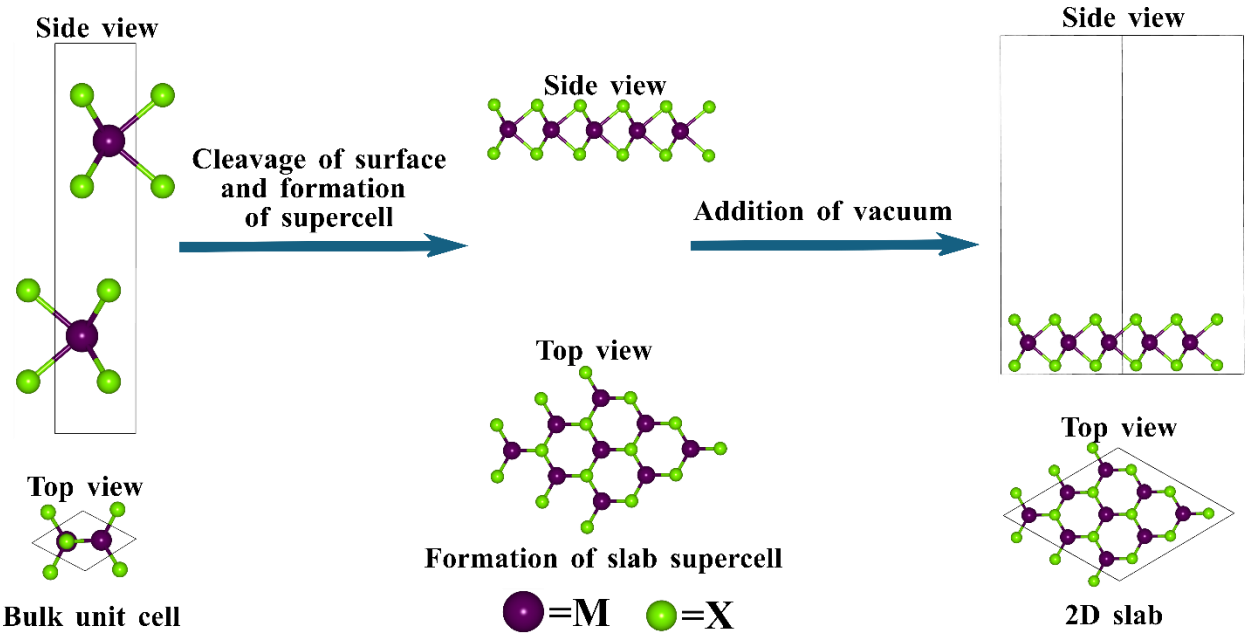

Figure 2.8. *Illustration of the procedure for the formation of the slab model to create a catalytic surface from the bulk material.*

measurements. The CIF file contains detailed information about crystal structure, including the arrangements of atoms. In any crystal structure, the orientation of the planes is represented by the indices formed by three numbers (hkl) called Miller indices. These Miller indices indicate the direction of the crystallographic planes. The slab is created by cutting the crystal unit cell through a specific crystallographic plane (hkl) and by imposing periodic boundary conditions, as shown in Figure 2.8. The formation of the slab model can be summarized as follows: (1) construct the bulk unit cell, (2) specify the Miller indices of the selected crystallographic face, (3) specify the surface termination, and (4) specify the slab thickness. We have employed the periodic slab model to study the catalytic activity of the materials in this thesis. We employed a supercell in our calculation, which is created by repeating the slab unit cell in two directions. Then, a vacuum is added above below the supercell to ensure the absence of the neighboring layers and create an isolated surface environment. The size of the vacuum region may vary depending on the system under study, the desired level of accuracy, and based on the software. In this thesis, the TMDs are created by a slab model, and the adsorbates (reactant and reaction intermediates) are introduced on the surface of the supercell to study the catalytic activity of the material. The process of formation of the slab is represented in Figure 2.8. The initial geometries are subjected to relaxation and optimization and processes to minimize the total energy of the system and achieve a stable slab structure.

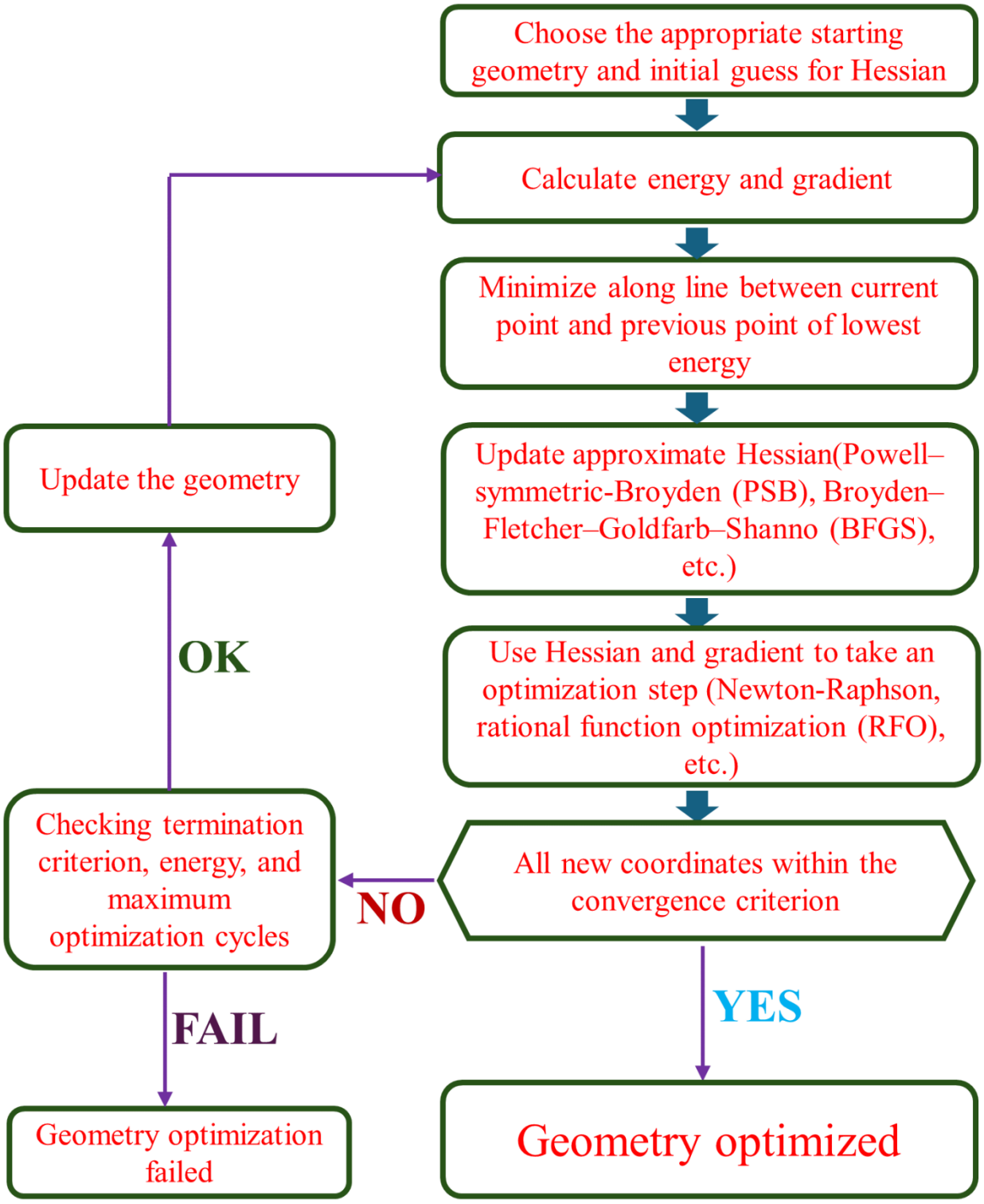

Figure 2.9. *Schematic illustration of iterative optimization cycle employed to obtain the equilibrium structure of the system.*

2.23 Geometry Optimization: To make the theory more representative of experimental results, the next logical step is to explore not just one, but all possible structural configurations for a given

chemical formula. All possible structures of a system are characterized by the potential energy surface (PES). The PES is (3N-6 coordinate dimension, where N is the number of atoms>3) hyperspace defined by the energy of a collection of the atoms in a structure over all possible atomic arrangements. A comprehensive PES provides insight into all possible molecular structures and the isomerization pathways connecting them, offering a complete description of the atomic arrangements for a given set of atoms[18]. The process of locating a stationary point on the PES and calculating its geometry and energy is called optimization. The stationary point might be a maximum, minimum, or high-order saddle point. The first-order saddle point is maxima in one direction and minima in all other directions in PES. The second saddle point is maxima in two directions and minima in all other remaining directions. The first-order saddle point in the PES surface corresponds to the transition state (TS) structure connecting two equilibrium structures. The difference between the energy of TS structure and reactant is the energy barrier for the reaction. The process of locating TS in the PES is called transition state optimization. The process of locating a minima in the PES is called the geometry optimization[18]. Geometry optimization is employed to find the minimum energy structure (equilibrium structure) of a molecular system. The minima in PES represents the equilibrium structure of the reactant, intermediate, and the product of the reaction. The energy difference between the reactant minima and product minima in the PES represents the energy of the reaction. A minimum can be a local minimum, which is the lowest point in some limited region in the PES, or it can be a global minimum, the lowest energy point anywhere on the PES. Generally, the successive search for minima finds the local minima but not necessarily the lowest. The optimization will greatly depend on the initial estimation of the coordinates of the atoms because the optimized structure obtained is closest in geometry on the PES to the input structure. Thus, a good initial estimation for atomic coordinates will greatly decrease the speed of DFT calculations and successfully define the energy minimum structure in the PES. The widely used algorithm for geometry optimization is to use the first and second derivatives of the energy with respect to the geometric parameters[18]. Let us construct a local quadratic approximation to the PES with the help of the Taylor expansion: -

$$E(x_k) = E(x_0) + \epsilon\, E'(x_0) + \epsilon^2\, E''(x_0) + \cdots \qquad (26)$$

Where x_0 is the reference point, and $\epsilon = x_k - x_0$, $E'(x_0) = \frac{d}{dx_k} E(x_k)|_{x_k=x_0}$, $E''(x_0) = \frac{d^2}{dx_k^2} E(x_k)|_{x_k=x_0}$

At the stationary point, the derivative equation 26 should be zero with respect to all coordinates of x_k.

$$0 = g = \frac{d}{dx_k} E(x_k) = E(x_0) + \epsilon\, E'(x_0) + \epsilon^2\, E''(x_0) \qquad (27)$$

$$x_k = x_0 - \frac{E'(x_0)}{E''(x_0)} \qquad (28)$$

Generalizing this to n-dimensional, the first derivative becomes the gradient (g_0), and the second derivative becomes the Hessian matrix (H_0).

In the n-dimensional, the new iteration can be written as:

$$q_k = q_0 - g_0 H_0^{-1} \qquad (29)$$

This is known as the Newton or Newton-Raphson step. The equation (28) provides a description of the location of the stationary point. In principle, starting from an arbitrary structure having coordinates q_0, one would compute the gradient and Hessian matrix H and then select the new geometry coordinates q_k according to equation 29. For these new geometry coordinates, the gradient would be zero, i.e., a stationary point in the PES. However, our truncation of full Taylor series expansion up to the second order, so equation 27 only approximates g and may not necessarily be zero. However, $g(x_k)$ would be smaller than that of close paren. However, after a sufficient number of iterations, the gradient g will become too small to be considered insignificant. Thus, after that we declare our geometry to be converged. There are an infinite number of methods to update the Hessian matric, but the Broyden-Fletcher-Goldfarb-Shanno (BFGS) scheme is the most successful and widely used method. For the geometry optimization, the gradient must be zero, and all the eigenvalues of the Hessian matrix corresponding to molecular vibration must be positive, and vibrational frequencies must be real. For the TS optimization, the gradient must be zero, and Hessian should have one and only one negative eigenvalue and have one and only one

imaginary vibrational frequency. The Newton and Quasi-Newton methods are the most efficient and widely used procedures for optimizing geometries and can also be used to find the TS.

In CRYSTAL17, the optimization is done under the Quasi-Newton optimization scheme, and the gradient is evaluated each time the energy is computed, and the second derivative matrix is updated by means of the BFGS algorithm. The convergence of the optimization process is checked on the root mean square and the absolute value of the largest component of both the gradient and the estimated displacements. In CRYSTAL17, the threshold criterion on the gradient and displacement used for the optimization process are summarized in Table 2.14[9,19]:

Table 2.14. *The optimization threshold criterion on the gradient and displacement in the CRYSTAL17 suite code.*

Optimization Parameters	**Threshold criterion (a. u.)**
RMS Gradient	0.000300
MAX Gradient	0.000450
RMS Displacement	0.001200
MAX Displacement	0.001800

After the geometry optimization, we will have the following information: (1) The equilibrium atomic coordinates of the structure, (2) the equilibrium energy, (2) the equilibrium parameters such as bond length and bond angles, (3) the Mulliken charges, (4) dipole moment and so on. The flow chart of the important steps during the optimization process in CRYSTAL17 is shown in Figure 2.9.

2.24 Descriptors of ORR Activity: The theoretical descriptors of electrochemical ORR catalysts provide fundamental insights into the fundamental properties that influence the performance of the electrocatalyst. These descriptors help in designing and optimizing catalysts for various applications, including fuel cells and metal-air batteries (MABs). Here is a detailed explanation of theoretical descriptors for choosing a good electrocatalyst for ORR.

(1) Adsorption Energy of the Key Reaction Intermediates: The adsorption energy refers to the energy change associated with the adsorption of reactants, intermediates, and products into the

surface of the electrocatalyst. In the context of the ORR, it signifies the energy requirement for oxygen molecules or reaction intermediates to bind to the active site on the electrocatalytic surface. The adsorption energy plays a pivotal role in determining the kinetics and mechanism of ORR. It influences the strength of the interactions between the reactants and the catalytic surface, thereby affecting the activation barrier for the reaction steps. In this thesis, the adsorption energy during the reaction has been calculated by employing the first principle-based DFT through the following equation:

$$E_{ads} = E_{adsorbate+catalytic\ surface} - E_{adsorbate} - E_{catalytic\ surface}$$

Where $E_{adsorbate+catalytic\ surface}$, $E_{adsorbate}$, and $E_{catalytic\ surface}$ represent the energy of the electrocatalytic surface with the adsorbates, the energy of the adsorbates, and the energy of the clean electrocatalytic surface.

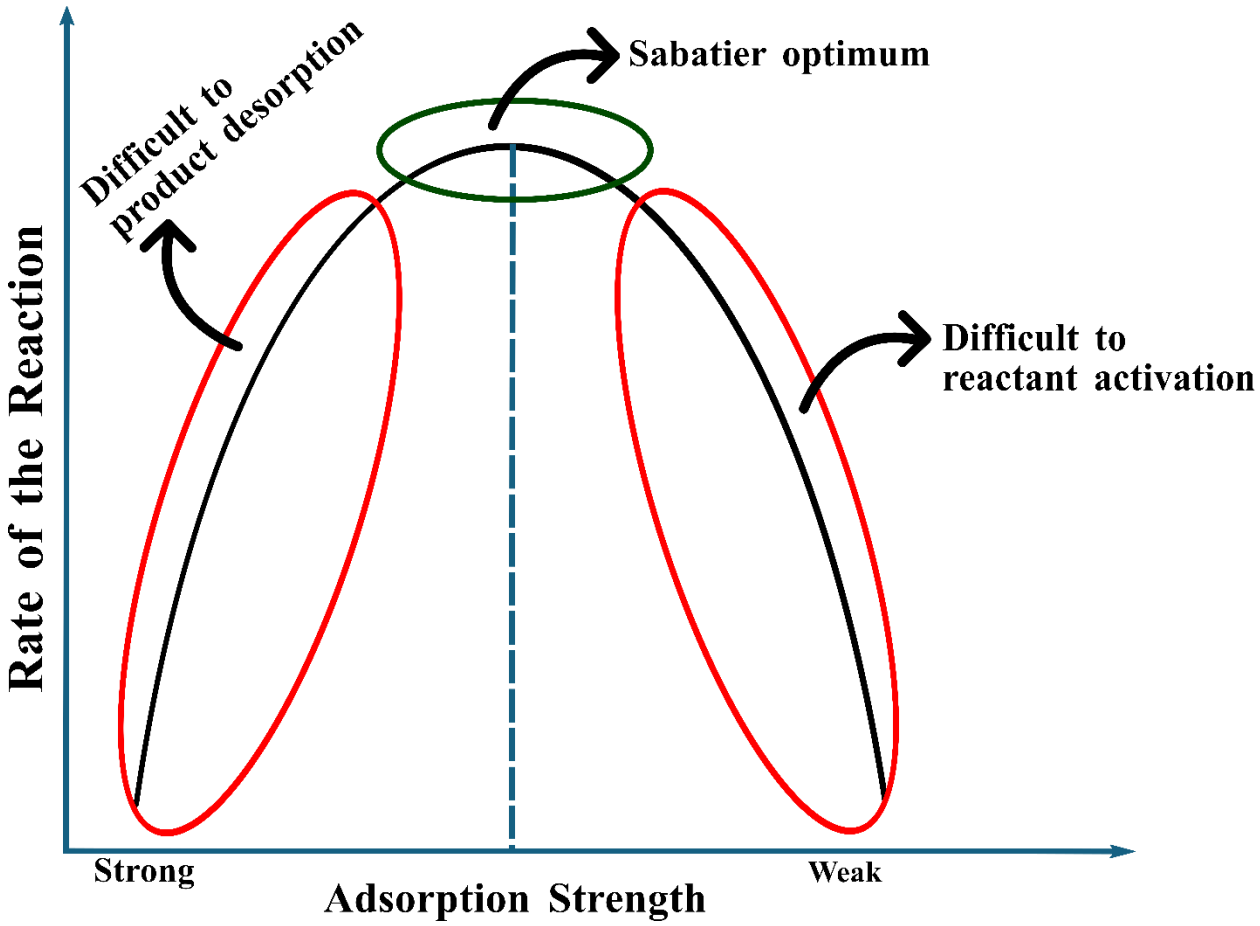

Figure 2.10. *Schematic representation of the qualitative Sabatier principle that predicts the activity of heterogeneous catalysts based on the interactions between the catalyst and the reactant.*

The qualitative concept of evaluating the performance of the electrocatalyst based on the adsorption energy is given by the Sabatier principle. This principle is named after its developer, Paul Sabatier. This principle states that, in order for an electrocatalyst to be ideal for a particular reaction, its interaction with the reactants/reaction intermediates should be neither too strong nor too weak. If the adsorption strength is too weak, reaction intermediates may desorb before undergoing the desired chemical transformations. Conversely, if adsorption is too high, reaction intermediates may bind too strongly, hindering their mobility and the desorption of desirable products. The geometrical representation of the qualitative Sabatier principle is shown in Figure 2.10. This can lead to sluggish reaction rates and potential catalyst poisoning due to irreversible adsorption. Thus, the Sabatier principle suggests that the reactants/reaction intermediates adsorption strength with the catalytic site should be in optimal range. This balance allows for sufficient strong adsorption to stabilize reaction intermediates yet weak enough to facilitate their mobility and reaction turnover[20,21].

(2) Gibbs Free Energy and Theoretical Overpotential: The change of Gibbs free energy (ΔG) is a thermodynamic quantity that quantifies the energy change associated with the overall reaction under specific conditions. In the case of the O_2 reduction reaction (ORR), ΔG is a crucial descriptor for understanding the thermodynamic feasibility and spontaneity of the ORR. In this thesis, we have employed the following expression for the ΔG calculations[20,21]:

$$\Delta G = \Delta E_{ads} - T\Delta S + \Delta ZPE + \Delta G_U + \Delta G_{pH}$$

Here ΔE_{ads} is the reaction energy obtained from the DFT calculations, ΔZPE is the zero-point energy, and S is the entropy. ΔG_U = -eU where is the potential at the electrode, e is the charge transferred, and ΔG_{pH} = $K_B T \ln_{10} pH$, where K_B is the Boltzmann constant and T=298K. We have considered the Computational Hydrogen Electrode (CHE) model for the calculation of proton and electron free energies in processes involving electron and proton transfers. In this model, the standard hydrogen electrode (SHE) is used as a reference to determine the free energy of protons and electrons. To ensure the applicability of the SHE, the following reaction must be in equilibrium:

$$H^+ + e^- \longrightarrow \frac{1}{2} H_2$$

Under standard conditions, the chemical potentials of $\mu(H^+) + \mu(e^-)$ is equal to $\mu(\frac{1}{2}H_2)$. Therefore, the free energy of H_2 can be used as a substitute for the free energy of electrons and protons. It is important to note that while the equation above is valid under standard conditions (at 0 V potential and pH = 0), modifications are necessary to incorporate the effects of applied voltage and pH. In this thesis, the calculations have been done assuming U = 0V and pH = 0.

Let us consider the associative ORR path mentioned in Chapter 1, for the calculation of the ΔG values during the reaction. The ORR starts with the adsorption of the O_2 molecule and ends with the desorption of the water molecule. The associate route has three key ORR intermediates: OOH*, O*, and OH*. The ΔG during the formation of the ORR intermediates has been calculated by considering the O_2 + * as a reference state. The value of ΔG of the key intermediates has been calculated as follows:

$$\Delta G_{OOH^*} = G_{OOH^*} + 3(G_{H^+} + G_{e^-}) - [G_* + G_{O_2} + 4(G_{H^+} + G_{e^-})]$$

$$\Delta G_{O^*} = G_{O^*} + G_{H_2O} + 2(G_{H^+} + G_{e^-}) - [G_* + G_{O_2} + 4(G_{H^+} + G_{e^-})]$$

$$\Delta G_{OH^*} = G_{OH^*} + G_{H_2O} + (G_{H^+} + G_{e^-}) - [G_* + G_{O_2} + 4(G_{H^+} + G_{e^-})]$$

$$\Delta G_{H_2O} = G_* + 2G_{H_2O} - [G_* + G_{O_2} + 4(G_{H^+} + G_{e^-})]$$

and the ΔG of the adsorption of the O_2* can be calculated as

$$\Delta G_{O_2^*} = G_{O_2^*} - [G_* + G_{O_2}]$$

Where G_* and G_{OOH^*}, G_{O^*}, G_{OH^*} are the Gibbs free energy of the clean catalytic surface and the catalytic surface binding with OOH*, O*, and OH* intermediates, respectively. The relative free energy of each elementary reaction step can be defined as the difference between two adjacent steps and can be expressed as,

$$\Delta G_1 = \Delta G_{OOH^*} - \Delta G_{O_2^*}$$

$$\Delta G_2 = \Delta G_{O^*} - \Delta G_{OOH^*}$$

$$\Delta G_3 = \Delta G_{OH^*} - \Delta G_{O^*}$$

$$\Delta G_4 = \Delta G_{H_2O} - \Delta G_{OH^*}$$

The free energy diagram or potential energy surface (PES) of the ideal ORR electrocatalysts has been shown in Figure 2.11. The reaction intermediates of the ideal electrocatalyst have the relative free energy ΔG_{OOH^*} = -1.23 eV, ΔG_{O^*} = -2.46 eV, ΔG_{OH^*} = -3.69 eV, and ΔG_{H_2O} = -4.92 eV. For the overall ORR process, $O_2 + 2H_2 \longrightarrow 2H_2O$, at the standard conditions, the total change in Gibbs free energy should be -4.92 eV, as shown in Figure 2.11. From the free energy diagram of the ideal electrocatalysts, we can see that all the reaction steps are downhill, hence thermodynamically favorable. Thus, for an efficient ORR electrocatalyst, the reduction path in the PES should be in a downhill trajectory.

The catalytic activity of different electrocatalysts towards ORR can be estimated by determining the theoretical thermodynamical ORR limited potential (U_L) and theoretical overpotential (η). Within the CHE model, the highest potential at which all the reaction steps are downhill in the PES is called thermodynamic limited potential. In other words, the elementary step in PES with the highest ΔG value is called the potential determining step and can be expressed as U_L = max (ΔG_1, ΔG_2, ΔG_3, ΔG_4)/e. The η of the ORR under standard conditions can be defined as:

$$\eta = \frac{\max(\Delta G_1, \Delta G_2, \Delta G_3, \Delta G_4)}{e} + 1.23\ V$$

For an ideal electrocatalyst, the value of the U_L is -1.23 V at U=0 V, and the theoretical overpotential is 0 V. However, in practical conditions, the value deviates from the ideal conditions. In practical conditions, the activity and efficiency of the electrocatalysts towards ORR are benchmarked by comparing it with the very efficient electrocatalyst Pt (111), which has η = 0.43 V. Thus, the novel electrocatalyst is considered to be improved when it has $\eta \leq 0.43$ V ($U_L \geq$ 0.80 V).

(3) Surface-to-Volume Ratio and Electronic Properties: The study of the ORR in this thesis is mainly considered as a solid surface reaction that occurs on the surface of the electrocatalyst. In other words, the ORR mainly takes place at active sites that reside on the surface of the electrocatalyst. A high surface-to-volume ratio of an electrocatalyst is considered advantageous for good efficiency and performance during electrochemical reactions. A high surface-to-volume ratio ensures that more of the electrocatalytic surface is exposed to the reaction. This exposure

ensures that more active sites are available to participate in the reaction and potentially enhances electrocatalytic performance with activities. A large surface-to-volume ratio allows better diffusion of reactant molecules to the active sites and products away from them. This reduces the mass transport limitations, ensuring that a higher number of the reactant molecules can reach the catalytic surface and participate in the reaction. A higher surface-to-volume ratio also facilitates the electron transfer between the catalyst and the electrodes, leading to improved charge transport kinetics during the electrochemical reactions. Thus, the availability of more active sites, less mass transfer, and charge transfer limitations exists between the two phases participating in the electrochemical reaction, decreasing the activation energy required for the reaction to take place and leading to an overall speeding up of the kinetics of the electrochemical reaction. In the present

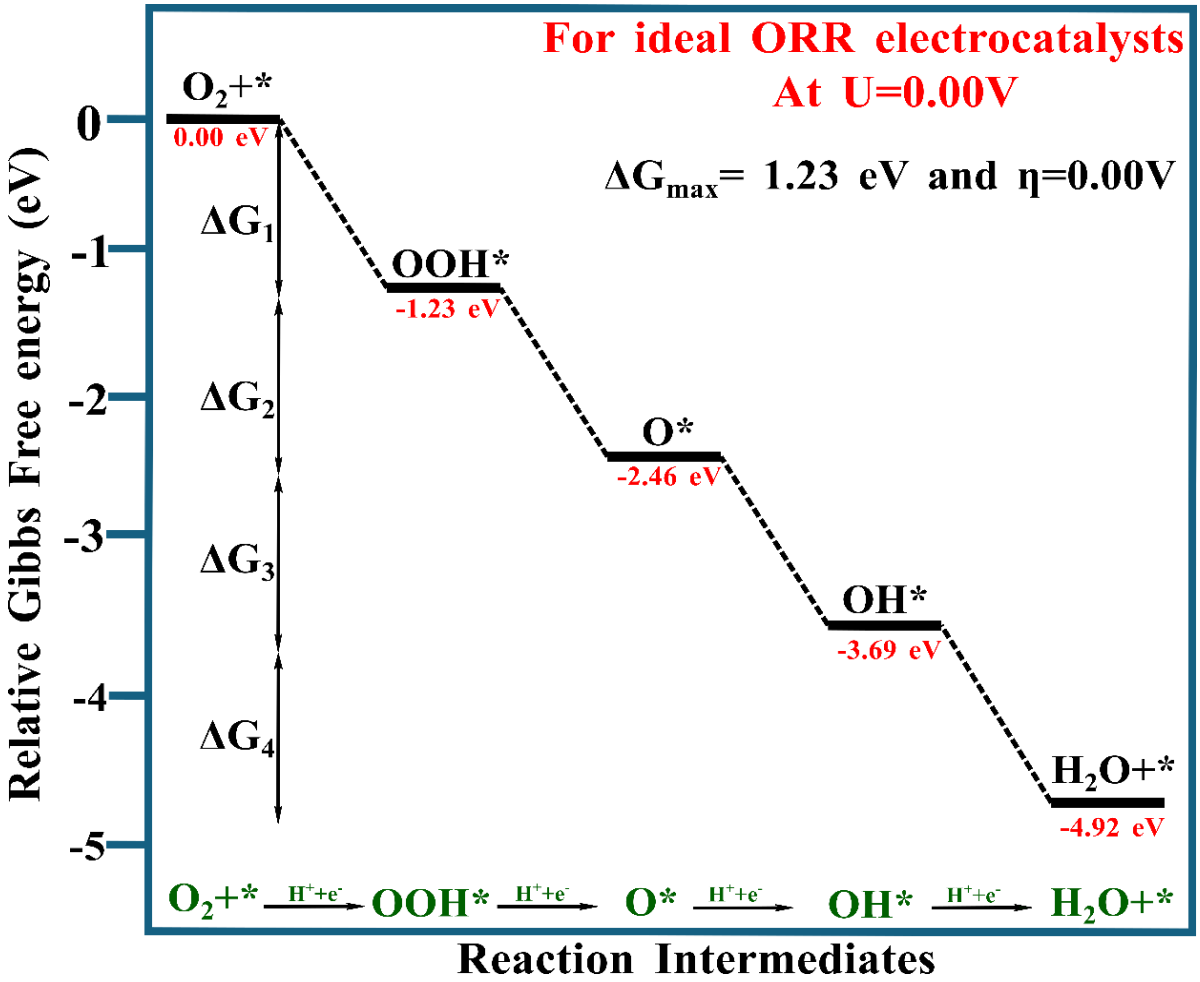

Figure 2.11. *The free-energy landscape of an ideal ORR electrocatalyst at U = 0 V (black lines) and the relative energies of each of the ORR intermediates have been indicated in red letters.*

thesis, we have considered 2D TMDs and carbon nanotubes as an electrocatalyst for ORR, which possess a high surface-to-volume ratio[22].

Another important factor called electronic properties of the electrocatalytic materials plays a crucial role in determining the efficiency of the electrocatalyst towards electrochemical reactions. Electrocatalysis, which occurs at the active site in electrical contact with the electrodes in the electrochemical cells, uses the flow of the electron as the driving force for many electrochemical reactions. The high electronic conductivity (metallic, semimetal, and semiconductors) can facilitate the electron transportation between the surface of electrocatalysts and the current collector (electrodes) and decreases the Ohmic potential drop and energy loss. Thus, electrocatalysts with favorable electronic properties (metallic, semimetal, and semiconductors) can have faster reaction kinetics and enhance the overall catalytic activity[23]. In this thesis, the electronic property analysis has been studied by computing the electronic band structure calculations and corresponding density of the states (DOS) profile of the electrocatalytic material. The electronic conductivities of materials are determined by the position of the valence band (VB) and conduction band (CB) in the band structure calculations. The forbidden area between VB and CB is referred to as the band gap, which is significantly influenced by the electronic states near the Fermi energy level (E_F). The density of states represents both occupied and unoccupied available states arising from the overlap of the atomic orbitals. The location of the E_F within the density of the state profile determines the electronic behavior of the electrocatalytic materials. In the insulator, the E_F lies within a large band gap from any available states. In the metal or semimetal, E_F lies within the delocalized band, and there is no electronic band. In an intrinsic and lightly doped semiconductor, the bands are sufficiently close to the E_F so that they can be populated by the thermal excitations of the electrons. In the present thesis, we have tuned the electronic properties of the 2D TMDs by doping the suitable metal atoms, and the electronic properties of the carbon nanotube have been tuned by the encapsulation of the metal nanocluster.

2.25 Instruments and Software Tools Used: In our research process, we have employed the following instruments and software tools:

(1) High-Performance Computing (HPC) clusters

(2) Software Packages (particularly CRYSTAL17 suite code)

(3) Computer workstation

(4) Visualization and analysis software (VESTA, Material Studio), high-quality graphics software (Inkscape), scripting and data analysis software (Python), and Plotting and visualizing data trends software (Gnuplot)

(5) Resources include Library databases and printing facilities

2.24 References:

[1] L. Wu, P. Liu, Z. Zhang, D. Zhu, H. Wang, Multiscale modeling for high-performance concrete: A review, Int. J. Multiscale Comput. Eng. 16 (2018) 267-283.

[2] L. Skubic, S. Gyergyek, M. Huš, B. Likozar, A review of multiscale modelling approaches for understanding catalytic ammonia synthesis and decomposition, J. Catal. 429 (2024) 115217.

[3] F. Giustino, (2014) Materials modelling using Density Functional Theory properties and predictions, First ed., Oxford University Press, UK (978–0–19–966243–2).

[4] P. Geerlings, F. De Proft, W. Langenaeker, Conceptual density functional theory, Chem. Rev. 103 (2003) 1793-1873.

[5] C. J. Cramer, (2004) Essentials of computational chemistry: theories and models, 2nd ed., John Wiley & Sons Ltd, England (0-470-09181-9).

[6] W. Kohn, L. J. Sham, Self-consistent equations including exchange and correlation effects, Phys. Rev. 137 (1965) A1697.

[7] R.O. Jones, Density functional theory: Its origins, rise to prominence, and future, Rev. Mod. Phys. 87 (2015) 897-923.

[8] N. Mardirossian, M. Head-Gordon, Thirty years of density functional theory in computational chemistry: An overview and extensive assessment of 200 density functionals, Mol. Phys. 115 (2017) 2315-2372.

[9] A. Erba, J. K. Desmarais, S. Casassa, B. Civalleri, L. Dona, I. J. Bush, B. Searle, L. Maschio,

L. Edith-Daga, A. Cossard, C. Ribaldone, E. Ascrizzi, N. L. Marana, J.-P. Flament and B. Kirtman, CRYSTAL23: A program for computational solid state physics and chemistry, J. Chem. Theory Comput. 19 (2023) 6891-6932.

[10] E. O. Bartaquim, R. C. Bezerra, A. F. B. Bittencourt, J. L. F. Da Silva, Computational investigation of van der Waals corrections in the adsorption properties of molecules on the Cu(111) surface, Phys. Chem. Chem. Phys. 24 (2022) 20294-20302.

[11] S. Grimme, S. Ehrlich, L. Goerigk, Effect of the damping function in dispersion corrected density functional theory, J. Comput. Chem. 32 (2011) 1456-1465.

[12] S. Grimme, J. Antony, S. Ehrlich, H. Krieg, A consistent and accurate ab initio parametrization of density functional dispersion correction (DFT-D) for the 94 elements H-Pu, J. Chem. Phys. 132 (2010) 154104.

[13] S. Grimme, A. Hansen, J.G. Brandenburg, C. Bannwarth, Dispersion-corrected mean-field electronic structure methods, Chem. Rev. 116 (2016) 5105-5154.

[14] R. Dovesi, A. Erba, R. Orlando, C. M. Zicovich-Wilson, B. Civalleri, L. Maschio, M. Rérat, S. Casassa, J. Baima, S. Salustro, B. Kirtman, Quantum-mechanical condensed matter simulations with CRYSTAL, Wiley Interdiscip. Rev. Comput. Mol. Sci. 8 (2018) e1360.

[15] www.crystal.unito.it/index.html

[16] E. R. Davidson, Basis set selection for molecular calculations, Chem. Rev. 86 (1988) 681-96.

[17] F. Jensen, Atomic orbital basis sets, Wiley Interdiscip. Rev. Comput. Mol. Sci. 3 (2013) 273-295.

[18] H. B. Schlegel, Geometry optimization, Wiley Interdiscip. Rev. Comput. Mol. Sci. 1 (2011) 790-809.

[19] P. Pulay, G. Fogarasi, Geometry optimization in redundant internal coordinates, J. Chem. Phys. 96 (1992) 2856-2860.

[20] M. Li, L. Zhang, Q. Xu, J. Niu, Z. Xia, N-doped graphene as catalysts for oxygen reduction

and oxygen evolution reactions: Theoretical considerations, J. Catal. 314 (2014) 66-72.

[21] J. Zhang, H. Bin Yang, D. Zhou, B. Liu, Adsorption energy in oxygen electrocatalysis, Chem. Rev. 122 (2022) 17028-17072.

[22] S. Sun, H. Li, Z.J. Xu, Impact of surface area in evaluation of catalyst activity, Joule 2 (2018) 1024-1027.

[23] Lakhanlal, M. Caspary Toroker, Filling the gaps on the relation between electronic conductivity and catalysis of electrocatalysts for water splitting using computational modelling, Curr. Opin. Electrochem. 40 (2023) 101342.

CHAPTER 3

Synergistic Niobium Doped Two-Dimensional Zirconium Diselenide: An Efficient Electrocatalyst for O_2 Reduction

The development of high-activity and low-price cathodic catalysts to facilitate the electrochemically sluggish O_2 reduction reaction (ORR) is very important to achieve the commercial application of fuel cells. This chapter specifically examines the electrocatalytic activity of the two-dimensional single-layer Nb-doped zirconium diselenide (2D Nb-$ZrSe_2$) toward ORR by employing the first principles-based dispersion-corrected density functional theory (DFT-D) method. The chapter begins by introducing the significance of the ORR in sustainable and renewable energy systems and the role of electrocatalysts in enhancing reaction efficiency. It then provides a detailed description of the methods and computational techniques employed to model and analyze the properties and electrocatalytic activity of the 2D Nb-$ZrSe_2$ system, including theoretical frameworks and simulation procedures. The final section presents and deliberates the results of computational experiments, exploring structural properties, electronic properties, and energetics of the 2D Nb-$ZrSe_2$ and ORR intermediates to analyze the electrocatalytic performance of 2D Nb-$ZrSe_2$ towards ORR. In the result section, we begin by examining the electronic properties of the 2D monolayer $ZrSe_2$, which depict that the 2D monolayer $ZrSe_2$ has a large band gap of 1.48 eV, which is not favorable for the ORR mechanism. After the doping of Nb, the electronic band gap vanishes, and 2D Nb-$ZrSe_2$ acts as a conductor. The section further addresses both the dissociative and associative reaction pathways through which the ORR can proceed to reduce the oxygen molecule (O_2). Our results show that the more

favorable path for O_2 reduction on the surface of the 2D Nb-$ZrSe_2$ is the $4e^-$ associative path. The detailed ORR mechanisms (both associated and dissociative) have been explored by computing the changes in Gibbs free energy (ΔG). All the ORR reaction intermediate steps are thermodynamically stable and energetically favorable. The free energy profile for the associative path shows the downhill behavior of the free energy vs the reaction steps, suggesting that all ORR intermediate structures are catalytically active for the $4e^-$ associative path and a high $4e^-$ reduction pathway selectivity. Finally, we wrap up the chapter by addressing the key results and findings, highlighting the potential of 2D Nb-$ZrSe_2$ as a cost-effective and efficient ORR catalyst for fuel cell applications. Therefore, 2D Nb-$ZrSe_2$ is a promising catalyst for the ORR, which can be used as an alternative ORR catalyst compared to expensive platinum (Pt).

3.1 Introduction: The escalating global population and the ongoing advancements in global industrialization and society have led to a significant surge in global energy demand, primarily met by depleting fossil fuels[1]. Consequently, the urgent need to address the energy crisis, pollution, and climate change has driven scientists and researchers worldwide to develop renewable, sustainable, eco-friendly, and highly efficient energy resources. Renewable energy systems like fuel cells and metal-air batteries offer efficient solutions to environmental challenges and growing energy demands[2]. Among alternatives to fossil fuels, fuel cells stand out due to their high conversion efficiency, reliable performance, rapid startup, low-temperature operation, and minimal emissions[3]. However, the widespread adoption of fuel cells is limited by the slow kinetics of the oxygen reduction reaction (ORR). So, today's demand is to develop active material that can serve as an efficient catalyst and assist in accelerating the kinetics of the cathodic reaction.

To date, platinum (Pt) and Pt-based materials serve as a suitable catalyst for the reduction of O_2 at the cathode in the fuel cell[4]. Moreover, a sizable overpotential higher than 0.20 V is observed, even with the state-of-art Pt-based catalyst[5]. The utilization of Pt catalysts accounts for approximately 40-50% of the total cost associated with fuel cell stacks[6]. So, the cost of the fuel cell imposes serious limitations on the commercialization of the fuel cell. Moreover, the shortage of noble metals in the earth's crust and their insufficient stability towards the byproducts hinder their widespread applications in modern science and technology. In this pursuit, researchers have explored various metals both in their pure state and through the process of alloying with other metals. Pt, Pd, Au, Ag, and Ni clusters are to be effective in catalyzing oxygen reduction in their

pure form[7]. Wang et al. have extensively documented the efficacy of synergistic Mn-Co catalysts in facilitating high-rate ORR[8]. Numerous recent studies have provided substantial evidence to support the exceptional catalytic properties of metal oxides and sulfides in the context of ORR, which gives efficiency as good as the state-of-the-art Pt/C catalyst[9,10]. Although metal catalysts have demonstrated excellent catalytic activity but considering the low availability of metal in the earth's crust and huge cost, the expansion of a cheap and efficient catalyst is a paramount need for realizing the practical applications of fuel cells.

Two-dimensional transition metal dichalcogenides (2D TMDs) have gained significant interest as a catalyst for electrochemical reactions due to their unique properties. The unique properties include a high surface-to-volume ratio that provides numerous active sites, planar covalent bonding that ensures excellent mechanical strength, resilience, and efficient heat dispersion, and tunable electronic properties that can be adjusted through defects, doping, and stress[11,12]. In the wide family of 2D TMDs, 2D MoS_2 has emerged as a highly investigated material due to its remarkable catalytic capabilities[13]. MoS_2 has been considered a promising non-noble HER catalyst, but only the edge site shows high HER activity[14]. In other words, experimental and computational studies confirm that the electrocatalyst activity of the MX_2 (where M is transition metal atoms and X is chalcogens) is closely correlated with the edge side while the basal plane with a large area is generally inactive[15,16]. To the best of our knowledge, the optimization of both active site and electronic properties of the 2D MX_2 electrocatalysis is highly required. As we know, the basal planes of the 2D TMDs constitute a large surface area; therefore, if the inert basal planes could be activated, high electrocatalytic activity would be expected. To activate the inert basal plane and tailor the electronic properties, various strategies have been developed, such as creating defects, metal doping, nonmetal substitution, strain engineering, phase engineering, etc. [17–20].

Among all the strategies, substitutional doping is considered a suitable technique as it provides long-term stability without degrading performance. The dopant atoms change the spin-density distribution around them, which would change the strength of O_2 adsorption and other reaction species. So, the ORR process can be performed on the surface of the 2D TMDs near the appropriate doping atoms. For instance, Xiao et al. theoretically demonstrated the favorable catalytic activity of the Co/Ni-doped 2D MoS_2 towards ORR[21]. Pumera et al. put forward the

idea that introducing Fe and Mn dopants into the 2D MoS_2 can promote its catalytic activity in the context of ORR[22]. Recently, Singh and Pakhira computationally analyzed that the 2D monolayer Pt-doped ZrS_2 exhibits a superior catalytic activity towards ORR[23]. Moreover, the doping of MoS_2 by heteroatoms such as P and N exhibits moderate adsorption strength of oxygen molecules and enhances the ORR[24,25]. In a recent study by Tain and Tang, it was discovered that the addition of Ni or Co to materials such as 1T-TiS_2, 2H-TiS_2, 1T-ZrS_2, 1T-NbS_2, and 2H-TaS_2 results in a promising electrocatalytic activity for the ORR. The overpotential required for ORR on these doped materials was found to be within the range of 0.32-0.55 V, which is comparable to that of the most advanced electrocatalysts currently available (i.e., Pt)[26]. It has been shown that the 2D monolayer $ZrSe_2$ is a new material of TMDs and has been successfully prepared experimentally and it has 1T phase as a stable structure[27]. Moreover, earlier predictions show that at low vacancy density, the $ZrSe_2$ and $ZrTe_2$ TMDs have a low value of hydrogen adsorption energy (ΔE_H), and the value of ΔG is very close to that of Pt[28].

In a recent theoretical study, Som and Jha showed an important observation regarding the catalytic activity of both the 2D single-layer ZrS_2 and $ZrSe_2$ materials. They found that the edge sites of these materials, rather than the basal planes, play a crucial role in accelerating the HER. To further enhance the HER kinetics, the researchers decided to introduce the Nb, Pt, and W dopants in both the 2D ZrS_2 and $ZrSe_2$ materials. Interestingly, they discovered that the 2D Nb-doped systems, namely Nb-ZrS_2 and Nb-$ZrSe_2$, exhibited a robust metallic nature, which significantly boosted their catalytic activity towards HER. Furthermore, they observed that, on the basis of ΔG calculations, 2D monolayer Nb-$ZrSe_2$ has the best catalytic activity towards HER[29]. In addition, 2D $ZrSe_2$ possesses important characteristics that make it a favorable choice. It is non-toxic, affordable, and exhibits strong resistance to corrosion. Furthermore, it has been successfully synthesized on a large scale and experimented with in the form of thin atomic layers[30]. In the context of sulfur/selenium-based ZrS_2 or $ZrSe_2$ TMDs, the presence of S or Se with a 2^- valence (S^{2-} or Se^{2-}) enhances the reduction capacity, thereby promoting the activity of the ORR.

Motivated by the extensive research attention and extraordinary catalytic activity of the Nb-doped $ZrSe_2$ toward HER, it is of fundamental interest to explore the more catalytic applications of the 2D Nb-$ZrSe_2$ towards ORR. In this work, a DFT-D calculation has been performed to explore the catalytic activity of the 2D monolayer Nb-$ZrSe_2$ towards ORR. In

principle, we have aimed to answer these questions: how does the doping of Nb alter the structural and electronic properties of the 2D monolayer $ZrSe_2$? Does the 2D Nb-$ZrSe_2$ catalyst act as an efficient ORR catalyst? If yes, which path will it follow to reduce the O_2? To answer these questions, we have analyzed the structural and electronic properties of the 2D Nb-$ZrSe_2$ and examined the changes of Gibbs free energy (ΔG) for all ORR intermediates at their minimum-energy condition. This study addresses some unique properties of the 2D monolayer Nb-$ZrSe_2$ and suggests that it can act as an efficient and useful catalyst for the ORR mechanism. Thus, this 2D Nb-$ZrSe_2$ can serve as an efficient cathodic material in fuel cells and metal-air batteries (MABs).

3.2 Theory, Methodology, and Computational Details:

The ORR has an essential role in the functioning of fuel cells. These electrochemical devices are designed to convert the chemical energy of the fuel, typically H_2, directly into electrical energy. The working principle of the fuel cell can be defined as follows: H_2 is produced by the electrocatalytic cell as fuel is brought into the anode side of the fuel cell. At the anode side, H_2 undergoes a reaction, resulting in the generation of electrons and protons[31]:

$$H_2 \longrightarrow 2H^+ + 2e^-$$

The protons (H^+) pass through the membrane while the accompanying electrons travel through the electric circuit. They combine at the cathode side of the fuel cell with oxygen. At the cathode, oxygen is reduced to water by reacting with H^+ and e^- through the electrochemical reaction[32]:

$$2H^+ + \frac{1}{2}O_2 + 2e^- \longrightarrow H_2O$$

All these processes rely on some electrochemical reactions. Among them, ORR is one of the reactions at the cathode that reduces the oxygen molecule to water. The detailed mechanism and possible reduction pathways have been elaborated in Chapter 1.

The catalytic potential of the 2D Nb-$ZrSe_2$ toward ORR has been investigated combinedly by computing and analyzing the adsorption energy with the values of relative Gibbs free energy (ΔG) of each intermediate species during the subject reaction. We used the computational hydrogen electrode (CHE) method to determine the adsorption energy and the values of ΔG of each intermediate. In this method, the energies are calculated under the standard conditions (pH = 0, p = 1 bar, T = 298.15 K, and U = 0 V). We have implemented the approach introduced by Nørskov et al. in our study. Their research showcased a significant finding that the chemical potential of $H^+ + e^-$ can be correlated with 1/2 H_2 in the gaseous state, which was determined using

the standard hydrogen electrode. Consequently, under the standard conditions, we can calculate the energy change of the reaction $A + H \rightarrow A + H^+ + e^-$ by employing the reaction $A + H \rightarrow A + 1/2\ H_2$[5]. The adsorption (or binding) energies (ΔE) presented in this study have been calculated as the energy difference between the energy of the model with adsorbed species [$E_{slab+adsorbate}$] and the energy of the catalytic model [E_{slab}] and the energy of the adsorbate [$E_{adsorbate}$] according to the following equation[33]:

$$\Delta E = E_{slab+adsorbate} - E_{slab} - E_{adsorbate}$$

The value of negative adsorption energy indicates that the adsorbed oxygen intermediates are attached to the catalytic surface stably. In other words, a negative adsorption energy signifies that the adsorbate is likely to bind energetically to the catalyst surface, indicating a favorable interaction between them. Therefore, negative adsorption energy is favorable for elementary reactions over the catalytic surface. The value of ΔG in each reaction step was evaluated as[34]:

$$\Delta G = \Delta E + \Delta E_{ZPE} + T\Delta S$$

where ΔE denotes the adsorption energy obtained from the DFT-D calculations of the equilibrium structures, and ΔE_{ZPE} and ΔS represent the change in zero-point energy and entropy correction, respectively. T denotes room temperature 298.15 K in this calculation. The overpotential, which is noted by η, is an important parameter that reflects the energy barrier for a given electrochemical reaction, such as ORR. The relationship $\eta = \Delta G_{max}/e^- + 1.23$ V is employed to calculate the overpotential where ΔG is the maximum change in Gibbs free energy of elementary steps during the O_2 reduction reaction and 1.23 Vs SHE is the thermodynamic potential[35].

For all the systems studied here (i.e., $ZrSe_2$, Nb-$ZrSe_2$, and ORR intermediates), the equilibrium atomic configuration, structures, electronic properties, and energetics were obtained by using the spin-unrestricted B3LYP DFT framework implemented in CRYSTAL17 suite code[36]. The hybrid functional B3LYP provides reasonable accuracy in the band gap calculations. It has a much lower computational cost and is easier to converge. Additionally, the inclusion of Grimme's "-D3" dispersion correction further improves the performance of the hybrid functionals. To account the weak nonbonding van der Waals (vdW) interactions between the reactants or intermediates and the interface, we incorporated the damped vdW dispersion correction (-D3) within the framework of density functional theory (DFT), specifically known as DFT-D3[37]. Ying et al. reported in their review article that the B3LYP hybrid functional improves the energy gaps of a variety of materials from bulk to surface[38]. Muscat et al.

established the reliability of the B3LYP hybrid functional to predict the band gap of a variety of materials using the local Gaussian basis set in CRYSTAL suite code or software. They claimed that the B3LYP hybrid functional reproduced observed band gap reliably in a wide range of materials, which are in good agreement with the experimental values and obtained from more sophisticated correlated calculations or perturbation theories[39]. By considering the advantages and reasonable accuracy, and the track record of the B3LYP hybrid functional in computational science, we employed the B3LYP hybrid functional. To utilize the hybrid functional, we used the "FMIXING" keyword to mix the FOCK/KS matrix, and we employed 80% FOCK/KS matrix mixing to maintain the accuracy of the calculations. A 2×2 supercell of the 2D monolayer structure of the pristine $ZrSe_2$ was considered and one Zr atom was substituted by one Nb atom to form the 2D monolayer Nb-$ZrSe_2$ structure, and all the ORR reaction steps on the surface of the 2D Nb-$ZrSe_2$ were investigated in the present study. We have utilized the Gaussian types of atomic basis sets to define the atomic orbitals, which have been found to yield more precise outcomes compared to plane wave basis sets[40]. In simpler terms, although the computational procedure differs from the plane wave code (i.e., VASP, Quantum Espresso), both approaches yield identical results. In the realm of hybrid density functionals, localized Gaussian basis set codes are inherently well-suited for addressing the Hartree−Fock (HF) component of the outcome[41]. For the Zr, Se, O, H, and Nb atoms, a triple-ζ valence polarized (TZVP) Gaussian basis set was used in the present calculations[42,43]. We employed a full optimization process, i.e., all atomic coordinates and lattice parameters were allowed to relax during geometry optimization. The convergence criterion for the self-consistent field (SCF) was established as a total energy difference of 10^{-7} a.u. between two consecutive iterations. The threshold controlling of the coulomb exchange integral calculation was controlled by the five-threshold sets 7, 7, 7, 7 (ITOL1 to ITOL4), and 14 (ITOL5) for both the geometry optimization and electronic property calculations. The CRYSTAL17 code utilizes the default threshold for geometry optimization on all atoms, employing specific values for maximum and RMS force (0.000450 and 0.00300 a.u., respectively) and maximum and RMS displacement (0.001800 and 0.001200 a.u., respectively). To ensure accurate 2D monolayer, i.e., SLAB calculations using the CRYSTAL17 code, we have established a separation of 500 Å in the normal surface direction of the 2D monolayer Nb-$ZrSe_2$ along the Z direction where there is no symmetry. This distance effectively prevents any spurious interactions between the periodic images of the monolayer slab. Our current calculations indicate that this separation is sufficient to mitigate any

undesired influences. While no computational tool is entirely exempt from limitations, we believe that our use of the CRYSTAL17 code is justified based on its track record. Numerous studies have been performed which provide a comprehensive overview of CRYSTAL's capabilities, algorithms, and validation of the outcomes against experimental data and other benchmark data[44,45]. These studies provide insights into code reliability. Furthermore, various applications of this code in the fields of solid-state chemistry and physics, quantum mechanics, and catalysis have been done. In this work, to ensure that the code CRYSTAL accurately captured the properties under investigation, we rigorously validated our results by comparing them with available experimental data and complementary calculations from other well-established codes. To perform the integration within the Brillouin zone, we have used 16×16×1 k-mesh in the Monkhorst pack scheme for the pristine 2D $ZrSe_2$, Nb-$ZrSe_2$, and all the reaction intermediates for both the geometry optimization and electronic property calculations[46]. The electronic band structure was constructed along the high-symmetrical k-path direction Γ-M-K-Γ of the corresponding irreducible Brillouin zone. All the equilibrium structures with the images were plotted by using VESTA software[47].

3.3 Results and Discussions: The equilibrium structure of the 2D monolayer $ZrSe_2$, which is the main object of this present work, belongs to the 1T phase (i.e., one atom of Zr is octahedrally coordinated by six atoms of Se) as shown in Figures 3.1 and 3.2. By using VESTA software, a 2D monolayer $ZrSe_2$ primitive cell was computationally designed, and a model system has been developed for further studies, and the structure was optimized by using the first principle-based periodic dispersion-correction hybrid DFT (DFT-D3, noted by B3LYP-D3) method as shown in Figure 3.1. The structure is a trigonal 2D slab system with $p\bar{3}m1$ layer group symmetry, and the computed unit cell parameters, i.e., the lattice constants are about a = b = 3.75 Å of the 2D pristine monolayer $ZrSe_2$, which is well consistent with the previously reported values[29]. Each unit cell consists of one Zr and one Se atom, as shown in Figures 3.1 and 3.2. Then, the doped system is constructed by substituting one Zr atom with one transition metal Nb per 2×2 supercell of the 2D monolayer pristine $ZrSe_2$ as illustrated in Figure 3.1. The doping was defined by the following equations:

$$\theta = \frac{number\ of\ doping\ atoms\ per\ 2 \times 2\ supercell}{number\ of\ total\ metal\ atoms\ in\ 2 \times 2\ supercell}$$

So, the Nb dopant atom amounts to 25% (only metal atom doping) atomic substitution per 2×2 supercell of the 2D $ZrSe_2$. The 2D monolayer 2×2 structure of the Nb-$ZrSe_2$ consists of one Nb, three Zr, and eight Se atoms per one unit cell, as represented in Figure 3.2. The 2D Nb-$ZrSe_2$ system is then fully relaxed with respect to both atomic coordinates and cell parameters by the same level of the DFT-D method during optimization. The equilibrium lattice parameters of the 2D Nb-$ZrSe_2$ were found to be = b = 7.38 Å, as represented in Figure 3.2. All the fully relaxed geometrical data of the 2D monolayer $ZrSe_2$ and Nb-$ZrSe_2$ material have been reported in Table 3.1 and represented in Figure 3.2. The ORR mechanism involves the movements of the electrons, i.e., the transfer or transportation of electrons is a key process during the electrochemical ORR mechanism. Previous studies have shown that the electronic properties (i.e., electronic band gap, band structure, and total density of states) of catalysts have a significant impact on their catalytic efficiency. The

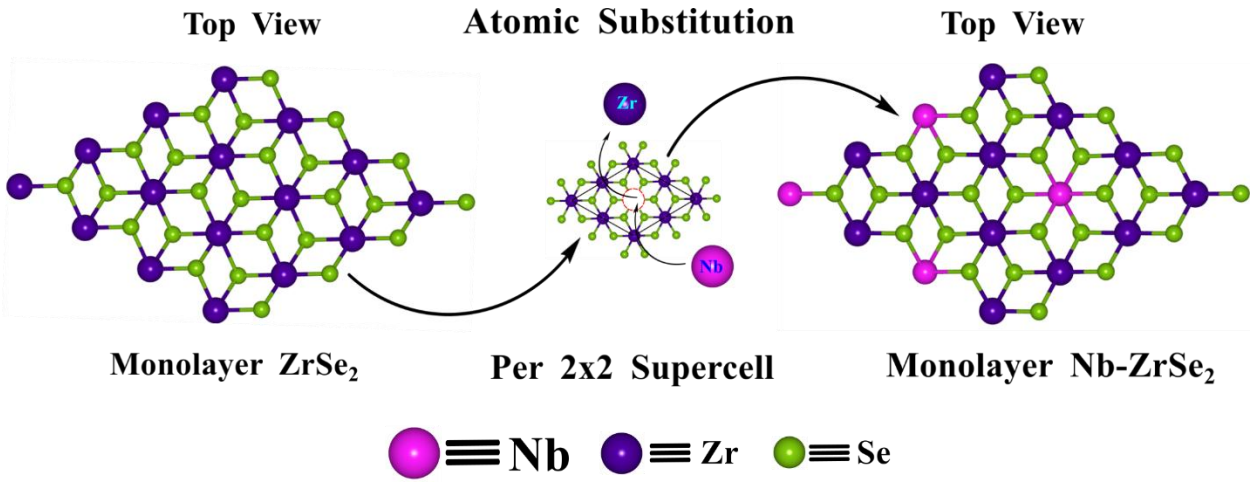

Figure 3.1. *Representation of the 2D monolayer $ZrSe_2$ and 2D monolayer Nb-$ZrSe_2$.*

electronic properties have been analyzed by computing and observing the electronic band structure and total density of states (DOSs) of both the 2D monolayer $ZrSe_2$ and Nb-$ZrSe_2$ materials. Analysis of the electronic properties can be useful to obtain information about electron distribution on the catalytic surface, which is useful to understand fully the catalytic performance of the catalyst. The electronic properties of the 2D monolayer $ZrSe_2$ and Nb-$ZrSe_2$ materials have been obtained by employing the same DFT-D theory. The electronic band structure of the pristine $ZrSe_2$ was plotted in the highly symmetric k-path direction Γ-M-K-Γ with respect to the vacuum. The highly symmetric path is shown in Figure 3.3a, and the equilibrium electronic structure of the 2D monolayer $ZrSe_2$ material is shown in Figure 3.3b (top and side view). The Fermi energy level

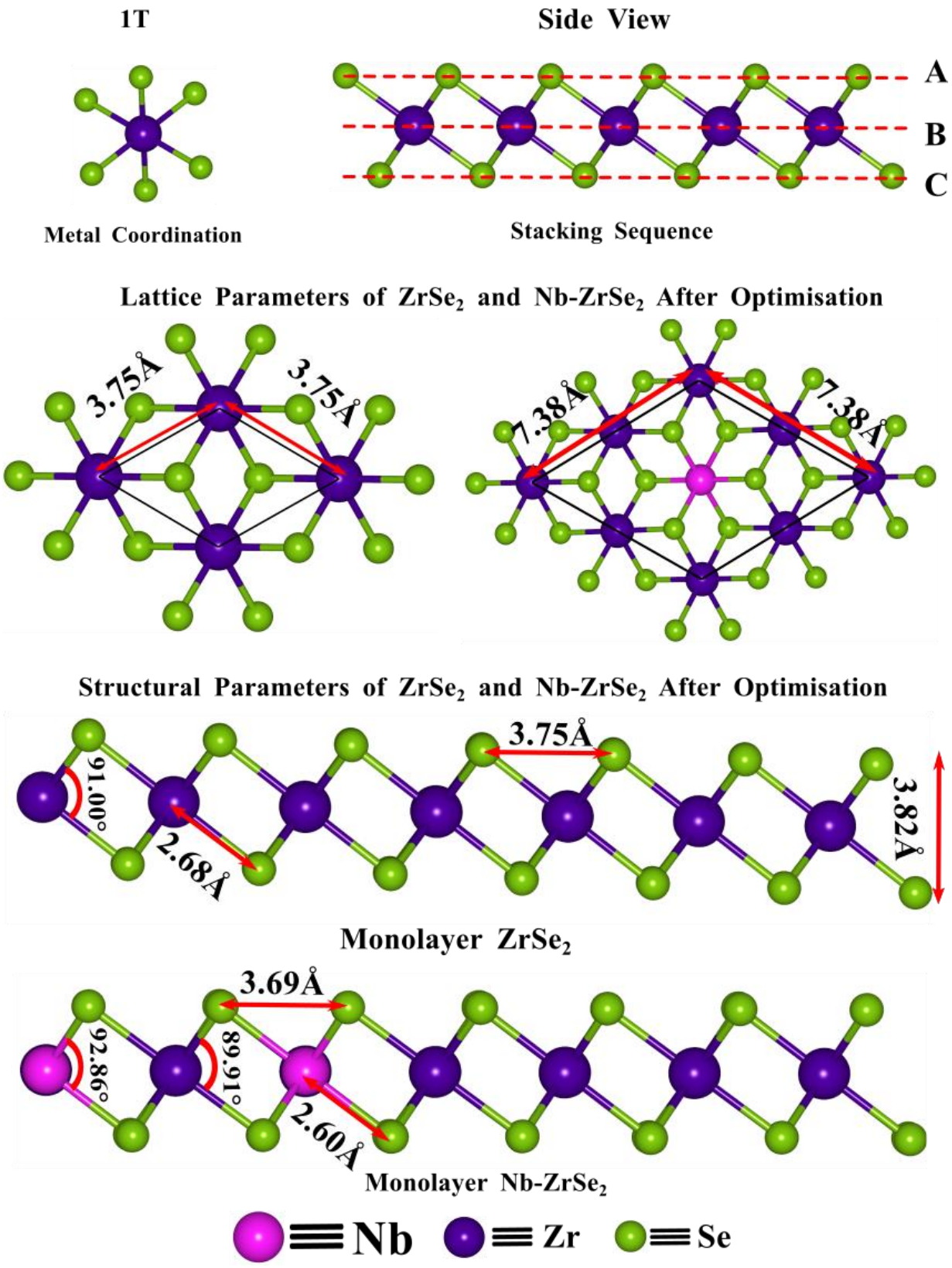

Figure 3.2. *Metal coordination, stacking sequence, unit cell, and structural properties of the $ZrSe_2$ and Nb-$ZrSe_2$.*

(E_F) of the pristine $ZrSe_2$ was found at the energy value of -5.34 eV, as shown by the dotted line in Figure 3.3c and d. The 2D single-layer $ZrSe_2$ material shows semiconducting characteristics with an indirect electronic band gap (E_g) of about 1.48 eV, as represented in Figure 3.3c. The DOSs has been computed by the same level of DFT-D theory, and the profile of DOSs supports the electronic band gap of the 2D pristine $ZrSe_2$, which was obtained by the electronic band structure calculations, as shown in Figure 3.3d. The calculated electronic band gap of the pristine 2D $ZrSe_2$ is consistent with the previously reported values[29]. Doping Nb in the pristine 2D monolayer $ZrSe_2$ (Nb-$ZrSe_2$) disrupts its symmetry and introduces additional unsaturated electrons. The equilibrium structure with the electronic properties of the 2D Nb-$ZrSe_2$ has been calculated at its equilibrium geometry by using the same level of the DFT-D theory as depicted in Figure 3.3e-g. This alteration leads to an augmented charge density in the basal plane of the 2D monolayer Nb-$ZrSe_2$, resulting in enhanced catalytic activity toward ORR. We have drawn the electronic band structure of the 2D Nb-$ZrSe_2$ along the highly symmetric *k*-path direction Γ-M-K-Γ like the pristine 2D monolayer $ZrSe_2$ material with respect to the vacuum for comparison. The E_F of the 2D Nb-$ZrSe_2$ was found at -4.87 eV, as represented by the dotted line in Figure 3.3f-h. The results from our present DFT-D analysis demonstrate that the introduction of Nb doping in the pristine 2D monolayer $ZrSe_2$ causes the energy gap to disappear, stemming in a zero-band gap where the bands are overlapped around the E_F, making it a conductor. In other words, the 2D Nb-$ZrSe_2$ has metallic characteristics, as shown in Figure 3.3f. The zero-band gap indicates easier electron transfer from the valence band to the conduction band. To support this, we computed the DOSs calculations using the same level of DFT-D theory. The DOSs profile shows that there is sufficient carrier concentration about the E_F, as shown in Figure 3.3g. An increased concentration of electrons near the E_F enhances electronic conductivity, thereby facilitating faster electron transfer to the reactants during the process of ORR. The carrier density around the E_F mostly comes from the dopant (Nb) d-subshell electron density of states. Based on our analysis of partial density of states (PDOS) calculations, we have successfully established the influence of the d-subshell electron density of states of the Nb atom on the carrier concentration around the E_F, as depicted in Figure 3.3h. The contributing component of the d-subshell electron density of the Nb atom in the total DOSs has been computed to examine the conducting properties of the material where the d-subshells electron density of states of the Nb atom follows the locus of the total DOSs of the 2D monolayer Nb-$ZrSe_2$ material. In other words, this indicates that the d subshell electrons of the Nb atom regulate and

tune the electronic properties of the 2D monolayer Nb-$ZrSe_2$ material, which may enhance the electrocatalytic activities of the material. The distinctive electronic characteristics of the 2D monolayer Nb-$ZrSe_2$ can be summarized as follows: (1) the rapid transfer of charges is facilitated by the presence of continuous band states in close proximity to the E_F; (2) enhanced electron mobility can be observed due to the significant density of states surrounding the E_F; (3) the metallic properties of the 2D monolayer Nb-$ZrSe_2$ contribute to accelerate charge transfer leading to improve the ORR activity. Considering the previous studies of the ORR mechanism on TMDs, the surface chalcogen atomic layer takes part in the reduction process of the molecular oxygen (O_2). Recently, Upadhyay and Pakhira investigated the ORR mechanism on the surface chalcogen (Se) atomic layer of the 2D

Table 3.1. *The equilibrium structural properties of the 2D monolayer $ZrSe_2$, 2D monolayer Nb-$ZrSe_2$, and comparison with previously reported data.*

System	Lattice parameters (Å)	Interfacial angle in degree	Layer group and symmetry	Average bond length		References
				Zr-Se (Å)	Nb-Se (Å)	
$ZrSe_2$ monolayer	a=b=3.75	a=β=90˚ γ=120˚	$p\bar{3}m1$	2.68	-	This work
$ZrSe_2$ monolayer (previously reported)	a=b=3.77	a=β=90˚ γ=120˚	$p\bar{3}m1$	2.70	-	[29,30]
Nb-$ZrSe_2$ monolayer	a=b=7.38	a=β=90˚ γ=120˚	*P1*	2.67	2.60	This work

monolayer Pt-$MoSe_2$ using DFT-D methods[48]. So, in the case of TMDs, it can be concluded that the surface chalcogen atomic layer is the active center of the catalyst during the electrochemical ORR mechanism. In this work, we have investigated the ORR mechanism in an acidic media, where the protons (H^+) and electrons (e^-) transfer take place simultaneously on the ORR adsorbates to reduce the O_2. We considered the Se site as an active site (near the Nb-doped region) for the

ORR adsorbates including the O_2*, 2O*, OOH*, O*, and OH*. The ORR mechanism was started by analyzing the interaction of O_2 with the active site Se of the 2D monolayer Nb-$ZrSe_2$. The adsorption of O_2 with the active site is the crucial step to initiate the ORR process and significantly affects the catalytic activity of the material. Here, we calculated the adsorption energy of the O_2 molecule by taking the difference between the electronic energy of the absorbed Nb-$ZrSe_2$ of the O_2 denoted by the O_2*_Nb-$ZrSe_2$ with the electronic energy of isolated 2D Nb-$ZrSe_2$ and the gaseous state of the O_2 molecule. The adsorption energy of O_2 should not be too positive or too negative for a good electrocatalyst[23,48]. The higher positive adsorption energy value between O_2 and the active site (called the O_2-active site interaction) depicts that it is not able to capture the O_2 molecule. In other words, the higher and positive value of O_2 adsorption energy (around the active center) leads to poor adsorption of O_2 molecules, so it is very difficult to start the ORR process. A very negative adsorption energy value between O_2 and catalyst is not ideal for the ORR mechanism because a very strong O_2-active site interaction may lead to the occupation of the active site by the O_2 molecule and hinder the further reaction steps[23,48,49]. Thus, very large positive and negative values of the O_2 adsorption energy around the active site of the catalyst diminish the electrocatalytic activity of the material toward the ORR process. So, the adsorption energy of O_2 should be optimum to efficiently start the ORR on the catalytic surface. Based on the above discussion, we computed the O_2 activation energy, which could be a good descriptor of the catalytic activity of the 2D monolayer Nb-$ZrSe_2$ toward ORR. In other words, the determination of the optimal value of O_2 adsorption energy on the Nb-$ZrSe_2$ surface plays a crucial role in initiating the ORR process. For an ideal condition, the adsorption energy of O_2 on the catalytic surface should be close to zero, which is not the case in real life. Noble metals, such as Pt, are considered the best catalyst to date for electrochemical reactions, especially for ORR. So, for practical applications, the O_2-active center interaction energy for a good catalytic candidate should be close to or slightly weaker than that of the Pt. Chen et al. reported that the Pt-based catalyst shows good ORR reactivity and, therefore, can be used as a reference to evolute the catalytic activity of other materials. The O_2 adsorption energies on the Pt (111) and Pt (100) surfaces were found to be -0.69 eV and -1.10 eV, respectively[50,51]. It was found in the present calculations that O_2 adsorption energy on the surface of the 2D monolayer Nb-$ZrSe_2$ was about -0.15 eV which is smaller than that of the O_2-active site interaction energy of Pt. Thus, this negative and small adsorption energy of

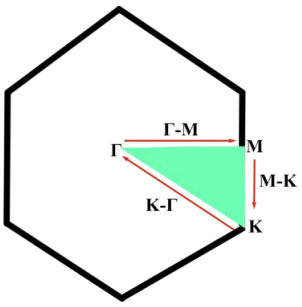

(a) Hexagonal Brillouin Zone of Unit Cell With High Symmetry Points

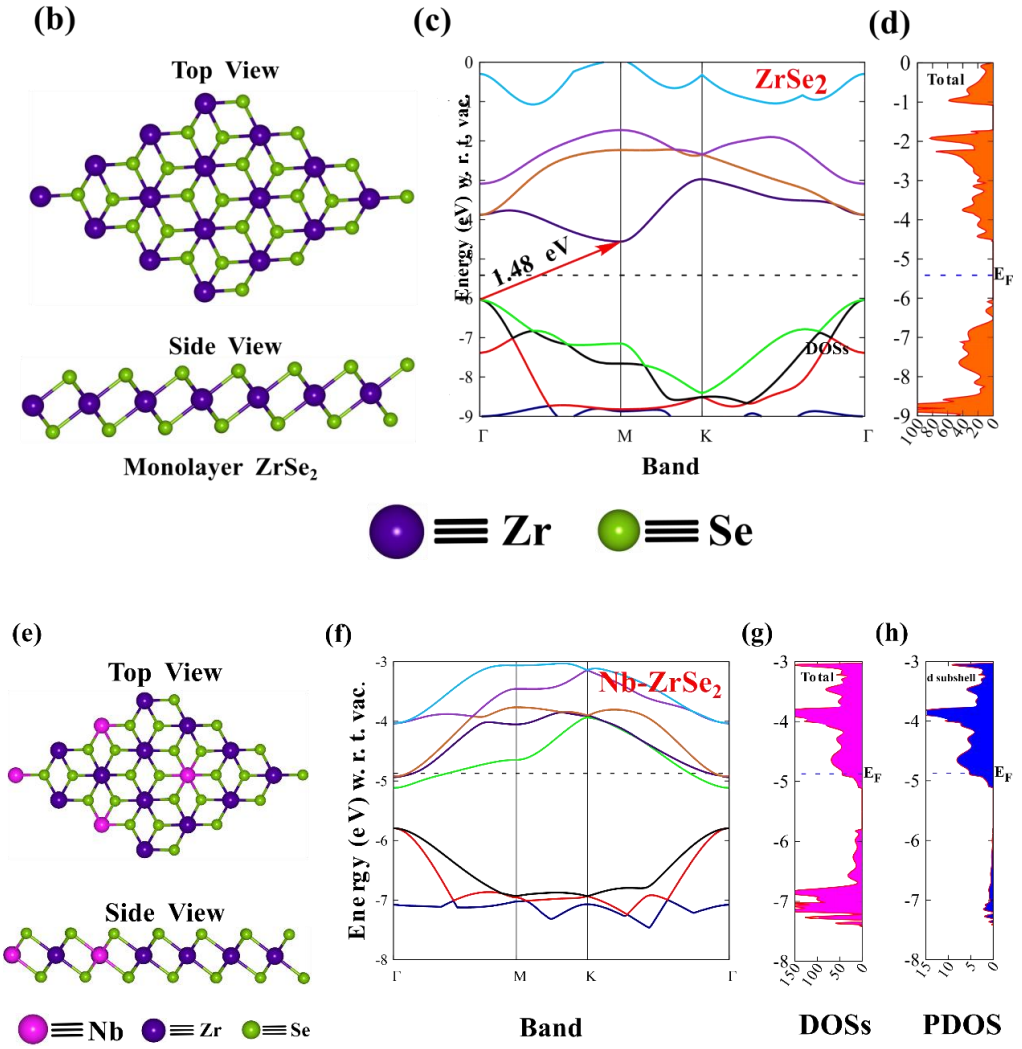

Figure 3.3. *(a) Brillouin zone with high symmetry k-points, (b) top and side view of equilibrium structure of the monolayer $ZrSe_2$, (c) band structure, (d) total DOSs of the monolayer $ZrSe_2$, (e) top and side view of the equilibrium structure of the monolayer Nb-$ZrSe_2$, (f) band structure of the monolayer Nb-$ZrSe_2$, (g) total DOSs of the Nb-$ZrSe_2$, and (h) contribution of d subshell of Nb in the total DOSs.*

O_2 suggests that the 2D monolayer Nb-$ZrSe_2$ can be energetically favorable for electrochemical ORR to proceed further, which indicates that the 2D monolayer Nb-$ZrSe_2$ material would show an efficient catalytic activity toward ORR.

Now, the removal of the water (H_2O) molecule is the last step of the ORR mechanism. After the removal of the H_2O molecule, the new ORR cycle of the ORR mechanism starts. So, suitable H_2O adsorption energy is essential during the ORR mechanism. The adsorption energy of H_2O on the catalytic site should not be too large. The adsorption energy of the H_2O molecule was found to be -1.54 eV on the Se-site, as depicted in Figure 3.4. This value might seem like moderate adsorption energy (not too large) in one context, and it could be favorable for a particular reaction mechanism, as in the case of the subject reaction. This value may not appear extremely small in isolation; it is indeed a suitable moderate value for the ORR mechanism. This value supports the efficient adsorption, reaction, and subsequent desorption of H_2O molecules, enabling the catalytic site to remain accessible and active throughout multiple cycles of the ORR. This means that the Se site remains accessible for the subsequent cycles of the ORR. Moreover, the favorable adsorption energies of O_2 and H_2O on the Se site of the 2D Nb-$ZrSe_2$ indicate that this material has the potential to serve as an effective catalyst for converting O_2 into H_2O during the reduction process. Now, after the adsorption of the O_2 molecule, which is the initial step of the ORR mechanism, ORR can proceed via two ways. The path of the ORR mechanism depends on how the O-O bond cleaves. The first way is called the associative path, which involves both the proton and electron transfer simultaneously to form OOH species, then followed by the successive protonation steps to reduce O_2. The second path is known as the dissociative path, which involves the breaking of the O-O bond after the adsorption of the O_2 molecule into two O atoms on the active site of the catalytic surface. In this work, we have studied both possible pathways of the ORR mechanism on the surface of the 2D monolayer Nb-$ZrSe_2$. We computed the adsorption energy of the reaction intermediates with the active site Se of 2D Nb-$ZrSe_2$ for both associative and dissociative reaction pathways. The adsorption energy for the hydrogenation of O_2* into the OOH* species during the associative reaction was found to be -0.18 eV obtained by the DFT-D calculation, as represented in Figure 3.4b. The adsorption energy of the dissociative pathway (i.e., dissociation of the adsorbed O_2* into 2O*) was found to be 1.94 eV, i.e., the dissociation energy of O_2*. According to computed adsorption energy, the associative pathway is more energetically favorable than that of the dissociative pathway. The adsorption energy for the associative pathway

(O_2* → OOH*) indicates

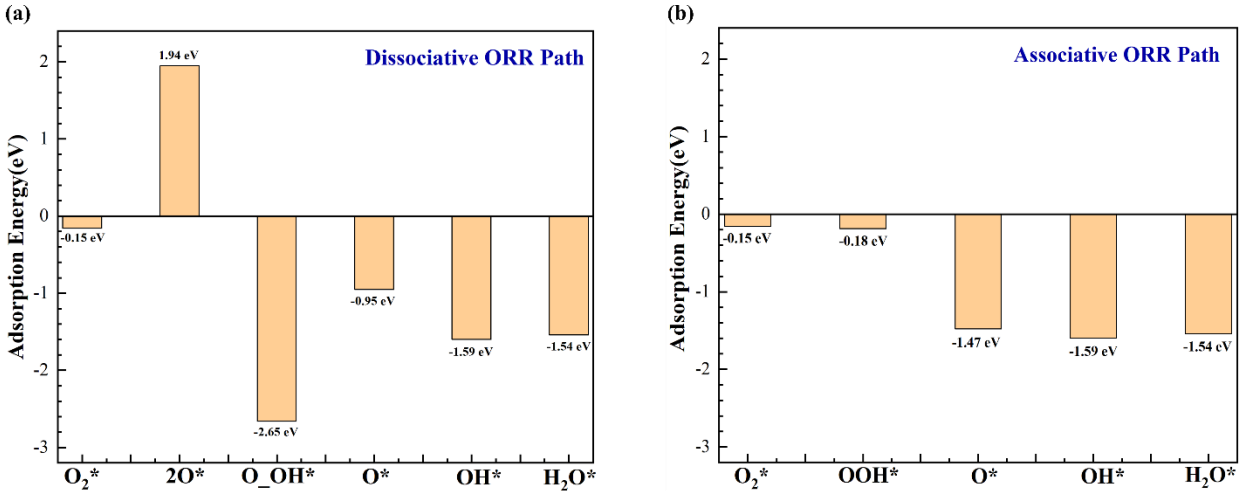

Figure 3.4. *Graphical representation of adsorption energy of the various ORR intermediates in (a) dissociative, and (b) associative mechanism.*

that the OOH* species is stably adsorbed on the Se site of the 2D Nb-$ZrSe_2$. As the adsorption energy of the associative path (-0.18 eV) is close to zero, i.e., very small and negative, we consider the associative ORR path to be thermodynamically favorable and feasible. Thus, we believe that the associative reaction path is energetically more favorable and efficient for catalyzing O_2 molecules. The associative reaction path is represented as O_2* + H^+ + e^- → OOH*. The large positive adsorption energy of dissociation of the O_2 molecule to the atomic O indicates that this step is not stable and would be greatly suppressed by the associative 4e^- mechanism. A positive adsorption energy implies that the dissociation of O_2 is not energetically favorable, which hinders the progression of subsequent reaction steps. So, the whole ORR mechanism will proceed as O_2* → OOH* → O* + H_2O → OH* → H_2O. The adsorption energy of all ORR intermediates has been calculated by the same level of theory. The graphical representation of the adsorption energy of all intermediate steps is shown in Figure 3.4a-b. For all the intermediate states involved in the associative path, the adsorption energy is negative and optimum, revealing highly exothermic characteristics and thermodynamically favorable. We also computed the adsorption energy for all the ORR intermediates that occur in the dissociative ORR pathway, as represented in Figure 3.4a. From the above discussion, we can conclude that the ORR mechanism on the surface of the 2D monolayer Nb-$ZrSe_2$ material will follow the 4e^- associative mechanism. To further analyze the catalytic activity of the 2D monolayer Nb-$ZrSe_2$ toward ORR, we have computed the values of ΔG for each intermediate reaction step. In this work, we have calculated the values of ΔG by

computing the harmonic vibrational frequency of each intermediate step of the ORR mechanism using the CRYSTAL17 code. We will discuss the ΔG, structural properties, and electronic properties of each reaction intermediate step involved in both associative and dissociative mechanisms during the ORR.

3.4 Reaction Intermediate Steps Involved in Associative Mechanism:

First Step. The first step of the ORR mechanism, irrespective of the path, is the adsorption of O_2 onto the reaction site of the 2D monolayer Nb-$ZrSe_2$ slab. To model this step, we placed an O_2 molecule on the surface near the Nb atom in the 2D Nb-$ZrSe_2$ at a distance1.60 Å, which is equal to the equilibrium bond length of the Se-O. The same DFT-D method has been employed to perform the geometry optimization of the 2D Nb-$ZrSe_2$ with an O_2 molecule attached to the Se site (represented as O_2*_Nb-$ZrSe_2$). The equilibrium structure of the O_2*_Nb-$ZrSe_2$ has been represented in Figure 3.5(1a) (top and side view). We analyzed and calculated the intrinsic electronic characteristics of the equilibrium structure O_2*_Nb-$ZrSe_2$. To gain insights into the electronic properties, we calculated the electronic band structure and DOSs of the equilibrium structure O_2*_Nb-$ZrSe_2$ as depicted in Figure 3.5(1b) and 3.5(1c), respectively. We have drawn a total of eight bands around the E_F, which are sufficient for collecting the electronic behavior of the O_2*_Nb-$ZrSe_2$. We calculated the band structure of the O_2*_Nb-$ZrSe_2$ along the Γ-M-K-Γ high symmetry ***k***-vector direction with respect to vacuum, which is consistent with the 2D Nb-$ZrSe_2$ band structure with the band pathway along the same ***k***-vector direction for comparison. The E_F was found at -4.94 eV, as represented by the dotted line in Figure 3.5(1b-1c). From the band structure calculations, we observed that some of the electronic bands overlap around the E_F. Thus, the band structure of the O_2*_Nb-$ZrSe_2$ predicts the conducting nature of the O_2*_Nb-$ZrSe_2$ system. To confirm the conducting nature of the O_2*_Nb-$ZrSe_2$, we computed and analyzed the DOSs of the O_2*_Nb-$ZrSe_2$. According to the DOSs profile, there appears to be an ample amount of electron density surrounding the E_F, as shown in Figure 3.5(1c). Therefore, the intermediate O_2*_Nb-$ZrSe_2$ has metallic characteristics. After optimization, the equilibrium Se-O and O-O bond lengths were

Table 3.2. *The equilibrium geometrical data of the ORR intermediates involved in associative and dissociative mechanisms.*

Reaction steps	Average bond length (Å)

	Lattice parameters (Å)	Interfacial angle (°)	Layer group and symmetry	Electronic band gap (eV)	Zr-Se	Nb-Se	Se-O	Se-OH
Nb-$ZrSe_2$	a=7.38, b=7.38	a=β=90 γ=120	*P1*	0	2.67	2.60	-	-
O_2*_Nb-$ZrSe_2$	a=7.37, b=7.38	a=β=90 γ=120.01	*P1*	0	2.67	2.58	1.69	-
2O*_Nb-$ZrSe_2$	a=7.39, b=7.35	a=β=90 γ=120.36	*P1*	0	2.66	2.60	1.67	1.67
OOH*_Nb-$ZrSe_2$	a=7.39, b=7.40	a=β=90 γ=120.20	*P1*	0.66	2.66	2.66	2.00	-
O*_OH*_Nb-$ZrSe_2$	a=7.39, b=7.43	a=β=90 γ=120.32	*P1*	1.39	2.68	2.61	1.72	1.77
O*_Nb-$ZrSe_2$	a=7.37, b=7.41	a=β=90 γ=120.13	*P1*	0	2.67	2.60	1.67	-
OH*_Nb-$ZrSe_2$	a=7.38, b=7.40	a=β=90 γ=120.10	*P1*	0.66	2.65	2.61	1.87	-

found to be 1.67 Å and 2.20 Å, respectively. We observed an increased bond length of the O-O bond as compared to the free O_2 molecule bond length (1.21 Å) by the amount of 0.99 Å after the adsorption onto the surface of the Nb-$ZrSe_2$, as represented in Figure 3.6. The type of oxygen molecule is crucial for ORR. Usually, O_2 molecules have two bond states, singlet ($^1O_2$, metastable) and triplet ($^3O_2$ ground state), where $^1O_2$ has a very short lifespan and has 0.98 eV higher energy than $^3O_2$[52,53]. Therefore, O_2 is involved in the oxygen electrocatalysis in fuel cells and the electrochemical water splitting is specifically considered to be completely in its triplet ground

state[54]. The electron spin alignment facilitates the creation of spin, a selective channel to promote spin conversion during the reaction, which provides an opportunity to lower the reaction energy barrier by controlling the spin polarization of the catalyst[55]. The adsorption and activation of the triplet O_2 molecule should involve charge transfer from the catalytic site to the antibonding π^* orbital of O_2. Such an orbital interaction on the present system arises from the interaction of the ligands Se site orbital of the Nb-$ZrSe_2$ and π^* orbital of adsorbed O_2 on the surface of the Nb-$ZrSe_2$. We have employed the Mulliken charge transfer analysis by including the "PPAN" and spin polarization calculation by including the keyword "SPIN" in the calculations. The optimized geometry of the O_2*_Nb-$ZrSe_2$ suggests the charge transfer of 0.64 |e| from the Se site to the adsorbed O_2 molecule. The charge transfer thus resulted in the elongation of the equilibrium bond length of the O_2 molecule to 2.20 Å as compared to the free optimized O_2 bond length (1.21 Å). Thus, the charge transfer and bond elongation of the O_2 molecule are responsible for the activation of the O_2 molecule on the surface of 2D Nb-$ZrSe_2$. The increment in the bond length and charge transfer indicates that the O_2 molecule is activated and is available for the next ORR steps. The value of ΔG during the reaction $O_2 + * \rightarrow O_2*$ was found to be -0.10 eV. The negative value of ΔG indicates that the reaction is exothermic. Thus, the negative and small value of ΔG suggests that the adsorption of O_2 on the active site is thermodynamically stable and kinetically feasible for the ORR mechanism.

Second Step. The next step (in the $4e^-$ transfer associative reaction mechanism of the subject reaction) is the hydrogenation of adsorbed activated oxygen molecule around the Se site near the Nb atom. To model this ORR intermediate, we have placed one H atom near the one O atom, and the present DFT-D study has found that the equilibrium O-H distance is about 0.97 Å from the outer O atom in the O2*_Nb-$ZrSe_2$. Here, we have assumed that an H^+ coming from the anode side through a proton exchange membrane and an e^- coming through an external circuit reacts with the adsorbed O_2 molecule to form an OOH (noted by OOH*_Nb-$ZrSe_2$). The full geometry optimization (i.e., atomic coordinates and lattice parameters) of the so formed system of the OOH*_Nb-$ZrSe_2$ reaction intermediate was performed by employing the same DFT-D method, and the equilibrium structure of the OOH*_Nb-$ZrSe_2$ intermediate is shown in Figure 3.5(2a) (top and side view). We computed and examined the electronic properties of the OOH*_Nb-$ZrSe_2$ using the same DFT-D method. The E_F was found at -5.42 eV, as shown by the dotted line in Figure 3.5(2b−2c). The band structures of the OOH*_Nb-$ZrSe_2$ depict the semiconducting nature

of the OOH*_Nb-$ZrSe_2$ reaction intermediate with an indirect band gap of 0.66 eV. The conduction band minima and the valence band maxima of the OOH*_Nb-$ZrSe_2$ are located as Γ- and M- points, respectively. The DOSs corresponding to the band structures of the OOH*_Nb-$ZrSe_2$ were also calculated and plotted by using the same DFT-D method, as shown in Figure 3.5(2c). The DOSs plot is very consistent with the band structures, and this computation supports the band gap of the OOH*_Nb-$ZrSe_2$ intermediate. The value of ΔG during the reaction $O_2^* + H^+ + e^- \rightarrow$ OOH* was found to be 0.13 eV. This positive value of the ΔG indicates the endothermic nature of the reaction. The value of ΔG is close to zero, which suggests a thermodynamically favorable process and proceeds for the further reaction steps.

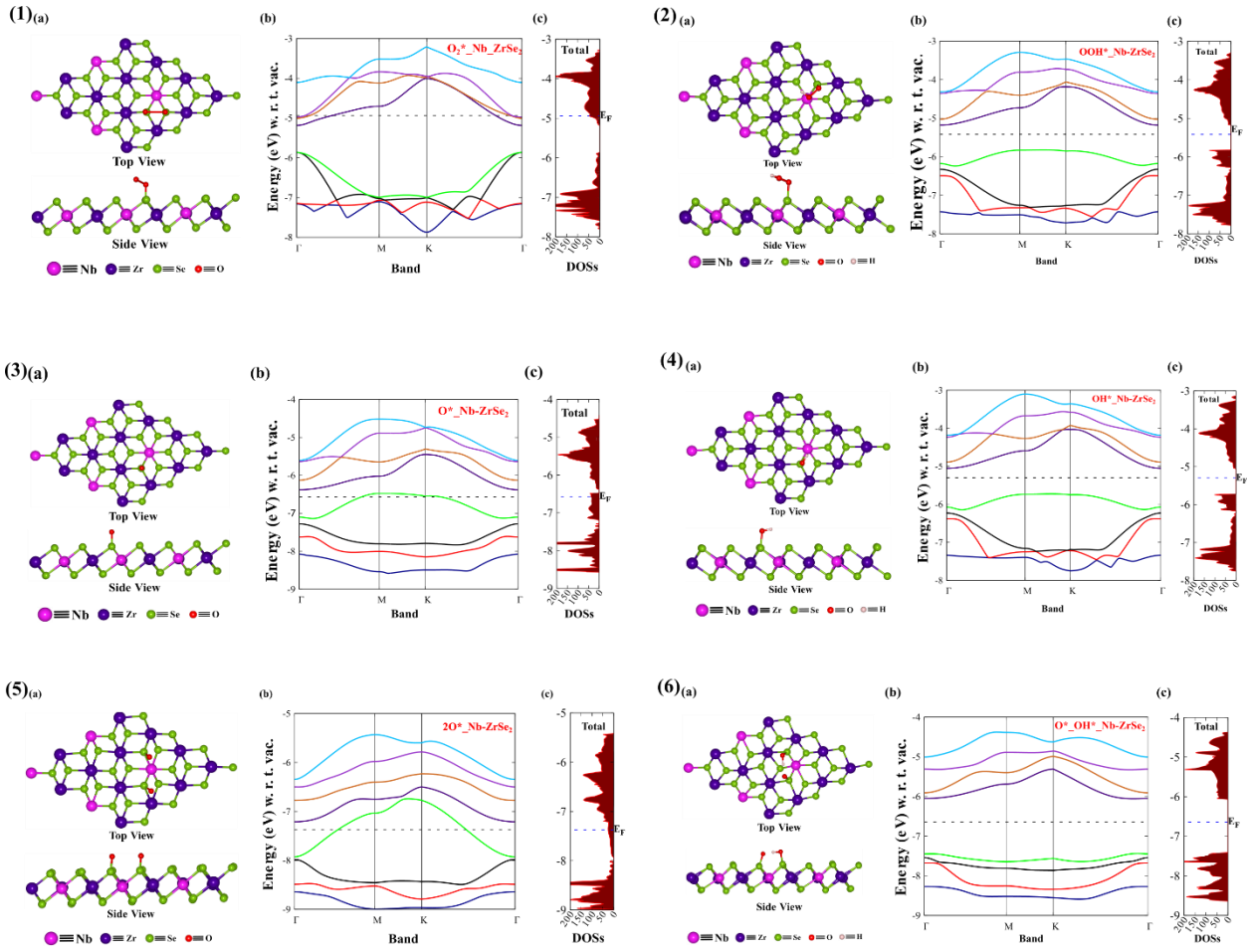

Figure 3.5. *(a) Top and side view of equilibrium structure, (b) band structure, and (c) total DOSs of (1) O_2*_Nb-$ZrSe_2$, (2) OOH*_Nb-$ZrSe_2$, (3) O*_Nb-$ZrSe_2$, (4) OH*_Nb-$ZrSe_2$, (5) 2O*_Nb-$ZrSe_2$ and (6) O*_OH*_Nb-$ZrSe_2$.*

Third Step. The next step of $4e^-$ associative mechanism is the reduction of OOH* into O* through the process of hydrogenation of the reaction intermediate OOH*_Nb-$ZrSe_2$. We assume that a

proton (H^+) coming from the anode side through proton exchange membrane and simultaneously, electron (e^-) flow through an external circuit, reacts with OOH* to form O* intermediate species. We have modeled this intermediate state by placing an oxygen atom at a distance of 1.62 Å from the Se site, which is close to the equilibrium bond length of Se-O. The full optimization (lattice parameters and atomic coordinates) of the reaction intermediate O*_Nb-$ZrSe_2$ was performed and the equilibrium 2D layer structure (top and side view) of the O*_Nb-$ZrSe_2$ is represented in Figure 3.5(3a). Figure 3.5(3b-3c) represents the electronic band structure and DOSs profile of the O*_Nb-$ZrSe_2$ computed by the DFT-D method. The E_F of the O*_Nb-$ZrSe_2$ system was found at -6.57 eV as shown by the dotted line in Figure 3.5(3b-3c). From the band structure calculations of the O*_Nb-$ZrSe_2$ intermediate, it has been found that some of the energy bands cross the E_F, which indicates the metallic nature of the O*_Nb-$ZrSe_2$. The DOSs calculations of the O*_Nb-$ZrSe_2$ show that there is electron density around the E_F, as shown in Figure 3.5(3c). So, both the band structure and the DOSs profile show the metallic nature of the O*_Nb-$ZrSe_2$, which supports the transportation of electrons involved in this reaction step. The value of ΔG in this reaction step (OOH* → O*) was found to be -1.82 eV. The negative value of ΔG reveals a highly exothermic character of this reaction. This intermediate reaction step is thermodynamically stable and energetically favorable for the ORR mechanism.

Fourth Step. The next step of the $4e^-$ associative mechanism is the hydrogenation of the O*_Nb-$ZrSe_2$ intermediate by reacting with H^+ and e^- coming from the anode side of the fuel cell. We assume that O* at the Se site captures one H^+ and e^- to form OH* species. To model this intermediate state, we put an H atom at a distance 0.90 Å from the O atom, which is the equilibrium bond distance of a free O-H molecule. The reaction intermediate OH*_Nb-$ZrSe_2$ was then optimized, and the equilibrium structure of the OH*_Nb-$ZrSe_2$ intermediate is illustrated in Figure 3.5(4a). To examine the electronic behavior, we studied the electronic properties of the OH*_Nb-$ZrSe_2$ intermediate. The E_F of the OH*_Nb-$ZrSe_2$ was found at -5.30 eV, as depicted by the dotted line in Figure 3.5(4b-4c). From the band structure calculations, we can see that the OH*_Nb-$ZrSe_2$ displays a semiconducting nature with an indirect band gap of 0.66 eV, as shown in Figure 3.5(4b). The conduction band minima and the valence band maxima of the OH*_Nb-$ZrSe_2$ are located at Γ and M, respectively, like the previous intermediate step. To confirm this band gap, we have drawn the DOSs profile corresponding to the band structure calculations, and the DOSs profile well supports the band gap of the OH*_Nb-$ZrSe_2$ as shown in Figure 3.5(4c). The value of ΔG for

this reaction step (O* → OH*) was found to be -1.23 eV computed by the same DFT-D method. The negative value of ΔG indicates that this step is exothermic. Hence, this process is thermodynamically and energetically favorable for the reduction of O_2.

Table 3.3. *The change in Gibbs free energy (eV) of the reaction steps during the associative mechanism at the surface of the 2D monolayer Nb-$ZrSe_2$ material.*

Various reaction steps are involved in the associative mechanism	**ΔG (eV)**
[Nb-$ZrSe_2$ + O_2 → O_2*_Nb-$ZrSe_2$]	-0.28
[O_2*_Nb-$ZrSe_2$ + H^+ + e^- → OOH*_Nb-$ZrSe_2$]	0.13
[OOH*_Nb-$ZrSe_2$ + H^+ + e^- → O*_Nb-$ZrSe_2$ + H_2O]	-1.82
[O*_Nb-$ZrSe_2$ + H^+ + e^- → OH*_Nb-$ZrSe_2$]	-1.23
[OH*_Nb-$ZrSe_2$ + H^+ + e^- → Nb-$ZrSe_2$ + H_2O]	-1.76

Fifth Step. This is the last step of the ORR mechanism. This step of the $4e^-$ associative mechanism is the hydrogenation of the OH*_Nb-$ZrSe_2$ intermediate by reacting with H^+ and e^- coming from the anode side of the fuel cell. We have assumed that the OH* at the Se site captures one H^+ and e^- to form the second H_2O molecule and it is removed from the catalytic site. The value of the ΔG of this reaction step (OH* → H_2O + *) was found to be -1.76 eV computed by the same DFT-D method. The negative value of ΔG indicates that this ORR step is exothermic, and hence, this process is thermodynamically and energetically favorable for the reduction of O_2. The value of ΔG of each reaction's intermediate during the associative mechanism has been reported in Table 3.3, and similarly, the value of ΔG of each is summarized in Table 3.2 and represented in Figure 3.6 (for both associative and dissociative reaction mechanisms).To summarize the catalytic activity of the 2D Nb-$ZrSe_2$ toward ORR, we drew and analyzed the ΔG curve (potential energy curve) for both associative and dissociative mechanisms based on the DFT-D calculations, as shown in Figures 3.7 and 3.8. We constructed these diagrams by considering the 2D Nb- $ZrSe_2$ as a reference geometry, i.e., 2D Nb-$ZrSe_2$ considered corresponding to energy of 0 eV for both associative and dissociative mechanisms of ORR. At a standard condition (i.e., at a temperature of 298.15 K with

pressure 1 atm), the total value of ΔG for full reaction $O_2 + 2H_2 \rightarrow 2H_2O$ should be -4.92 eV. From our Gibbs energy landscape, the total value of ΔG was found to be -4.94 eV and -4.96 eV for dissociative and associative reaction mechanisms, respectively. So, from our DFT-D calculations, we can see that the total value of ΔG for the ORR mechanism is very consistent with the experimental value. In the dissociative path, the free energy landscape shows

Table 3.4. *The change in Gibbs free energy of reaction steps in dissociative mechanism at the surface of the 2D monolayer Nb-$ZrSe_2$ material.*

Various reaction steps are involved in the dissociative mechanism	**ΔG (eV)**
[Nb-$ZrSe_2$ + O_2 → O_2*_Nb-$ZrSe_2$]	-0.28
[O_2*_Nb-$ZrSe_2$ → 2O*_Nb-$ZrSe_2$]	1.99
[2O*_Nb-$ZrSe_2$ + H^+ + e^- → O*_OH*_Nb-$ZrSe_2$]	-2.26
[O*_OH*_Nb-$ZrSe_2$ + H^+ + e^- → O*_Nb-$ZrSe_2$ + H_2O]	-1.40
[O*_Nb-$ZrSe_2$ + H^++e^- → OH*_Nb-$ZrSe_2$]	-1.23
[OH*_Nb-$ZrSe_2$ + H^+ + e^- → Nb-$ZrSe_2$ + H_2O]	-1.76

that all the reaction steps are downhill except O_2* → 2O*, as shown in Figure 3.7. For the associative path, all the reaction steps are also downhill in the free energy landscape except for the reaction steps for O_2* → OOH*, as shown in Figure 3.8. But by comparing both the free energy landscapes, the O_2* → 2O* step of the dissociative mechanism has a higher uphill than that of the associative mechanism. Thus, the 2O* step is not stable and thermodynamically feasible for the ORR mechanism, which makes the further ORR steps through the dissociative path difficult. Whereas the uphill in the associative mechanism is very small, which is kinetically surmountable. Furthermore, all values of ΔG are negative, indicating that the entire ORR process through associative mechanism is exothermic and thermodynamically favorable. Therefore, the associative $4e^-$ pathway for the ORR on the surface of 2D Nb-$ZrSe_2$ is the most favorable path. The potential energy surface for both the associative and dissociative paths has been discussed for

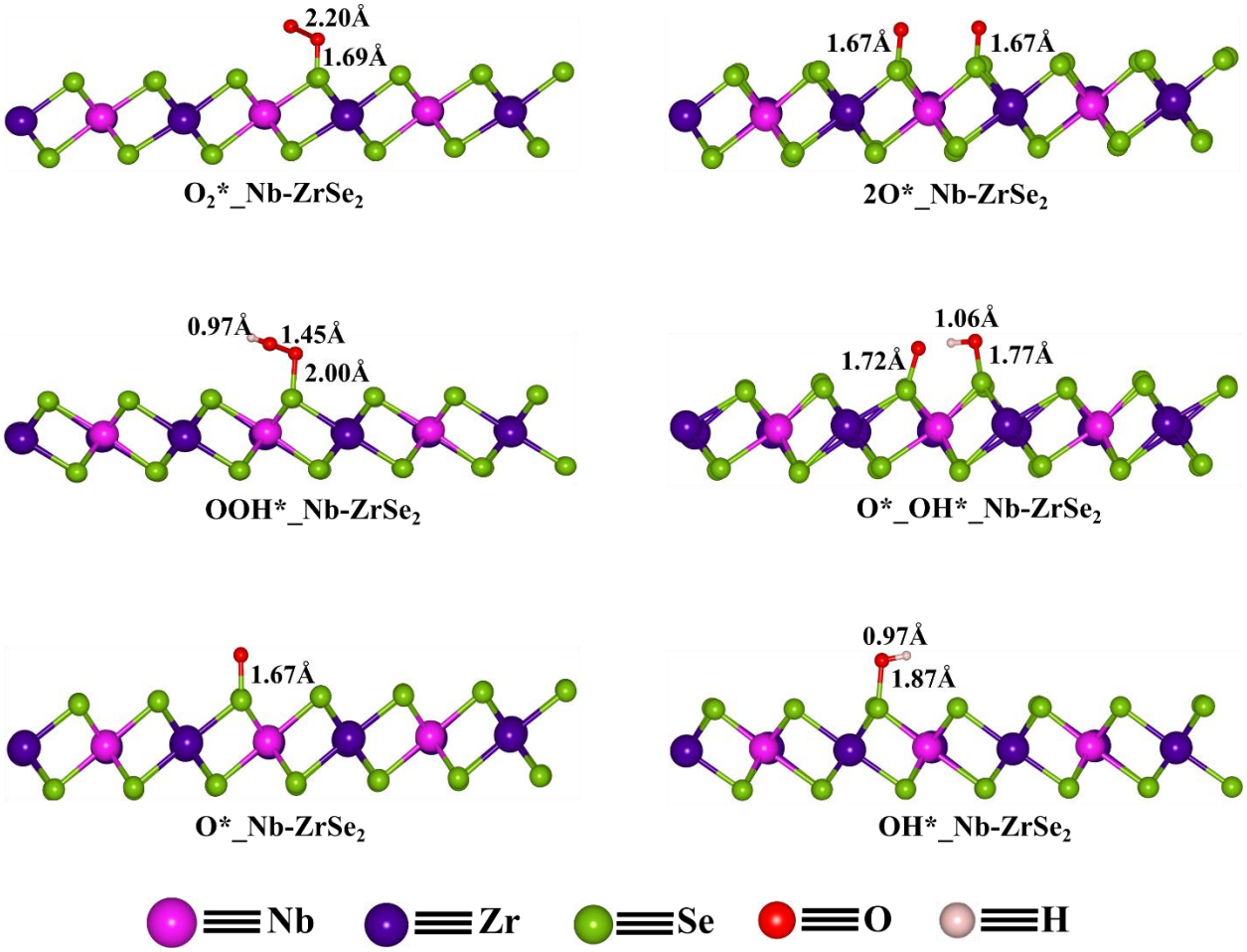

Figure 3.6. *Structural properties of the various ORR intermediate structures.*

the sake of a quick comparison of results in both mechanisms. The total values of ΔG for two reaction pathways (4.94 eV for the dissociative ORR mechanism and 4.96 eV for the associative mechanism) are marginally different (only 0.02 eV), which lies in the DFT-D error bar. This slight difference in the total value of ΔG for two reaction pathways might come from the different reaction energies (i.e., the different interaction strengths) of different intermediate species occurring on both the associative and dissociative mechanisms. The specific bond-breaking and bond-formation steps in a different pathway may possess distinct reaction energies due to variations in the bond strength, atomic interactions, and stabilities of intermediates, ultimately affecting the calculated total ΔG values. In our present calculations, the reaction energies of $O_2^* \rightarrow 2O^*$ and $O_2^* + H^+ + e^- \rightarrow OOH^*$ were found to be 1.94 eV and -0.18 eV, respectively. Another factor is the change in the entropy during each process that contributes to the overall value of ΔG. Different changes in entropy arise from different reaction mechanisms and different translational

and variational degrees of freedom of intermediate species (2O* and OOH*). In the context of electrocatalytic reactions, the concept of entropy helps us to understand how the arrangement of molecules and their energy distribution change as a reaction proceeds. When molecules transition occurs from reactants to products, their spatial arrangement and energy distribution can change, leading to differences in entropy. Besides these factors, the rate of electron transfer differs between reaction pathways due to variations in the redox potential of intermediates and the effect on the total ΔG values. Thus, the reaction energies, electron transfer rate, and entropy contribution of different reaction intermediates may cause minor differences in the values of ΔG during both associative and dissociative reaction mechanisms. The difference in ΔG is only about 0.02 eV, which is negligible and lies in the DFT-D error bar.

In the case of the 2D monolayer Nb-$ZrSe_2$, the value of η has been determined to be 1.09 V for the associative reaction path of the ORR. The overpotential of the benchmark Pt (111) was calculated to be 0.45 V at the same level of theory[5]. This discrepancy indicates that the 2D monolayer Nb-$ZrSe_2$ requires a higher driving potential to achieve the desired ORR rate compared to Pt. This observation suggests that the 2D monolayer Nb-$ZrSe_2$ might not be as efficient as Pt (111) as a cathode material for ORR; however, this material can be used as a Pt-free electrocatalyst where the performance is remarkable. To provide a comprehensive comparison, we considered some of the 2D surfaces, such as 2D transition metal-based, organic framework-based materials, and Pt-doped transition metal dichalcogenides. Recently, Upadhyay and Pakhira reported that the Pt-doped $MoSe_2$ (Pt-$MoSe_2$) 2D transition metal dichalcogenides is an efficient electrocatalyst for ORR by employing the same level of theory. They computationally showed that the 2D transition metal dichalcogenides possess the value of η about 1.53 V, which is higher than that of the overpotential of 2D single-layer Nb-$ZrSe_2$ material[48]. Zhau et al. studied the efficiency of double carbon vacancy C_3N monolayer with embedded a range of transition metals denoted by TM-V_{cc} (TM = Mn, Fe, Co, Cu, Ru, Rh, Pd, and Pt) toward ORR[56]. The overpotential of the Nb-$ZrSe_2$ is quite near most of the TM-V_{cc} catalysts. Furthermore, Ji et al. counted the first principle calculations to investigate the catalytic performance of the 2D M-COFs (M = Sc, Zn, Ru, Pd, Ag, and Ir)[57]. According to their findings, most of the M-COFs represent an overpotential comparable to that of the 2D monolayer Nb-$ZrSe_2$. The overpotential of the 2D monolayer Nb-

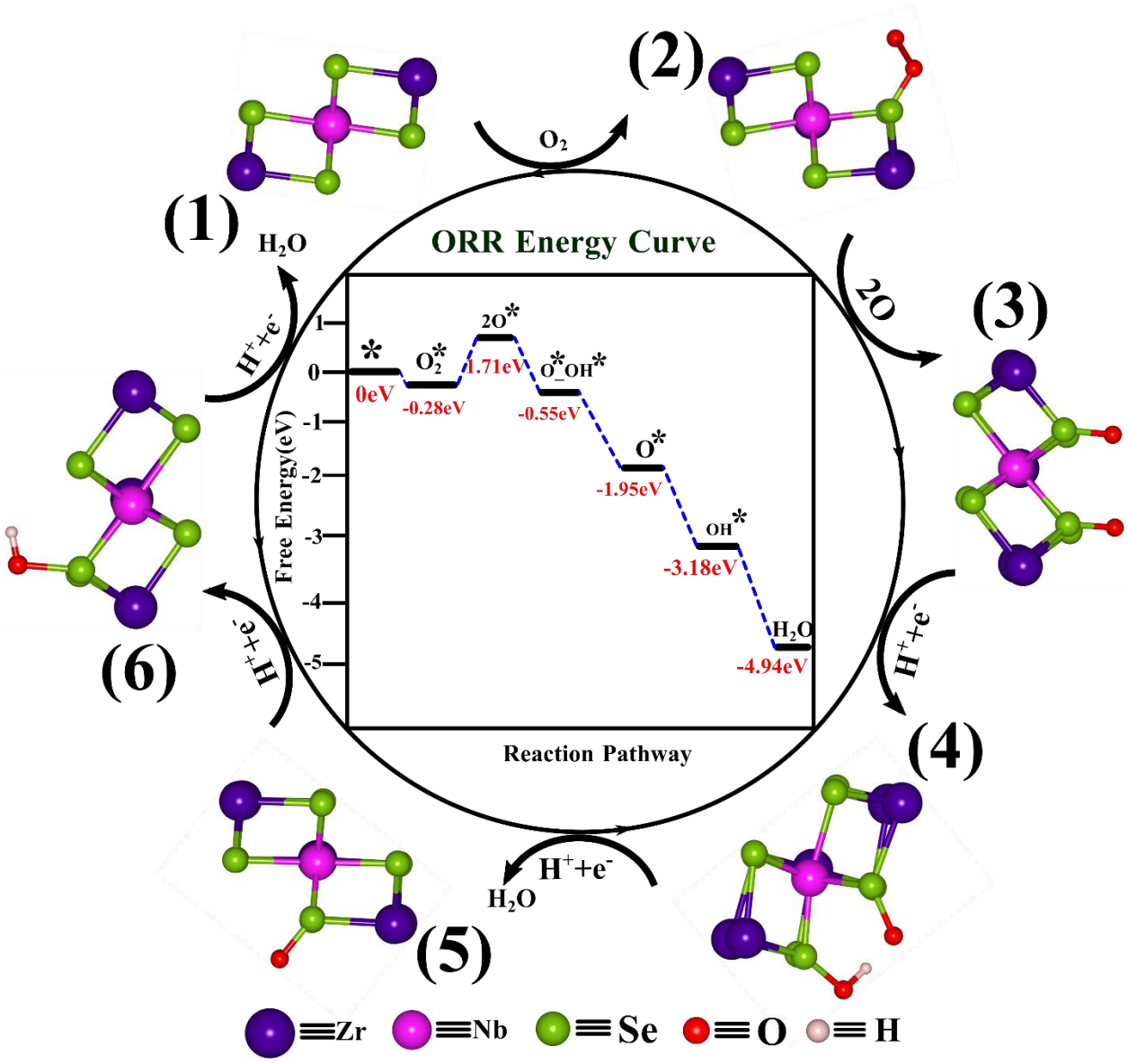

Figure 3.7. *Free energy diagram of dissociative ORR mechanism at the surface of the 2D monolayer Nb-$ZrSe_2$ material.*

$ZrSe_2$ is comparable to various previously reported 2D materials overpotential studied using the DFT method for ORR catalyst[58,59].

While the lower value of overpotential comparable to that of the Pt catalyst suggests enhanced catalytic activity, it is important to consider other factors to evaluate catalytic efficacy. As the 2D monolayer Nb-$ZrSe_2$ possesses a conducting nature, it facilitates the charge transfer, and the ORR happens on the surface of the Nb-$ZrSe_2$. Hence, it provides more exposure to the active catalytic sites, providing more opportunities for the ORR to take place. The availability and sustainability of the constituent elements, Nb, Zr, and Se, and the cost-effectiveness of the Nb

$ZrSe_2$ in comparison to precious metals like Pt present ecological and economically viable alternatives for large-scale applications. Our findings show that the 2D monolayer Nb-$ZrSe_2$ exhibits good selectivity for the favorable reaction path and moderate adsorption energy of the ORR intermediates on the catalytic surface. The unique structural and electronic properties, stability, cost-effectiveness, and path selectivity of the 2D monolayer Nb-$ZrSe_2$ for ORR collectively positioned it as a promising catalyst for ORR despite a slightly higher overpotential.

The study of the ORR is a solid surface reaction, and it happens on the outer surface of the 2D layer of the Nb-$ZrSe_2$ TMD. The examination of solvent impact holds significant relevance within the realm of catalysis. Additionally, gaining insights into the reaction mechanisms occurring in the solvent phase for various electrochemical reactions presents an equally interesting and important area of research study. Achieving a precise representation of the solvent model stands as a significant challenge within the realm of computational catalysis. Furthermore, the computational expense associated with modeling the various reaction steps (in the solvent phase) exacerbates this challenge[60,61]. When considering a solvent environment, it becomes apparent that the solvent possesses the capability to interact with the adsorbates and the catalytic surface through either chemical or physical processes. Notably, the solvent molecules can interact with adsorbates by hydrogen bonding. The effects of the solvent phase are very challenging owing to the difficulties in accurately defining complex systems that may involve simultaneous solvent-solvent, adsorbate solvent, adsorbent-solvent, and adsorbate-catalytic surface interactions. The primary focus revolves around precisely defining the interaction potential and the exchange-correlation functionals involved in the solvent phase. Introducing the solvent phase introduces complexity, often resulting in expansive systems characterized by numerous feasible thermodynamic and geometrical arrangements. Consequently, the task of identifying a relevant configuration becomes equally challenging. In addition to this, the solvent phase is the main component of the reaction medium. Consequently, its physical attributes, such as polarity, viscosity, and propensity to interact with adsorbates, play a transformative role in influencing reaction kinetics through their impact on both mass and heat transfer phenomena. Thus, the task of precisely understanding how the inherent properties of the solvent influence the reaction dynamics is far from straightforward. Owing to these complications, the solvent phase is neglected by the researchers in DFT calculations, instead approximating it using vacuum or gas-phase

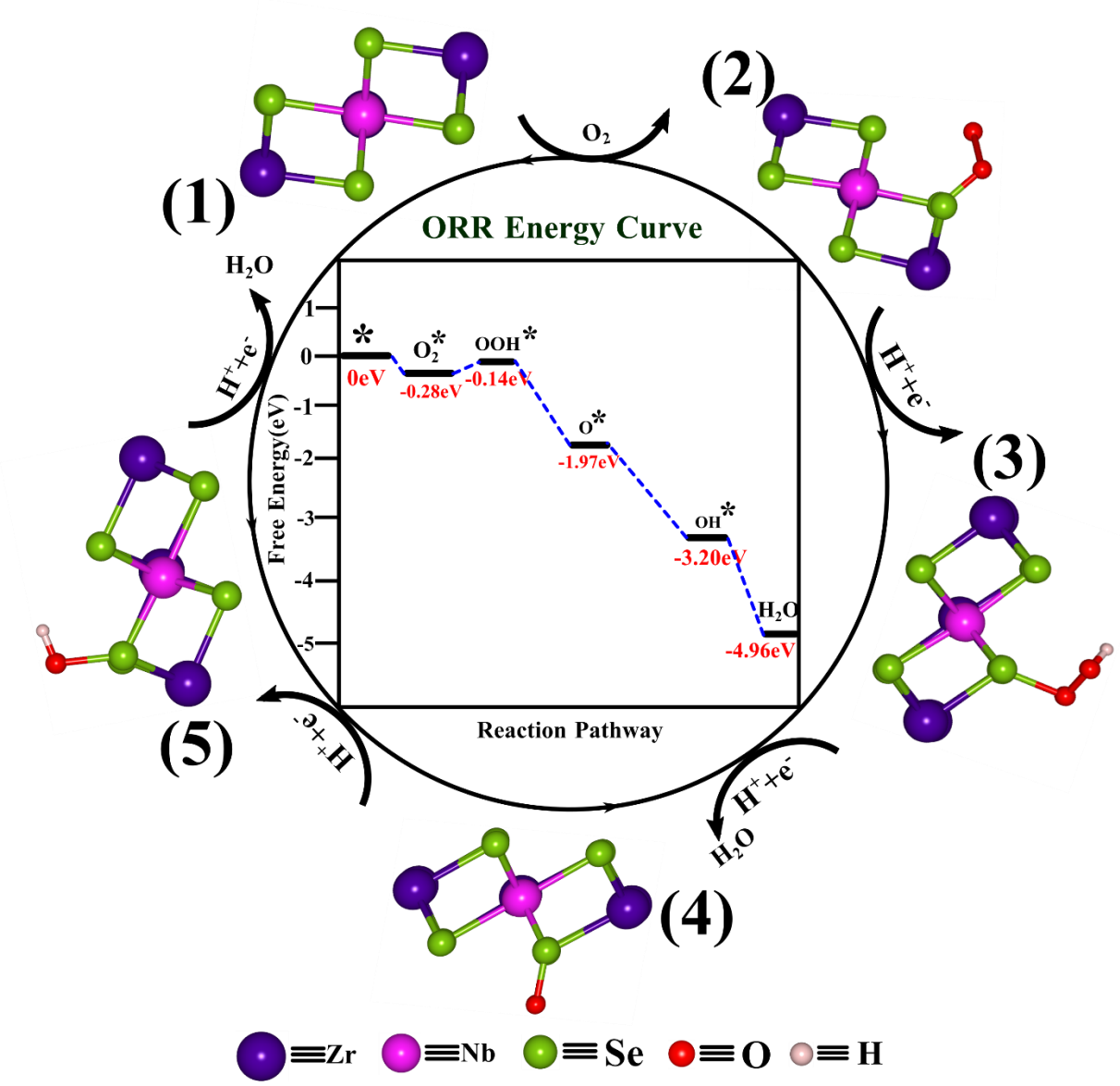

Figure 3.8. *Free energy diagram of associative ORR mechanism at the surface of the 2D monolayer Nb-$ZrSe_2$ material.*

conditions. moreover, we took the relative energy changes during the reactions where the solvation effects were negligible[62]. Because of computational limitations, we did not include calculations for the solvent phase in this study as the relative values of ΔG have been considered in the present investigation, and such big calculations should be left for future study.

3.5 Conclusions: In conclusion, we theoretically shed light on the geometrical structure, electronic properties, and catalytic activity of the 2D monolayer Nb-$ZrSe_2$ material as well as the detailed ORR mechanism on the surface of the 2D Nb-$ZrSe_2$ by using the DFT-D method. We investigated and examined both the possible path, i.e., associative and dissociative path, of the ORR mechanism

on the surface of the 2D Nb-$ZrSe_2$. The analysis of the electronic properties of pure monolayer $ZrSe_2$ demonstrated that a single layer of $ZrSe_2$ in a two-dimensional form exhibits semiconductor behavior characterized by a band gap of 1.48 eV. To alter the electronic properties and catalytic activity of the $ZrSe_2$, the substitutional doping of Nb has been done per 2 × 2 supercell of the $ZrSe_2$ monolayer. The 2D monolayer Nb-$ZrSe_2$ material has a zero-band gap, indicating the metallic nature of the 2D Nb-$ZrSe_2$. Conductivity of the 2D monolayer Nb-$ZrSe_2$ material plays a crucial role in facilitating the movement of electrons in the mechanism of ORR and 2D Nb-$ZrSe_2$ could act as an excellent catalyst toward ORR. To analyze the whole reaction process, ORR intermediate structures involved in both the associative and dissociative path were constructed and optimized by using the same DFT-D method. To examine the catalytic activity, we computed the adsorption energy of ORR intermediates involved in both associative and dissociative mechanisms. The dissociative mechanism involves the following intermediates O_2* → 2O* → O*_OH* → O* + H_2O → OH* and associative mechanism has the following intermediates O_2* → OOH* → O* + H_2O → OH*. For the dissociative mechanism, the value of ΔE of the 2O* intermediate was found to be 1.99 eV to the catalytic site on the surface of the 2D Nb-$ZrSe_2$, which indicates poor binding of 2O*. For the associative mechanism, the value of ΔE of the OOH* intermediate was found to be -0.18 eV, which indicates the optimum binding of the OOH* to the catalytic site on the surface of the 2D Nb-$ZrSe_2$. Thus, the dissociative path would be a less favorable path to reduce the O_2 molecule to water as compared to that of the associative path. In addition, for the associative mechanism, the value of ΔE for all intermediates is negative, which indicates that all the intermediates have good binding with the Se site, thus creating an energetically favorable path. The value of ΔG for all the reaction intermediates has also been computed. The values of ΔG also suggest that the associative path would be preferred over the dissociative mechanism. Thus, 2D Nb-$ZrSe_2$ can be used as an excellent catalyst for the ORR mechanism.

3.6 References:

[1] S. Chu, A. Majumdar, Opportunities and challenges for a sustainable energy future, Nature 488 (2012) 294–303.

[2] S. Chu, Y. Cui, N. Liu, The path towards sustainable energy, Nat. Mater. 16 (2016) 16–22.

[3] M. K. Mahapatra, P. Singh, Fuel cells. Energy conversion technology., Futur. Energy

Improv. Sustain. Clean Options Our Planet. 47 (2013) 511–547.

[4] A. Kulkarni, S. Siahrostami, A. Patel, J. K. Nørskov, Understanding catalytic activity trends in the oxygen reduction reaction, Chem. Rev. 118 (2018) 2302–2312.

[5] J. K. Nørskov, J. Rossmeisl, A. Logadottir, L. Lindqvist, J. R. Kitchin, T. Bligaard, H. Jónsson, Origin of the overpotential for oxygen reduction at a fuel-cell cathode, J. Phys. Chem. B. 108 (2004) 17886–17892.

[6] Z. Qiao, Z. Wang, C. Zhang, S. Yuan, Y. Zhu, J. Wang, PVAm–PIP/PS composite membrane with high performance for CO_2/N_2 separation, AIChE J. 59 (2012) 215–228.

[7] B. Wang, Recent development of non-platinum catalysts for oxygen reduction reaction, J. Power Sources 152 (2005) 1–15.

[8] Y. Wang, Y. Yang, S. Jia, X. Wang, K. Lyu, Y. Peng, H. Zheng, X. Wei, H. Ren, L. Xiao, J. Wang, D.A. Muller, H.D. Abruña, B.J. Hwang, J. Lu, L. Zhuang, Synergistic Mn-Co catalyst outperforms Pt on high-rate oxygen reduction for alkaline polymer electrolyte fuel cells, Nat. Commun. 10 (2019) 6–13.

[9] X. F. Lu, Y. Chen, S. Wang, S. Gao, X. W. Lou, Interfacing manganese oxide and cobalt in porous graphitic carbon polyhedrons boosts oxygen electrocatalysis for Zn–Air batteries, Adv. Mater. 31 (2019) 1902339.

[10] X. Feng Lu, S. Lin Zhang, W, Lok Sim, S, Gao, X, Wen (David) Lou, Phosphorized $CoNi_2S_4$ yolk-shell spheres for highly efficient hydrogen production via water and urea electrolysis, Angew. Chem. Int. Ed. 60 (2021) 22885–22891.

[11] D. Deng, K. S. Novoselov, Q. Fu, N. Zheng, Z. Tian, X. Bao, Catalysis with two-dimensional materials and their heterostructures, Nat. Nanotechnol. 11 (2016) 218–230.

[12] S. Chandrasekaran, D. Ma, Y. Ge, L. Deng, C. Bowen, J. Roscow, Y. Zhang, Z. Lin, R.D.K. Misra, J. Li, P. Zhang, H. Zhang, Electronic structure engineering on two-dimensional (2D) electrocatalytic materials for oxygen reduction, oxygen evolution, and hydrogen evolution reactions, Nano Energy 77 (2020) 105080.

[13] H. Huang, X. Feng, C. Du, S. Wu, W. Song, Incorporated oxygen in MoS_2 ultrathin nanosheets for efficient ORR catalysis, J. Mater. Chem. A. 3 (2015) 16050–16056.

[14] T. F. Jaramillo, K. P. Jørgensen, J. Bonde, J. H. Nielsen, S. Horch, I. Chorkendorff, Identification of active edge sites for electrochemical H_2 evolution from MoS_2 nanocatalysts, Science 317 (2007) 100–102.

[15] X. Chia, A. Ambrosi, P. Lazar, Z. Sofer, M. Pumera, Electrocatalysis of layered Group 5 metallic transition metal dichalcogenides (MX_2, M = V, Nb, and Ta; X = S, Se, and Te), J. Mater. Chem. A. 4 (2016) 14241–14253.

[16] R. J. Toh, Z. Sofer, M. Pumera, Catalytic properties of group 4 transition metal dichalcogenides (MX_2; M = Ti, Zr, Hf; X = S, Se, Te), J. Mater. Chem. A. 4 (2016) 18322–18334.

[17] Y. Shi, Y. Zhou, D.R. Yang, W.X. Xu, C. Wang, F. Bin Wang, J.J. Xu, X.H. Xia, H.Y. Chen, Energy level engineering of MoS_2 by transition-metal doping for accelerating hydrogen evolution reaction, J. Am. Chem. Soc. 139 (2017) 15479–15485.

[18] H. Li, C. Tsai, A. L. Koh, L. Cai, A. W. Contryman, A. H. Fragapane, J. Zhao, H. S. Han, H. C. Manoharan, F. Abild-Pedersen, J. K. Nørskov, X. Zheng, Erratum: Activating and optimizing MoS_2 basal planes for hydrogen evolution through the formation of strained sulphur vacancies, Nat. Mater. 15 (2016) 364.

[19] H. Jin, C. Guo, X. Liu, J. Liu, A. Vasileff, Y. Jiao, Y. Zheng, S. Z. Qiao, Emerging two-dimensional nanomaterials for electrocatalysis, Chem. Rev. 118 (2018) 6337–6408.

[20] B. You, M. T. Tang, C. Tsai, F. Abild-Pedersen, X. Zheng, H. Li, Enhancing electrocatalytic water splitting by strain engineering, Adv. Mater. 31 (2019) 1807001.

[21] B. B. Xiao, P. Zhang, L. P. Han, Z. Wen, Functional MoS_2 by the Co/Ni doping as the catalyst for oxygen reduction reaction, Appl. Surf. Sci. 354 (2015) 221–228.

[22] V. Urbanová, P. Lazar, N. Antonatos, Z. Sofer, M. Otyepka, M. Pumera, Positive and negative effects of dopants toward the electrocatalytic activity of MoS_2 and WS_2: experiments and theory, ACS Appl. Mater. Interfaces. 12 (2020) 20383–20392.

[23] A. Singh, S. Pakhira, Unraveling the electrocatalytic activity of platinum doped zirconium disulfide toward the oxygen reduction reaction, Energy Fuels 37 (2023) 567–579.

[24] Y. Singh, S. Back, Y. Jung, Activating transition metal dichalcogenides by substitutional nitrogen-doping for potential ORR electrocatalysts, ChemElectroChem. 5 (2018) 4029–4035.

[25] H. Huang, X. Feng, C. Du, W. Song, High-quality phosphorus-doped MoS_2 ultrathin nanosheets with amenable ORR catalytic activity, Chem. Commun. 51 (2015) 7903–7906.

[26] S. Tian, Q. Tang, Activating transition metal dichalcogenide monolayers as efficient electrocatalysts for the oxygen reduction reaction via single atom doping, J. Mater. Chem. C. 9 (2021) 6040–6050.

[27] M. Zhang, Y. Zhu, X. Wang, Q. Feng, S. Qiao, W. Wen, Y. Chen, M. Cui, J. Zhang, C. Cai, L. Xie, Controlled synthesis of ZrS_2 monolayer and few layers on hexagonal boron nitride, J. Am. Chem. Soc. 137 (2015) 7051–7054.

[28] J. Lee, S. Kang, K. Yim, K. Y. Kim, H. W. Jang, Y. Kang, S. Han, Hydrogen evolution reaction at anion vacancy of two-dimensional transition-metal dichalcogenides: Ab initio computational screening, J. Phys. Chem. Lett. 9 (2018) 2049–2055.

[29] N. N. Som, P. K. Jha, Hydrogen evolution reaction of metal di-chalcogenides: ZrS_2, $ZrSe_2$ and Janus ZrSSe, Int. J. Hydrogen Energy 45 (2020) 23920–23927.

[30] S. Mañas-Valero, V. García-López, A. Cantarero, M. Galbiati, Raman spectra of ZrS_2 and $ZrSe_2$ from bulk to atomically thin layers, Appl. Sci. 6 (2016) 264.

[31] R. A. Felseghi, E. Carcadea, M. S. Raboaca, C. N. Trufin, C. Filote, Hydrogen fuel cell technology for the sustainable future of stationary applications, Energies. 12 (2019) 4593.

[32] K. Maheshwari, S. Sharma, A. Sharma, S. Verma, A fuel cell and its applications: A review, International Journal of Engineering Research & Technology, 7 (2018) 6–10.

[33] D. Kan, D. Wang, X. Zhang, R. Lian, J. Xu, G. Chen, Y. Wei, Rational design of bifunctional ORR/OER catalysts based on Pt/Pd-doped Nb_2CT_2 MXene by first-principles

calculations, J. Mater. Chem. A. 8 (2020) 3097–3108.

[34] G. Fazio, L. Ferrighi, D. Perilli, C. Di Valentin, Computational electrochemistry of doped graphene as electrocatalytic material in fuel cells, Int. J. Quantum Chem. 116 (2016) 1623–1640.

[35] R. Hu, Y. Li, Q. Zeng, J. Shang, Role of active sites in N-coordinated Fe-Co dual-metal doped graphene for oxygen reduction and evolution reactions: A theoretical insight, Appl. Surf. Sci. 525 (2020) 146588.

[36] R. Dovesi, A. Erba, R. Orlando, C.M. Zicovich-Wilson, B. Civalleri, L. Maschio, M. Rérat, S. Casassa, J. Baima, S. Salustro, B. Kirtman, Quantum-mechanical condensed matter simulations with CRYSTAL, Wiley Interdiscip. Rev. Comput. Mol. Sci. 8 (2018) e1360.

[37] S. Grimme, J. Antony, S. Ehrlich, H. Krieg, A consistent and accurate ab initio parametrization of density functional dispersion correction (DFT-D) for the 94 elements H-Pu, J. Chem. Phys. 132 (2010) 154104.

[38] C. Zhao-ying, Y. Jin-long, The B3LYP hybrid density functional study on solids, Front. Phys. China 1(2006), 339–343.

[39] J. Muscat, A. Wander, N. M. Harrison, On the prediction of band gaps from hybrid functional theory, Chemical Physics Letters 342 (2001) 397–401.

[40] K. Adhikari, A. Chakrabarty, O. Bouhali, N. Mousseau, C. S. Becquart, F. El-Mellouhi, Benchmarking the performance of plane-wave vs. localized orbital basis set methods in DFT modeling of metal surface: a case study for Fe-(110), J. Comput. Sci. 29 (2018) 163–167.

[41] R. Dovesi, F. Pascale, B. Civalleri, K. Doll, N. M. Harrison, I. Bush, P. D'Arco, Y. Noel, M. Rera, P. Carbonniere, M. Causa, S. Salustro, V. Lacivita, B. Kirtman, A. M. Ferrari, F. S. Gentile, J. Baima, M. Ferrero, R. Demichelis, M. De La Pierre, The CRYSTAL code, 1976-2020 and beyond, a long story, J. Chem. Phys. 152 (2020) 204111.

[42] J. Laun, D. Vilela Oliveira, T. Bredow, Consistent Gaussian basis sets of double- and triple-zeta valence with polarization quality of the fifth period for solid-state calculations, J.

Comput. Chem. 39 (2018) 1285–1290.

[43] D. Vilela Oliveira, J. Laun, M.F. Peintinger, T. Bredow, BSSE-correction scheme for consistent Gaussian basis sets of double- and triple-zeta valence with polarization quality for solid-state calculations, J. Comput. Chem. 40 (2019) 2364–2376.

[44] Y. Fukuda, Y. Sasanuma, Computational characterization of Nylon 4, a biobased and biodegradable polyamide superior to nylon 6, ACS Omega 3 (2018) 9544–9555.

[45] D. Bocharov, S. Piskunov, Y.F. Zhukovskii, R.A. Evarestov, Ab Initio calculations on the electronic structure and photocatalytic properties of two-dimensional WS_2 (0001) nanolayers of varying thickness, Phys. Status Solidi RRL 2 (2018), 1800253.

[46] H. J. Monkhorst, J. D. Pack, Special points for Brillonin-zone integrations, Physical Review B 13 (1976) 5188.

[47] K. Momma, F. Izumi, VESTA 3 for three-dimensional visualization of crystal, volumetric and morphology data, J. Appl. Crystallogr. 44 (2011) 1272–1276.

[48] S. N. Upadhyay, S. Pakhira, Mechanism of electrochemical oxygen reduction reaction at two-dimensional Pt-doped $MoSe_2$ material: an efficient electrocatalyst, J. Mater. Chem. C. 9 (2021) 11331–11342.

[49] S. N. Upadhyay, V. B. Sardar, A. Singh, V. Kumar, S. Pakhira, Elucidating the oxygen reduction reaction mechanism on the surfaces of 2D monolayer $CsPbBr_3$ perovskite, Phys. Chem. Chem. Phys. 24 (2022) 28283–28294.

[50] Z. Duan, G. Wang, Comparison of reaction energetics for oxygen reduction reactions on Pt(100), Pt(111), Pt/Ni(100), and Pt/Ni(111) surfaces: A first-principles study, J. Phys. Chem. C. 117 (2013) 6284–6292.

[51] H. Sun, J. Li, S. Almheiri, J. Xiao, Oxygen reduction on a Pt(111) catalyst in HT-PEM fuel cells by density functional theory, AIP Adv. 7 (2017) 085020.

[52] S. Chŕtien, H. Metiu, O_2 evolution on a clean partially reduced rutile TiO_2(110) surface and on the same surface precovered with Au_1 and Au_2: The importance of spin conservation, J.

Chem. Phys. 129 (2008) 074705.

[53] J. W. Snyder, E. Skovsen, J. D. C. Lambert, P. R. Ogilby, Subcellular, time-resolved studies of singlet oxygen in single cells, J. Am. Chem. Soc. 127 (2005) 14558–14559.

[54] C. Schweitzer, R. Schmidt, Physical mechanisms of generation and deactivation of singlet oxygen, Chem. Rev. 103 (2003) 1685–1757.

[55] W. Mtangi, V. Kiran, C. Fontanesi, R. Naaman, Role of the electron spin polarization in water splitting, J. Phys. Chem. Lett. 6 (2015) 4916–4922.

[56] Y. Zhou, G. Gao, J. Kang, W. Chu, L. W. Wang, Transition metal-embedded two-dimensional C_3N as a highly active electrocatalyst for oxygen evolution and reduction reactions, J. Mater. Chem. A. 7 (2019) 12050–12059.

[57] J. Ji, C. Zhang, S. Qin, P. Jin, First-principles investigation of two-dimensional covalent-organic framework electrocatalysts for oxygen evolution/reduction and hydrogen evolution reactions, Sustain. Energy Fuels 5 (2021) 5615–5626.

[58] S. Lu, Y. Zhang, F. Lou, K. Guo, Z. Yu, Non-precious metal activated $MoSi_2N_4$ monolayers for high-performance OER and ORR electrocatalysts: A first-principles study, Appl. Surf. Sci. 579 (2022) 152234.

[59] B. Xiao, H. Zhu, H. Liu, X. Jiang, Q. Jiang, The activity improvement of the monolayer for oxygen reduction electrocatalysis : A density functional theory study, Front Chem. 6 (2018) 351.

[60] S. K. Iyemperumal, N. A. Deskins, Evaluating solvent effects at the aqueous/Pt(111) interface, ChemPhysChem. 18 (2017) 2171–2190.

[61] J. Carrasco, A. Hodgson, A. Michaelides, A molecular perspective of water at metal interfaces, Nat. Mater. 11 (2012) 667–674.

[62] Y. Wang, Y. Li, T. Heine, PtTe monolayer: two-dimensional electrocatalyst with high Basal plane activity toward oxygen reduction reaction, J. Am. Chem. Soc. 140 (2018) 12732–12735.

CHAPTER 4

Unraveling the Electrocatalytic Activity of Platinum-Doped Zirconium Disulfide toward the Oxygen Reduction Reaction

Oxygen reduction reaction (ORR) is one of the important reactions and the heart of renewable energy technology, ranging from fuel cells to metal-air batteries, and it is a big challenging task to build a cost-effective and efficient cathodic material for the electrocatalytic ORR. In this chapter, we present computationally designed Pt-doped 2D monolayer zirconium disulfide (i.e., Pt-ZrS_2) transition metal dichalcogenide (TMD) as an electrocatalyst for ORR. We have explored the electronic and structural properties and the electrocatalytic activity of Pt-ZrS_2 towards ORR by employing the hybrid periodic Density Functional Theory (DFT-D) method with van der Waals (vdW) dispersion corrections. The electronic properties calculations suggest the semiconducting character of Pt-ZrS_2 with the electronic band gap of 1.95 eV which is an important aspect in studying the ORR mechanism. The basal plane of 2D Pt-ZrS_2 shows exceptional electrocatalytic activities toward the ORR with a high four-electron ($4e^-$) reduction reaction pathway selectivity. Here, the detailed ORR pathway with the mechanism has been envisaged on the surfaces of 2D monolayer Pt-ZrS_2 TMD by employing the same DFT-D method. Both the dissociative ($O_2^* \rightarrow 2O^*$) and associative ($O_2^* \rightarrow O\_OH^*$) ORR mechanisms have been investigated, and it has been found that only the dissociative reaction path is energetically favorable. The adsorption energy has been calculated in each intermediate state during the ORR which guides us to predict the potential of Pt-ZrS_2 as an effective electrocatalyst for the ORR. This study reveals that substituting a Zr atom in the 2 × 2

supercell of the monolayer ZrS_2 with a Pt atom activates the inert basal planes, advancing to its superior electrochemical reactivity for boosting the molecular O_2 and successive ORR steps. Therefore, Pt-ZrS_2 can be used to design 2D cathode material for fuel cell contents.

4.1 Introduction: The global energy demand has been increasing drastically and is expected to increase by 30% to 50% by 2040, according to the International Energy Report. The promising solution to mitigate and resolve the energy deficiency is the use of fuel cells, which have been considered an effective energy resource that has high reliability, high efficiency, low operating temperature, and low emissions[1,2]. To achieve a significant performance of the fuel cells in order to enjoy their commercial use, it is a paramount need to accelerate the slack rate of the ORR process. Currently, platinum (Pt) and Pt-containing materials serve as catalysts to hasten the rate of the ORR mechanism in fuel cells. Unfortunately, commercialization of the pristine Pt and Pt-based catalysts is limited by the unfavorable price, scarcity, and reliability as Pt is a too expensive and rare material (only 5 μg/kg), and it has poison sensitivity i.e., low stability[3–6]. Various non-noble metal-based catalysts that have improved activity in comparison to Pt have also been discovered as a result of the search for improved ORR catalysts. Different metals have been examined in this endeavor, either in their pure form or by alloying with other metals such as Ni, Pd, Ag, Au, and Pt clusters are suitable to catalyze O_2 in their pure form[7].

Wang et al. have widely reported that synergistic Mn-Co catalysts act as good ORR catalysts[8]. Many recent articles reveal that metal oxide and sulfide can also be utilized as effective catalysts for the ORR, which gives efficiency close to Pt/C catalysts[9–11]. However, this kind of catalyst also has some limitations, such as low stability in an acidic medium (or in the Proton Exchange Membrane Fuel Cells (PEMFC) operation environment)[12]. Cutting the quantity of Pt in Pt-based materials while maintaining good catalytic performance is essential for sustainable fuel cell development; this necessitates a high usage of Pt atoms. To cut the amount of Pt metal and to replace the expensive Pt electrocatalyst, various approaches are used, e.g., developing a Pt nanostructure, alloying Pt with some earth-abundant metals, metal composites, and so on[13]. The commercial use of these catalysts is generally hindered due to their poor stability, low conductivity, small surface area, and cost.

The finding of 2D materials was a breakthrough in the era of nanoscience and especially in electrochemical energy applications, as they hold some exceptional mechanical, electronic,

chemical, and optoelectronic properties. For the practical application of the 2D materials, Mortazani et al. theoretically computed and examined the dynamical stability of 2D materials by computing phonon dispersion relations. The results thus obtained depict that 2D materials possess exceptional dynamical stability, and so are suitable for practical applications such as electrocatalysts, biosensing, etc. [14]. Among the 2D materials, the application of TMDs as an electrocatalyst for electrochemical reactions has been widely studied[15–17]. The 2D TMDs are considered suitable catalysts to catalyze the electrochemical reactions for the following reasons: (i) high surface area, (ii) abundant uncoordinated surface atoms, (iii) planar structure with atomic thickness, (iv) high tunable properties, and (v) earth-abundant and cost-effective[18]. Among the large number of TMDs, 2D MoS_2 has been widely researched, and the MoS_2 serves as an efficient catalyst because of its catalytic capability close to the Pt catalysts[19]. Recently, Sofer et al. disclosed the electrocatalytic behavior of the TaS_2 material and proposed that the 2T and 1H phases of the TaS_2 exhibit the ORR activity quite near the Pt/C catalysts[20]. However, a limited number of active edge sites is a major hindrance or concern in realizing the practical applications of these TMDs as catalysts. This drawback of TMDs can be promoted by activating the inert basal plane, which constitutes a large surface area. To activate the basal plane, different strategies have been adopted both experimentally and theoretically such as external atom doping, creating defects and vacancies, strain engineering, etc.[21,22]. Standard substitutional doping gives durable stability and hence is considered the best technique. Recently, Martin Pumera reported that a constrained and definite amount of dopants in transition metal dichalcogenides can alter their properties significantly and can create a positive impact on their utilization as electrocatalysts[23]. It was found that the Ge-doped MoS_2 offers a wonderful electrocatalytic activity toward the ORR as it shows moderate binding energy with the ORR intermediates[24]. Veronika et al. demonstrated experimentally and theoretically that the Rh doping on TMDs (e.g., $MoSe_2$, WSe_2) tailors the electron transfer properties and can serve as a good photocatalyst for water-splitting applications[25].44 Very recently, Upadhyay and Pakhira computationally found that the Pt doped $MoSe_2$ TMD exhibits a good catalytic activity toward the ORR[26]. Besides being a catalyst, TMDs can be used for many great applications, such as biosensing, memory storage, etc., by changing their structural configuration. Chia et al. demonstrated in their review that controlled doping and decorating legends material (e.g., TMDs) can enhance their sensing capabilities and can act as an efficient biosensor with high sensitivity[27]. TMDs can also be used to engineer the

electronic states of molecules by making hybrid organic/2D interfaces. Such a type of hybrid organic interface can be used as a single molecule device for memory storage applications[28]. The above useful findings also support the importance of TMDs in the energy application field.

Recent research revealed that the monolayer ZrS_2 possesses a superior catalytic performance toward water splitting and for the H_2 evolution reaction (HER)[29–31]. Moreover, ZrS_2 is nontoxic, inexpensive, and resistant to corrosion and can be synthesized as a large-scale and thin atomic layer experimentally[32]. Additionally, in the case of sulfur-based ZrS_2 TMD, with S having a 2^- valence (S^{2-}), it has a strong reduction performance that facilitates the ORR electrocatalytic activities. Therefore, the development of novel, cheaper catalysts with optimum performance and ideal stability is highly desired. To achieve the aim, two possible techniques can be adopted: (1) the use of metals that are more cost-effective and plentiful in the Earth's crust, and (2) lowering the number of precious metals to the employment of their maximum efficiency.

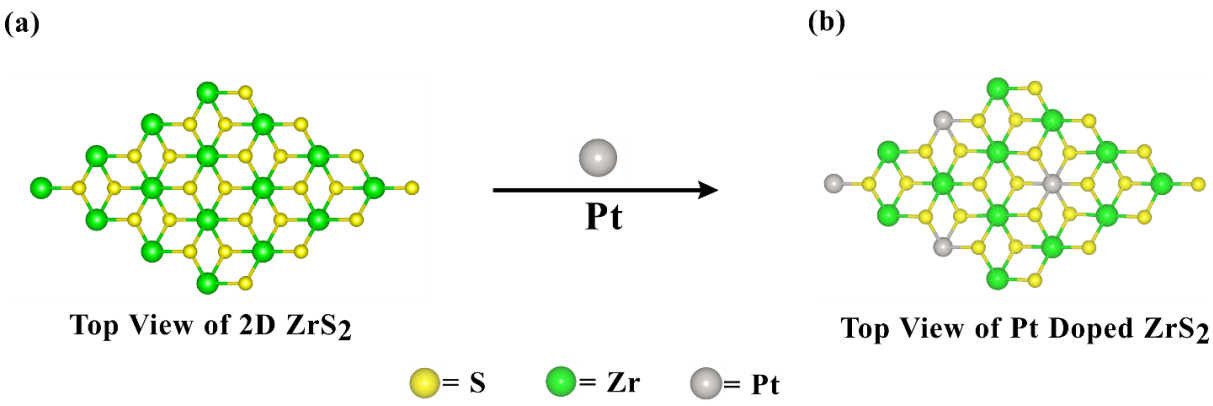

Figure 4.1. *The equilibrium monolayer structure of (a) the 2D pristine ZrS_2 and (b) platinum-doped 2D monolayer ZrS_2 (Pt-ZrS_2) material (2 × 2 supercell) are shown here.*

In view of the vast applications of the 2D TMDs as important and efficient electrocatalysts, it is crucial to study and investigate the electrocatalytic behavior of one of the TMDs, ZrS_2, in more detail as it has been unfortunately ignored in the past. We performed theoretical calculations on a 2 × 2 cell of the 2D monolayer ZrS_2 doped with one dopant atom (Pt) per unit cell, which indicates that the amount of 25% Pt atoms has been substituted in the system. The atomic substitution can be defined by a mathematical formula $\frac{N_{dopant}}{N_{transition-metal}}$, where N_{dopant} is the number of dopant atoms and $N_{transition-metal}$ is the total number of transition-metal atoms in the TMD supercell considered in the system studied here[33]. In this manuscript, we present an

exciting ORR catalyst, specifically the Pt-ZrS_2 monolayer, on the foundation of the comprehensive first-principles-based DFT-D technique. We computationally designed a 2D monolayer pristine ZrS_2 and Pt-ZrS_2 TMD materials, and the DFT-D calculations were used to explore the ORR electrocatalytic efficiency of the Pt-ZrS_2 TMD by calculating and analyzing the adsorption energies of reaction intermediates contained inside the ORR mechanism. At first, we explored the intrinsic properties such as electronic band structures, electronic band gap (E_g), the total density of states (DOS), the position of the Fermi energy level (E_F), etc., of both the 2D monolayer pristine ZrS_2 and Pt-ZrS_2 TMDs by employing the DFT-D method. The computed results showed that after the Pt doping in the monolayer ZrS_2 material, the E_g decreased from 2.13 eV to 1.95 eV. Pt increases the carrier concentration and electron density of states around the E_F, which enhances the overall electronic semi-conductivity of the material. Therefore, we expected that Pt-ZrS_2 would exhibit promising ORR activity. Then, for the Pt-ZrS_2 catalyst, the ORR mechanism has been studied by investigating various reaction steps contained inside the ORR mechanism. It is remarkable that the 2D Pt-ZrS_2 monolayer has high four-electron ($4e^-$) selectivity and possesses superior catalytic activity toward the electrochemical ORR mechanism, which makes them promise fuel cell materials.

4.2 Theory, Methodology and Computational Details: Equilibrium 2D layer structures, geometries, lattice parameters (i.e., cell parameters), and intrinsic electronic properties (such as electronic band structures, electronic band gap (E_g), total density of states (DOS), the position of the Fermi energy level (E_F), etc.) of both the 2D monolayer pristine ZrS_2 and Pt-ZrS_2 TMDs were obtained by the quantum mechanical based exchange-correlation hybrid functional B3LYP spin-unrestricted DFT method implemented in the CRYSTAL17 suite Package[33]. To incorporate weak nonbonding van der Waals (vdW) interactions along with the interface, we have incorporated the damped vdW dispersion corrections "-D3" in the DFT method (noted by DFT-D, i.e., the B3LYP-D3 functional method) developed by Grimme and co-workers[34]. The present DFTD method was employed to describe the exchange-correlation effects, so we have used the DFT-D method throughout the calculations to describe the adsorption energy during the ORR process correctly. Gaussian-type basis sets were employed to define the atomic orbitals in the *ab initio*-based CRYSTAL17 suite code/package. These Gaussian types of atomic basis sets provide more precise outcomes/data during the hybrid DFT-D computations than the results based on plane wave basis sets[35–37]. In other words, the computation procedure diverges from the plane-wave codes

such as VASP, Quantum Espresso, etc. More interestingly, both computational methods contribute to similar findings and outcomes. It is more easier to solve the Hartree−Fock (HF) part of the total Hamiltonian by using the localized Gaussian basis set codes in the case of the hybrid density functional methods. For the Zr, S, O, and H atoms, triple-ζ valence polarized (in short TZVP) Gaussian types of atomic basis sets have been used here during all the calculations. The relativistic effective core potentials (ECPs) with the Pt_dool_2004 basis set for the Pt atoms are used in the present computations. The 2D Pt-ZrS_2 is constructed by creating a 2 × 2 supercell of the pristine 2D monolayer ZrS_2 material, including eight (8) S atoms and four (4) transition metal (Zr) atoms. Among the four transition metals (Zr) atoms, one Zr atom has been substituted by a Pt atom to form the Pt- ZrS_2 2D monolayer TMD material considered here. All the 2D monolayer periodic slab structure images were plotted by using VESTA software[38]. To exclude the spurious interactions between the repeated layers of the 2D monolayer slab, an inert space of 500 Å (which is quite sufficient according to our present calculations using the CRYSTAL17 suite code) was employed along the normal surface direction (z-direction) of the 2D Pt-ZrS_2. The optimization of all the monolayer 2D structures was performed by using the convergence criterion of energies and forces to 10^{-7} a.u., and the electronic self-consistent field (SCF) tolerance was set to 10^{-7} a.u. in all the computations. For the pristine ZrS_2, Pt-ZrS_2, the Brillouin zone was sampled on an 8 × 8 × 1 Monkhorst-Pack k-mesh grid for geometry optimization and electronic structure calculations[39]. The top and side views of the optimized structure of the 2D monolayer ZrS_2 with an increased unit cell 2 times (2 × 2) in the X and Y directions with no change in the Z direction are shown in Figure 4.1.

To develop an efficient catalyst, knowledge of the ORR mechanism is important, and this ORR is a very significant and vital mechanism in renewable energy sources. The kinetics of the well-known cathodic ORR determines the fuel cell's efficiency. In this process, the electrons from the anode are transported to the cathode (by an external circuit) in a fuel cell, where they combine with a proton and oxygen to form water. In other words, we can say that the oxygen (O_2) reduction starts with the adsorption of the O_2 molecule, and then the adsorbed O_2 molecule reacts with some e^- and H^+ pair and ends up with the formation of the H_2O/H_2O_2 molecule. In the acidic solution, the ORR process can follow two paths, either two electrons ($2e^-$) or four electrons ($4e^-$), depending on how the O=O bond cleaves[40,41].

A direct and more efficient four-electron ($4e^-$) transfer reaction pathway includes acid solutions with the following steps:

$$O_2 + 4H^+ + 4e^- \longrightarrow 2H_2O \ (1.229V \text{ vs SHE})$$

where SHE stands for the Standard Hydrogen Electrode.

The indirect two-electron ($2e^-$) transfer reaction pathway includes the following steps:

$$O_2 + 2H^+ + 2e^- \longrightarrow H_2O_2 \ (0.65 \text{ V vs SHE})$$

$$H_2O_2 + 2H^+ + 2e^- \longrightarrow 2H_2O \ (1.76 \text{ V vs SHE})$$

For the four-electron ($4e^-$) transfer reaction pathway, there are two universally accepted ORR pathways: the dissociation pathway and the association pathway, as discussed in Chapter 1.

The estimation of the catalytic performance of the 2D monolayer Pt-ZrS_2 was obtained by analyzing the adsorption energy of the adsorbate on the reaction site of the electrocatalyst. The adsorption energy (E_{ads}) of the adsorbate species appearing during the ORR process on the adsorption system (Pt-ZrS_2) has been computed by the following equation below[41,42]:

$$E_{ads} = E_{adsorbate+adsorbent} - E_{adsorbate} - E_{adsorbent}$$

where $E_{adsorbate+adsorbent}$, $E_{adsorbate}$, and $E_{adsorbent}$ are the total energy for the adsorbed system, adsorbate species, and adsorption system (Pt-ZrS_2), respectively. According to the equation, a negative value of E_{ads} tells the exothermic nature of the reaction, i.e., negative value adsorption energy suggests that the reaction species are favorably adducted to the Pt-ZrS_2 surface, which is thermodynamically stable. All the adsorption energies were evaluated with respect to a common reference state, which is the slab of Pt-ZrS_2 in this study.

4.3 Results and Discussion: The equilibrium geometry of the 2D monolayer pristine ZrS_2 is computed by employing the first principles-based dispersion-corrected B3LYP-D3 DFT method, as displayed in Figure 4.2a. The unit cell of pristine ZrS_2 after the optimization was defined by the equilibrium lattice parameters a = b = 3.65 Å and α = β = 90° and γ = 120° with the layer group $p\bar{3}m1$ symmetry, as reported in Table 4.1. The 2D monolayer ZrS_2 belongs to the 1T phase with layer symmetry $p\bar{3}m1$, which was found to be in the ground state and in which Zr atoms are

octahedrally bonded by six chalcogen (here S) atoms, as shown in Figure 4.1 and Figure 4.2a. The average equilibrium Zr-S bond length between the Zr and S atoms was found to be 2.55 Å, which is in full agreement with earlier reports[30]. To form the Pt-ZrS_2 2D monolayer slab structure, a 2 × 2 supercell of the pristine 2D monolayer ZrS_2 has been employed, and one Pt atom has been doped by substituting one Zr atom in the unit cell. The optimized geometries of Pt-ZrS_2 were acquired by employing the same DFT-D technique. The equilibrium lattice constants of the optimized unit cell of Pt-ZrS_2 were obtained to be a = b = 7.14 Å and α = β = 90° and γ = 120° with the 2D layer group symmetry P1. After structural relaxation, the equilibrium lattice constants (a = b = 7.14 Å of Pt-ZrS_2) have decreased by 0.14 Å compared to the 2 × 2 supercell of the monolayer ZrS_2. The average Zr-S equilibrium bond length of Pt-ZrS_2 was found to be 2.54 Å, and the Pt-S bond length was 2.46 Å obtained by the DFT-D method. The equilibrium Zr-S bond length of Pt-ZrS_2 was 0.01 Å shorter than that of the Zr-S bond length in the ZrS_2. The equilibrium structural parameters of the 2D monolayer ZrS_2 are well consistent with the earlier reported results [30]. The equilibrium bond lengths and symmetry of both the pristine 2D monolayer ZrS_2 and Pt-ZrS_2 TMDs were tabulated in Table 4.1. It should be mentioned here that the 2D monolayer ZrS_2 possesses a diamagnetic ground state suggesting the lack of unpaired electrons or dangling bonds in the pristine ZrS_2 monolayer, which implies that it would not be prone to oxidation and is stable at ambient conditions.

The efficiency of a material to serve as a good electrocatalyst relies on its stability and interaction between adsorbate intermediates and adsorbent (here Pt-ZrS_2). The study of electronic properties is a major factor in finding a suitable catalyst for the ORR. We have explored their intrinsic properties, i.e., electronic band structure, E_g, and total DOS, by employing the same DFT-D method at the equilibrium structures of both the pristine ZrS_2 and Pt-ZrS_2. The stability of the

Table 4.1. *Equilibrium lattice constants with optimized structural parameters and unit cell parameters of both the 2D monolayer ZrS_2 and Pt-ZrS_2 are tabulated here.*

Equilibrium systems	**Lattice constant or parameters (Å)**	**Interfacial angles in deg.**	**Layer group and symmetry**	**Average bond distance in atoms (Å)**		**Ref.**
				Zr-S	Pt-S	
2D monolayer ZrS_2	a = b = 3.65	α = β = 90, γ = 120	$p\bar{3}m1$	2.55		this work

2D monolayer ZrS_2 (previously reported	a = b = 3.66	α = β = 90, γ = 120	$p\bar{3}m1$	2.59		[30]
Pt-ZrS_2 (2 × 2)	a = b = 7.14	α = β = 90, γ = 120	*P1*	2.54	2.46	this work

subject materials have been confirmed by calculating the energy and thermodynamic parameters before the electronic property computations. The electronic properties of both the 2D single layer ZrS_2 and Pt-ZrS_2 have been computed and analyzed at equilibrium geometries by adopting the same DFT-D method. To analyze and study the electronic properties of the ZrS_2, we calculated the electronic band structure, E_g, E_F, and DOS using the same calculation parameters. The electronic band structures of the 2D monolayer ZrS_2 were calculated along the band pathway Γ-M-K-Γ with respect to vacuum considering the symmetry of the material, as shown in Figure 4.2b. We have taken into account a number of four valence bands (VBs) and four conduction bands (CBs) to calculate the

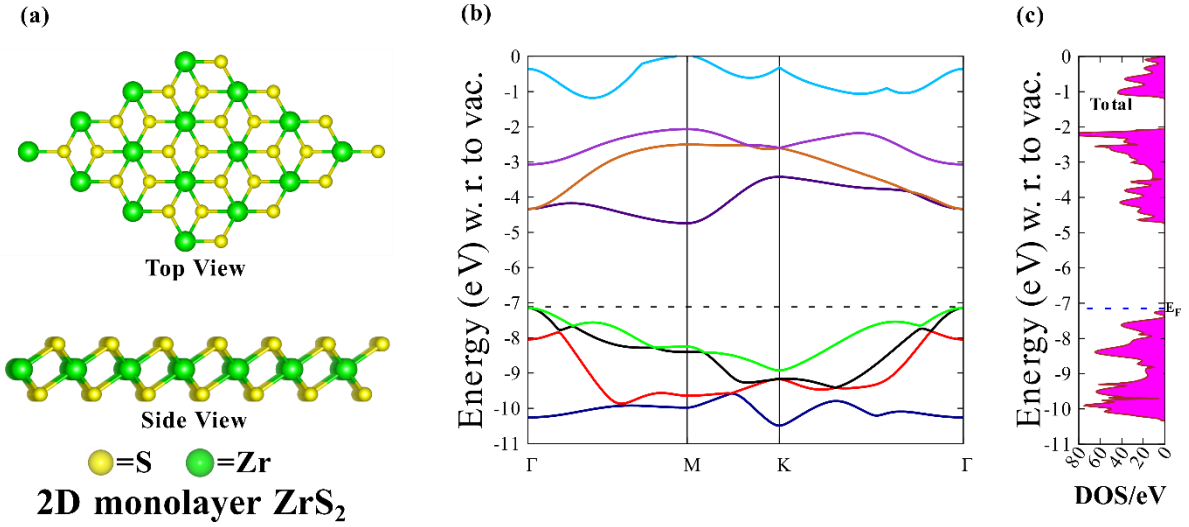

Figure 4.2. *(a) Illustration of the pristine 2D monolayer ZrS_2 material, (b) electronic band structure, and (c) total density of states (DOS).*

electronic band structures around the E_F, as shown in Figure 4.2b. The present computations found that the E_F of the monolayer ZrS_2 was at -7.14 eV, and it has an indirect E_g of about 2.13 eV (in the Γ-M direction), which is consistent or quite identical with the earlier reported data. The DOS of the monolayer ZrS_2 has been computed by employing the same theory, and the DOS has been plotted in Figure 4.2c, which corresponds to the electronic band structures of the pristine ZrS_2. The

DOS calculation confirms that the electronic bandgap E_g of the monolayer ZrS_2 TMD is about 2.13 eV. Thus, the electronic properties calculations reveal that the pristine 2D monolayer ZrS_2 has a noticeable Eg, and it is a high bandgap semiconductor. The bandgap of monolayer ZrS_2 was found to be quite large, which hinders its use as an electrocatalyst for the effective ORR. Now, we substituted one Zr atom (2 × 2 supercell of the 2D monolayer ZrS_2) with a Pt atom in place of the Zr atom to form Pt ZrS_2 and studied its electronic properties. The structure relaxation of the 2D monolayer Pt-ZrS_2 was carried out by adopting the B3LYP-D3 DFT method, and the relaxed equilibrium structure is shown in Figure 4.3a. The intrinsic electronic and structural properties were obtained at the equilibrium geometries by employing the same DFT-D method.

After obtaining the equilibrium structure (see Table 4.1), we computed the electronic properties of the 2D slab structure of the monolayer Pt-ZrS_2 TMD by employing the B3LYP-D3 method. The band structure of Pt-ZrS_2 was computed w.r.to vacuum and along with the high symmetric Γ-M-K-Γ direction to compare the electronic properties with the pristine 2D monolayer ZrS_2 TMD material. The E_g of Pt-ZrS_2 is about 1.95 eV, indicating that it is a semiconductor, and this study reveals that the electronic band gap Eg has been significantly reduced by an amount of 0.18 eV due to the presence of the Pt atoms in the 2D slab structure of the ZrS_2 supercell. The electronic band structures have been drawn around the Fermi energy level shown in Figure 4.3. The Fermi

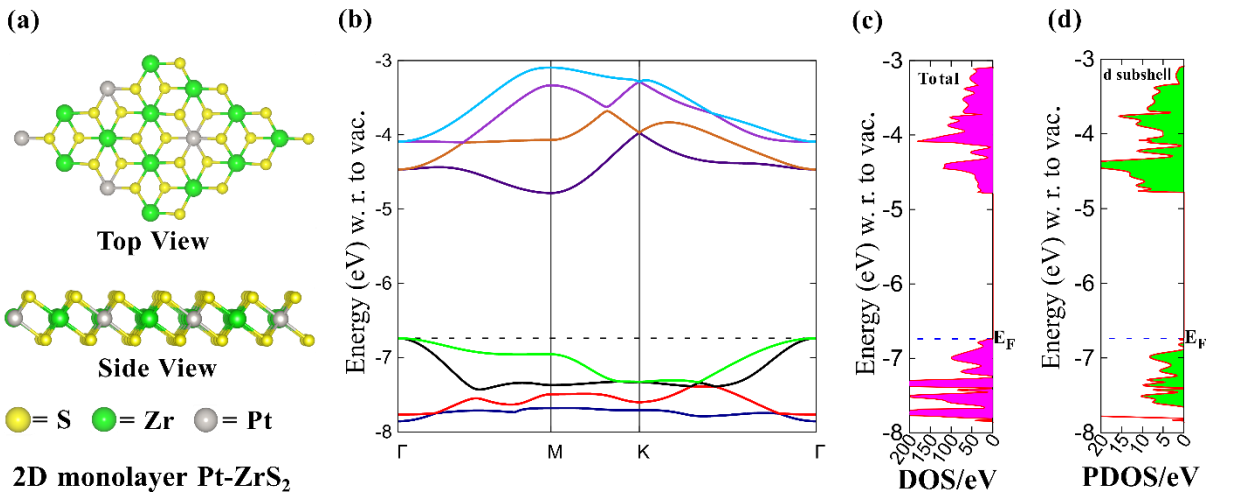

Figure 4.3. *(a) The equilibrium structure of the 2D monolayer Pt-ZrS_2, (b) electronic band structure, (c) total density of states, and (d) contribution of the d-subshells of the Pt atom in DOS.*

level (E_F) of this material was found at -6.73 eV, which has been moved toward the conduction bands around 0.41 eV compared to the pristine ZrS_2, and the E_F level is represented by a dotted line in Figure 4.3b-c. In the present study, the total number of eight electronic energy bands (four conduction bands (CBs) and four valence bands (VBs)) has been plotted around the Fermi level as shown in Figure 4.3b. The value of E_g (~1.95 eV) of Pt-ZrS_2 is smaller as compared to the pristine 2D monolayer ZrS_2 (2.13 eV), which indicates the contribution of 5d subshell electron density of states of the Pt atom. To support this, we computed and analyzed the DOS of Pt-ZrS_2 and the contributing components of the 5d orbital electron DOS of the Pt atom. From the DOS calculations, we observed that there is an electron density of states around the E_F, which makes the 2D monolayer Pt-ZrS_2 somewhat semiconducting in nature and may help to increase the catalytic efficiency, as the ORR involves the transportation of electrons. The 5d electron density was calculated by employing the similar DFT-D method, and the observed density close to the E_F comes from the doped Pt atom, i.e., the DOS follows the trace of the 5d orbital electron DOS of the Pt atom in Pt-ZrS_2, as represented in Figure 4.3c-d. So, the reduced bandgap and the existence of a small density near the E_F may enhance the conductivity of the 2D monolayer Pt-ZrS_2 which will help to quickly transfer electrons to the reaction during the ORR process. So, it is expected that Pt-ZrS_2 can serve as a good catalyst toward the ORR.

4.3.1 ORR Pathway: After determining the electronic properties and geometrical parameters of Pt-ZrS_2, the catalytic activity of this Pt-ZrS_2 TMD material toward the ORR has been explored by using the same level of theory. The Zr atom was replaced by the Pt atom to activate the inactive basal plane of the 2D monolayer ZrS_2, and the basal plane can provide a significant number of reaction sites, i.e., catalytic active sites for chemical reactions, especially the ORR. The active basal planes can distinctly boost the ORR activity of Pt-ZrS_2 due to the presence of Pt in the basal planes.

In this study, we have used a 2 × 2 supercell of the Pt-ZrS_2 slab to investigate the ORR steps based on a Computational Hydrogen Electrode (CHE) model developed by Nørskov et al[43]. The CHE approach allows the alignment of theoretical electrochemical potentials calculated with ab initio methods to those measured in the experiment. It contributed greatly to opening up the fields of electrochemistry and photo electrochemistry to theoretical treatment. The CHE method enables the evaluation of the relative free energies of intermediates along an electrochemical reaction network. The simple description of the ORR mechanism includes the

transportation of electrons and protons, which come from the anode side of the fuel cell, and adsorption preferences of reaction species involved in the ORR mechanism, such as O, OOH, and OH, on the surface of Pt-ZrS_2. The next step is to analyze the overall energetics for the ORR process along with the various chemical reaction pathways. To understand the whole ORR process in acidic media on the surfaces of Pt-ZrS_2, we need to explore and study the adsorption energies of the different intermediates or species/reaction steps and the possible molecular adsorption configurations of the various species in the reaction mechanism, including O_2, OOH, O, and H_2O at the CHE. The inactive site, where Pt is substitutionally doped in place of Zr, is the most favorable reaction site, i.e., highly active for the reaction at standard conditions, i.e., SHE conditions. There could be three active sites of the Pt-ZrS_2 system (namely the Pt site, Zr site, and S site) for the reduction of O_2. ORR can happen among any of the active sites. In search of an appropriate reaction site or to find the most favorable active site for the O_2 molecule adsorption, we computed the adsorption energy strength of the O_2 molecule at each possible site. The adsorption energy was calculated to be 1.24 eV, 0.80 eV, and 0.14 eV at the Pt site, Zr site, and S site, respectively, as tabulated in Table 4.2. It was found that the adsorption of the O_2 molecule on the Pt (1.24 eV) and Zr (0.80 eV) sites is endothermic with a high positive value of energy as compared to the S site (0.14 eV). So, comparing the adsorption energy strength of O_2 molecules at different possible sites suggests that the S site will be the most favorable site for the ORR mechanism. So, the whole reaction will occur at the S site of Pt-ZrS_2, and the S site will serve as the most active site for ORR intermediates. The role of Pt doping is to influence the electronic properties and activate the chalcogen atomic plane

Table 4.2. *Adsorption energy strength of O_2 at the different possible sites.*

Possible reaction sites	Adsorption energy of the O_2 molecule (eV)
Pt	1.24
Zr	0.80
S	0.14

of the ZrS_2. Recently, Pakhira and Upadhyay reported that for the 2D monolayer Pt-$MoSe_2$ and Janus MoSSe transition metal dichalcogenides, the chalcogen atomic layer (especially edges or doping area) acts as an active site for the electrochemical reactions such as the ORR and HER[44,45]. These articles quite support our findings. It was found that the various reaction

intermediates prefer to attach at the top of the upper sulfur atom (S) site i.e., the top layer of Pt-ZrS_2 is energetically more favorable for the adsorption during the ORR process than inner or lower layer. To study the different reaction pathways for the ORR, we considered the change in adsorption of possible reaction species or intermediates at U = 0 V and pH = 0 i.e., on the principle of the CHE model. The equilibrium geometries of the reaction intermediates formed during the ORR process were obtained by using the same level of theory, and they (top and side view structures of all the ORR intermediates) are shown in Figure 4.4. At the very beginning of the ORR process, adsorption and activation of O_2 are taken into consideration first. The adsorption of O_2 plays an important role in the opening stage of ORR catalysis, and the adsorption of the O_2 molecule on the catalytic surface further affects the whole catalytic performance. The adsorption of O_2 on the surface of Pt-ZrS_2 is done by adding the O_2 molecule on the S site (nearest to the Pt atom) i.e., by forming a bond to the S atom, which is bonded with the Pt atom, as depicted in Figure 4.4. The O_2 molecule prefers to adsorb on the S site as the S layer is the topmost layer of the 2D monolayer Pt-ZrS_2 and the active site for the ORR. We can say that this S site (nearest to the Pt atom) works as an active site for the adsorption of the O_2 molecule. The adsorption energy of the O_2 molecule should be moderate, i.e., neither too positive nor too negative. The high value of negative adsorption energy suggests the strong adsorption force between the O_2 molecule and the adsorption site of the catalyst. This strong adsorption force between the O_2 and catalytic surface causes the catalytic surface to be covered by the O_2 molecule, which would constrain further ORR steps. A positive adsorption energy indicates a weak adsorption force between the O_2 and catalytic surface. This weak interaction between the O_2 and catalytic surface would cause difficulty in the initiation of the ORR mechanism.

The adsorption energy of O_2*_Pt-ZrS_2 was calculated to be +0.14 eV, which can be considered fair in this study. The positive adsorption energy indicates that O_2 on the S site is not stable and would readily proceed for the subsequent steps of the ORR. The equilibrium O-O bond length in O_2*_Pt-ZrS_2 has been slightly elongated from 1.21 Å (in the case of the pure O_2 molecule) to 1.26 Å, and now, this will dissociate into two oxygen atoms at the two different S sites near the substituted Pt atom. In other words, compared with the original equilibrium O-O bond length in O_2 (1.21 Å), the adsorbed O-O bond length on the surfaces of Pt-ZrS_2 stretches by an amount of 0.05 Å, reflecting that the O_2 molecule has been readily activated by Pt-ZrS_2 and is ready to proceed further with the ORR mechanism. For an electrochemical reaction to occur spontaneously,

the change in reaction energy should be zero ideally. But practically, the change in reaction energy should be close to zero. The activation of the O_2 molecule on the Pt-ZrS_2 surface depends on two factors: (1) adsorption energy of O_2 with an active catalytic site and (2) bond elongation (i.e., charge transfer mechanism) of the adsorbed O_2 molecule on the catalytic site. For the adsorption of O_2, the change in adsorption energy was found at 0.14 eV, which is positive but, it is very close to zero. The positive change in adsorption energy indicates the endothermic nature of the reaction, suggesting the weak binding of the O_2 molecule on the S site of Pt-ZrS_2. However, weak binding is also beneficial for this case. As the O_2 adsorption is the initial step of the ORR mechanism, due to this very weak interaction, the O_2 will easily leave the active site, and the site will be readily available for the next O_2 activation cycle. This will help to increase the kinetics of the reaction. The next important factor which is crucial to activate the O_2 molecule is the bond elongation of the covalent bond O-O as compared to the original O-O equilibrium bond length (1.21 Å), which suggests that the bond dissociation begins during this stage. In our case, the O-O bond has been elongated by an amount of 0.05 Å from the equilibrium bond distance. The bond elongation happens due to the partial charge transfer from the S site to the adsorbed oxygen molecule. With the help of Mullikan charge transfer, we have observed that a charge transfer of 0.034|e| occurs during the oxygen molecule adsorption on the S site. This charge transfer thus results in the elongation process. So, considering all these factors, we have claimed that oxygen has been activated on the catalytic site. It was computationally reported that there is a small increment during the O_2 adsorption of PtTe monolayer material and Pt (111) surfaces[46].

The average equilibrium bond length of Zr-S was found to be 2.54 Å in O_2*_Pt-ZrS_2, which has not been stretched much after the adsorption of the O_2 molecule on the surfaces of Pt- ZrS_2, as tabulated in Table 4.5. Upon being adsorbed on the S site of Pt-ZrS_2, the equilibrium average S-O bond length was calculated to be 3.11 Å, as tabulated in Table 4.5. After the adsorption of O_2 on the 2D monolayer Pt-ZrS_2 surface, it may hydrogenate to form O_OH*, or the adsorbed O_2* may dissociate into two activated oxygen atoms at the two different adsorption sites on the surface of the 2D monolayer Pt-ZrS_2. The formation of O_OH* occurs in the associative path of the ORR mechanism. The O_OH* species formation happens by the hydrogenation of the adsorbed O_2* molecule with a proton-electron ($H^+ + e^-$) pair coming from the anode side of the fuel cell. We attempted to identify the favorability of the formation of O_OH* by calculating the adsorption energy of O_OH. The change in adsorption energy for the reaction ($O_2^* + H^+ + e^- \rightarrow$ O_OH*) was

found to be +5.44 eV, as reported in Table 4.3. This indicates that the reaction $O_2 + H^+ + e^- \rightarrow$ O_OH* is highly endothermic in nature and hence thermodynamically unfavorable. Therefore, it requires +5.41 eV extra energy to start the ORR during the associative reaction for the ORR. Thus, the 2D monolayer Pt-ZrS_2 is not favorable for O_OH* production. Thus, we have skipped the associative $4e^-$ and $2e^-$ pathways, and the results are excluded from the main manuscript; on the other hand, the dissociative $4e^-$ pathway is energetically favorable toward the ORR.

Table 4.3. *Adsorption energy of the O_OH* intermediate.*

Reaction intermediate	Adsorption energy (eV)
O_OH*	+5.44

The adsorption energy for the protonation of adsorbed O_2 was found to be 5.44 eV, and for the dissociation of adsorbed O_2 into two oxygen atoms, it was found to be -0.34 eV, reported in Tables 4.3 and 4.4. Comparing the adsorption energies of both reaction steps, it was found that the hydrogenation of O_2 has quite large positive adsorption energy (5.44 eV) as compared to the ideal adsorption energy (-0.34 eV) for the dissociation of the O_2 molecule into its constituents. So, from the analysis of the values of adsorption energy, it is concluded that the four-electron transfer associative reaction path and two-electron sluggish path are energetically unfavorable and would be compressed by the four-electron dissociative pathway. Hence, the adsorbed O_2* on the surface of the 2D monolayer Pt-ZrS_2 prefers the four-electron ($4e^-$) dissociative pathway to complete the ORR mechanism. The equilibrium Zr-S, Pt-S, and S-O bond lengths of the reaction intermediate 2O*_Pt-ZrS_2 formed during the ORR were found to be 2.55 Å, 2.48 Å, and 1.55 Å, respectively, as tabulated in Table 4.5.

Now, the next step of the ORR in the dissociative mechanism is hydrogenation of the 2O*, in which one of the adsorbed oxygen atoms reacts with the proton (H^+). Toward the cathode side, the proton exchange membrane transfers the proton, while the electron is transported by the external circuit to the cathode side; then, this electron-proton pair reacts with the O atom. The hydrogenation of 2O* gives O*_OH* with an adsorption energy of -1.22 eV, which is also negative, so this is an exothermic reaction and energetically favorable, as reported in Table 4.4. The equilibrium S-OH bond length between the S and OH was found to be 1.66 Å, which is greater

than that of the S-O bond length in the previous step. This result indicates that adsorbed OH species could react with another H^+ species and an electron to proceed further with the ORR steps. The equilibrium Zr-S, Pt-S, and S-O bond distances were calculated to be 2.55 Å, 2.51 Å, and 1.58 Å, respectively, as tabulated in Table 4.5.

Table 4.4. *Change in adsorption energy (ΔE) of all the ORR intermediates.*

Various ORR steps	ΔE (eV)
[Pt-ZrS_2] → [O_2*_Pt-ZrS_2]	0.14
[O_2*_Pt-ZrS_2] → [2O*_Pt_ZrS_2]	-0.34
[2O*_Pt-ZrS_2] → [O*_OH*_Pt-ZrS_2]	-1.22
[O*_OH*_Pt-ZrS_2] → [O*_Pt-ZrS_2]	-2.34
[O*_Pt-ZrS_2] → [OH*_Pt-ZrS_2]	-0.83
[OH*_Pt-ZrS_2] → [Pt-ZrS_2]	-2.42

Now, the hydrogenation of O*_OH* can occur by two pathways: (i) in the first one, the adsorbed O_OH* reacts with an H^+ species, and an electron is generated at the anode to form hydrogen peroxide (H_2O_2). (ii) The second path could be that the adsorbed O*_OH* reacts with H^+ and e^- to form O* and a water molecule (H_2O). The product of the hydrogenation of O*_OH* will be H_2O_2* based on the first possibility of the hydrogenation of the same O_OH*. The adsorption energy of this reaction step was calculated as -7.65 eV, which is highly exothermic. So, it will be very difficult to remove H_2O_2 from the catalytic surface as it has a very high adsorption energy of about -7.65 eV, calculated by the DFT-D method. Hence, the value of adsorption energy for the hydrogenation reaction to form hydrogen peroxide (i.e., O*_OH* to H_2O_2* formation in this ORR process) is another support, which suggests that the $2e^-$ reduction of O_2 to form H_2O_2 is thermodynamically unfavorable. So, this path is greatly suppressed by the mechanism O*_OH* → O* + H_2O. The adsorption energy for the reaction step O*_OH* → O* + H_2O was calculated to be -2.34 eV, which is exothermic and thermodynamically favorable. So, it can be said that this reaction path is energetically favorable to process further ORR steps. During this step, the equilibrium S-O bond length was calculated as 1.55 Å, and the Zr-S and Pt-S bond lengths were

found to be 2.54 Å and 2.47 Å, respectively, as reported in Table 4.5. Now, after releasing the first H_2O, the hydrogenation of one remaining active O* takes place by absorbing another $H^+ + e^-$ pair generated at the anode. The initial state of this reaction step is adsorbed O* with a proton and electron species, and the final state would be adsorbed OH* at the S site of Pt-ZrS_2 ($O^* + H^+ + e^- \rightarrow OH^*$). The adsorption energy for this reaction step has been calculated to be -0.83 eV, which is negative and close to zero, so it is thermodynamically favorable for the reaction to proceed

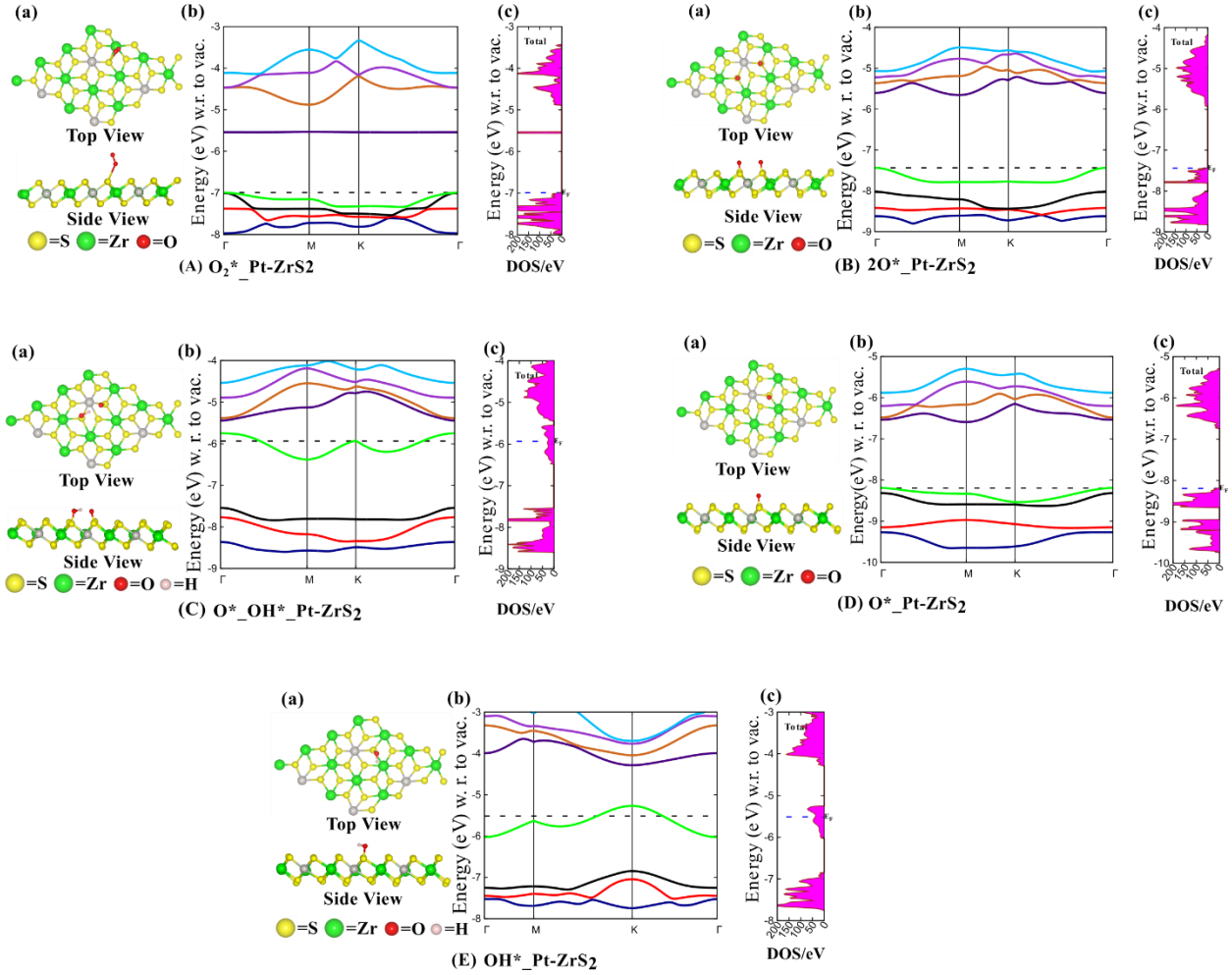

Figure 4.4. *Schematic illustrations of the equilibrium geometries and electronic properties of all the intermediate states appearing during the ORR process are plotted here: (a) O_2*_Pt-ZrS_2; (b) 2O*_Pt-ZrS_2; (c) O*_OH*_Pt-ZrS_2; (d) O*_Pt-ZrS_2; (e) OH*_Pt-ZrS_2.*

further. The equilibrium S-OH bond distance between S and OH was found to be 1.71 Å, which is larger than that of the previous step, as reported in Table 4.5. In the last step, the H^+ and e^- react with OH* to produce another H_2O molecule with the adsorption energy of -2.42 eV. The change of adsorption energy in each intermediate of the ORR steps was tabulated in Table 4.4. So, the

reaction pathway follows the $4e^-$ dissociative reaction pathway, and the reaction steps for the path are $O_2 \rightarrow O_2^* \rightarrow 2O^* \rightarrow O^*\_OH^* \rightarrow O^* + H_2O \rightarrow OH^* \rightarrow H_2O$. The equilibrium lattice constants, space group symmetry, and average bond lengths of each reaction intermediates in various steps during the ORR process are tabulated in Table 4.5 for a detailed comparison of these intermediates during

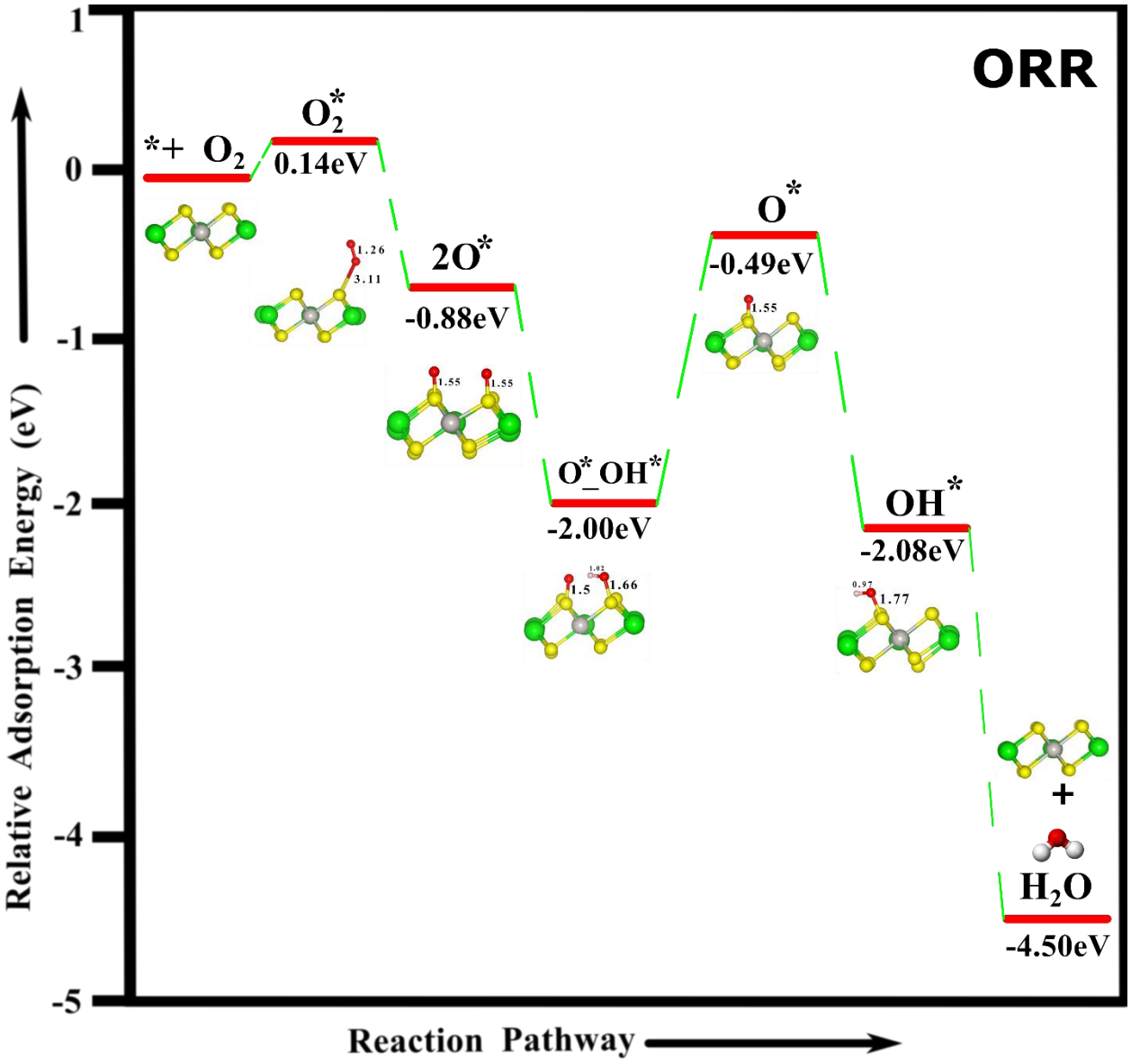

Figure 4.5. *Relative adsorption energy (eV) diagram i.e., potential energy surfaces (PESs), for $4e^-$ dissociative ORR pathways on the surfaces of Pt-ZrS_2.*

the subject reaction process. The electronic properties (i.e., band structure and DOS) of all reaction intermediates were computed and analyzed to observe the change in electronic properties during

the ORR steps. The electronic band structure and the DOS for each reaction intermediate step during the subject reaction were shown in Figure 4.4a-e. We observed that in the band structure calculations of the first hydrogenation step i.e., a step where the involvement of hydrogen takes place, i.e., O*_OH*_Pt-ZrS_2, the conduction band (CB) has been shifted toward the Fermi energy (E_F) level, and finally it crosses the Fermi level. The total DOS calculations show that there is a large electron density emerged at the Fermi energy level, indicating that the reaction intermediate O*_OH*_Pt-ZrS_2 (as shown in Figure 4.4a) has a metallic character in nature and will help in the propagation of electrons, which in turn enhances the efficiency of the ORR mechanism. We observed the same behavior in the next hydrogenation step, OH*_Pt-ZrS_2, i.e., in step four, where hydrogen reacts with the oxygen atom,

which is adsorbed in the 2D monolayer Pt-ZrS_2 surface. We have observed that both the valence bands and conduction bands from both sides shifted toward the Fermi energy level, and one of the conduction bands has crossed the Fermi level. This shows that the OH*_Pt-ZrS_2 material has metallic characteristics, as depicted in Figure 4.4e. The presence of electron density around the Fermi level

Table 4.5. *Equilibrium structural parameters and lattice constant and electronic band gap for different ORR intermediates.*

Reaction steps	**Lattice parameters (Å)**	**Interfacial angles (°)**	**Layer group symmetry**	**Electronic band gap (eV)**	**Average bond distance between atoms (Å)**			
					Zr-S	Pt-S	S-O	S-OH
O_2*_Pt-ZrS_2	a = 7.126, b = 7.120	α = β = 90.00, γ = 120.00	*P1*	1.44	2.551	2.463	3.11	
2O*_Pt-ZrS_2	a = 7.145, b = 7.211	α = β = 90.00, γ = 119.85	*P1*	1.65	2.550	2.484	1.551	
O*_OH*_Pt-ZrS_2	a = 7.090, b = 7.280	α = β = 90.00, γ = 119.43	*P1*	0.0	2.559	2.513	1.586	1.667

O*_Pt-ZrS$_2$	a = 7.144, b = 7.144	α = β = 90.00, γ = 119.48	*P1*	1.59	2.545	2.475	1.555	
OH*_Pt-ZrS$_2$	a = 7.219, b = 7.139	α = β = 90.00, γ = 120.17	*P1*	0.0	2.551	2.504		1.717

was confirmed by drawing the electronic band structure for this intermediate OH*_Pt-ZrS_2. The electronic band structure and total density of states for other ORR reaction intermediates/steps were also calculated at the same level of theory. The electronic band structure for reaction steps, including adsorption of O_2, O_2*_Pt-ZrS_2, O*_Pt-ZrS_2, and 2O*_Pt_ZrS_2, showed that these systems have some energy bandgaps obtained by the DFT-D method. But the conduction and valence bands have shrunk toward the Fermi energy level as compared to the 2D monolayer Pt-ZrS_2 material. The conduction band has somewhat touched the Fermi level in these systems, which suggests that these systems favor electron conduction. The band gap for these systems belongs to the semiconducting range, which can be considered ideal for the ORR mechanism.

To sum up the entire ORR mechanism, we constructed the chemical reaction pathway (i.e., potential energy surfaces (PESs) considering the relative adsorption energies of the reaction intermediates, which is also known as free energy vs. reaction coordinate diagram) of various ORR steps involved in the subject reaction with respect to relative changes in the adsorption energy of various ORR intermediates, as displayed in Figure 4.5. Here, the relative energy landscape has been plotted by taking into account the formation energy of the 2D monolayer Pt-ZrS_2 TMD material as a reference geometry with the change of relative energy about 0 eV. From the PES or reaction free energy diagram, i.e., the relative adsorption energy diagram, we observed that all the reaction intermediate steps are downhill in the diagram except O_2* and O*. The adsorption of O_2 on Pt-ZrS_2 is the starting point of the ORR, where the exterior S atomic layer (near the Pt atoms) of Pt-ZrS_2 was found to be the active site for O_2 activation rather than the inner Pt atoms, which is different from what was previously reported for the Pt-containing ORR electrocatalysts. The protonation of OH* to H_2O is the potential-limiting step for the whole ORR process in this case. The downhill steps in the energy curve suggest that all the reaction steps at the S site of Pt-ZrS_2 occur spontaneously. The activation energy values obtained here for all the reaction intermediates or species involved in the subject reaction are energetically favorable and kinetically

surmountable. Thus, it can be predicted that the $4e^-$ dissociative pathway of the ORR mechanism at the S site of Pt-ZrS_2 is thermodynamically favorable and kinetically feasible. Thus, Pt-ZrS_2 can be used as the cathode material of the fuel cell to reduce O_2 into water efficiently. The ORR takes place on the surface of the Pt-ZrS_2 TMD, considering the periodic 2D slab model. This is a solid-surface reaction. The reaction mechanism is explained by considering the adsorption energy of the reaction intermediates. It is not possible to calculate/locate the transition states in the periodic calculations on the surface of Pt-ZrS_2. So, in this study, the transition state calculations have not been performed. Similar kinds of studies were found in the literature[46].

4.4 Solvent Effect: Here, we employed the hybrid periodic DFT-D method to calculate the equilibrium structure and energies through the ORR process at the S site of the Pt-ZrS_2 TMD. This is a solid surface reaction, and it happens on the outer surface of the 2D layer of the Pt-ZrS_2 TMD. The study of the solvent effect is very relevant in the area of catalysis. Furthermore, understanding the reaction mechanism in the solvent phase for different electrochemical reactions is equally interesting and relevant. However, to accurately model the solvent model is a great task in computational catalysis, and it is also computationally costly to model the reaction steps[47,48]. In the case of a solvent environment, the solvent can chemically or physically interact with the adsorbates and catalytic surface. The solvent molecule can interact with adsorbates by hydrogen bonding. The effect of the solvent phase is very challenging due to the difficulties in precisely defining complex systems that can include simultaneous solvent-solvent, adsorbate solvent, adsorbent-solvent, and adsorbate-catalytic surface interactions. The main concern is to define accurately the interaction potential and exchange-correlation functional involved in the solvent phase. Adding the solvent phase can lead to large systems that have a number of possible thermodynamic and geometrical configurations. So, finding a relevant configuration is equally challenging. In addition to this, the solvent phase is the main component of the reaction medium. So, the physical properties (polarity, viscosity, ability to react with adsorbates) alter the reaction kinetics by affecting mass and heat transfer. So, defining accurately the effect of the solvent due to its own properties on the reaction is not trivial. Due to these complications, often the solvent phase for DFT calculations is ignored and approximated by the vacuum or gas phase, and moreover, we incorporated the relative energy changes during the reactions where the solvation effects are negligible.

However, the presence of a solvent environment can have some effect on the adsorption strength of the reaction intermediates. A vast majority of studies have been done by employing different models and methods to accurately define the solvent effect on electrochemical reactions. One of the approaches to describe the solvent effect is to use the implicit solvent model. The system is surrounded by a continuous solvent in the implicit model. This method is computationally cheaper but ignores the adsorbate solvent interactions, such as hydrogen bonding, which is crucial in stabilizing the reaction intermediates. Molecular dynamics (MD) simulation is considered one of the elegant methods and models to accurately define the solvent effect. *Ab initio* molecular dynamics (AIMD) and classical force field simulation are one of the suitable simulations for this task[49]. However, these methods have high computational costs, and simulation requires a reliable potential for adsorbate-metal surface interaction, which is difficult to find due to the lack of experimental data in this field. To overcome these limitations, a combined quantum mechanical/molecular mechanical (QM/MM) approach has been employed to predict the more accurate effect of a solvent during an electrochemical reaction[50]. Due to the cost of computations, we excluded the solvent phase calculations in the present study.

4.5 Conclusions: In summary, we have carried out a DFT-D based systematic theoretical and computational study of structural and electronic properties with the electrocatalytic activity of the 2D monolayer Pt-ZrS_2 toward ORR. We computed the intrinsic electronic band structures and DOS of the 2D monolayer pristine ZrS_2 and Pt-ZrS_2 TMDs to investigate their electronic properties. We found that the electronic band gap E_g of both the 2D monolayer ZrS_2 and Pt-ZrS_2 are about 2.13 eV and 1.95 eV, respectively. The lower value of E_g i.e., the electronic bandgap of the 2D monolayer Pt-ZrS_2, suggests that it can be used as an electrocatalyst for the ORR. The catalytic performance of the 2D monolayer Pt-ZrS_2 was studied based on the changes in the adsorption energy of the intermediates/species involved in the subject reaction during the ORR process on the surface of the 2D monolayer Pt-ZrS_2. We observed that the 2D monolayer Pt-ZrS_2 not only provides active reaction sites but also shows excellent performance for the ORR. It was found that for all the considered adsorbates, the most preferred site is S, which is bonded with the Pt atom. So, the whole ORR mechanism has been carried out by considering the S site as the active site for the ORR intermediates. The ORR catalyzed by the 2D monolayer Pt-ZrS_2 is initiated by the adsorption of O_2 on the S site which is bonded with the Pt atom and completed by the removal of the H_2O molecule. We observed that the adsorption of O_2 is the weakest, having an adsorption

energy of 0.14 eV. So, this suggests that the O_2 dissociates easily into its fragments, which is essential to start the ORR mechanism. We noticed that the change in adsorption energy in each intermediate reaction step is negative suggesting that all the reaction steps are energetically favorable in the subject reaction. We found that the ORR steps prefer to take place through a more efficient $4e^-$ dissociative pathway. This study indicates that the 2D monolayer Pt-ZrS_2 acts as a promising ORR catalyst and follows the $4e^-$ path to reduce O_2. According to the relative adsorption energy diagram of the ORR intermediates obtained by the B3LYP-D3 method, all the reaction steps in acidic environments are downhill in the potential energy surface. The change in adsorption energy of the reaction step $O_2 \rightarrow O_2*$ was found to be 0.14 eV (which indicates a little hump). Therefore, our theoretical results would be useful to design highly efficient 2D monolayer Pt-ZrS_2 based catalysts for fuel cells. It is expected that these results would bring more experimental and theoretical insights to explore the potential of 2D monolayer Pt-ZrS_2 based materials as an efficient electrocatalyst for the ORR.

4.6 References:

[1] Y. Shao, S. Park, J. Xiao, J. G. Zhang, Y. Wang, J. Liu, Electrocatalysts for nonaqueous lithium-air batteries: Status, challenges, and perspective, ACS Catal. 2 (2012) 844–857.

[2] Y. Jiao, Y. Zheng, M. Jaroniec, S. Z. Qiao, Design of electrocatalysts for oxygen- and hydrogen-involving energy conversion reactions, Chem. Soc. Rev. 44 (2015) 2060–2086.

[3] J. Ying, Atomic-scale design of high-performance Pt-based electrocatalysts for oxygen reduction reaction, Front. Chem. 9 (2021) 753604.

[4] S. Sui, X. Wang, X. Zhou, Y. Su, S. Riffat, C. jun Liu, A comprehensive review of Pt electrocatalysts for the oxygen reduction reaction: Nanostructure, activity, mechanism and carbon support in PEM fuel cells, J. Mater. Chem. A. 5 (2017) 1808–1825.

[5] S. Zaman, L. Huang, A.I. Douka, H. Yang, B. You, B.Y. Xia, Oxygen reduction electrocatalysts toward practical fuel cells: progress and perspectives, Angew. Chemie - Int. Ed. 60 (2021) 17832–17852.

[6] A. Kulkarni, S. Siahrostami, A. Patel, J. K. Nørskov, Understanding catalytic activity Trends in the oxygen reduction reaction, Chem. Rev. 118 (2018) 2302–2312.

[7] B. Wang, Recent development of non-platinum catalysts for oxygen reduction reaction, J. Power Sources 152 (2005) 1–15.

[8] Y. Wang, Y. Yang, S. Jia, X. Wang, K. Lyu, Y. Peng, H. Zheng, X. Wei, H. Ren, L. Xiao, J. Wang, D.A. Muller, H.D. Abruña, B.J. Hwang, J. Lu, L. Zhuang, Synergistic Mn-Co catalyst outperforms Pt on high-rate oxygen reduction for alkaline polymer electrolyte fuel cells, Nat. Commun. 10 (2019) 6–13.

[9] X. Feng Lu, S. Lin Zhang, W, Lok Sim, S, Gao, X, Wen (David) Lou, Phosphorized $CoNi_2S_4$ Yolk-Shell Spheres for Highly EfficientHydrogen Production via Water and Urea Electrolysis, Angew. Chem. Int. Ed. 60 (2021) 22885–22891.

[10] X. F. Lu, Y. Chen, S. Wang, S. Gao, X. W. Lou, Interfacing manganese oxide and cobalt in porous graphitic carbon polyhedrons boosts oxygen electrocatalysis for Zn–air batteries, Adv. Mater. 31 (2019) 1902339.

[11] S. Zhang, D. Zhai, T. Sun, A. Han, Y. Zhai, W.C. Cheong, Y. Liu, C. Su, D. Wang, Y. Li, In situ embedding Co_9S_8 into nitrogen and sulfur codoped hollow porous carbon as a bifunctional electrocatalyst for oxygen reduction and hydrogen evolution reactions, Appl. Catal. B Environ. 254 (2019) 186–193.

[12] Y. Li, D. Xiong, Y. Liu, M. Liu, J. Liu, C. Liang, C. Li, J. Xu, Correlation between electrochemical performance degradation and catalyst structural parameters on polymer electrolyte membrane fuel cell, Nanotechnol. Rev. 8 (2020) 493–502.

[13] X. F. Lu, B. Y. Xia, S. Q. Zang, X. W. Lou, Metal-organic frameworks based electrocatalysts for the oxygen reduction reaction, Angew. Chemie - Int. Ed. 59 (2020) 4634–4650.

[14] B. Mortazavi, I. S. Novikov, E. V. Podryabinkin, S. Roche, T. Rabczuk, A. V. Shapeev, X. Zhuang, Exploring phononic properties of two-dimensional materials using machine learning interatomic potentials, Appl. Mater. Today. 20 (2020) 100685.

[15] S. H. Mir, S. Chakraborty, P. C. Jha, J. Wärnå, H. Soni, P. K. Jha, R. Ahuja, Two-dimensional boron: Lightest catalyst for hydrogen and oxygen evolution reaction, Appl.

Phys. Lett. 109 (2016) 053903.

[16] N. N. Som, V. Mankad, P. K. Jha, Hydrogen evolution reaction: The role of arsenene nanosheet and dopant, Int. J. Hydrogen Energy. 43 (2018) 21634–21641.

[17] A. Eftekhari, Electrocatalysts for hydrogen evolution reaction, Int. J. Hydrogen Energy. 42 (2017) 11053–11077.

[18] F. Li, M. Xue, . Two-Dimensional Transition Metal Dichalcogenides for Electrocatalytic Energy Conversion Applications. Two-dimensional Materials - Synthesis, Characterization and Potential Applications, 1st edition; Intech Open: London, United Kingdom, 2016; pp 64−84, DOI: 10.5772/63947.

[19] H. Xu, J. Zhu, Q. Ma, J. Ma, H. Bai, L. Chen, S. Mu, Two-dimensional MoS_2: Structural properties, synthesis methods, and regulation strategies toward oxygen reduction, Micromachines. 12 (2021) 240.

[20] J. Luxa, V. Mazánek, M. Pumera, P. Lazar, D. Sedmidubský, M. Callisti, T. Polcar, Z. Sofer, 2H→1T phase engineering of layered tantalum disulfides in electrocatalysis: Oxygen reduction reaction, Chem. - A Eur. J. 23 (2017) 8082–8091.

[21] X. Yu, Y. Ding, J. Sun, Design principles for 2D transition metal dichalcogenides toward lithium−sulfur batteries, IScience. 26 (2023) 107489.

[22] H. Jin, C. Guo, X. Liu, J. Liu, A. Vasileff, Y. Jiao, Y. Zheng, S. Z. Qiao, Emerging two-dimensional nanomaterials for electrocatalysis, Chem. Rev. 118 (2018) 6337–6408.

[23] M. Pumera, Materials electrochemists' never-ending quest for efficient electrocatalysts: The devil is in the impurities, ACS Catal. 10 (2020) 7087–7092.

[24] J. Xiao, J. Wang, Z. Xue, T. Zhang, J. Wang, Q. Li, The study of oxygen reduction reaction on Ge-doped MoS_2 monolayer based on first principle, Int. J. Energy Res. 45 (2021) 13748–13759.

[25] V. Urbanová, N. Antonatos, J. Plutnar, P. Lazar, J. Michalička, M. Otyepka, Z. Sofer, M. Pumera, Rhenium doping of layered transition-metal diselenides triggers enhancement of

photoelectrochemical activity, ACS Nano. 15 (2021) 2374–2385.

[26] S. N. Upadhyay, S. Pakhira, Mechanism of electrochemical oxygen reduction reaction at two-dimensional Pt-doped $MoSe_2$ material: an efficient electrocatalyst, J. Mater. Chem. C. 9 (2021) 11331–11342.

[27] H. L. Chia, C. C. Mayorga-Martinez, M. Pumera, Doping and decorating 2D materials for biosensing: Benefits and drawbacks, Adv. Funct. Mater. 31 (2021) 2102555.

[28] L. Zhang, T. Yang, W. Zhang, D. Qi, X. He, K. Xing, P. K. J. Wong, Y. P. Feng, A. T. S. Wee, Bi-stable electronic states of cobalt phthalocyanine molecules on two-dimensional vanadium diselenide, Appl. Mater. Today. 18 (2020) 100535.

[29] Y. Wen, Y. Zhu, S. Zhang, Low-temperature synthesis of ZrS_2 nanoflakes and their catalytic activity, RSC Adv. 5 (2015) 66082–66085.

[30] N. N. Som, P. K. Jha, Hydrogen evolution reaction of metal di-chalcogenides: ZrS_2, $ZrSe_2$ and Janus ZrSSe, Int. J. Hydrogen Energy. 45 (2020) 23920–23927.

[31] R.J. Toh, Z. Sofer, M. Pumera, Catalytic properties of group 4 transition metal dichalcogenides (MX_2; M = Ti, Zr, Hf; X = S, Se, Te), J. Mater. Chem. A. 4 (2016) 18322–18334.

[32] Y. Shimazu, Y. Fujisawa, K. Arai, T. Iwabuchi, K. Suzuki, Synthesis and characterization of zirconium disulfide single crystals and thin-film transistors based on multilayer zirconium disulfide flakes, ChemNanoMat. 4 (2018) 1078–1082.

[33] R. Dovesi, A. Erba, R. Orlando, C. M. Zicovich-Wilson, B. Civalleri, L. Maschio, M. Rérat, S. Casassa, J. Baima, S. Salustro, B. Kirtman, Quantum-mechanical condensed matter simulations with CRYSTAL, Wiley Interdiscip. Rev. Comput. Mol. Sci. 8 (2018) e1360.

[34] S. Grimme, J. Antony, S. Ehrlich, H. Krieg, A consistent and accurate ab initio parametrization of density functional dispersion correction (DFT-D) for the 94 elements H-Pu, J. Chem. Phys. 132 (2010) 154104.

[35] S. Pakhira, J.L. Mendoza-Cortes, Tuning the Dirac cone of bilayer and bulk structure

graphene by intercalating first-row transition metals using first-principles calculations, J. Phys. Chem. C. 122 (2018) 4768–4782.

[36] K. Liang, S. Pakhira, Z. Yang, A. Nijamudheen, L. Ju, M. Wang, C.I. Aguirre-Velez, G. E. Sterbinsky, Y. Du, Z. Feng, J. L. Mendoza-Cortes, Y. Yang, S-Doped MoP nanoporous layer toward high-efficiency hydrogen evolution in pH-universal electrolyte, ACS Catal. 9 (2019) 651–659.

[37] S. Pakhira, Rotational dynamics of the organic bridging linkers in metal-organic frameworks and their substituent effects on the rotational energy barrier, RSC Adv. 9 (2019) 38137–38147.

[38] K. Momma, F. Izumi, VESTA 3 for three-dimensional visualization of crystal, volumetric and morphology data, J. Appl. Crystallogr. 44 (2011) 1272–1276.

[39] H. J. Monkhorst, J. D. Pack, Special points for Brillonin-zone integrations, Physical Review B 13 (1976) 5188.

[40] R. Ma, G. Lin, Y. Zhou, Q. Liu, T. Zhang, G. Shan, M. Yang, J. Wang, A review of oxygen reduction mechanisms for metal-free carbon-based electrocatalysts, Npj Comput. Mater. 5 (2019) 78.

[41] G. Fazio, L. Ferrighi, D. Perilli, C. Di Valentin, Computational electrochemistry of doped graphene as electrocatalytic material in fuel cells, Int. J. Quantum Chem. 116 (2016) 1623–1640.

[42] Y. Ji, M. Yang, H. Dong, L. Wang, T. Hou, Y. Li, Monolayer group IVA monochalcogenides as potential and efficient catalysts for the oxygen reduction reaction from first-principles calculations, J. Mater. Chem. A. 5 (2017) 1734–1741.

[43] J. K. Nørskov, J. Rossmeisl, A. Logadottir, L. Lindqvist, J.R. Kitchin, T. Bligaard, H. Jónsson, Origin of the overpotential for oxygen reduction at a fuel-cell cathode, J. Phys. Chem. B. 108 (2004) 17886–17892.

[44] S. N. Upadhyay, S. Pakhira, Mechanism of electrochemical oxygen reduction reaction at two-dimensional Pt-doped $MoSe_2$ material: an efficient electrocatalyst, J. Mater. Chem. C.

9 (2021) 11331–11342.

[45] S. Pakhira, S. N. Upadhyay, Efficient electrocatalytic H_2 evolution mediated by 2D Janus MoSSe transition metal dichalcogenide, Sustain. Energy Fuels 6 (2022) 1733–1752.

[46] Y. Wang, Y. Li, T. Heine, PtTe monolayer: Two-dimensional electrocatalyst with high Basal plane activity toward oxygen reduction reaction, J. Am. Chem. Soc. 140 (2018) 12732–12735.

[47] S. K. Iyemperumal, N. A. Deskins, Evaluating Solvent Effects at the Aqueous/Pt(111) Interface, ChemPhysChem. 18 (2017) 2171–2190.

[48] J. Carrasco, A. Hodgson, A. Michaelides, A molecular perspective of water at metal interfaces, Nat. Mater. 11 (2012) 667–674.

[49] H. Cao, G.J. Xia, J. W. Chen, H. M. Yan, Z. Huang, Y. G. Wang, Mechanistic insight into the oxygen reduction reaction on the Mn-N_4/C single-atom catalyst: The role of the solvent environment, J. Phys. Chem. C. 124 (2020) 7287–7294.

[50] S. N. Steinmann, P. Sautet, C. Michel, Solvation free energies for periodic surfaces: comparison of implicit and explicit solvation models, Phys. Chem. Chem. Phys. 18 (2016) 31850–31861.

CHAPTER 5

Revealing the Mechanism and Activity of O_2 Reduction Reaction of Co Nanocluster Encapsulated by Carbon Nanotube

Exploration of inexpensive electrocatalysts with excellent catalytic activity and chemical stability for the oxygen reduction reaction (ORR) is crucial for the widespread adoption of sustainable and renewable energy conversion technologies in practical applications. In this chapter, we introduce the potential of cobalt nanoparticle-encapsulated single-wall carbon nanotubes (Co@SWCNT) as efficient electrocatalysts for ORR. This study represents a significant step forward in the quest for high-performance, non-precious metal catalysts for energy conversion technologies. We have begun this chapter by discussing the extensive efforts in the field to develop carbon-based electrocatalysts for electrochemical reactions, particularly the oxygen reduction reaction (ORR). We have also highlighted the distinctive properties of carbon-based materials that have made them suitable for ORR electrocatalysis. The chapter has then transitioned to a brief highlight of different types of carbon nanotubes (CNTs), including armchair, zig-zag, and chiral nanotubes. It has provided an overview of their structural variations and significance in electrocatalysis. Among these, the chapter has specifically focused on the (6,6) armchair SWCNT, which has been used in this study due to its advantageous stability and electronic properties. The chapter has then highlighted the computational methods and theoretical framework that have been employed to conduct the ORR mechanism on the surface of Co@SWCNT., exploring reaction pathways and catalytic efficiency. Following this, we have presented a detailed analysis of the results obtained from these simulations. The results section has initially examined the impact of Co nanoparticles on the electronic properties of the SWCNT and has observed that Co@SWCNT has exhibited metallic characteristics. The study has focused on determining the adsorption

energy (ΔE) of ORR species on the Co@SWCNT surface to comprehend its electrocatalytic efficiency and performance toward ORR. Within this, we have proposed two potential ORR mechanisms: a direct four-electron ($4e^-$) transfer pathway and a series of two-electron ($2e^-$) transfer pathways. The value of ΔE of the 2O ORR intermediate has been determined to be -0.35 eV, and for the OOH* ORR intermediate, the value of ΔE is about -3.59 eV. This suggests that the $4e^-$ dissociative pathway could be the thermodynamically favorable path for the O_2 reduction reaction compared to the $4e^-$ associative and $2e^-$ pathways of ORR. The chapter concludes by discussing the broader implications of our research, emphasizing the promise of Co@SWCNT as a cost-effective and highly durable nonmetal catalyst and its potential to advance renewable energy and fuel cell technologies.*

5.1 Introduction: To tackle the issues related to the utilization of carbon-containing fossil fuels, there has been a growing global focus on transitioning toward cleaner and more sustainable energy sources. Devices that generate electrical energy from chemical reactions, such as batteries and fuel cells, are receiving considerable attention in applications ranging from electronics to automotive industries[1,2]. Designing an effective and sustainable electrocatalyst is a focal point to enhance the ability of the electrode toward O_2 reduction to have widespread accessibility and commercialization of sustainable and renewable energy conversion devices. A variety of catalytic materials have been proposed as suitable electrocatalysts for the ORR. Pt-based substances or materials have served as dynamic and efficient electrocatalysts for the ORR[3]. Nevertheless, these catalytic materials encounter various challenges and issues, for instance, byproduct sensitivity and instability over prolonged operation periods. Moreover, the exorbitant expenses and limited availability hinder their widespread implementation in practical large-scale applications. Currently, there is a significant focus on research aimed at creating nonprecious and nonmetal electrocatalysts for applications in metal−air batteries, renewable energy technology, sustainable energy processes, and fuel cells. Among various candidates, carbon-based electrocatalysts such as carbon nanotubes (CNTs) and nitrogen-doped CNTs have demonstrated their effectiveness as metal-free electrocatalysts toward the high-performance ORR[4]. They exhibit robust durability and resistance to byproduct poisoning. These carbon-based electrocatalysts have been shown to meet these practical requirements. Especially the CNTs have demonstrated a great capability to serve as substitutes for conventional catalyst support owing to their considerable advantages[5,6]: (a) large specific area, (b) high electric conductivity, (c) impressive mechanical and thermal stabilities, (d) tolerance against poisoning effect, (e) facilitate easy

chemical surface functionalization, (f) enable the deposition of catalytic phases on their external surfaces or within their inner cavities, and (g) alter their chemical composition such as nitrogen-doped and boron-doped CNTs.

Numerous carbon materials incorporating heteroatoms, such as B-doped CNTs, sulphur-doped graphene, and phosphorus-doped graphite layer, were investigated for ORR[7–9]. In recent studies, researchers discovered that nitrogen-doped CNTs embedded with Fe-Co-Cr alloy-based nanoparticles show promising potential for enhancing the electrocatalytic activity in the Zn-air batteries[10]. Niu et al. experimentally and theoretically reported that the encapsulated CoNi nanoparticles within the N-doped carbon nanotube (NCNT), i.e., CoNi@NCNT, show remarkable catalytic activity in both ORR and oxygen evolution reaction (OER)[11]. They concluded that the CoNi@NCNT appears as an advanced electrocatalyst for effective ORR and OER, and the activity primarily arises from the synergetic contributions of NCNT, and the active sites located proximately to CoNi nanoparticles on NCNT. Liu et al. conducted a study on the utilization of Fe, Co, and Ni nanoparticles encapsulated in nitrogen-doped CNTs as electrocatalysts for ORR. They demonstrated that the Co@NCNT catalyst displayed exceptional catalytic activity, demonstrating high efficiency, selectivity, and long-term durability[12]. In addition, researchers recently synthesized CNTs doped with the Co and N atoms through various experimental methods and investigated their effectiveness in catalyzing the ORR. These synthesized Co- and N-doped CNTs displayed impressive catalytic activity, stability, and resistance to fuel cell crossover effects in both acidic and alkaline environments[13]. Additionally, Wang et al. created cobalt-embedded N-doped carbon nanotubes and examined their catalytic performance toward both the ORR and OER. Their findings demonstrated that these nanotubes exhibit comparable performance to Pt/C in alkaline and neutral conditions for ORR[14]. Rao et al. experimentally synthesized the S, N-co-doped CNT encased Co nanoparticles and studied their stability and electrocatalytic performance for both the ORR and OER. They found that the S, N-Co@CNT demonstrates excellent durability and stability in an alkaline medium and shows good catalytic activity toward both the ORR and OER[15]. In a recent publication, the researchers reported the synthesis of the M/CeO_2 (M = Fe, Co, Ni) electrocatalyst via the coprecipitation method, followed by the creation of the M@CNT/CeO_2 composites through ethanol decomposition. Their finding showcased a notable variation in the electrocatalytic activity toward H_2 evolution reaction (HER) among different variants, with the Co@CNT/CeO_2 demonstrating significantly higher performance than both the Fe@CNT/CeO_2 and Ni@CNT/CeO_2[16]. Furthermore, the stability of the Co@CNT was

assessed through cyclic voltammetry, revealing its remarkable durability even after 800 cycles, indicating its potential as a nonprecious metal electrocatalyst. They also studied the catalytic activity of Co encapsulated in CNT by density functional theory (DFT) calculations, indicating a consistent relationship between experimental and theoretical results. Han et al. recently studied the carbon nanotube (CNT) encapsulated by transition-metal (TM) clusters for efficient HER by employing DFT method. They showed that the interaction of metal cluster atoms with carbon nanotube boosts the HER catalytic activity of the carbon nanotube[17]. Inspired by these intriguing findings, our aim is to investigate the electrocatalytic activity of Co nanoparticle-encapsulated SWCNT electrocatalyst toward ORR. Despite extensive research and considerable advancements made over several years, we still lack a complete understanding of the slow reaction rates and underlying mechanisms that govern the ORR.

Here, we have conducted a thorough investigation into the ORR mechanism and activity on the surface of the Co nanocluster encapsulated by a single-wall carbon nanotube denoted by Co@SWCNT in short. We computationally designed the Co@SWCNT structure and obtained its equilibrium configuration by employing the DFT-D3 method. The electronic property calculations have been performed at the relaxed geometry of the Co@SWCNT to reveal its conductive nature. Next, we focused on studying the ORR mechanism on the Co@SWCNT surface, especially near the Co nanoparticles. To assess the ORR activity of Co@SWCNT, we evaluated the ΔE of intermediates participating in both the $4e^-$ associative and dissociative reaction pathways. Our analysis demonstrates that the $4e^-$ dissociative pathway exhibits lower energy barriers compared to those of the associative pathway. Additionally, we constructed a potential energy surface (PES) based on the ΔE of ORR intermediates. The PES indicates that the Co@SWCNT exhibits a promising catalytic activity for ORR. Consequently, our findings suggest that the equilibrium Co@SWCNT catalyst demonstrates notable effectiveness and sustained stability in facilitating the ORR process. Our research highlights the potential of Co@SWCNT as an effective catalyst for ORR, offering opportunities to develop sustainable and durable ORR catalysts.

5.2 Methods and Computational Details:

5.2.1 Model. CNTs can be conceptualized as cylindrical structures formed by rolling up sheets of two-dimensional (2D) graphene. The distinct types of CNTs arise from variations in the rolling axis orientation during their fabrication process. This choice of axis alignment, relative to the hexagonal lattice of the graphene sheet, along with the cylinder's closing radius,

determines the characteristics of the resulting CNTs. The wrapping pattern of the graphene sheet is denoted by a pair of indices (m,n), where m and n are integers that represent the chiral symmetry. An (m=n) tube is referred to as an "armchair" configuration, as the hexagons in the tube align straight along its length, resembling the arms of an armchair. Conversely, a tube with indices (m,0) is termed a "zigzag" tube, as the hexagons zigzag down the length of the tube. Tubes with indices between these two extremes, such as (5,4), are called "chiral" tubes. SWCNT holds significant importance among carbon nanotubes, as many of their properties, such as band gap and electrical conductivity, exhibit notable variations based on the values of (m,n)[18,19].

In this work, the calculation was performed on a periodically repeated unit cell of a single-wall carbon nanotube (in short, SWCNT) as depicted in Figure 5.1a. We utilized an armchair SWCNT with a (6,6) chiral symmetry in our research investigation. A Co metal nanoparticle cluster (Co_4) has been encapsulated inside the channel of the SWCNT, i.e., the

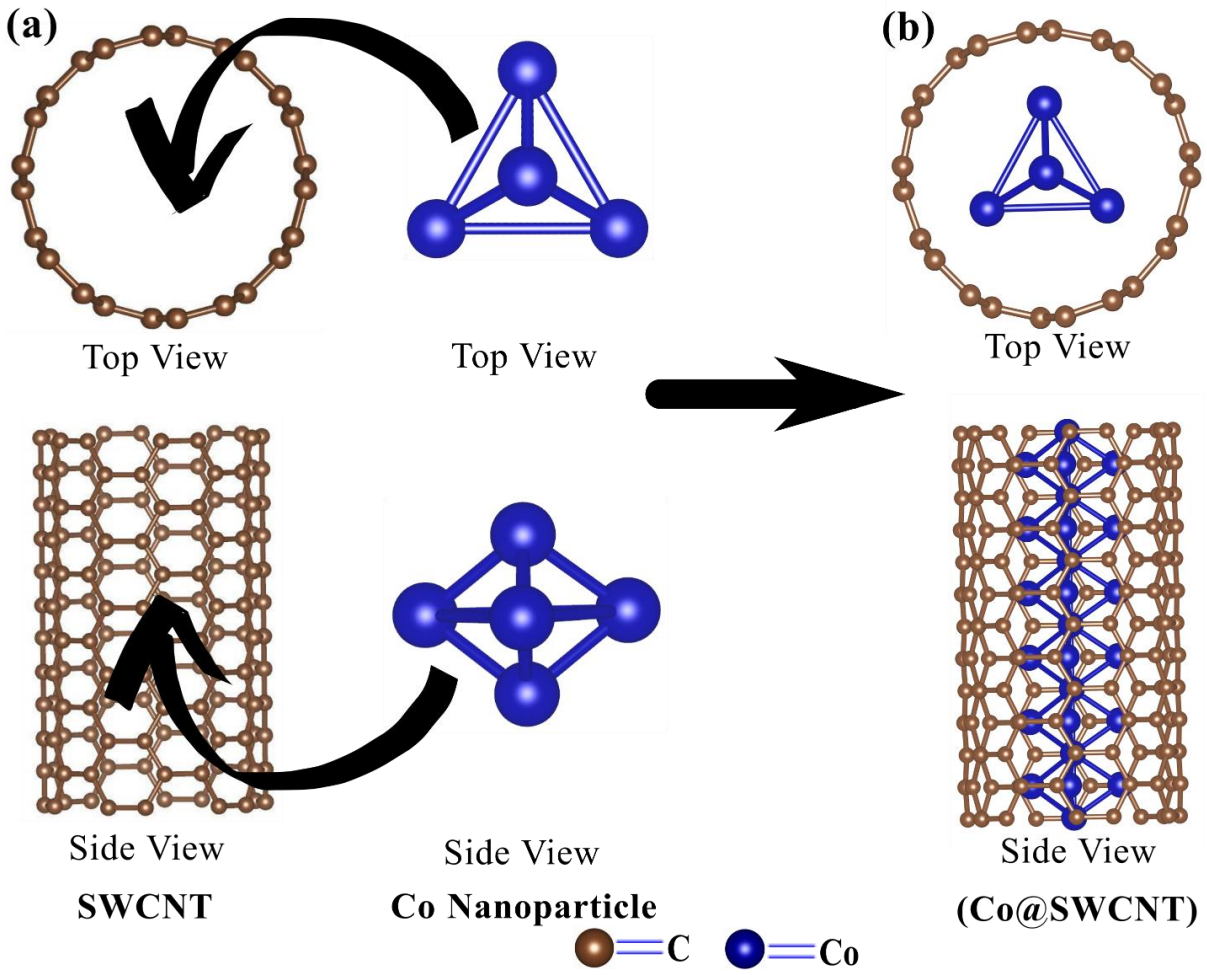

Figure 5.1. *Schematic representation of the (a) single wall carbon nanotube (SWCNT) (armchair (6,6)) and Co nanoparticle. (b) Co-encapsulated single-wall carbon nanotube (Co@SWCNT).*

system of interest in this work is Co@SWCNT, as demonstrated in Figure 5.1b. The computed results presented here illustrate that Co@SWCNT is a metallic material that is expected to be obtained by some new experiments in the future. There is strong interest in determining whether this unique Co-encapsulated nanotube structure of SWCNT holds promise for fuel cell applications, especially when compared to Pt-based nanomaterials known for their exceptional performance in catalyzing the sluggish ORR kinetics. Numerous previously reported research studies demonstrated that a carbon nanotube with chirality (6,6) could be synthesized by various methods, including laser vaporization, chemical vapor depositions, and bottom-up processes[20–22]. This foundation was laid by the previous experimental synthesis, demonstrating the viability and stability of the (6,6) carbon nanotubes. Moreover, Hedman et al. computed the stability of the SWCNT of different chiralities through computational modelling and DFT calculations. This theoretical research supports the experimental findings and demonstrates that the (6,6) SWCNT exhibits enhanced stability compared to other chirality combinations[23]. These empirical findings motivated us to choose the (6,6) SWCNT as a stable and reliable material as an electrocatalyst for ORR applications. However, the metal nanoparticle electrocatalyst seriously suffers from stability issues in both acidic and alkaline environments during the reaction. The stability of the nonprecious metal nanoparticles could be significantly enhanced by cooperating these nanoparticles with carbon materials and exhibiting high electrocatalytic stability and activity. Cui et al. introduced a straightforward and adaptable technique for the fabrication of a diverse array of NPs encapsulated within SWCNT[24]. Xiao et al. experimentally fabricated the M_4@CNT (M = Co, Fe, Ni) material and utilized it as an electrocatalyst for HER. Additionally, Lu et al. fabricated the Co nanoparticle encapsulated NCNT, and they reported that the Co nanoparticle-encapsulated NCNT possesses superior stability in harsh environments and exhibits high catalytic activities toward ORR in alkaline solution with super methanol tolerance[25]. The enduring strength and stability of carbon-nanotube-encapsulated Co nanoparticles have consistently been highlighted in prior studies. This durability is credited to the distinctive carbon-coated core-shell nanostructure. Within this framework, the carbon shell plays a crucial role by effectively shielding the Co nanoparticles from leaching and aggregation during the reaction process, especially under challenging reaction conditions. Thus, building upon these prior experimental and theoretical studies, we have observed that cobalt-encapsulated carbon nanotubes exhibit commendable stability under electrochemical reaction conditions, as evidenced by their successful utilization as an electrocatalyst for various electrochemical reactions. Accordingly, the remarkable stability demonstrated by the Co nanoparticle encapsulated carbon nanotube,

which is coupled with its promising electrocatalytic activity toward various electrochemical reactions, has inspired us to explore the electrocatalytic capabilities of this system for other electrochemical reactions such as ORR. In this study, the possible reaction intermediates involved in the subject reaction (i.e., ORR) were strategically positioned on the surface of Co@SWCNT to investigate the electrocatalytic performance of the Co@SWCNT toward ORR. Our study reveals that the Co@SWCNT catalyst demonstrates notable electrocatalytic efficiency with superior performances and exhibits remarkable stability in facilitating the ORR.

5.2.2 Computational Details. In this work, all the periodic DFT calculations, such as geometry optimization, equilibrium structure, lattice parameters, electronic properties, and the various energies of the system involved in the subject reaction, were conducted by using the B3LYP hybrid DFT method as incorporated in the CRYSTAL17 suite code[26]. The hybrid DFT approach has gained significant popularity for addressing the self-interaction error in the approximate exchange potentials. This is achieved by combining local or semi-local DFT exchange functionals with the exact nonlocal Hartree-Fock (HF) exchange. However, the computational cost of this method increases due to the complexity involved in managing the integration of Hartree-Fock integrals. In this calculation, the Fock/KS matrix mixing parameter was taken 90%. The long-range van der Waals (vdW) dispersion interaction has been taken into account using Grimme's D3 correction, which provides a better description of all types of vdW interactions[27,28]. The DFT-D (B3LYP-D3) is an advantageous method that gives not only an excellent geometry of the structure but also a consistent value of energy, band gap, and density of states (DOS)[29,30]. A periodic supercell of carbon nanotube structure and the structural parameters of the unit cell were created and designed using visualization for electronic structural analysis (VESTA) code[31]. The Gaussian-type (GTO, i.e., Gaussian-type orbital) basis set has been used as atomic orbital basis sets in the CRYSTAL17 program for all DFT calculations, such as geometry optimization and single-point energy calculation[32,33]. The basis set used to represent the atomic orbitals of C, Co, O, and H is the triple-ζ valence with polarization quality (TZVP) Gaussian basis set. The self-consistent field (SCF) calculation utilized a convergence criterion of 10^{-7} a.u. for the change in total energy for all the calculations. In the CRYSTAL17 code, geometry optimization has been performed on all atoms using predefined default thresholds. The maximum and RMS force thresholds are set at 0.000450 and 0.000300 a.u., respectively, while the maximum and RMS displacement thresholds are set at 0.001800 and 0.001200 a.u., respectively. Brillouin zone integration was conducted using a Monkhorst-Pack method using 4 × 4 × 8 k-points[34]. For plotting the

electronic band structure, we employed a high-symmetry k-path, which includes the points Γ, K, M, L, A, H, L, and Γ in the selected direction. The band structure and DOS were plotted in this study by using the GNU plot and Python codes developed by our group. The geometrical representation and atomic structure visualization for all the systems involved in this calculation were performed by using the VESTA Code[31].

5.2.3 Reaction Pathways. The precise chemical reaction mechanism governing the ORR remains the subject of ongoing scientific investigation. Extensive research, encompassing both theoretical and experimental approaches, has proposed the existence of two distinct pathways through which the ORR can occur. The ORR proceeds through the ideal high rate $4e^-$ pathways in one step without generating extra byproducts or a sluggish, less efficient two-electron pathway. The two-electron reaction pathway facilitates the reduction of O_2 to the metastable intermediate H_2O_2, which poses a potential risk of catalyst surface corrosion owing to its high

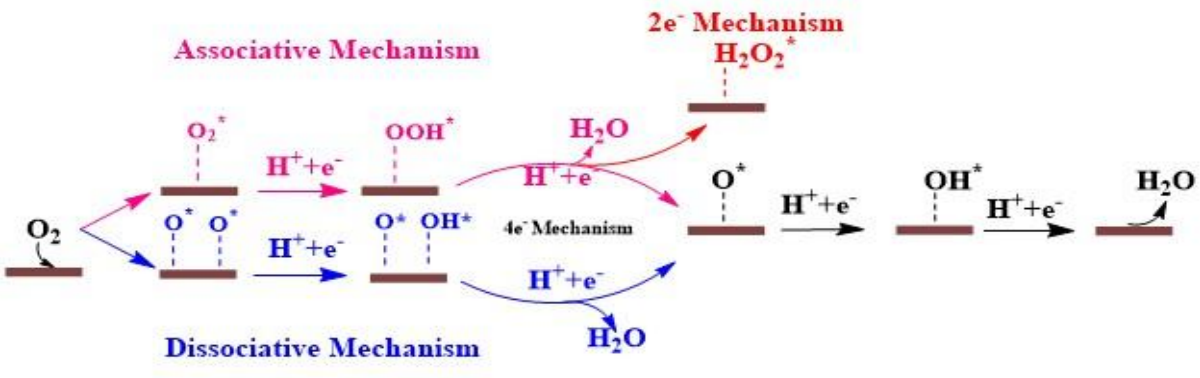

Scheme 1. *The reaction scheme illustrates the ORR mechanism, highlighting both the $4e^-$ and $2e^-$ pathways.*

oxidizing capability. Subsequently, H_2O_2 can undergo a two-electron and proton coupling process to produce water (H_2O) or dissociate into a separate water molecule and an oxygen atom[35].

$$O_2 + 4H^+ + 4e^- \longrightarrow 2H_2O \quad (1.229\ \text{V vs SHE})$$

$$O_2 + 2H^+ + 2e^- \longrightarrow H_2O_2 \quad (0.695\ \text{V vs SHE})$$

$$H_2O_2 + 2H^+ + 2e^- \longrightarrow 2H_2O \quad (1.77\ \text{V vs SHE})$$

5.2.4 Computational Method for Energy Calculations. The determination of the adsorption energy for ORR species plays a vital role in evaluating the reactivity and stability of electrocatalysts. In this study, the adsorption energy of ORR species is computed by employing the following methodology:

$$\Delta E = E_{tot}[* + \text{adsorbate}] - E_{tot}[*] - E_{tot}[\text{adsorbate}]$$

where $E_{tot}[* + \text{adsorbate}]$, $E_{tot}[*]$, and $E_{tot}[\text{adsorbate}]$ are the electronic energy correspond to the adsorption system, the individual adsorbent, and the adsorbate, respectively[36].

In this energy calculation, we employed the method introduced by Nørskov et al. to study the electron-transfer reaction. They demonstrated a correlation between the chemical potential of $H^+ + e^-$ and $\frac{1}{2}H_2$ in the gas phase using the computational hydrogen electrode (CHE) technique[37]. By applying this approach under standard CHE conditions, we were able to determine the energy difference for the reaction $* + H \longrightarrow H^+ + e^-$ through the reaction $* + H \longrightarrow * \frac{1}{2}H_2$.

5.3 Results and Discussion.

5.3.1 Structural and Electronic Properties. The equilibrium structures of both the SWCNT and Co@SWCNT materials have been determined using the full relaxation process (both atomic positions and lattice parameters are allowed to change during the optimization calculations), and they are represented in Figure 5.2a, b. The equilibrium SWCNT exhibits the *p6* space group symmetry with the equilibrium lattice parameters a = 22.06 Å, b = 22.06 Å, c = 2.45 Å, α = 90.00°, β = 90.00°, and γ = 120.00° obtained by the periodic B3LYP-D3 method. On the other hand, the relaxed Co@SWCNT also possesses the $p\bar{6}$ space group symmetry and the system has been characterized by equilibrium lattice parameters of a = 21.71 Å, b = 21.71 Å, c = 2.46 Å, and α = 90.00°, β = 90.00°, and γ = 120.00° computed by the same DFT-D approach. A comprehensive summary of the structural parameters for both the SWCNT and Co@SWCNT can be found in Table 5.1.

Table 5.1. *The equilibrium structural properties of the SWCNT and Co@SWCNT.*

System	Lattice parameters (Å)	Interfacial angles in degree (˚)	Space group and symmetry	Average bond distance between atoms (Å)		References
				C-C	Co-Co	
SWCNT	*a*=*b*= 22.06, *c*= 2.45	*α*=*β*= 90, *γ*= 120.00	***P6***	1.39	-	This work
Co@SWCNT	*a*=*b*= 21.71, *c*= 2.46	*α*=*β*= 90, *γ*= 120.00	***P$\bar{6}$***	1.42	2.32	This work

In the electrochemical ORR, the electron-transfer phenomenon holds particular significance during the reaction. To achieve maximum efficiency from a catalyst, it is crucial for the catalyst to exhibit exceptional electrical conductivity. Investigating the electronic band structure characteristics and determining the extent of the electronic band gap of both the SWCNT and Co@SWCNT materials are essential for a comprehensive analysis. We computationally investigated and analyzed the electronic properties of both the SWCNT and Co@SWCNT. The electronic band structure calculation has been performed along with the high-symmetry k-path directions following the original space group symmetries $p6$ and $p\bar{6}$, and the high-symmetry pathway of the k-path is defined by the points Γ-K-M-L-A-H-L-Γ as schematized in Figure 5.2c, d. Figure 5.2c represents the electronic band structures and the total DOS of the SWCNT. The electronic band structure of the SWCNT reveals intriguing properties with certain energy bands intersecting the Fermi level (E_F). However, it is evident from Figure 5.2c that the electron density of states near E_F is exceedingly low. This observation indicates the semi-metallic nature of the SWCNT. When a Co nanoparticle is encapsulated inside the ring (Co@SWCNT), it results in a notable alteration in the electronic properties of the carbon nanotube, as depicted in Figure 5.2d. The band structure diagram of the Co@SWCNT reveals that several energy bands intersect around the E_F, as illustrated in Figure 5.2d. Furthermore, an analysis of the DOS calculations of Co@SWCNT has been conducted to investigate the electronic behavior of the Co@SWCNT system. The total DOS clearly demonstrates a substantial electron density in proximity to the E_F. Thus, both the electronic band structure and DOS calculations of Co@SWCNT reveal that Co@SWCNT has a metallic character and can be useful for applications in electrocatalysis. To investigate how the Co nanoparticles influence the electron density near the E_F of the Co@SWCNT material, we have conducted the calculations of the partial density of states (PDOS) of the 3***d*** orbital of the Co nanoparticles, i.e., the contributing components of the "***d***-orbital" electron density of states of the Co nanoparticles, which are encapsulated by the SWCNT in the total DOS. Our results reveal that the PDOS profile of the 3d-orbital of Co nanoparticles closely resembles the DOS of the Co@SWCNT system, as illustrated in Figure 5.2e. This PDOS analysis highlights the substantial contribution of the 3***d***-orbital of the Co nanoparticles influencing the overall electronic density of states near the E_F in the DOS of Co@SWCNT. Consequently, the increased carrier concentration around the E_F implies a facilitated transfer of electrons to reactants during the ORR. Thus, the Co@SWCNT may provide an improved electrocatalytic performance for the overall ORR.

5.3.2 Adsorption of ORR Species on the Co@SWCNT Material. In our exploration of the ORR mechanism, we computationally investigated the values of ΔE for different reaction intermediate species that were formed during the subject reaction on the Co@SWCNT surface. The adsorption energy of reaction intermediates on a catalytic site significantly influences the determination of the comprehensive performance and selectivity of a catalyst. Ideally, a catalytic material should exhibit minimal adsorption energy to facilitate efficient reaction kinetics but be large enough to hold the reaction species on the surface of the catalytic material

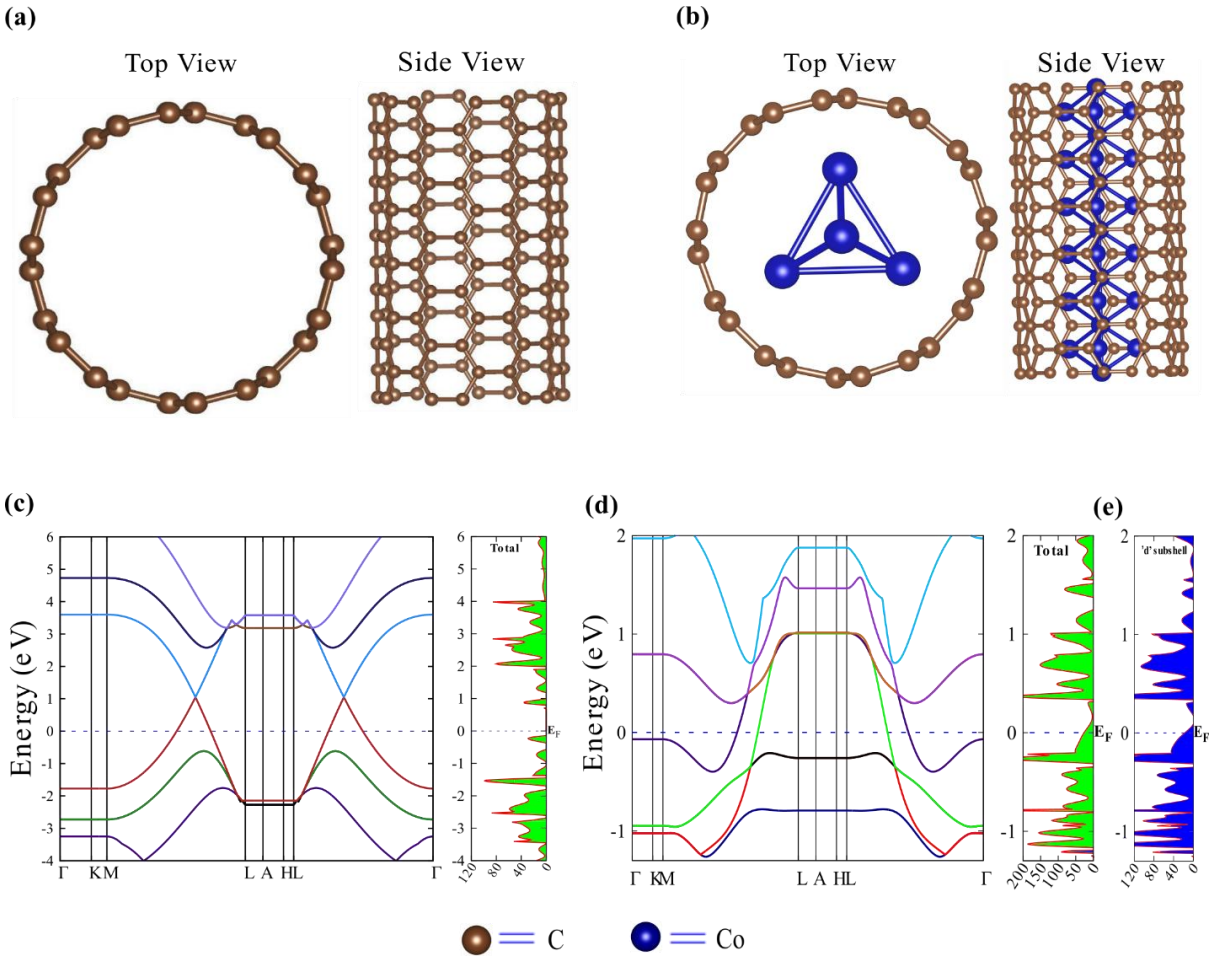

Figure 5.2. *Equilibrium structure (top and side view) of the (a) pristine SWCNT and (b) Co@SWCNT; and the corresponding band structure and DOS of (c) SWCNT, (d) Co@SWCNT, and (e) "**d**" orbital partial density of states of Co nanoparticle.*

surface. For adsorption and desorption reaction steps, both very high and very low adsorption energies can have profound effects on selectivity, reaction kinetics, and stability of intermediates. The active site resides on the surface of the Co@SWCNT, a key area activated by encapsulation of the Co nanoparticles. In the present investigation, we have defined the active site as the carbon atoms situated on SWCNT, forming a Co-C bond with the encapsulated Co nanoparticles, as depicted in Figure 5.3a, b. Previous research has demonstrated the effectiveness of such systems in activating and studying the catalytic activity

of CNTs. The present investigation, followed by a previous research work by Niu et al., where they investigated the ORR activity of the CoNi@NCNT, has similarly regarded the active sites as existing on the surface of the CoNi@NCNT[11]. In a recent study, scientists investigated the utilization of metal-encapsulated CNTs as catalysts across multiple applications. Their findings emphasized the crucial role of interactions between metal atoms and the inner surface of CNTs in activating the CNT surface. The authors performed the electrochemical reaction mechanisms by considering the active site on the surface of CNT[16,17].

5.3.2.1. O_2 Adsorption and Dissociation Reactions. In the present study, the O_2 molecule primarily adsorbs on the surface of the SWCNT rather than directly on the Co nanoparticles, i.e., SWCNT acts as an active site of the Co@SWCNT material. The Co nanoparticles are strategically encapsulated within the SWCNT to activate its surface for the electrocatalytic ORR. The adsorption of the O_2 and ORR intermediate species has been considered on the surfaces of the SWCNT attached to the carbon atom near the metal nanoparticle, forming a Co-C bond between the metal nanoparticle and SWCNT as represented in Figure 5.3a, b. The external surfaces of CNT remain stable due to the strong covalent bonds among the C atoms, rendering them resistant to adsorption and inappropriate for electrocatalytic applications. However, sp^2 CNT possesses abundant π electrons that could potentially serve as catalysts for electron-demanding electrochemical reactions like the ORR[38]. Nonetheless, these π electrons are typically too inert for direct use in the ORR. Recently, it has been discovered that encapsulating the metal nanoparticle inside the CNT is a promising strategy to alter the sp^2 hybridization of carbon atoms to create charge sites and activate carbon π electrons for effective utilization in electrocatalytic reactions. For instance, Han et al. recently reported that the transition metal encapsulated CNT for efficient HER[17]. They elucidated that an electron charge distribution of CNT happens in the electronic interaction of the ***d***-orbital of transition-metal atoms and carbon atoms[17]. This charge transfer weakens the π conjugation between carbon atoms and enhances the adsorption of the H atom on the surface of the TM@CNT. Similarly, Deng et al. proposed that the iron encapsulation carbon nanotubes can possess good catalytic activity toward ORR, which arises from the electron transfer from the Fe atoms to the CNT[39]. To investigate the SWCNT activation by encapsulating the Co nanoparticle, we conducted the Mulliken charge analysis of the Co@SWCNT material. The Mulliken charge analysis demonstrates that there is an average of +0.10 |e| charge transfer from the Co nanoparticles to the SWCNT. This charge transfer disrupts the π bond of the SWCNT, creating charged sites that favor O_2 adsorption and activate the carbon π electrons for effective

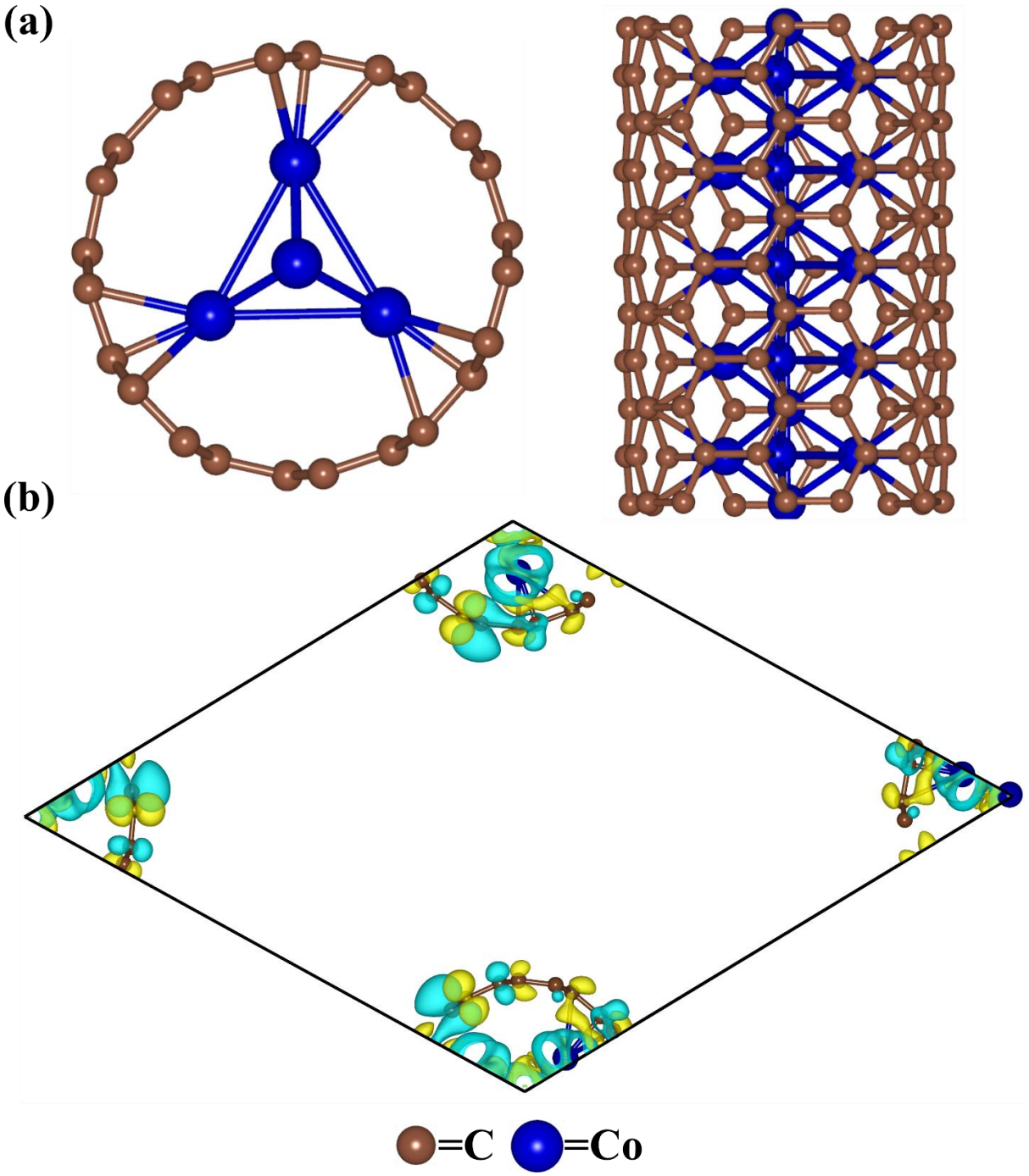

Figure 5.3. *(a) The equilibrium calculation model Co@SWCNT, which represents the interactions between Co nanoparticles and SWCNT, (b) spin density isosurface of the unit cell of Co@SWCNT, arises from the interaction of Co nanoparticles with the SWCNT.*

utilization by O_2 molecules during reduction. Additionally, spin density isosurface calculations were conducted to examine the interaction between the Co nanoparticles and the SWCNT surface. The spin density isosurface of the Co@SWCNT has been represented in Figure 5.3b, where the yellow contour represents the charge accumulations, and the blue contour denotes charge depletion. From the spin density isosurface calculations, it is evident that the electrons from **d**-orbital of the Co atoms interact (or hybridize) with the electrons from **p**-orbital of the

carbon atoms of the SWCNT, which can significantly promote the efficiency of electron transfer. These charge-transfer analyses and spin density isosurface computations indicate that the Co nanoparticle encapsulation has activated the surface of the SWCNT, which provides enhanced adsorption for the O_2 on the surface of Co@SWCNT.

The initial stage of the ORR involves the adsorption of an O_2 molecule on the surface of the Co@SWCNT. In the present investigation, we strategically placed an O_2 molecule in close proximity to the cobalt nanoparticles on the Co@SWCNT surface to assess the adsorption energy of the O_2 molecule, which is a critical factor in influencing the kinetics of the ORR mechanism. The precise adsorption strength of the O_2 molecule at the catalytic site carries substantial importance in shaping the development of efficient catalytic systems. If the adsorption energy is excessively high, then the intermediates create a strong bond to the catalytic site, effectively blocking the active sites and inhibiting the catalytic activity. This can result in catalyst deactivation or a reduced catalytic efficiency of the material. If the interaction of the ORR species with the catalytic site is very low, the intermediates weakly interact with the catalyst surface. Weakly adsorbed intermediates tend to dissociate quickly from the catalyst surface, reducing the residence time and limiting the opportunity for subsequent reactions. This can lead to lower catalytic activity and decreased reaction rates. The charge transfer from the Co atoms (in Co nanoparticles) to C atoms (in the SWCNT), as evidenced by the Mulliken charge transfer and spin density analysis, signifies the establishment of interactions with the chemical bonds between the Co nanoparticles and C atoms. The encapsulation of the Co nanoparticles leads to unique host-guest interactions and activates the surrounding nanotube, consequently enhancing the catalytic activity of the Co@SWCNT material toward ORR. The equilibrium structure of the Co@SWCNT is represented in Figure 5.4a, which contains a Co-C bond between the Co nanoparticles and carbon atoms of the SWCNT. Our study focuses on the ORR conducted on the bonded C atoms on the surface of the Co@SWCNT. We have examined the adsorption of all the ORR intermediate species on the surfaces of the subject material attached to the C atoms (active sites), which form a bond with Co nanoparticles (Co NPs).

In Figure 5.4b, we showed the equilibrium configuration of the O_2 adsorption on the surface of the Co@SWCNT material, specifically focusing on the adsorption of the O_2 molecule on the bonded C atom with Co NPs. To provide a clear illustration for the readers, we have omitted the depiction of the Co-C bond in the intermediate reaction structures,

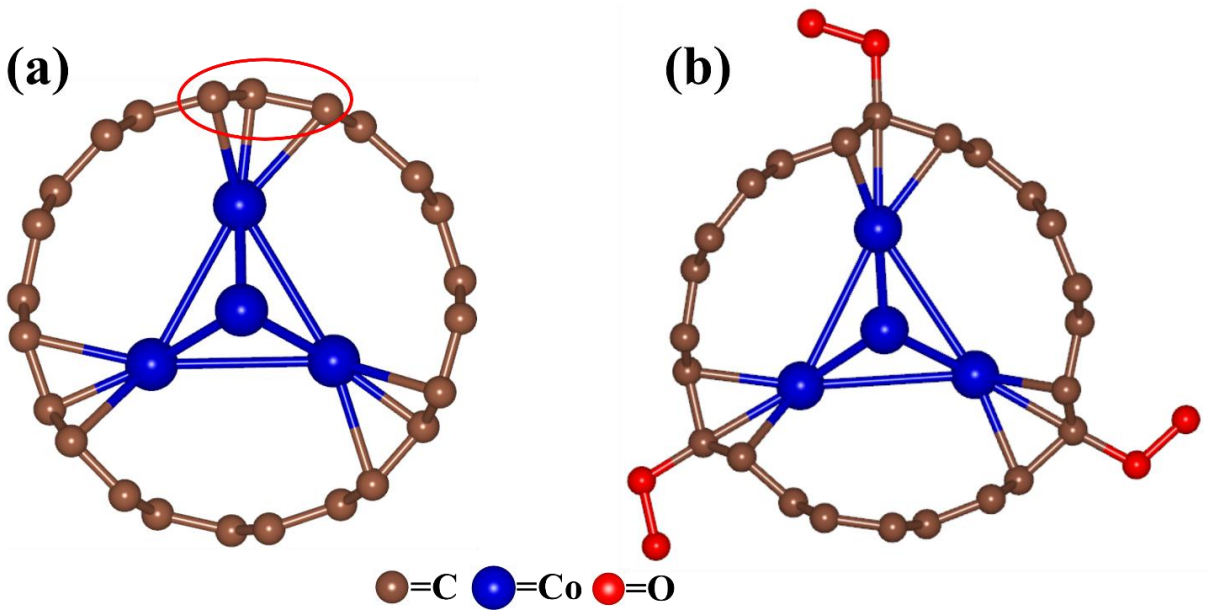

Figure 5.4. *Representation of (a) the possible active sites (C atoms of the SWCNT) for the ORR intermediate species adsorption (highlighted by the red circle) and (b) the equilibrium structure of the O_2*_Co@SWCNT, where O_2 is adsorbed on the carbon atom bonded with cobalt nanoparticles.*

highlighting the effective encapsulation of the Co NPs by the carbon layer.

The O_2 adsorbed Co@SWCNT material has been represented by O_2*_SWCNT, and the equilibrium structure of the O_2*_SWCNT intermediate was obtained under the full optimized scheme by employing the B3LYP-D3 DFT method. The equilibrium lattice parameters of the intermediate of the O_2*_Co@SWCNT have been found to be a = 22.52 Å, b = 22.52 Å, c = 2.47 Å, $\alpha = \beta = 90.00°$, and $\gamma = 120.00°$. The equilibrium bond distance of C-O and O-O was calculated to be 1.49 and 1.37 Å, respectively. The electronic band structure calculations of the O_2*_SWCNT have been studied through the high symmetric Γ-K-M-L-A-H-L-Γ k-path using the equilibrium geometry of the O_2*_Co@SWCNT reaction intermediate. The original k-paths of the pristine SWCNT and Co@SWCNT were followed during the electronic band structure calculations of all the reaction intermediates. The band structure of the O_2*_Co@SWCNT depicts the zero-band gap with the conducting nature of the O_2*_Co@ SWCNT, as displayed in Figure 5.5a. To confirm the conducting nature of the O_2*_SWCNT, we have studied the DOS of it by using the equilibrium structure of the O_2*_Co@SWCNT. The DOS profile indicates that there is a large electron density of states available around the E_F, supporting the conducting nature of the O_2*_Co@SWCNT. The contribution of the Co nanoparticle in the total DOS has been studied here by calculating the PDOS for the 3***d***-orbital of the Co nanoparticle, and it was observed that the total DOS follows the electron density of state profile of the 3***d***-orbital of the Co nanoparticle near the E_F. Hence, the PDOS analysis

suggests that the 3***d***-orbital of Co nanoparticles significantly contributes to the electronic density near the E_F, as shown in Figure 5.5a. This study reveals that the value of ΔE for an O_2* molecule adsorption on the Co@SWCNT surface is about +0.15 eV, indicating proximity to the optimal range. This small positive adsorption energy implies relatively weak bonding between the O_2* molecules and the Co@SWCNT surface, making them readily available for subsequent steps in the ORR process. Ulbrient et al. experimentally investigated the adsorption energy of the O_2 on the CNT bundle and graphite. They reported that the O_2 adsorption energy obtained from the molecular mechanics (MM) simulations of the SWCNT bundles was 0.80 eV, and for graphite, it was 0.52 eV[40]. Deng et al. reported that the adsorption energy of the O_2 molecule on the surface of the pristine SWCNT (6,6) was found to be 1.43 eV obtained by the DFT method[39]. In our current

Table 5.2. *Comparison of ΔE (eV) of dissociative and associative mechanisms.*

Reaction mechanism	ΔE (eV)
O_2* ⟶ 2O*	-0.35
O_2* + H^+ + e^- ⟶ OOH*	-3.59

study, we have found the O_2 adsorption energy on the surface of the Co@SWCNT to be +0.15 eV, which is optimal for the subject reaction. This comparison suggested that O_2 can readily be adsorbed on the surface of the Co@SWCNT and is remarkably and less positive than the adsorption energy on the pristine CNT surface (0.80 eV experimentally obtained in the past and 1.43 eV theoretically obtained in earlier reports). Similar trends of the adsorption energy of the O_2 molecule have been observed in previously reported articles based on the carbon nanotube electrocatalyst. For instance, Deng et al. conducted a study on the Fe cluster-encapsulated (6,6) SWCNT and examined its electrocatalytic efficiency toward ORR. They obtained the O_2 adsorption energy to be 0.03 eV on the surface of the Fe@SWCNT[39]. Moreover, Xu et al. presented the experimental measurements and theoretical calculations of the ORR activity of the N-doped carbon nanotubes. The reported O_2 adsorption energy on the surface of the N-doped carbon nanotubes is consistent with our computed results[41]. The equilibrium bond distance between the C and O atoms was calculated to be 1.49 Å. After optimization, the O-O bond length at the equilibrium position was determined to be 1.37 Å, and it was observed that the equilibrium O-O bond distance has been elongated by an amount of 0.14 Å from the equilibrium position of a free O_2 molecule (where the O-O bond length is about 1.23 Å computed by the DFT-D method here). This substantial elongation of the O-O

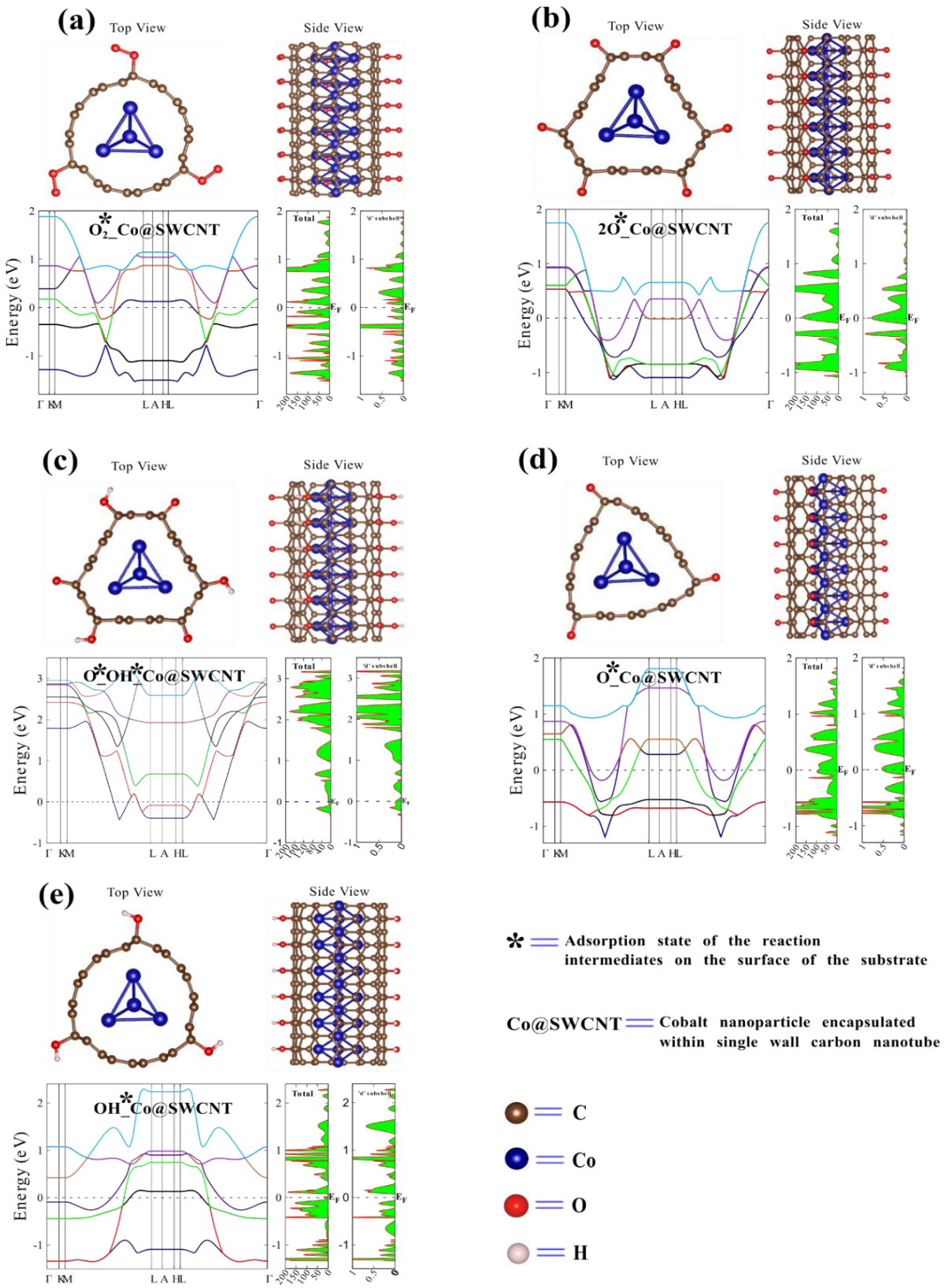

Figure 5.5. *The equilibrium structure and corresponding band structure with DOS of various intermediates; (a) O_2^*, (b) $2O^*$, (c) O^*_OH^*, (d) O^*, and (e) OH^* of electrochemical reduction of O_2 to H_2O on the surface of the Co@SWCNT.*

bond, from 1.23 Å to 1.37 Å, indicates significant activation of the O_2 molecule, rendering it highly reactive and prepared for subsequent chemical reactions. The Mulliken charge

population analysis was performed, and it revealed a transfer of approximately 0.101 |e| charge from the Co@SWCNT to the adsorbed O_2* molecule. This charge transfer contributes to the elongation of the O-O bond length. As a result, the O_2* bond eventually breaks, facilitating its reactivity in subsequent reaction steps. There are two possible ways to break the O-O bond after the adsorption of O_2* at the catalytic site. We have calculated and explored the possibility of two possible reaction pathways, i.e., direct dissociation into 2O* or hydrogenation into an OOH* species, by considering the value of ΔE of the ORR species associated with the two possible reaction pathways. The value of ΔE for both the reaction pathways is tabulated in Table 5.2.

The value of the ΔE for the dissociation of O_2* into 2O* has been calculated to be -0.35 eV on the surface of the Co@SWCNT, and the value of the ΔE for the hydrogenation of the O_2* into the OOH* has been computed to be -3.59 eV obtained by the DFT-D method during the subject reaction. Therefore, the dissociation of O_2* exhibits significantly more favorable energy characteristics compared to the hydrogenation reaction of O_2* on the Co@SWCNT surface. So, the rate of protonation of O_2* has a lower value of ΔE, indicating that the protonation of O_2* into OOH* is energetically unfavorable compared to that of the dissociative pathway. Hence, both the $4e^-$ associative and $2e^-$ indirect reaction pathways are suppressed by the $4e^-$ dissociative pathway of the ORR mechanism to reduce O_2* into H_2O on the surface of the Co@SWCNT. Hence, the $4e^-$ dissociative ORR pathway would be more thermodynamically favorable on the surface of the Co@SWCNT, and it has been discussed in the subsequent section.

5.3.2.2 H_2O Removal from the Catalytic Surface. The ultimate step in the ORR mechanism involves the removal of water molecules from the catalytic site, marking the completion of one ORR cycle and the initiation of the next ORR cycle. To investigate the potential of the Co@SWCNT for ORR, computation and analysis of the value of ΔE of the H_2O molecule on the surface of the Co@SWCNT are the key steps for the subject reaction. The present analysis reveals that the value of ΔE during the formation of H_2O is about -0.84 eV indicating a weaker binding to the Co@SWCNT surface, as tabulated in Table 5.3. This implies that H_2O exhibits a weak interaction with the catalytic site, leading to an easy desorption from the catalytic surface. The lower value of binding energy in terms of the value of ΔE observed for H_2O is a favorable characteristic for ORR, as it facilitates the removal of water molecules from the catalytic surface. Consequently, the Co@SWCNT catalytic surface becomes readily available to initiate the next cycle of the ORR mechanism, thereby enhancing the kinetics of the process.

5.3.2.3 Adsorption of Key Intermediates. The key intermediates associated with the $4e^-$ dissociative ORR pathway are 2O*, O*_OH*, O*, and OH*. Following the initiation of O_2 molecule activation on the Co@SWCNT surface, it undergoes dissociation, leading to the formation of two distinct oxygen atoms at separate catalytic sites situated on the surface of the Co@SWCNT material and denoted by the 2O*_Co@SWCNT. The equilibrium structure of 2O*_Co@SWCNT has been obtained by the full optimization process, and the equilibrium structure of the 2O*_Co@SWCNT is represented in Figure 5.5b. The equilibrium lattice parameters of the 2O*_Co@SWCNT were found to be a = 21.82 Å, b = 21.82 Å, c = 2.48 Å, $\alpha = \beta = 90.00°$, and $\gamma = 120.00°$, and the equilibrium C-O bond length in the 2O*_Co@SWCNT was calculated to be 1.37 Å as listed in Table 5.4. We computed the electronic properties of the 2O*_Co@SWCNT reaction intermediate by employing the equilibrium geometry of the 2O*_Co@SWCNT. The electronic band structure of the 2O*_Co@SWCNT intermediate depicts that the energy bands cross the E_F indicating the zero band of the 2O*_Co@SWCNT complex formed during the subject reaction, as represented in Figure 5.5b. The total DOS profile of the 2O*_Co@SWCNT intermediate was drawn in the same energy range using the B3LPY-D3 method. The DOS calculation shows significant electron density of states around the E_F as displayed in Figure 5.5b. The contribution of the Co nanoparticle is also studied by calculating the PDOS for the 3***d***-orbital of the Co nanoparticle, and it has been observed that the 3***d***-orbital of the Co nanoparticle follows the electron density profile near the Femi level. Hence, the PDOS analysis suggests that the 3***d***-orbital of the Co nanoparticles significantly contributes to the electronic density of states near the E_F. Thus, the 2O*_Co@SWCNT reaction intermediate has a metallic behavior in nature and would facilitate electron transfer during the ORR. The value of ΔE in this reaction step was found to be -0.35 eV obtained by the DFT-D method. This negative value indicates that the process is thermodynamically feasible and favorable. The activated oxygen atoms are now located at distinct sites within the Co@SWCNT structure. Among them, one of the oxygen atoms would be hydrogenated by reacting with H^+ species and e^- to form the second reaction intermediate O*_OH* ORR during the subject reaction. This intermediate structure has been denoted by the letter O*_OH*_Co@SWCNT and optimized under the full optimization process. The equilibrium structure of the reaction intermediate O*_OH*_Co@SWCNT formed during the subject ORR is represented in Figure 5.5c. The equilibrium structure of the O*_OH*_Co@SWCNT is defined by the lattice

Table 5.3. *The calculated value of ΔE (eV) for the intermediate reaction steps in the dissociative mechanism on the surface of the Co@SWCNT.*

Various ORR steps	ΔE (eV)	Relative adsorption energy (eV)
$[\mathbf{Co@SWCNT}] \longrightarrow [\mathbf{O_2^*\_\ Co@SWCNT}]$	0.15	0.15
$[\mathbf{O_2^*\_\ Co@SWCNT}] \longrightarrow [\mathbf{2O^*\_\ Co@SWCNT}]$	-0.35	-0.20
$[\mathbf{2O^*\_\ Co@SWCNT}] \longrightarrow [\mathbf{O^*\_OH^*\_Co@SWCNT}]$	-1.22	-1.42
$[\mathbf{O^*\_OH^*\_Co@SWCNT}] \longrightarrow [\mathbf{O^*\_\ Co@SWCNT}]$	-1.72	-3.14
$[\mathbf{O^*\_\ Co@SWCNT}] \longrightarrow [\mathbf{OH^*\_Co@SWCNT}]$	-0.83	-3.97
$[\mathbf{OH^*\_Co@SWCNT}] \longrightarrow [\mathbf{Co@SWCNT}]$	-0.84	-4.81

parameters a = 20.35 Å, b = 20.35 Å, c = 2.49 Å, α = β = 90.00°, and γ = 120.00° as tabulated in Table 5.4. The equilibrium C-O and C-OH bond lengths were calculated to be 1.37 and 1.42 Å, respectively, as reported in Table 5.4. To investigate the electronic properties of the O*_OH*_Co@SWCNT, both the electronic band structure and DOS of the reaction intermediate O*_OH*_Co@SWCNT have been computed and analyzed here. The electronic band structure of the O*_OH*_Co@SWCNT reaction intermediate depicts the zero-band gap, as depicted in Figure 5.5c. Upon examination of the DOS profile aligned with the band structure of the intermediate O*_OH*_Co@SWCNT, it was noted that ample electron density of states surrounds the EF within the total DOS profile of the O*_OH*_Co@SWCNT as portrayed in Figure 5.5c. This concentration of electron density of states around the E_F serves as a confirmation of the conductive nature exhibited by these intermediate structures. The PDOS profile suggests that the 3***d***-orbital of the Co nanoparticle follows the profile of the electron density of the states around E_F, as depicted in Figure 5.5c. Here, the value of ΔE was found to be -1.22 eV. The negative value of ΔE indicates that this reaction step is thermodynamically feasible and downhill. This step is followed by the hydrogenation of the O*_OH* species by reacting with an $H^+ + e^-$ to form the O* species and removal of the first water molecule. This intermediate configuration has been denoted by the O*_Co@SWCNT and optimized under the full optimization process. The equilibrium structure of the reaction intermediate O*_Co@SWCNT formed during the ORR process is represented in Figure 5.5d and has the equilibrium lattice parameters, a = 25.14 Å, b = 25.14 Å, c = 2.48 Å, α = β = 90.00°, and γ = 120.00° as tabulated in Table 5.4. Here, the equilibrium C-O bond distance was calculated to be 1.36 Å reported in Table 5.4. The electronic property calculations of the

O*_Co@SWCNT indicate a significant overlapping of the electronic energy bands around the E_F, indicating a zero-band gap of the O*_Co@SWCNT, as illustrated in Figure 5.5d. The DOS profile indicates the sufficient electron density of states around E_F, suggesting the metallic behaviour of the O*_Co@SWCNT reaction intermediate constructed during the subject reaction. The contribution of Co nanoparticles to the electronic properties of the O*_Co@SWCNT reaction intermediate has been studied by computing the PDOS of the Co 3d-orbital. The PDOS of the 3***d***-orbital follows the same electron density profile as the total DOS profile and mainly contributes around the E_F, as depicted in Figure 5.5d. The value of the ΔE in this reaction step was found to be -1.72 eV, indicating that the O atom is favorably adducted to the catalytic site. The negative value of the ΔE suggests that this step is an energetically favorable step. The remaining O* on the catalytic surface is hydrogenated to form OH* species on the catalytic surface, denoted as OH*_Co@SWCNT. The relaxed structure of the reaction intermediate OH*_Co@SWCNT is displayed in Figure 5.5e. The equilibrium structure of the OH*_Co@SWCNT complex is defined by the lattice parameters a = 23.62 Å, b = 23.62 Å, c = 2.47 Å, α = β = 90.00°, and γ = 120.00° as tabulated in Table 5.4. The equilibrium C-OH bond length was calculated to be 1.44 Å. The electronic band structure of the OH*_Co@SWCNT system formed during the ORR process depicts that a few energy bands cross the E_F, indicating the zero band of the OH*_Co@SWCNT, as represented in Figure 5.5e. The DOS plot shows a large number of electron density of states around E_F, as shown in Figure 5.5e. The contribution

Table 5.4. *The equilibrium geometry parameters and electronic band gap of all the reaction intermediates of the dissociative path.*

Reaction steps	Lattice parameters (Å)	Interfacial angles (˚)	Space group and symmetry	Electronic band gap (eV)	Average bond distance between atoms (Å)			
					C-C	Co-Co	C-O	C-OH
O_2^*_ Co@SWCNT	*a*= 22.52 *b*= 22.52 c= 2.47	*α*=*β*= 90.00 *γ*= 120.00	$P\bar{6}$	0.0	1.44	2.42	1.49	-
$2O^*$_ Co@SWCNT	*a*= 21.82 *b*= 21.82 c= 2.48	*α*=*β*= 90.00 *γ*= 120.00	$P\bar{6}$	0.0	1.44	2.38	1.37	-

O*_OH*_Co@SWCNT	*a*= 20.35 *b*= 20.35 c= 2.49	*α*=*β*= 90.00 *γ*= 120.00	$P\bar{6}$	0.0	1.47	2.42	1.37	1.42
O*_ Co@SWCNT	*a*= 25.14 *b*= 25.14 c= 2.48	*α*=*β*= 90.00 *γ*= 120.00	$P\bar{6}$	0.0	1.44	2.38	1.36	-
OH*_Co@SWCNT	*a*= 23.62 *b*= 23.62 c= 2.47	*α*=*β*= 90.00 *γ*= 120.00	$P\bar{6}$	0.0	1.47	2.39	-	1.44

of the Co nanoparticle is also studied by calculating the PDOS for the 3***d***-orbital of the Co nanoparticle, and PDOS suggests that the 3***d***-orbital of the Co nanoparticle follows the electron density profile near the E_F. Hence, the PDOS analysis indicates that the 3d-orbital of Co nanoparticles significantly contributes to the electronic density near the E_F. Thus, the OH*_Co@ SWCNT reaction intermediate has a metallic nature and would facilitate electron transfer during the ORR. The value of the ΔE for this reaction step was found to be -0.83 eV. The value of the ΔE is very small and negative for this reaction step which indicates that the present reaction is energetically favorable. The last step of the $4e^-$ dissociative pathway is the hydrogenation process in which the initial state is OH* at a site with an H^+ and e^-, while the final state is the removal of the second H_2O molecule. After that, the catalytic surface Co@SWCNT would be readily available for the next cycle of the ORR. The conducting nature of these intermediate structures would help in the transportation of electrons and eventually help to enhance the ORR activity of the Co@SWCNT. Moreover, the small value (close to zero) of ΔE for each reaction step involved during the $4e^-$ dissociative pathway suggests a better catalytic activity of the Co@SWCNT toward ORR. Kuzmin et al. investigated the ORR activity of CNT doped with MN_4(M = Cu, Ag, Zn). Their study focused on (6,6) carbon nanotubes with an examination of the adsorption energies of ORR intermediates such as OH* on both the MN_4 site and the C_2 active site. They discovered that the adsorption energies for the O* and OH* on the C_2 active site of CuN_4_CNT were -5.02 and -2.43 eV, respectively. Similarly, on AgN_4_CNT and ZnN_4_CNT, the adsorption energies for these species were -5.29, -2.48, and -5.49, -2.70 eV, respectively[42]. Xu et al. recently studied the ORR activity of nitrogen-doped CNTs. They adopted experimental measurement techniques and comprehensive theoretical calculations to assess and contrast the ORR activity of graphitic and pyridinic nitrogen doping

in the N-doped CNTs. The reported adsorption energies of O* on grp-eNCNT (a single graphitic N dopant replacing a carbon atom next to the carbon on the edge of CNT), grp-bNCNT (a single graphitic N dopant replacing a carbon atom inside CNT), grp-p2NCNT (two graphitic N dopants replacing two adjacent C atoms in CNT), and pyd-eNCNT (a single pyridinic N dopant replacing a carbon atom on the edge of CNT) were -3.89, -3.26, -3.68, and -3.29 eV respectively. Additionally, the adsorption energies of OH* on the grp-eNCNT, grp-bNCNT, grp-p2NCNT, and pyd-eNCNT were reported as -2.40, -2.48, -2.00, and -1.65 eV, respectively[41]. Our results showed that the adsorption energy of the ORR species on the Co@SWCNT is more optimal and ideal than that of the previously reported carbon nanotube-based materials. The comprehensive analysis of the adsorption energy of the ORR intermediate species on the surface of the Co@SWCNT suggests that the adsorption energy of the ORR intermediate species is negative and optimal (not too negative or too positive). Thus, the ORR on the surface of the Co@SWCNT is a thermodynamically favorable process.

5.3.2.4 The Whole ORR Pathway. Under the standard conditions, through an examination of adsorption energies, we observed that the ORR mechanism on the surfaces of Co@SWCNT would follow the $4e^-$ dissociative pathway. The values of ΔE for all the reaction steps involved in the ORR on the surface of Co@SWCNT are calculated as follows. In the initial reaction step, $O_2 \rightarrow O_2*$, the value of ΔE has been obtained to be +0.15 eV. The subsequent reaction step involves the dissociation of O_2*, i.e., $O_2* \rightarrow 2O*$, with a calculated ΔE value of -0.35 eV. When one of the adsorbed oxygen atoms is hydrogenated, i.e., $2O* \rightarrow O*\_OH*$, the computed value of ΔE has been found to be -1.22 eV. During the reduction of O*_OH* to O* + H_2O, the value of ΔE has been determined to be -1.72 eV. For the hydrogenation of the next O*, i.e., $O* \rightarrow OH*$, the value of ΔE has been determined to be -0.83 eV. Lastly, for the formation of the second H_2O molecule, i.e., $OH* \rightarrow H_2O$, the value of the ΔE has been computed to be -0.84 eV. We observed that the adsorption energy for each ORR step is negative except for the first step, as shown in Table 5.3. The negative values of the ΔE show that all the reaction steps are thermodynamically favorable and feasible. To summarize the whole ORR mechanism, we constructed the potential energy surface (PES) or reaction energy diagram based on the values of ΔE of different ORR species, i.e., reaction intermediates formed during the ORR, as depicted in Figure 5.6. We constructed the reaction energy diagram or potential energy surface by considering the Co@SWCNT as a reference geometry, i.e., Co@SWCNT is considered to correspond to an energy of 0 eV, as shown in Figure 5.6. The reaction energy landscape shows

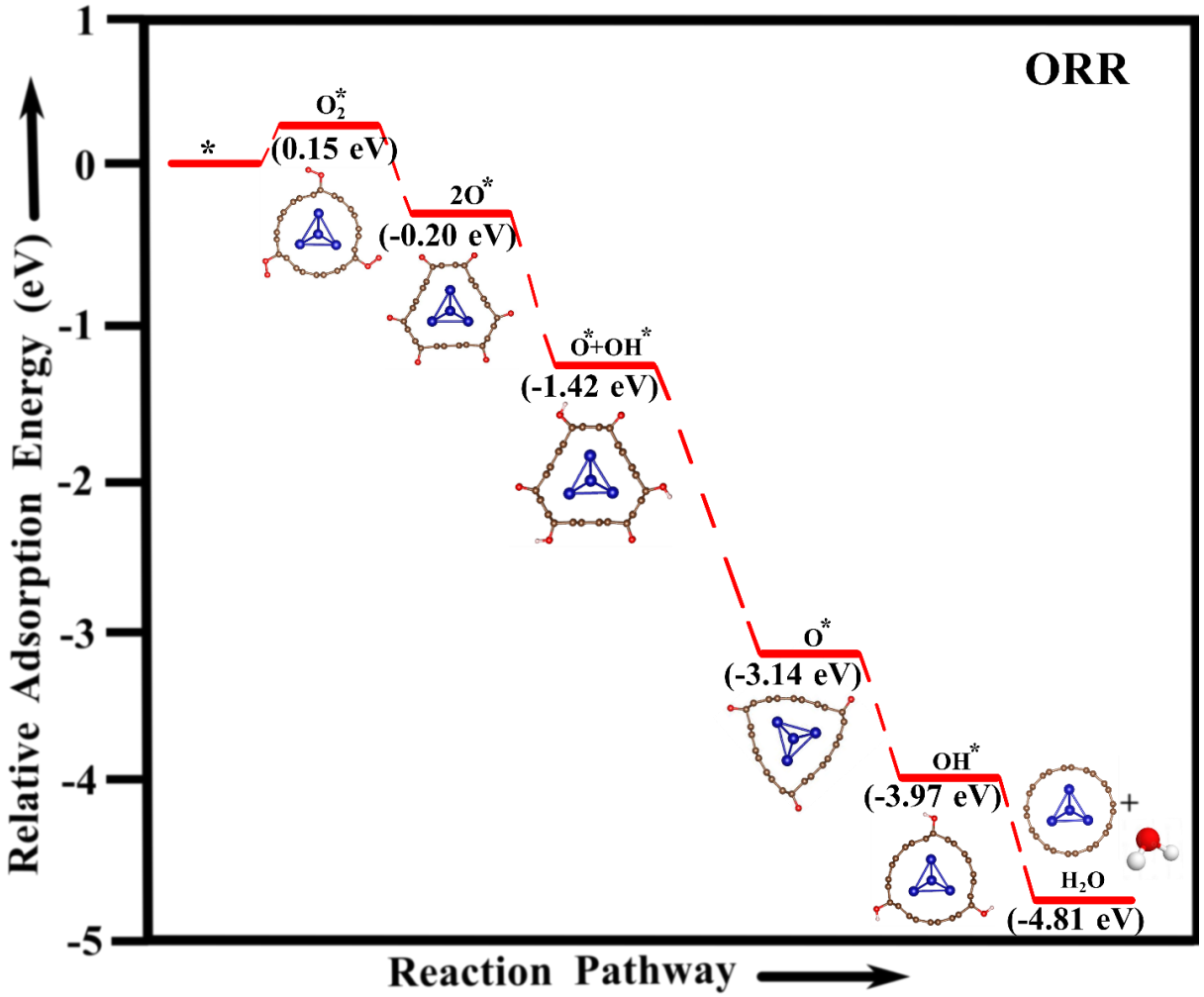

Figure 5.6. *The reaction adsorption energy (eV) diagram for the 4e- dissociative ORR mechanism on the surface of the Co@SWCNT on the surface of the Co@SWCNT is a thermodynamically favorable process.*

that all the reaction steps are downhill except O_2 adsorption on the surfaces of the catalysts Co@SWCNT, i.e., the value of ΔE decreases along the whole reaction pathway, making reduction of oxygen to water energetically favorable on the surface of the Co@SWCNT.

The novelty of the present work involves the unique and detailed analysis of the properties and electrocatalytic application of the Co@SWCNT toward the O_2 reduction reaction using a first principles-based DFT-D method. Previous studies reported the synthesis of the Co@SWCNT and examined the different catalytic applications, such as HER and lithium-sulphur batteries, based on experimental and theoretical studies[16,43]. Similar kinds of systems, such as cobalt-encapsulated nitrogen-doped carbon nanotubes, have been experimentally reported for their potential applications in ORR, OER, and zinc-air batteries[44–46]. Existing studies have predominantly relied on experimental data with limited theoretical explorations. Whatever theoretical investigations reported previously are not in detail and are done mainly by taking the molecular modelling structure of the metal cluster,

which does not precisely represent the practical nanostructure. In contrast, our work utilizes a periodic system approach, specifically modelling cobalt cluster encapsulation within a single-wall carbon nanotube, thus faithfully replicating the practical structure for a more comprehensive understanding of its properties and electrocatalyst applications, particularly toward ORR. One key novelty of our research lies in the comprehensive computational approach, where we have employed the periodic hybrid DFT method with Grimme's "-D3" corrections providing a robust and accurate framework for understanding the electronic properties and catalytic behaviour of the Co@SWCNT. While previous research has examined the Co@SWCNT as a catalyst, our study especially highlighted the impact of the Co nanoparticles on the electronic properties of the SWCNT revealing the metallic characteristics of Co@SWCNT with the application in ORR. Additionally, we have investigated the electronic properties of each ORR intermediate step, which is crucial for understanding the catalytic behaviour of the Co@SWCNT. While previous studies have explored similar systems, our work uniquely provides a more detailed and systematic investigation into the adsorption energy of the ORR species and the underlying mechanism of ORR on the surface of the Co@SWCNT. Here, we have also performed the Mulliken charge analysis, which confirms the charge transfer, and we have also computed the electron spin densities to explain the ORR process. We not only propose multiple ORR pathways but also quantify the adsorption energies of the key reaction intermediates, such as 2O* and OOH* shedding light on the most favorable reaction pathways. We believe that our findings hold significant promise for advancing future renewable energy and fuel cell applications, providing a novel perspective that adds significant value to the existing area of this field.

5.4 Conclusions. In this study, we have conducted a systematic computational investigation using the DFT method to analyze the catalytic properties of the Co@SWCNT toward ORR. Our focus was on examining the structural and electronic characteristics of the system as well as understanding the reaction mechanism involved in ORR. The study was conducted on a periodic Co@SWCNT model with chirality (6,6). In our initial analysis, we delved into the structural and electronic characteristics of both the SWCNT and Co@SWCNT materials. Our observations unveiled that while SWCNT exhibited a zero-band gap, the electron density of states in the vicinity of the E_F was exceedingly low indicative of its behavior as a semimetal. Subsequently, we explored both the electronic band structure and the DOS of the Co@SWCNT system. Remarkably, our investigation revealed a noteworthy alteration in both the electronic band structure and DOS of the Co@SWCNT marked by the emergence of electronic states in

proximity to the E_F. Notably, the presence of the Co nanoparticle had a discernible impact, leading to an augmentation in the electron density surrounding the E_F. Combining these results of a zero-band gap and enhanced electron density, we can conclude here that the Co@SWCNT has displayed a metallic nature making it act as a potentially efficient electrocatalyst for ORR. The Co nanoparticles have been securely enclosed within the SWCNT structure, ensuring that they are shielded from direct exposure to harsh conditions such as acidic environments and oxygen. This protective arrangement allows the Co@SWCNT system to maintain long-term stability when used in fuel cells. In order to assess the catalytic effectiveness and activity of Co@SWCNT in facilitating the ORR, we have conducted theoretical calculations to determine the value of ΔE of ORR species on the surface of Co@SWCNT. The O_2 molecule undergoes adsorption and subsequently follows one of two distinct routes: it either dissociates into two oxygen atom species (denoted as 2O*, constituting the direct pathways) or gives rise to the formation of the OOH* intermediate species (characterizing the series pathways). The value of ΔE of the 2O* ORR intermediate was determined to be -0.35 eV, and for the OOH* ORR intermediate, it was determined to be -3.59 eV in this study. By comparing the value of ΔE of both reaction intermediates formed during the ORR process on the surface of Co@SWCNT, it was found that the $4e^-$ dissociative reaction pathway is thermodynamically more favorable. The adsorption energies of various reaction intermediate species involved in the $4e^-$ dissociative ORR pathway have been evaluated. All of the reaction intermediate step of the $4e^-$ dissociative ORR pathway is thermodynamically during the ORR process on the surface of the Co@SWCNT. The theoretical analysis based on the CHE model, along with our computational investigation, reveals that the Co@SWCNT is a promising ORR electrocatalyst with exceptional catalytic activity, performance, and a high four-electron reduction pathway selectivity. Consequently, the Co@SWCNT material possesses several desirable qualities, including cost-effectiveness, high activity, and robust stability, making it a promising catalyst for modern fuel cell applications.

5.5 References:

[1] J. Fu, Z. P. Cano, M. G. Park, A. Yu, M. Fowler, Z. Chen, Electrically rechargeable zinc-air batteries: progress, challenges, and perspectives, Adv. Mater. 29 (2016) 1604685.

[2] C. Qin, J. Wang, D. Yang, B. Li, C. Zhang, Proton exchange membrane fuel cell reversal: A review, Catalysts 6 (2016) 197.

[3] C. Zhang, X. Shen, Y. Pan, Z. Peng, A review of Pt-based electrocatalysts for oxygen reduction reaction, Front. Energy. 11 (2017) 268–285.

[4] X. Tong, X. Zhan, D. Rawach, Z. Chen, G. Zhang, S. Sun, Low-dimensional catalysts for oxygen reduction reaction, Prog. Nat. Sci. Mater. Int. 30 (2020) 787–795.

[5] R. Shoukat, M.I. Khan, Carbon nanotubes: a review on properties, synthesis methods and applications in micro and nanotechnology, Microsyst. Technol. 27 (2021) 4183–4192.

[6] S. Rathinavel, K. Priyadharshini, D. Panda, A review on carbon nanotube: An overview of synthesis, properties, functionalization, characterization, and the application, Mater. Sci. Eng. B. 268 (2021) 115095.

[7] J. Wang, R. Ma, Z. Zhou, G. Liu, Q. Liu, Magnesiothermic synthesis of sulfur-doped graphene as an efficient metal-free electrocatalyst for oxygen reduction, Sci. Rep. 5 (2015) 9304.

[8] L. Yang, S. Jiang, Y. Zhao, L. Zhu, S. Chen, X. Wang, Q. Wu, J. Ma, Y. Ma, Z. Hu, Boron-doped carbon nanotubes as metal-free electrocatalysts for the oxygen reduction reaction, Angew. Chem. Int. Ed. 50 (2011) 7132–7135.

[9] Z. W. Liu, F. Peng, H. J. Wang, H. Yu, W. X. Zheng, J. Yang, Phosphorus-doped graphite layers with high electrocatalytic activity for the O_2 reduction in an alkaline medium, Angew. Chem. Int. Ed. 50 (2011) 3257–3261.

[10] R. Kumar, S. Kumar, S. G. Chandrappa, N. Goyal, A. Yadav, N. Ravishankar, A. S. Prakash, B. Sahoo, Nitrogen-doped carbon nanostructures embedded with Fe-Co-Cr alloy based nanoparticles as robust electrocatalysts for Zn-air batteries, Journal of Alloys and Compounds 984 (2024) 173862.

[11] W. Niu, S. Pakhira, K. Marcus, Z. Li, J. L. Mendoza-Cortes, Y. Yang, Apically dominant mechanism for improving catalytic activities of N-doped carbon nanotube arrays in a rechargeable zinc-air battery, Adv. Energy Mater. 8 (2018) 1800480.

[12] Y. Liu, H. Jiang, Y. Zhu, X. Yang, C. Li, Transition metals (Fe, Co, and Ni) encapsulated in nitrogen-doped carbon nanotubes as bi-functional catalysts for oxygen electrode reactions, J. Mater. Chem. A. 4 (2016) 1694–1701.

[13] B. Liu, H. Zhou, H. Jin, J. Zhu, Z. Wang, C. Hu, L. Liang, S. Mu, D. He, A new strategy to access Co/N co-doped carbon nanotubes as oxygen reduction reaction catalysts, Chinese Chem. Lett. 32 (2021) 535–538.

[14] Z. Wang, S. Xiao, Z. Zhu, X. Long, X. Zheng, X. Lu, S. Yang, Cobalt-embedded nitrogen-doped carbon nanotubes: A bifunctional catalyst for oxygen electrode reactions in a wide pH range, ACS Appl. Mater. Interfaces. 7 (2015) 4048–4055.

[15] P. Rao, Y. Liu, Y. Q. Su, M. Zhong, K. Zhang, J. Luo, J. Li, C. Jia, Y. Shen, C. Shen, X. Tian, S, N co-doped carbon nanotube encased Co NPs as efficient bifunctional oxygen electrocatalysts for zinc-air batteries, Chem. Eng. J. 422 (2021) 130135.

[16] Y. Xiao, W. Wang, Q. Wu, High active and easily prepared cobalt encapsulated in carbon nanotubes for hydrogen evolution reaction, Int. J. Hydrogen Energy 45 (2020) 3948–3958.

[17] Y. Han, X. Mao, X. Yan, Q. Wu, H. Xu, Q. Fang, Y. Jia, X. Yao, Q. Li, A. Du, Carbon nanotubes encapsulated transition metals for efficient hydrogen evolution reaction: coupling effect of 3d orbital and π-bond, Materials Today Chemistry 30 (2023) 101573.

[18] N. Saifuddin, A.Z. Raziah, A.R. Junizah, Carbon nanotubes: A review on structure and their interaction with proteins, Journal of Chemistry 2013 (2013) 676815.

[19] W. H. Duan, Q. Wang, K. M. Liew, X. Q. He, Molecular mechanics modeling of carbon nanotube fracture, Carbon N. Y. 45 (2007) 1769–1776.

[20] A. A. Puretzky; D. B. Geohegan; X. Fan; S. J. Pennycook, In situ imaging and spectroscopy of single-wall carbon nanotube synthesis by laser vaporization, Appl. Phys. Lett. 76 (2000) 182–184.

[21] L. Qiu, F. Ding, Understanding single-walled carbon nanotube growth for chirality controllable synthesis, Accounts Mater. Res. 2 (2021) 828–841.

[22] J. R. Sanchez-Valencia, T. Dienel, O. Gröning, I. Shorubalko, A. Mueller, M. Jansen, K. Amsharov, P. Ruffieux, R. Fasel, Controlled synthesis of single-chirality carbon nanotubes, Nature. 512 (2014) 61–64.

[23] D. Hedman, H. Reza Barzegar, A. Rosén, T. Wågberg, J.A. Larsson, On the stability and abundance of single-walled carbon nanotubes, Sci. Rep. 5 (2015) 16850.

[24] T. Cui, X. Pan, J. Dong, S. Miao, D. Miao, X. Bao, A versatile method for the encapsulation of various non-precious metal nanoparticles inside single-walled carbon nanotubes, Nano Res. 11 (2018) 3132–3144.

[25] F. Liu, X. Zhang, X. Zhang, L. Wang, M. Liu, J. Zhang, Dual-template strategy for electrocatalyst of cobalt nanoparticles encapsulated in nitrogen-doped carbon nanotubes for oxygen reduction reaction, J. Colloid Interface Sci. 581 (2021) 523–532.

[26] R. Dovesi, A. Erba, R. Orlando, C. M. Zicovich-Wilson, B. Civalleri, L. Maschio, M. Rérat, S. Casassa, J. Baima, S. Salustro, B. Kirtman, Quantum-mechanical condensed matter simulations with CRYSTAL, Wiley Interdiscip. Rev. Comput. Mol. Sci. 8 (2018) e1360.

[27] S. Grimme, A. Hansen, J.G. Brandenburg, C. Bannwarth, Dispersion-corrected mean-field electronic structure methods, Chem. Rev. 116 (2016) 5105–5154.

[28] S. Pakhira, J. L. Mendoza-Cortes, Quantum nature in the interaction of molecular hydrogen with porous materials: implications for practical hydrogen storage, J. Phys. Chem. C. 124 (2020) 6454–6460.

[29] S. Pakhira, B.S. Lengeling, O. Olatunji-Ojo, M. Caffarel, M. Frenklach, W.A. Lester, A Quantum Monte Carlo study of the reactions of CH with acrolein, J. Phys. Chem. A. 119 (2015) 4214–4223.

[30] A. Singh, S. Pakhira, Synergistic niobium doped two-dimensional zirconium diselenide: an efficient electrocatalyst for O_2 reduction reaction, ACS Phys. Chem. Au. 4 (2024) 40–56.

[31] K. Momma, F. Izumi, VESTA 3 for three-dimensional visualization of crystal, volumetric and morphology data, J. Appl. Crystallogr. 44 (2011) 1272–1276.

[32] J. Laun, D. Vilela Oliveira, T. Bredow, Consistent Gaussian basis sets of double- and triple-zeta valence with polarization quality of the fifth period for solid-state calculations, J. Comput. Chem. 39 (2018) 1285–1290.

[33] S. Pakhira, J. L. Mendoza-Cortes, Intercalation of first-row transition metals inside covalent-organic frameworks (COFs): A strategy to fine-tune the electronic properties of porous crystalline materials, Phys. Chem. Chem. Phys. 21 (2019) 8785–8796.

[34] H. J. Monkhorst, J. D. Pack, Special points for Brillonin-zone integrations, J. Mater. Chem. A. 13 (1976) 5188– 5192.

[35] A. Singh, S. Pakhira, Unraveling the electrocatalytic activity of platinum doped zirconium disulfide toward the oxygen reduction reaction, Energy Fuels 37 (2023) 567–579.

[36] Y. Ji, M. Yang, H. Dong, L. Wang, T. Hou, Y. Li, Monolayer group IVA monochalcogenides as potential and efficient catalysts for the oxygen reduction reaction from first-principles calculations, J. Mater. Chem. A. 5 (2017) 1734–1741.

[37] J. K. Nørskov, J. Rossmeisl, A. Logadottir, L. Lindqvist, J. R. Kitchin, T. Bligaard, H. Jónsson, Origin of the overpotential for oxygen reduction at a fuel-cell cathode, J. Phys. Chem. B. 108 (2004) 17886–17892.

[38] E. Ali, D. Hadis, K. Hamzeh, K. Mohammad, Z. Nosratollah, A. Abolfazl, A. Mozhgan, H. Younes, J. S. Woo, Carbon nanotubes: properties, synthesis, purification, and medical applications, Nanoscale Res. Lett. 9 (2014) 393.

[39] D. Deng, L. Yu, X. Chen, G. Wang, L. Jin, X. Pan, J. Deng, G. Sun, X. Bao, Iron encapsulated within pod-like carbon nanotubes for oxygen reduction reaction, Angew. Chem. Int. Ed. 52 (2013) 371–375.

[40] H. Ulbricht, G. Moos, T. Hertel, Physisorption of molecular oxygen on single-wall carbon nanotube bundles and graphite, Phys. Rev. B 66 (2002) 075404.

[41] Z. Xu, Z. Zhou, B. Li, G. Wang, P. W. Leu, Identification of efficient active sites in nitrogen-doped carbon nanotubes for oxygen reduction reaction, J. Phys. Chem. C. 124 (2020) 8689–8696.

[42] A. V. Kuzmin, B. A. Shainyan, Theoretical density functional theory study of electrocatalytic activity of MN_4-Doped (M = Cu, Ag, and Zn) single-walled carbon nanotubes in oxygen reduction reactions, ACS Omega. 6 (2021) 374–387.

[43] K. A. Samawi, E. A. A. Salman, H. A. Hasan, H. A. M. A. Mahmoud, S. M. Mohealdeen, G. Abdulkareem-Alsultan, E. Abdulmalek, M. F. Nassar, Single-atom cobalt encapsulated in carbon nanotubes as an effective catalyst for enhancing sulfur conversion in lithium-sulfur batteries, Mol. Syst. Des. Eng. 9 (2024) 464–476.

[44] S. Kumar, R. Kumar, N. Goyal, A. Vazhayil, A. Yadav, N. Thomas, B. Sahoo, N-doped carbon nanotubes nucleated through cobalt nanoparticles as bifunctional catalysts for Zinc-air batteries, ACS Appl. Nano Mater. 7 (2024) 7865–7882.

[45] S. Liang, C. Liang, High-density cobalt nanoparticles encapsulated with nitrogen-doped carbon nanoshells as a bifunctional catalyst for rechargeable zinc-air battery, Materials 12 (2019) 243.

[46] Y. Liu, H. Jiang, Y. Zhu, X. Yang, C. Li, Transition metals (Fe, Co, and Ni) encapsulated in nitrogen-doped carbon nanotubes as bi-functional catalysts for oxygen electrode reactions, J. Mater. Chem. A. 4 (2016) 1694–1701.

CHAPTER 6

Exploring the Active Site and Catalytic Activity of N-Coordinated Ni_2 Dual-Atom Catalysts for Oxygen Reduction

The O_2 reduction reaction (ORR) is a pivotal electrochemical process in fuel cells, yet its sluggish kinetics continue to hinder the performance and commercialization of fuel cell technologies. In this chapter, we present a Ni_2 dual atom anchored on a N-doped carbon nanotube (Ni_2_N_3_CNT and Ni_2_N4_CNT) and a Ni single-atom anchored on N-doped carbon nanotube (Ni_1_N_3_CNT and Ni_1_N_4_CNT) catalysts with two possible active sites, namely, Ni-site and N-site, as efficient catalysts toward the ORR. We have analyzed the energetically favorable active site for O_2 reduction on the surface of the Ni_1_N_3_CNT, Ni_1_N_4_CNT, Ni_2_N_3_CNT, and Ni_2_N_4_CNT catalysts by employing the density functional theory method with van der Waals (vdW) dispersion corrections (in short, the DFT-D3) method. Among all possible configurations, Ni_2_N_3_CNT is a more favorable configuration with the Ni catalytic active site toward the ORR. Then, we have studied the structural, electronic, and catalytic activity of Ni_2_N_3_CNT by using the same DFT-D3 method. The analysis of the ORR intermediate species reveals that the associative reaction pathway is a more favorable path for reducing the O_2 into H_2O at the Ni catalytic site of Ni_2_N_3_CNT than the dissociative reaction pathway. In the free energy profile, all the ORR reaction intermediate steps are downhill, indicating the good catalytic activity of Ni_2_N_3_CNT toward the ORR. Moreover, we have also studied the structural and electronic properties of all of the reaction intermediate steps by employing the same DFT-D3 method. These findings point out that the Ni_2 dual-atom catalysts provide an efficient electrocatalytic activity toward the ORR, and it holds great promise as a replacement for Pt-based catalysts in future proton-exchange membrane fuel cells. This work highlights the potential and importance of the subject material

as a durable electrocatalyst for the ORR, offering insights into Ni_2 dual-atom electrochemistry and the design of advanced catalysts, which may be promising candidate to substitute for Pt electrodes, and it is an excellent material for fuel-cell components.

6.1. Introduction: The growing global energy demand, driven by population growth, urbanization, and industrialization, has underscored the urgent need for sustainable and eco-friendly energy alternatives to fossil fuels, which are both finite and environmentally detrimental. While renewable energy sources like solar, wind, and hydro offer promise, their practical deployment faces challenges related to intermittency, cost, and geographic limitations[1-5]. In this context, electrochemical energy conversion technologies, particularly fuel cells and metal–air batteries, have emerged as promising solutions. A key bottleneck in these systems is the sluggish kinetics of the oxygen reduction reaction (ORR) at the cathode, which hampers their overall efficiency[6-9]. Therefore, the development of efficient, cost-effective electrocatalysts to accelerate the ORR is critical for advancing next-generation clean energy technologies. Until now, Pt group metals (PGMs) and Pt-based materials have been widely considered to be the most effective electrocatalysts for ORR[10−13]. The limited availability, expensive nature, and less durable characteristics of Pt and Pt group electrocatalysts pose significant obstacles to the widespread implementation of commercial renewable energy applications of these devices[14−17]. Therefore, it remains a considerable challenge to replace the PGM-based electrocatalysts in acidic media with earth-abundant materials for efficient ORR, which is crucial for large-scale applications of proton-exchange membrane fuel cells. Hence, finding an efficient, highly active, earth-abundant, low-cost electrocatalyst that matches the efficiency of Pt-based materials is still a challenging task. In the past few years, significant endeavors have been dedicated to the advancement of a catalyst that meets the aforementioned requirements. Recently, a large family of transition-metal-based electrocatalysts such as chalcogenides, phosphides, nitrides, and oxides have been synthesized and studied as electrocatalysts toward the ORR[18−21]. However, the majority of transition-metal-based electrocatalysts are still linked with severe limitations, including poor catalytic activity, inferior stability, inferior conductivity, etc. Simultaneously, extensive research has been dedicated to exploring non-noble-metal-based or metal-free kinds of electrocatalysts. Among numerous choices, carbon materials, including graphene, carbon nanotubes (CNTs), and covalent organic frameworks, are considered to be suitable candidates for the electrocatalyst to replace the PGM-based electrocatalyst[22,23]. Among the carbon materials, CNT materials have several unique properties and advantages that are best suited for effective

electrocatalysts, for instance, (1) high surface-to-volume ratio[24] (CNTs can provide a large density of catalytic active site because they have a high surface-to-volume ratio, which, in turn, will enhance the catalytic activity of the material); (2) high stability[25,26] [CNTs show exceptional stability (because they have covalent bonding and high mechanical strength) toward corrosion and reaction byproducts]; (3) good conductivity[27] (most CNTs possess excellent conductivity); (4) low cost (the cost of CNTs is less than that of noble-metal catalysts). Thus, commercialization of such types of catalysts would be easy due to such excellent properties, but the poor catalytic activity of carbon materials hinders their utilization as catalysts. Very recently, a few carbon materials, such as CNT, glassy carbon, and graphite, have been investigated and analyzed for the poor catalytic activity of these materials toward the ORR[28−30]. To enhance the catalytic performance of CNTs, numerous strategies, including doping, defects, and encapsulation engineering, have been proposed. Higher activity of N doped CNTs (NCNTs) was observed compared to pristine CNTs[31]. Chen et al. have successfully synthesized and analyzed the ORR activity of NCNTs[31]. Niu et al. discovered that the NCNTs encapsulating CoNi nanoparticles possess excellent catalytic activity toward the ORR, and the apical catalytic active site on CoNi@NCNT is near CoNi nanoparticles[32]. Wang et al. reported that the NCNT-supported Fe/Ce bimetallic catalysts have excellent catalytic activity toward the ORR[33]. Wang et al. recently synthesized cobalt or nickel nanoparticles-encapsulated NCNTs and claimed that they can serve as excellent catalysts for the ORR[34]. Huang et al. reported that the copper−nitrogen-doped carbon-based nano catalysts Cu-NCs), featuring atomically dispersed Cu− N_xC_{4-x} sites, effectively enhance the Fenton-like reaction, particularly under acidic conditions, where they generate hydroxyl radicals (OH), and under neutral conditions, where they generate both OH and superoxide radicals (O_2^-). Density functional theory (DFT) calculations reveal that the catalytic activity is linked to the adsorption strength of OH at the Cu sites, with Cu−N_2C_2 sites identified as optimal for this reaction[35]. Gao et al. investigated the structure transition and peroxidase mimic activity of the copper sites in copper-doped carbonized polymer dots (CPDs). They found that the doping of copper alters the coordination environment and enhances the catalytic properties of CPDs and revealed that the mechanism for catalyzing H_2O_2 followed a dual-site catalyzed pathway[36]. Zhou et al. studied an asymmetric dinitrogen coordinated nickel single-atom catalyst (Ni−N−C) for efficient CO_2 electroreduction. The findings reveal that the asymmetric and unsaturated Ni single sites could enable efficient CO_2 electroreduction[37]. These findings provide crucial insights for optimizing the design and performance of nitrogen-coordinated metal atoms in catalytic applications. In recent years, dual-atom catalysts have been given

significant attention because introducing an additional metal to a single-metal catalyst significantly improves the catalytic activity of a single-metal catalyst[38]. In dual-metal catalysts, due to the introduction of the adjacent metal atom, there will be a unique orbital interaction between two metal atoms that will perform a stronger synergistic effect. Thus, a dual-metal catalyst provides more possibility to enhance the catalytic activity of the catalytic site than a single-atom catalyst[39−41]. Tang et al. developed a novel dual-metal catalyst with FeN_3−CoN_3 sites on N-doped graphene nanosheets, which exhibited higher ORR activity than a single-atom catalyst[42]. Wang et al. reported that the Co and Fe dual-metal sites embedded in N doped porous carbon (Fe/Co-N_6-C) electrocatalysts express superior catalytic efficiency toward the ORR[43]. Ren et al. successfully created a catalyst known as Ni/Fe-N_6-C, which consists of a diatomic Ni/Fe site anchored on N-doped carbon. This catalyst demonstrates remarkable efficiency in the reduction of CO_2, resulting in the production of CO[44]. Moreover, Li et al. synthesized a dual-atom Ag_2/graphene catalyst and claimed that it exhibits a superior reduction capacity of CO_2[45]. Recently, Luo et al. designed heteronuclear and homonuclear graphene-based dual-metal catalysts for efficient CO_2 reduction on the basis of DFT computations and simulations[46]. Lian et al. recently synthesized a Ni anchored on a NCNT catalyst (single-atom and dual-atom catalyst) for CO_2 reduction. They experimentally obtained that the two adjacent Ni atoms act as an active catalytic center for the outstanding CO_2 reduction reaction (in short CO_2RR), and it was verified by the DFT calculations[47]. Although the Ni_2 dual atom shows excellent catalytic activity toward CO_2RR, there are still many research scopes for queries regarding the catalytic application of Ni_2 dual-atom catalysts toward electrochemical reactions, for instance, (1) what is the effect of dual-metal doping on the structural and electronic properties of CNT? and (2) could a Ni_2 dual-atom catalyst exhibit superior catalytic activity toward the ORR? In this work, we attempted to tackle the above interesting questions based on DFT calculations. We computationally designed all the experimentally synthesized Ni_2 dual and Ni single atoms anchored on NCNT catalysts and investigated their ORR catalytic activity by employing the first-principles-based DFT method. The Ni_2_N_3_CNT dual-atom catalyst exhibits superior catalytic activity among all other Ni based single and dual-atom catalysts.

6.2 Theory and Computational Details: The calculations, including structural properties, electronic properties, and energetics, in this work have been executed by employing the first-principles-based hybrid functional B3LYP DFT method implemented in the CRYSTAL17 suite package[48−50]. To consider the long-range interactions between the atomic layers, the

dispersion correction (-D3) scheme proposed by Grimme and co-workers has been incorporated with the B3LYP functional; i.e., the B3LYP-D3 method has been employed in the present computations[51]. In other words, all of the periodic DFT calculations have been explored using the hybrid B3LYP-D3 functional implemented in the CRYSTAL17 code package. The Gaussian-type basis sets for expansion of the crystalline orbital have been utilized, as implemented in the CRYSTAL17 code[20]. In the current work, the Gaussian basis set of triple-ζ valence with polarization quality (TZVP) for the C, N, Ni, O, and H atoms was adopted[52−56]. Full structural (i.e., atomic coordinates and cell vectors) optimization was carried out to obtain the equilibrium structure in the present work with the following convergence criterion: (1) The maximum and root-mean-square (RMS) forces were set to 0.000450 and 0.00300 au and the maximum and RMS displacements to 0.001800 and 0.001200 au, respectively. (2) The threshold of the coulomb exchange integral calculation was controlled by the five-threshold sets 7, 7, 7, 7 (ITOL1−ITOL4), and 14 (ITOL5) for geometry optimization. During the self-consistent-field (SCF) process, completion of the SCF process occurred when the energy discrepancy between two consecutive SCF cycles reaches a value of less than 10^{-7} au. The k-point sampling in the irreducible Brillouin zone was set based on the Monkhorst−Pack scheme[57]. For supercell calculations, integration in the Brillouin zone was performed by using an 8 × 8 × 1 k-point mesh under the Monkhorst−Pack scheme. The band profile was plotted by using the highly symmetric Γ−M−K−Γ direction k-point path in the first Brillouin zone. The visualization software VESTA was used to generate graphical drawings and analyze the structural properties for all systems in this work[58].

6.3: Theory and Methodology: The ORR is the cathodic reaction of fuel cells. ORR mainly starts from the adsorption of O_2 molecules and reduces it into water. The overall ORR mechanism can be represented as[59]:

$$O_2 + 4H^+ + 4e^- \rightarrow 2H_2O$$

ORR mainly proceeds via two pathways: $4e^-$ pathway and $2e^-$ pathway[60,61]. The detailed process for both possible ORR pathways has been illustrated in our previous publication[20].

The formation energy of all the single-atom catalysts (SAC) and dual-atom catalysts (DAC) configurations has been calculated by employing the following equation:

$$E_{FE} = E_{system} + a\mu_c - (E_{sheet} + b\mu_N + \mu_M) \quad \text{.....(1)}$$

Where E_{system} and E_{sheet} indicate the total energy of the SAC or DAC configurations and carbon sheet, respectively. The μ_C, μ_N, and μ_M denotes the chemical potential of the single carbon atom, single nitrogen atom, and single metal atom, respectively. In this expression, the letter "a" denotes the number of carbon atoms replaced by the nitrogen and metal atoms during the formation of the SAC and DAC. The letter "b" represents the number of nitrogen atoms in the SAC and DAC.

The efficiency of dual-metal catalysts in this work towards ORR and the favorable path to reduce O_2 into the water on the surface of the dual-metal catalysts has been evaluated at the standard conditions, i.e., at T = 298.3 K, P = 1 bar, and U = 0 V. The adsorption strength of adsorbate ORR species has been analyzed by calculating the difference between the energy of the resulting system (i.e., catalyst and ORR intermediate species) and the sum of the energy of isolated ORR intermediate species and isolated catalytic system. So, the adsorption energy can be calculated as[62,63]:

$$\Delta E_{ads} = E_{total} - E_{adsorbate} - E_{system} \quad \ldots\ldots\ldots\ldots\ldots\ldots (2)$$

Where E_{total} is the energy of the system after the adsorption of ORR intermediate species and $E_{adsorbate}$ is the energy of the isolated ORR intermediate species and E_{system} is the energy of the isolated catalytic system. The Gibbs free energy has been calculated using[20,62,64]:

$$\Delta G = \Delta E + \Delta ZPE - T\Delta S \quad \ldots\ldots\ldots\ldots\ldots\ldots (3)$$

Where ΔE is the adsorption energy calculated from the DFT calculations, ZPE represents the zero-point energy correction, T is the temperature, and ΔS is the change in entropy. We have considered the computational hydrogen electrode (CHE) model proposed by Nørskov and co-workers during this calculation, which tells the free energy of $H^+ + e^-$ under standard conditions without electrode potential equal to the ½ H_2[65]. All the energy calculations have been done at the equilibrium geometry of the system.

The zero-point vibrational energy and the entropy of the adsorbed species have been calculated by adopting the rigid-rotor-harmonic oscillator (RRHO) approximation using the equilibrium structure and computed vibrational frequencies. Rotational and translational entropy contributions were neglected for adsorbed species as these degrees of freedom are constrained. In this approach, the thermodynamic properties of solids can be determined using quantum-

mechanical methods by analyzing the lattice dynamics of the material and employing the principles of statistical thermodynamics, which rely on the formulation of a canonical partition function. The vibrational entropy of a harmonic oscillator with vibrational frequency ω has been calculated as[48,50]:

$$S_v = R\left[\frac{h\omega}{k\left(e^{\frac{h\omega}{kT}}-1\right)} - ln\left(1-e^{-h\omega/kT}\right)\right] \quad \ldots\ldots\ldots\ldots(4)$$

Here, R is the universal gas constant, h is Planck's constant, and k is Boltzmann's constant. The RRHO algorithm has been implemented in the CRYSTAL17 program. The harmonic vibration frequencies and harmonic thermodynamic functions can be activated by using the "FREQCALC" keyword in the input script for frequency calculation of the CRYSTAL17 program[48,50]. In the present calculation, we have adopted the RRHO approximation with the keyword "FREQCALC" in the input script for frequency calculation of the CRYSTAL17 program to find the vibrational entropies and the zero point energy of the adsorbed molecules and other systems used in this work. The rigid-rotor approximation is preferred due to its computational efficiency and its applicability to provide a good approximation to the thermodynamic properties of the systems involved in catalytic or adsorption studies[66]. Moreover, In the case of adsorbed species, the translational motion is restricted, and the rotational motion is often treated as being nearly free but constrained due to the adsorptive interaction with the surface. Thus, it is fairly straightforward to calculate the entropy of the system in RRHO approximation; all that is required is an optimized structure and vibrational frequency calculations. For example, the entropy and ZPE for H_2 using the CRYSTAL17 code was calculated S= 130.2527 J/(mol*K and ZPE= 0.009863 (Hartree/particle) respectively which is fairly close to the NIST database[67], that supports the accuracy of the calculations.

6.4 Results and Discussions: The catalytic activity of Ni anchored on NCNT materials toward the ORR was investigated using the computational modeling of these Ni-based materials. The potential of these materials as an electrocatalyst toward the ORR was investigated by detailed examinations of the structural, electronic, and energetics of these materials by using the first-principles DFT methods. We clarify that our calculations were conducted on a carbon sheet, specifically graphene[68,69]. We utilized a 4×4 supercell of graphene sheet for all calculations. The surface area of the 4×4 supercell of graphene sheet was calculated to be approximately

175.39 $Å^2$. In our present paper, we referred to the substrate as CNT and

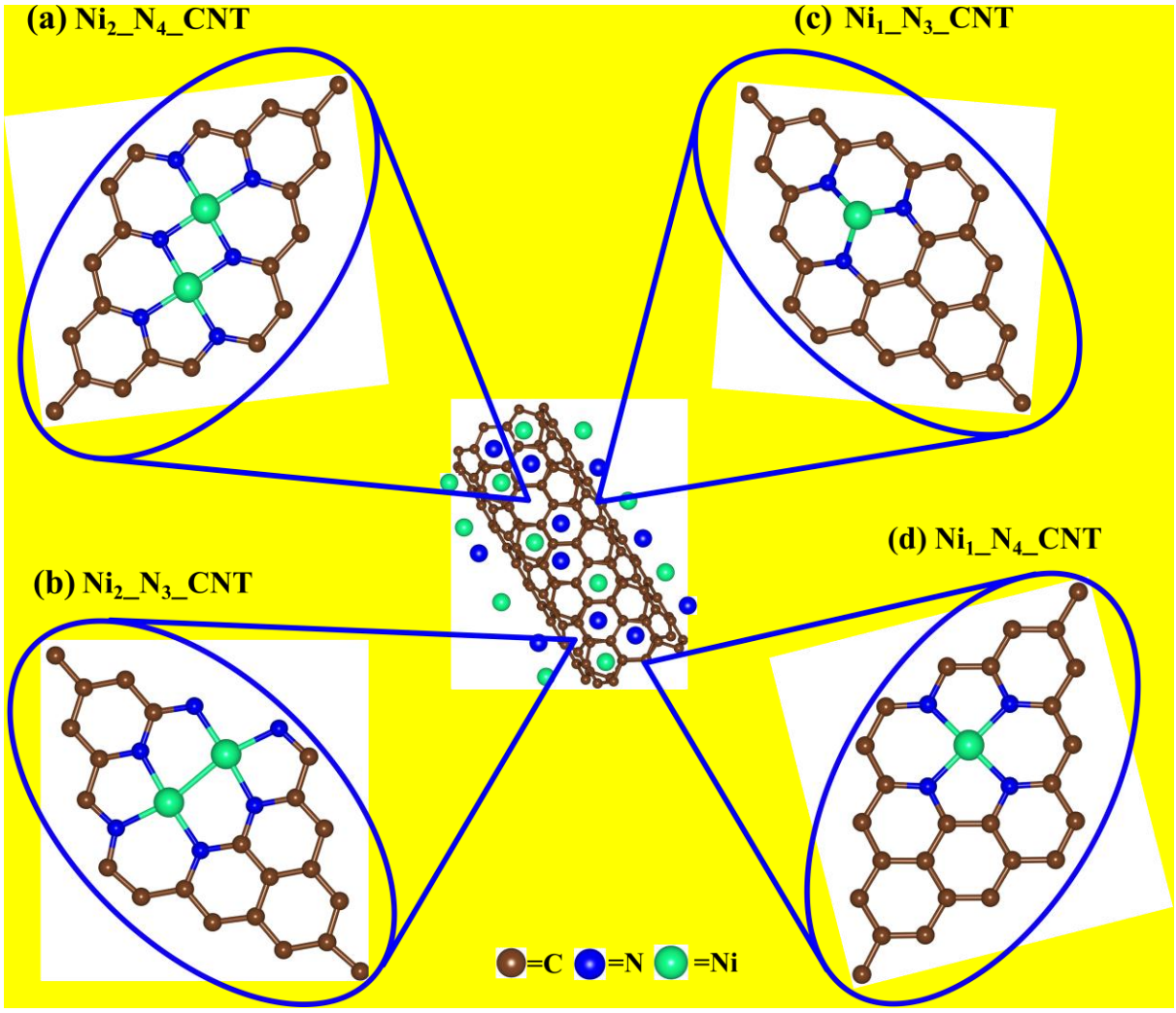

Figure 6.1. The systematic representation of the possible configurations of (a) Ni_2_N_4_CNT, (b) Ni_2_N_3_CNT, (c) Ni_1_N_3_CNT, and (d) Ni_1_N_4_CNT materials are considered here.

adopted the names of the configurations (i.e., Ni_1_N_3_CNT, Ni_1_N_4_CNT, Ni_2_N_3_CNT, and Ni_2_N_4_CNT) to maintain consistency with a previously reported paper by Liang et al. that served as inspiration for our work. It is important to note that the theoretical study by Liang et al. also utilized a carbon sheet for the calculations[47]. Inspired by their approach, we designed and modeled the system accordingly and investigated the electrochemical ORR, as illustrated in Figure 6.1. It should be noted here that when the diameter of the CNT is very large; then, computationally, we can assume that a certain region is a plane/surface, and it would be easier for the current purposes of the work to investigate the subject reaction. Graphene and CNTs, although both composed of sp^2-bonded carbon atoms, exhibit distinct differences primarily due to their geometrical structures. Graphene is a planar sheet of carbon atoms, while CNTs are cylindrical, with their properties varying based on the diameter and chirality. The flat nature of graphene

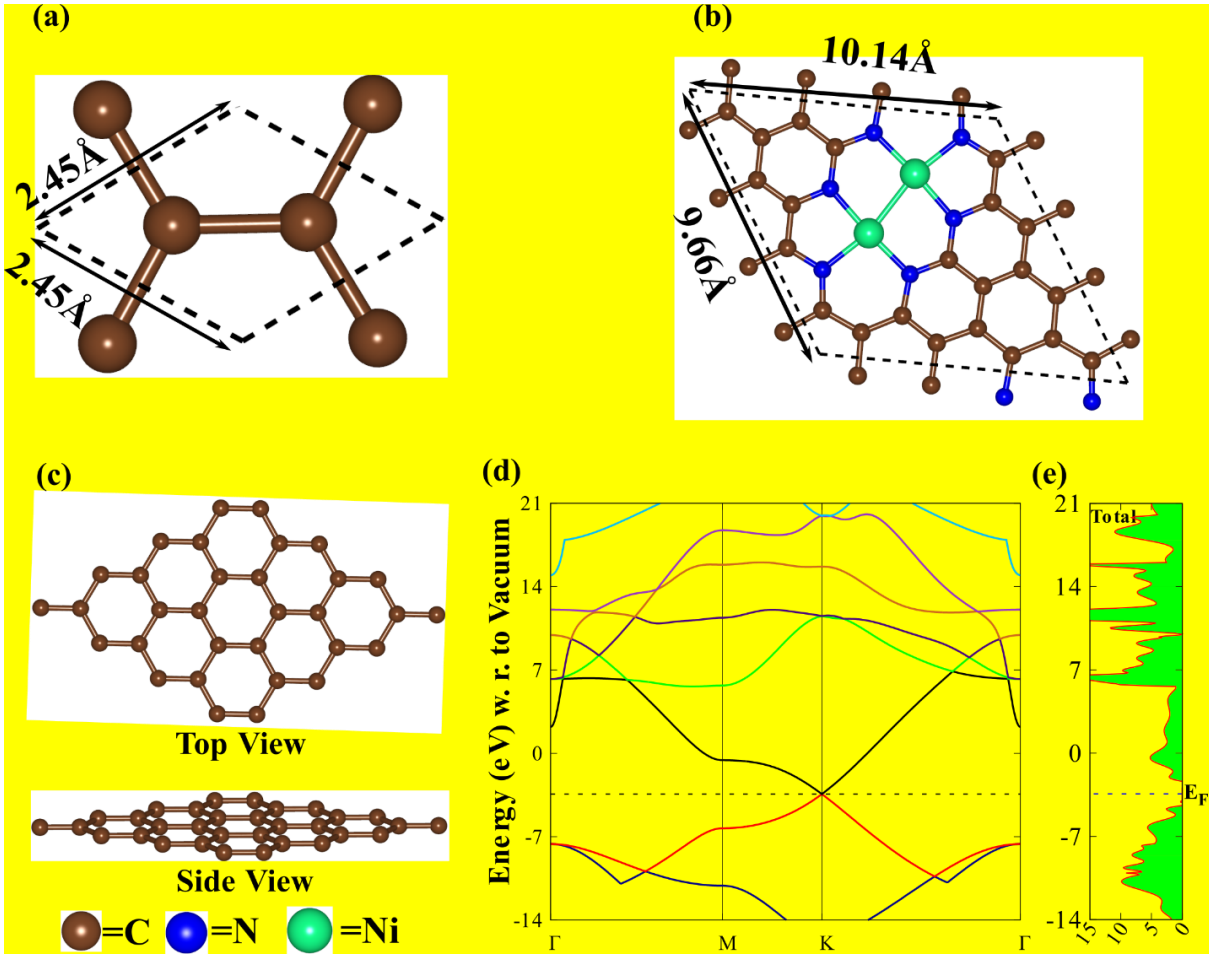

Figure 6.2. *The representation of (a) the equilibrium unit cell of the carbon sheet, (b) the equilibrium supercell of Ni-$_2$_N$_3$_CNT, (c) the equilibrium structure (top and side view) of the carbon sheet, (d) the band structure of the carbon sheet, and (e) TDOS of carbon sheet*

leads to uniform electronic properties across its surface. The absence of curvature results in delocalized π electrons contributing to its high electrical conductivity and other electronic characteristics. On the other hand, the curvature in CNTs causes rehybridization of the carbon atoms from sp^2 to a mix of sp^2 and sp^3 hybridization, affecting their electronic properties. As the diameter of the CNT decreases, the curvature increases, which can lead to variations in the band gap and electronic behavior[70]. Earlier reported literature highlighted that the curvature of the CNT introduces strain and affects the orbital overlap of the π electrons, which, in turn, modifies the electronic band structure. Specifically, the curvature results in a redistribution of

Table 6.1. *The summary of equilibrium structural properties of the carbon sheet, Ni_1_N_3_CNT, Ni_1_N_4_CNT, Ni_2_N_3_CNT, and Ni_2_N_4_CNT material studied here.*

Structures	Equilibrium lattice parameters	Layer group symmetry	Equilibrium average bond length (Å)			Band gap (eV)
			C-C	Ni-Ni	Ni-N	

Carbon Sheet	a=b= 2.45 Å, and α=β= 90˚, γ= 120.00˚	*P6/mmm*	1.41	-	-	0
Ni_1_N_3_CNT	a= 9.82 Å, b= 9.82 Å, and α= 90.00˚, β= 90.00˚, γ= 119.99˚	*P1*	1.43	-	1.85	0
Ni_1_N_4_CNT	a= 9.92 Å, b= 9.68 Å, and α= 90.00˚, β= 90.00˚, γ= 120.82˚	*P1*	1.42	-	1.88	0.55
Ni_2_N_3_CNT	a= 10.14 Å, b= 9.66 Å, and α= 90.00˚, β= 90.00˚, γ= 121.64˚	*P1*	1.44	2.47	1.92	0
Ni_2_N_4_CNT	a= 10.07 Å, b= 9.60 Å, and α= 90.00˚, β= 90.00˚, γ= 121.64˚	*P1*	1.44	2.64	1.84	0.73

π and σ orbitals, leading to altered reactivity and changes in the electronic properties. Meanwhile, for large-diameter CNTs, these curvature-induced effects become negligible, allowing their electronic properties to closely resemble those of planar graphene. The curvature effect remains non-negligible, especially in small-diameter CNTs, where the curvature is more pronounced[71−73]. In our theoretical calculations, CNTs were approximated as graphene under the assumption that the diameters were sufficiently large to minimize the curvature effects. This approach simplifies the computational framework while effectively capturing the dominant electronic characteristics relevant to the catalytic activity under investigation. Nevertheless, we acknowledge that this approximation may not fully capture curvature-induced modifications, particularly for smaller-diameter CNTs, where such effects are more pronounced. Specifically, the graphene model is effective for analyzing general trends and catalytic activity in largerdiameter CNTs, and curvature-induced effects should be carefully considered in studies focusing on smaller-diameter CNTs or precise electronic property analyses. By varying the number of Ni atoms, we modeled four configurations based on the recent experiment[44], where the authors synthesized the systems experimentally[47]. The first configurations have a single Ni atom anchored on N-doped carbon sheet material called a

single-atom catalyst (SAC), namely, Ni_1_N_3_CNT and Ni_1_N_4_CNT, and the other configurations have a double Ni atom anchored on N-doped carbon sheet material called a dual-atom catalyst (DAC), namely, Ni_2_N_3_CNT and Ni_2_N_4_CNT, as represented in Figure 6.1a−d. All of the basic models were initially relaxed to guarantee that the model energy tends to be steady and more identical with the real material and verify that the parameters used in the

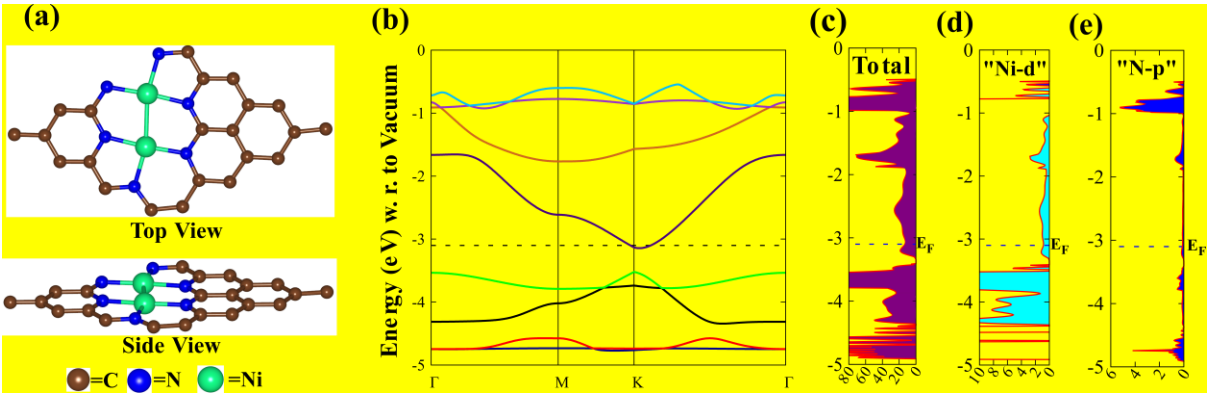

Figure 6.3. *The representation of (a) equilibrium structure (top and side view) of Ni_2_N_3_CNT, (b) band structure of Ni_2_N_3_CNT, (c) TDOS of Ni_2_N_3_CNT, (d) PDOS of d orbital of Ni atom, and (e) PDOS of p orbital of N atom.*

calculations produce reliable outcomes. Initially, the unit cell of the carbon sheet has been optimized by using the DFT-D3 method, and the equilibrium structure is displayed in Figure 6.2a. The carbon sheet has hexagonal symmetry with P6/mmm layer group symmetry. The geometry optimization of the carbon sheet gives the equilibrium lattice parameters a = 2.45 Å and b = 2.45 Å, as represented in Figure 6.2a, obtained by the DFT-D3 method. All of the C atoms are uniformly arranged, having a C−C average bond length of 1.41 Å computed by the same method, and this value is in accordance with the previously reported results[74]. By employing the optimized structure of the carbon sheet, we created a 4× 4 supercell along the X and Y directions. Then, we modeled two SACs and two DACs from the 4×4 supercell of the carbon sheet and optimized them under the full optimization process; i.e., both lattice parameters and atomic coordinates were allowed to relax. The average equilibrium Ni−N bond lengths for Ni_1_N_3_CNT, Ni_1_N_4_CNT, Ni_2_N_3_CNT, and Ni_2_N_4_CNT were found to be 1.85 1.88, 1.92, and 1.84 Å, respectively, obtained by the DFT-D3 method. The equilibrium lattice parameters of the carbon sheet and both the SAC and DAC are presented in Table 6.1, which are in close agreement with the previously reported structural properties of this kind of material[75]. Keeping in mind that the electrochemical reaction is not possible without the contribution of electrons, we can proceed to investigate the electronic properties of the carbon sheet and all Ni-based catalytic systems, i.e., both SAC and DAC, which have been considered in the present investigation. The electronic properties of these systems were examined based

on the electronic band structure, total density of states (TDOS), and partial density of states (PDOS) calculations of the materials considered here. First, we computed the electronic properties of the carbon sheet without any doping. We plotted eight electronic energy bands

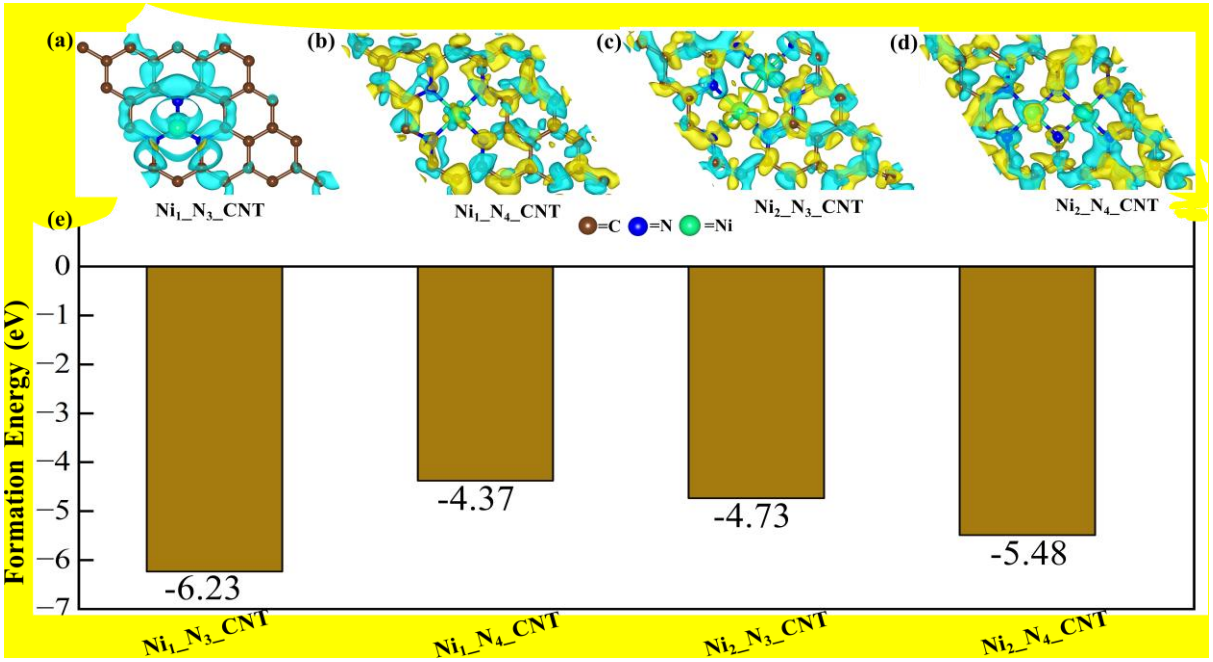

Figure 6.4. *Representation of the electron spin density isosurface of the (a) Ni_1_N_3_CNT, (b) Ni_1_N_4_CNT, (c) Ni_2_N_3_CNT, and (d) Ni_2_N_4_CNT, respectively, and (e) representation of formation energy of the possible SAC and DAC configurations.*

around the Fermi energy level (E_F), which are sufficient for collecting the electronic behavior of the material(s). We plotted the electronic band structure of the pristine carbon sheet along

Table 6.2. *The comparison adsorption strength of O_2*, O*, and H_2O species.*

Catalytic structures	Adsorption energy of O_2* (eV)		Adsorption energy of O* (eV)		Adsorption energy of H_2O (eV)
	Ni	N	Ni	N	Ni
Ni_1_N_3_CNT	-2.20	-1.98	-2.40	-2.19	2.55
Ni_1_N_4_CNT	0.98	0.98	1.91	1.46	-1.58
Ni_2_N_3_CNT	-1.48	-0.27	-1.19	1.21	0.80
Ni_2_N_4_CNT	1.24	0.04	1.98	1.92	-1.71

the Γ−M−K−Γ high-symmetry direction with respect to vacuum, followed by the original layer group symmetry of the 2D monolayer graphene. E_F is shown by the dotted line, and the respective value of the Fermi energy is −3.41 eV. The band structure shows a Dirac cone at the k-symmetric point in the band structure plot. The bands cross E_F, indicating that it may act as

Table 6.3. *The comparison adsorption energy of key ORR intermediate reaction involved in the dissociative and associative path.*

ORR intermediate reaction	Adsorption energy ΔE (eV)
$O_2^* \rightarrow 2O^*$	1.94
$O_2^* + H^+ + e^- \rightarrow OOH^*$	-0.23

a metal. To confirm this, we plotted the TDOS corresponding to the band structure energy range. The TDOS depicts that there is no electron density around E_F. The band structure and TDOS combined clarify the semi metallic nature of the carbon sheet. The band structure and TDOS of the carbon sheet are represented in Figure 6.2d,e. The electronic characteristics of the carbon sheet observed in our research closely align with those reported in prior studies[32]. The electronic properties of Ni-based materials (both SAC and DAC) were computed using the same DFT. We considered eight energy bands to study the band structure of these materials around the E_F. We followed the high-symmetric path Γ−M−K−Γ to plot the band structure of these systems. E_F is presented by the dashed line, and its respective values for Ni_1_N_3_CNT, Ni_1_N_4_CNT, Ni_2_N_3_CNT, and Ni_2_N_4_CNT were found to be −2.66, −2.87, −3.10, and −3.41 eV, respectively. Upon examination of the band structures of the Ni1 SAC and Ni2 DAC, it becomes evident that the Ni_1_N_4_CNT and Ni_2_N_4_CNT configurations demonstrate semiconducting behavior. Conversely, in the Ni_1_N_3_CNT and Ni_2_N_3_CNT configurations, some energy bands intersect E_F, indicating metallic character within these systems. The TDOS plots correspond to the band structure plots showing considerable electron density around E_F for Ni_1_N_3_CNT and Ni_2_N_3_CNT, supporting the metallic character of these systems. The effect of Ni and N atoms in the electronic structure of the carbon sheet was analyzed by computing the PDOS of Ni and N atoms in the system Ni_2_N_3_CNT. The PDOS of the d orbital of Ni follows the profile of the TDOS near E_F and contributes largely to the electron density, whereas the p orbital of the N atom contributes negligibly to the electron density around E_F for Ni_2_N_3_CNT. Thus, the d orbital of Ni mainly affects the electronic properties of the carbon sheet after the doping. The presence of the bands across E_F plays a crucial role in electron transport during the electrochemical ORR mechanism. Thus, the better conducting ability of the Ni-based materials (SAC and DAC) indicates that these materials can be efficient electrocatalysts toward electrochemical ORR. The electronic band structure and TDOS plots of Ni_2_N_3_CNT are represented in Figure 6.3b−e, and both the electronic band structure and TDOS of Ni_1_N_3_CNT, Ni_1_N_4_CNT, and Ni_2_N_4_CNT are represented in Figures S1−S3 (in supporting information section), respectively. We conducted a detailed analysis of the electron

spin density distributions of the Ni_1_N_3_CNT, Ni_1_N_4_CNT, Ni_2_N_3_CNT, and Ni_2_N_4_CNT configurations, as represented in Figure 6.4a–d, where the blue contour (negative spin density) indicates an excess

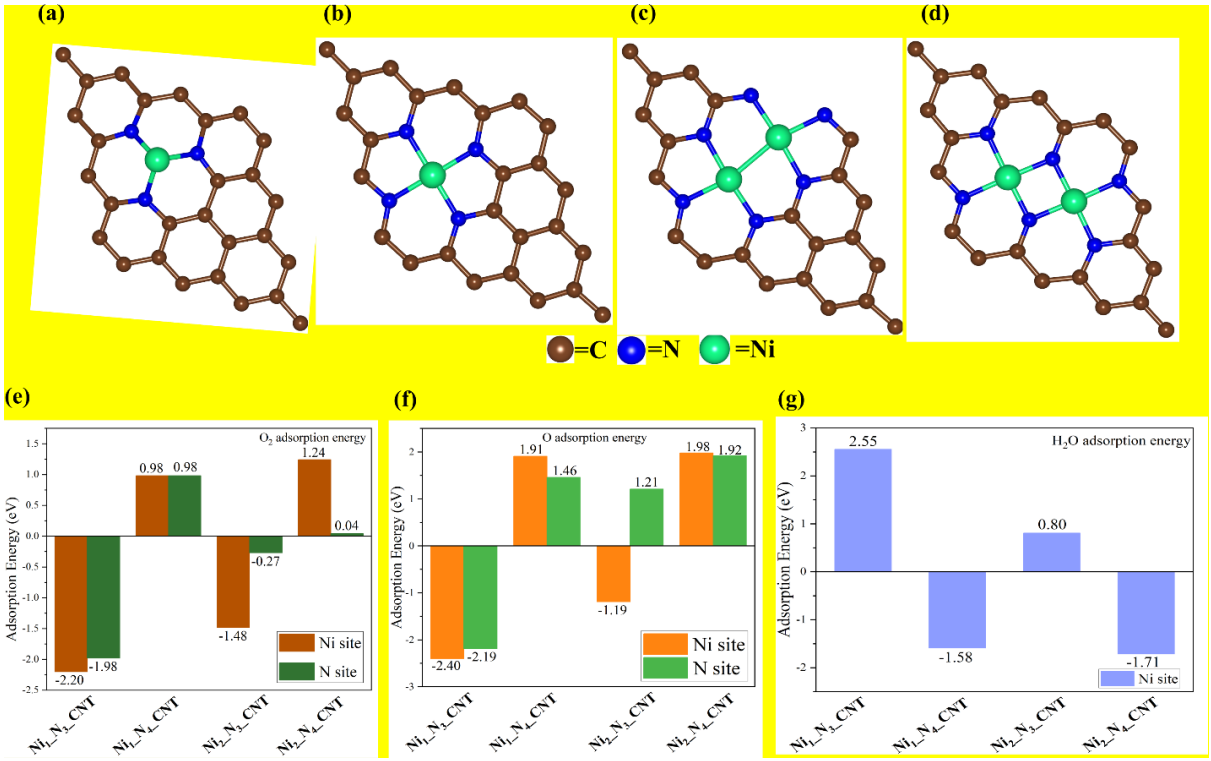

Figure 6.5. *The representation of equilibrium structure of (a) Ni_1_N_3_CNT, (b) Ni_1_N_4_CNT, (c) Ni_2_N_3_CNT, (d) Ni_2_N_4_CNT respectively, and adsorption energy of (e) O_2*, (f) O*, and (g) H_2O ORR intermediate species.*

of β-electron density, and the yellow contour (positive spin density) represents an excess of α-electron density. The spin-density distributions of the Ni_1_N_3_CNT, Ni_1_N_4_CNT, Ni_2_N_3_CNT, and Ni_2_N_4_CNT configurations show significant differences in the spin-density distributions around the Ni atoms and the neighboring N-doped sites. This configuration provides a synergistic effect, where the electronic interactions between the Ni atoms and N sites are maximized. The high electron spin density around Ni atoms indicates strong spin polarization, facilitating the adsorption and activation of O_2 molecules on the surface of Ni_1_N_3_CNT, Ni_1_N_4_CNT, Ni_2_N_3_CNT, and Ni_2_N_4_CNT. The induced spin

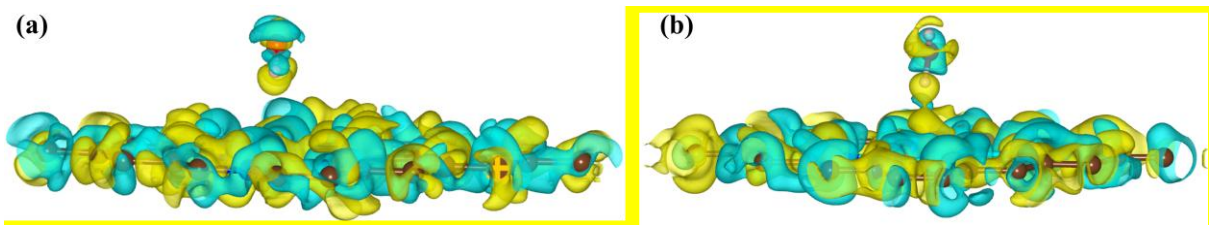

Figure 6.6. *Spin density plot of the (a) H_2O_Ni_2_N_3_CNT and (b) H_2O_Ni_2_N_4_CNT.*

density on adjacent carbon atoms enhances the electron-transfer processes, resulting in them promoting the ORR on the surface of the subject material. The observed asymmetry in the spin distribution highlights the complex electronic interactions within the Ni_1_N_3_CNT, Ni_1_N_4_CNT, Ni_2_N_3_CNT, and Ni_2_N_4_CNT materials, optimizing the binding energies of reaction intermediates and improving the overall efficiency and selectivity of the catalyst. These insights underline the potential of Ni_1_N_3_CNT, Ni_1_N_4_CNT, Ni_2_N_3_CNT, and Ni_2_N_4_CNT to serve as highly effective electrocatalysts in energy conversion applications,

Table 6.4. *The representation of adsorption energy of ORR intermediates in associative path.*

ORR associative mechanism	Adsorption energy ΔE (eV)
$O_2 + * \rightarrow O_2*$	-1.48
$O_2* + H^+ + e^- \rightarrow OOH*$	-0.23
$OOH* + H^+ + e^- \rightarrow O* + H_2O$	-1.96
$O* + H^+ + e^- \rightarrow OH*$	-2.09
$OH* + H^+ + e^- \rightarrow * + H_2O$	0.80

such as fuel cells and metal−air batteries. The thermodynamic stability of the Ni_1_N_3_CNT, Ni_1_N_4_CNT, Ni_2_N_3_CNT, and Ni_2_N_4_CNT configurations were verified through computation of their formation energies using eq 1. Remarkably, all configurations exhibited negative formation energies, as illustrated in Figure 6.4e. The negative formation energy indicates that the Ni_1_N_3_CNT, Ni_1_N_4_CNT, Ni_2_N_3_CNT, and Ni_2_N_4_CNT configurations are more thermodynamically stable than their constituent elements and their formation is energetically favorable. Their thermodynamic stability positions them as promising candidates for diverse applications, including their potential utilization as effective electrocatalysts toward the ORR. Here, we considered four configurations, including the Ni_1_N_3_CNT, Ni_1_N_4_CNT, Ni_2_N_3_CNT, and Ni_2_N_4_CNT materials, as a catalytic material toward the ORR mechanism. The equilibrium structures of both the SAC and DAC are displayed in Figure 6.5a−d. To study the activity of all of the considered configurations Ni_1_N_3_CNT, Ni_1_N_4_CNT, Ni_2_N_3_CNT, and Ni_2_N_4_CNT toward the ORR, we have two main challenges: (1) to search out the most efficient catalysts toward the ORR among Ni SAC and DAC; (2) to search out the most suitable and effective catalytic site for the reduction of O_2. There can be two catalytic sites, Ni and N, for the ORR mechanism in every configuration. To unveil both challenges, a systematic analysis of the adsorption energy calculation of O_2*, O*, and H_2O with the reaction intermediates was performed on the surface of all configurations at possible active sites (i.e.,

Ni and N sites) to investigate the ORR process. In other words, we investigated the adsorption strength of the key ORR intermediates,

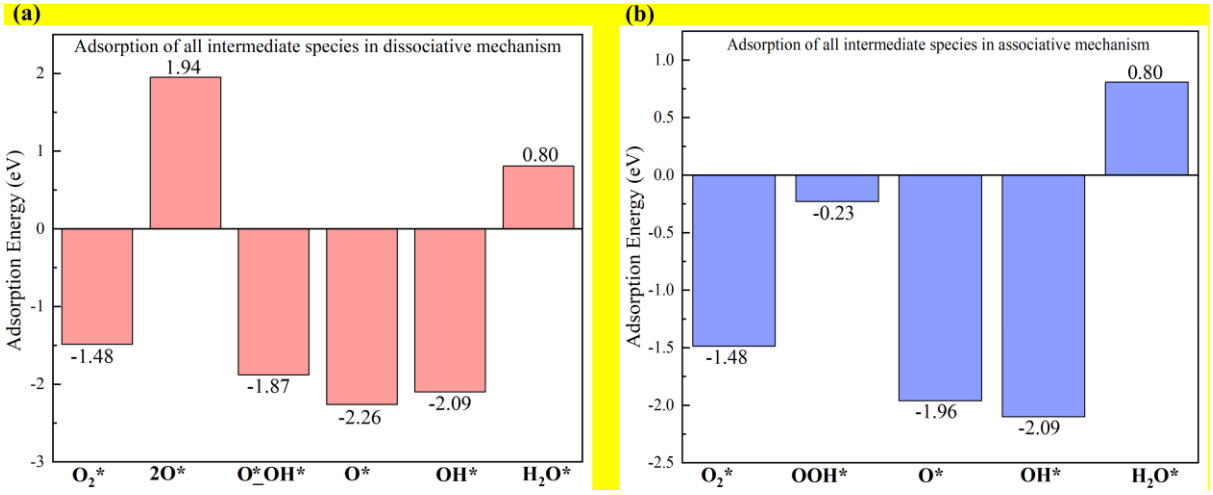

Figure 6.7. *Graphical representation of adsorption energy of ORR intermediates (a) in dissociative mechanism, (b) in associative mechanism.*

O_2*, O*, and H_2O, to determine the most favorable configuration for the ORR among the

Table 6.5. *The representation of adsorption energy of ORR intermediates in the dissociative path*.

ORR dissociative mechanism	**Adsorption energy ΔE (eV)**
$O_2 + * \rightarrow O_2*$	-1.48
$O_2* \rightarrow 2O*$	1.94
$2O* + H^+ + e^- \rightarrow O*\_OH*$	-1.87
$O*\_OH* + H^+ + e^- \rightarrow O* + H_2O$	-2.26
$O* + H^+ + e^- \rightarrow OH*$	-2.09
$OH* + H^+ + e^- \rightarrow * + H_2O$	0.80

various configurations considered here (SAC and DAC). Adsorption of the O_2* molecule is the initial step of the ORR mechanism, and adsorption of O_2* controls the overall activity of the catalysts. The adsorption strength of O_2* at the active site should not be too strong or too weak to get the best performance of the electrocatalysts toward the ORR. A strong interaction of reaction intermediates with the catalytic site results in difficulty in desorbing from the active site, and a too weak interaction results in difficulty in activating the O_2* molecule and initiating the reaction. So, analyzing the adsorption strength of the O_2* molecule on the possible active sites (Ni and N) is an important parameter. The investigation into the adsorption energy of the O_2* molecule on both the Ni_1 single-atom and Ni_2 dual-atom catalytic surfaces was conducted

by affixing an O_2 molecule to the Ni and N sites of each respective configuration. The resulting systems (O_2*_Ni_1_N_3_CNT, O_2*_Ni_1_N_4_CNT, O_2*_Ni_2_N_3_CNT, and

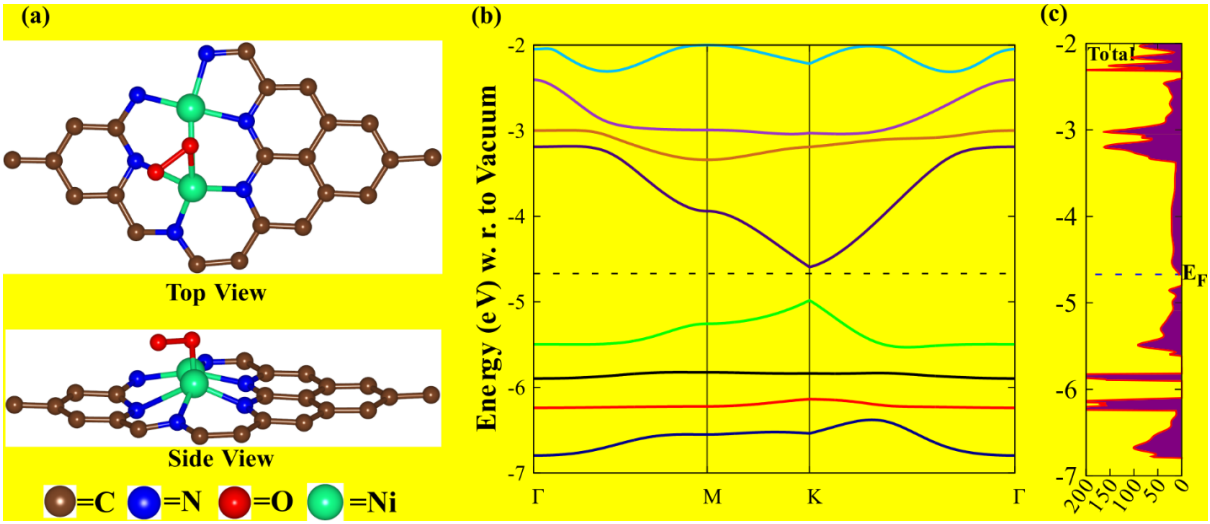

Figure 6.8. *The representation of (a) equilibrium structure (top and side view) of O_2*_Ni_2_N_3_CNT, (b) band structure of O_2*_Ni_2_N_3_CNT, (c) TDOS of O_2*_Ni_2_N_3_CNT.*

O_2*_Ni_2_N_4_CNT) were optimized to obtain the minimum energy configuration. The

Table 6.6. *The equilibrium structural properties of the ORR intermediate steps involved in the ORR associative path.*

Reaction intermediates	Equilibrium lattice constants	Equilibrium average bond length (Å)						Symmetry		Band gap (eV)
		Ni-O	Ni-OH	N-O	N-OH	O-O	O-H			
O_2*	a=10.01 Å, b= 9.66 Å, α=β=90°, γ=121.45°	1.88	-	-	-	1.48	-	*P1*		0.41
OOH*	a=10.10 Å, b= 9.67 Å, α=β=90°, γ=121.75°	1.95	-	-	-	1.52	0.96	*P1*		0
O*	a=10.05 Å, b= 9.66 Å, α=β=90°, γ=121.45°	1.82	-	-	-	-	-	*P1*		0.50
OH*	a=10.05 Å, b= 9.62 Å, α=β=90°, γ=121.40°	-	1.89	-	-	-	0.96	*P1*		0

adsorption energy of the O_2* molecule on the surface of the Ni_1_N_3_CNT, Ni_1_N_4_CNT, Ni_2_N_3_CNT, and Ni_2_N_4_CNT at the Ni site was found to be −2.20, 0.98, −1.48, and 1.24 eV, respectively, and, on the other hand, the value of the adsorption energy of the O_2* molecule at the N site was found to be −1.98, 0.98, −0.27, and 0.04 eV, respectively, as represented in Figure 6.5e and listed in Table 6.2. From the adsorption energy of O_2*, we analyzed whether Ni_1_N_3_CNT has a very strong adsorption strength. On the other hand, Ni_1_N_4_CNT and Ni_2_N_4_CNT have very weak adsorption strength. Thus, the adsorption of O_2* on the surface of Ni_1_N_3_CNT, Ni_1_N_4_CNT, and Ni_2_N_4_CNT is not favorable for the ORR reaction. On the other hand, the adsorption strength of the O_2* molecule on the Ni_2_N_3_CNT surface is moderate and considered to be suitable for the ORR mechanism. This indicates that Ni_2_N_3_CNT has a more suitable adsorption strength for ORR catalytic purposes and, hence, is considered to be a better catalyst among other configurations considered here. For the Ni_2_N_3_CNT structure, two active sites, namely, Ni and N, exist for the adsorption of O_2*. The adsorption energy of O_2* at the Ni and N sites of Ni_2_N_3_CNT was observed to be −1.48 and −0.27 eV, respectively, as represented in Figure 6.5e and listed in Table 6.2. Based on the

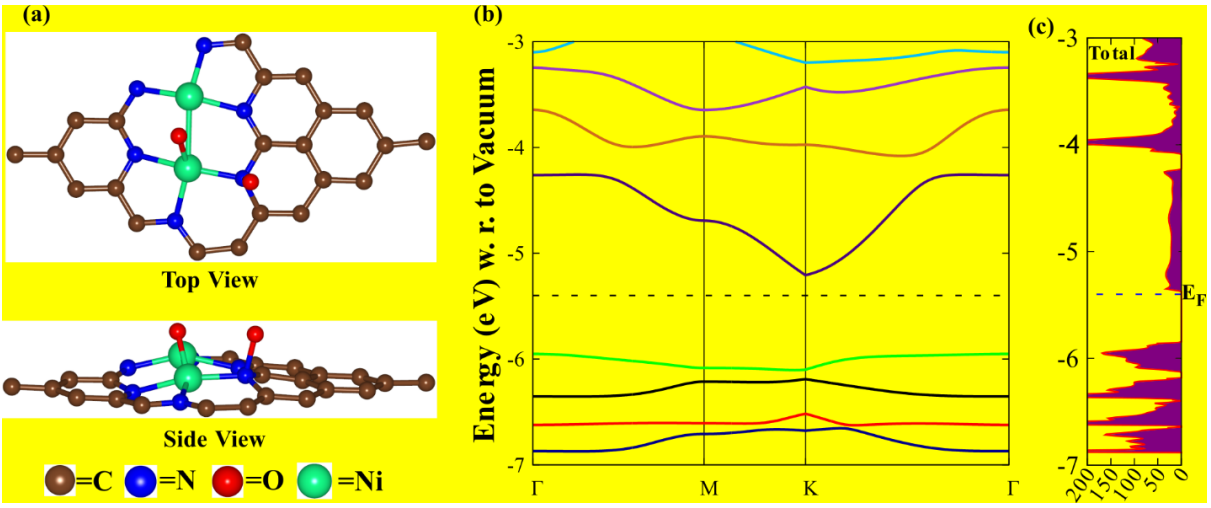

Figure 6.9. *The representation of (a) equilibrium structure (top and side view) of 2O*_Ni_2_N_3_CNT, (b) band structure of 2O*_Ni_2_N_3_CNT, (c) TDOS of 2O*_Ni_2_N_3_CNT.*

adsorption strength, we observed that the O_2* molecule would preferentially adsorb on the Ni site compared to the N catalytic site on the surface of Ni_2_N_3_CNT. Thus, it is considered that the Ni_2_N_3_CNT DAC with Ni as a catalytic active site is the most effective catalyst for ORR,

Table 6.7. *The equilibrium properties of the ORR intermediate steps involved in the ORR dissociative path.*

Reaction intermediates	Equilibrium lattice constants	Equilibrium average bond length (Å)						Symmetry	Band gap (eV)
		Ni-O	Ni-OH	N-O	N-OH	O-O	O-H		

O_2*	a=10.01 Å, b= 9.66 Å, α=β=90°, γ=121.45°	1.88	-	-	-	1.48	-	*P1*	0.41
2O*	a=10.07 Å, b= 9.66 Å, α=β=90°, γ=121.57°	1.82	-	1.49	-	-	-	*P1*	0.75
O*_OH*	a=10.04 Å, b= 9.62 Å, α=β=90°, γ=121.46°	1.77	-	-	1.60	-	0.97	*P1*	0
O*	a=10.05 Å, b= 9.66 Å, α=β=90°, γ=121.45°	1.82	-	-	-	-	-	*P1*	0.50
OH*	a=10.05 Å, b= 9.62 Å, α=β=90°, γ=121.40°	-	1.89	-	-	-	0.96	*P1*	0

among other configurations considered here. Ye et al. reported the Fe-based dual-atom electrocatalyst and its applications toward the ORR[76]. They noted that the O_2 adsorption

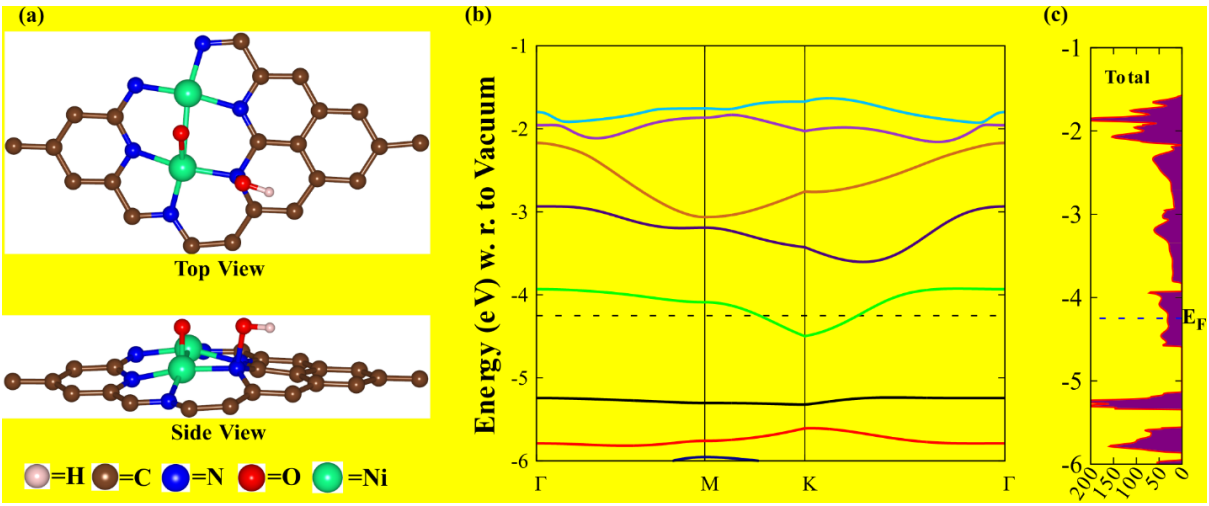

Figure 6.10. *The representation of (a) equilibrium structure (top and side view) of O*_OH*_Ni_2_N_3_CNT, (b) band structure of O*_OH*_Ni_2_N_3_CNT, and (c) TDOS of O*_OH*_Ni_2_N_3_CNT.*

energy on the Fe_2−N−C DAC was 3.10 eV[76]. In another study by Wang et al. on the (Fe,Cu)/NC DAC toward the ORR, the adsorption energy of O_2 was calculated to be −1.72 eV[77]. Comparing the previously reported data, the adsorption energy of O_2 (−1.48 eV) on

Ni_2_N_3_CNT in our present study is optimal and better than the previously reported adsorption energy. This implies better electrocatalytic activation of the O_2 molecule on the surface of Ni_2_N_3_CNT. As a benchmark and to better understand the catalytic active site and favorable configuration (SAC and DAC) for the ORR, we also performed the adsorption energy calculation of the O* atom at each possible active site, i.e., the Ni and N site of each possible structure. The absorption of the O* atom has been studied by placing an O atom on the Ni and N sites of each of the configurations (O*_Ni_1_N_3_CNT, O*_Ni_1_N_4_CNT, O*_Ni_2_N_3_CNT, and O*_Ni_2_N_4_CNT) and relaxed under the full optimization scheme. The adsorption energy of the O* atom at the surface of Ni_1_N_3_CNT, Ni_1_N_4_CNT, Ni_2_N_3_CNT, and Ni_2_N_4_CNT with a Ni site was found to be −2.40, 1.91, −1.19, and 1.98 eV, and that with a N site was found to be −2.19, 1.46, 1.21, and 1.92 eV, respectively, as shown in Figure 6.5f and tabulated in Table 6.2. We observed that adsorption of the O* atom on the surface of the different configurations with possible active sites is very consistent with the adsorption pattern of the O_2* molecule. Upon comparing the adsorption strength of the O* atom, we found that Ni_2_N_3_CNT is a more favorable configuration among all of the other possible configurations for adsorption of the O* atom. A comparison of the adsorption energy of the O* atom at the Ni and N sites of Ni_2_N_3_CNT indicates that the Ni site is a more

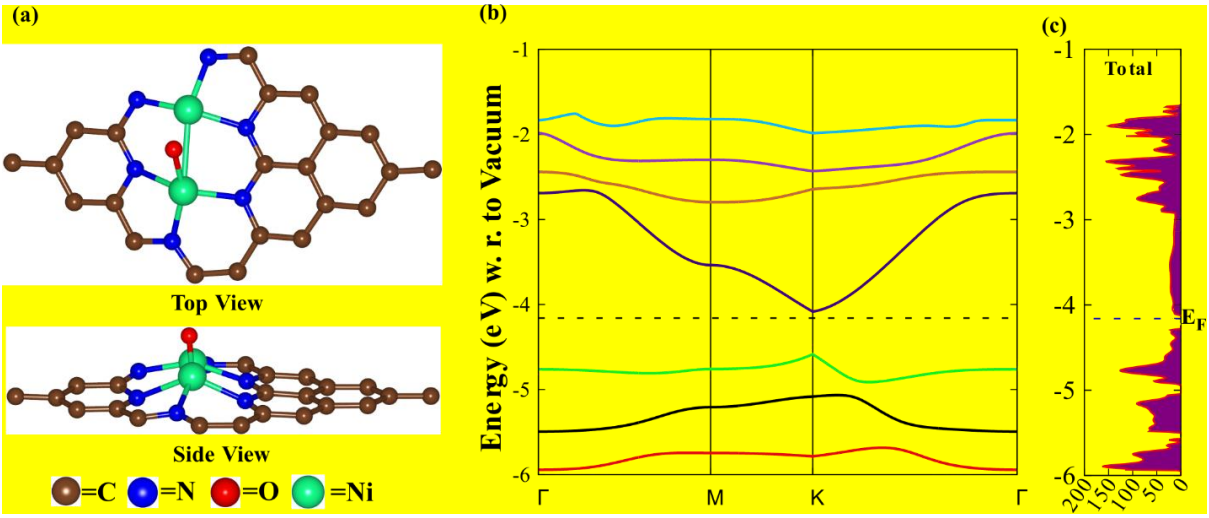

Figure 6.11. *The representation of (a) equilibrium structure (top and side view) of O*_Ni_2_N_3_CNT, (b) band structure of O*_Ni_2_N_3_CNT, and (c) TDOS of O*_Ni_2_N_3_CNT.*

favorable site for absorption. We concluded that Ni_2_N_3_CNT with Ni as an active site is the most favorable configuration among the other configurations and can serve as an efficient electrocatalyst for the ORR. A study of the desorption of water molecules from the catalytic surface can be another good descriptor of an efficient catalyst. The detachment of water molecules is the final step in the ORR process, and the new ORR cycle will then take place.

Table 6.8. *The change in Gibbs free energy during ORR dissociative path on the surface of the Ni_2_N_3_CNT.*

ORR dissociative mechanism	ΔG (eV)	Relative Gibbs free energy (eV)
$O_2 + * \rightarrow O_2*$	-1.36	-1.36
$O_2* \rightarrow 2O*$	1.91	0.55
$2O* + H^+ + e^- \rightarrow O*\_OH*$	-1.54	-0.99
$O*\_OH* + H^+ + e^- \rightarrow O* + H_2O$	-2.63	-3.62
$O* + H^+ + e^- \rightarrow OH*$	-1.76	-5.38
$OH* + H^+ + e^- \rightarrow * + H_2O$	0.43	-4.95

So, interaction of the water molecules with the catalytic site should be as small as possible. A strong interaction will hinder the easy desorption of the water molecule from the catalytic surface. Hence, the strong interaction of water molecules with the catalytic site will cover the catalytic site and corrode the catalytic surface. Thus, the strong interaction of H_2O molecules with the catalytic center reduces the number of catalytic sites for the next cycle, and there is concern about the stability of the catalytic material. The adsorption energy of the H_2O molecule for the Ni_1_N_3_CNT, Ni_1_N_4_CNT, Ni_2_N_3_CNT, and Ni_2_N_4_CNT systems were calculated to be 2.55, −1.58, 0.80, and −1.71 eV, respectively, as represented in Figure 6.5g and tabulated in Table 6.2. The adsorption strength of the H_2O molecule on the surface of Ni_2_N_3_CNT was found to be very weak, suitable among other configurations, and feasible

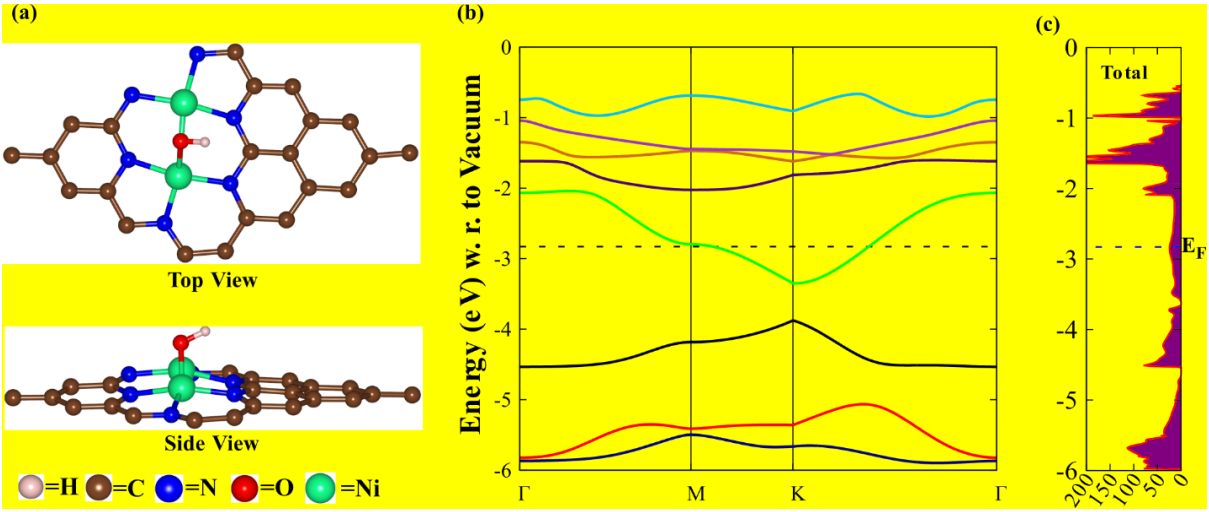

Figure 6.12. *The representation of (a) equilibrium structure (top and side view) of OH*_Ni_2_N_3_CNT, (b) band structure of OH*_Ni_2_N_3_CNT, and (c) TDOS of OH*_Ni_2_N_3_CNT.*

for the ORR process. In a recent study by Wang et al., the adsorption energy of H_2O on the (Fe,Co)/NC electrocatalyst for the ORR was found to be 0.32 eV[77]. Interestingly, when considering the Ni_2_N_3_CNT surface, the adsorption energy of H_2O is even more positive compared to previously reported values. This positive adsorption energy suggests that H2O molecules can easily desorb from the Ni_2_N_3_CNT catalytic site, thereby enhancing the kinetics of the ORR. We have conducted the spin-density analysis of the H_2O-adsorbed Ni_2_N_3_CNT (H_2O_Ni_2_N_3_CNT) and Ni_2_N_4_CNT (H_2O_Ni_2_N_4_CNT) systems, as shown in Figure 6a,b. The blue contour (negative spin density) indicates an excess of β-electron density, and the yellow contour (positive spin density) represents an excess of α

Table 6.9. *The change in Gibbs free energy during ORR associative path on the surface of the Ni_2_N_3_CNT.*

ORR associative mechanism	ΔG (eV)	Relative Gibbs free energy (eV)
$O_2 + * \rightarrow O_2*$	-1.36	-1.36
$O_2* + H^+ + e^- \rightarrow OOH*$	-0.01	-1.37
$OOH* + H^+ + e^- \rightarrow O* + H_2O$	-2.24	-3.61
$O* + H^+ + e^- \rightarrow OH*$	-1.76	-5.37
$OH* + H^+ + e^- \rightarrow * + H_2O$	0.43	-4.94

electron density. For the H_2O_Ni_2_N_3_CNT system (Figure 6.6a), the spin density is predominantly localized on the Ni atoms and the surrounding carbon framework, with minimal perturbation from the adsorbed H_2O molecule. This observation aligns with the weak interaction reflected by the calculated adsorption energy of 0.80 eV, indicating that H_2O is not

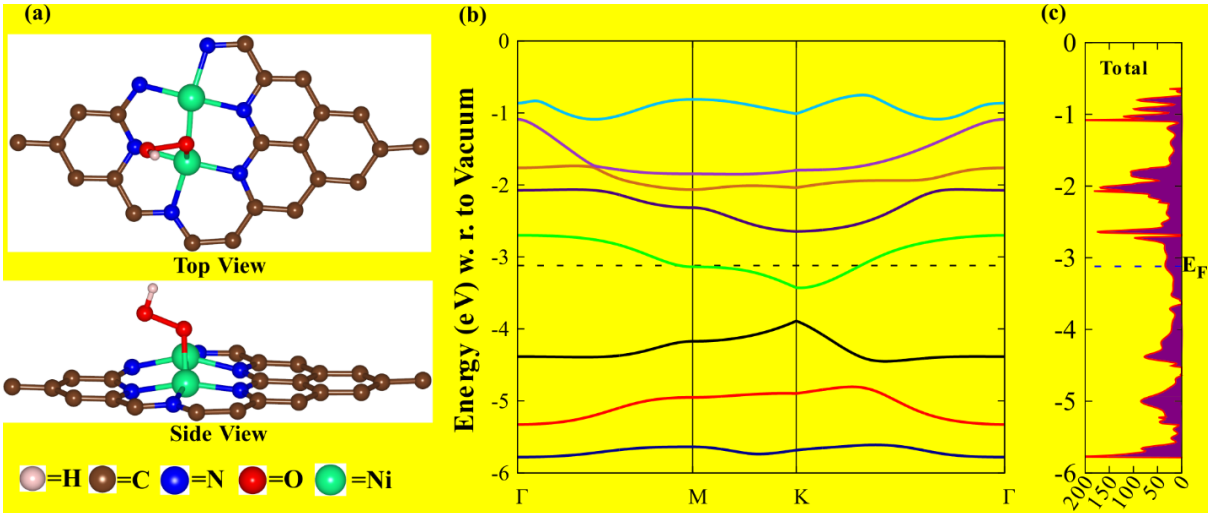

Figure 6.13. *The representation of (a) equilibrium structure (top and side view) of OOH*_Ni_2_N_3_CNT, (b) band structure of OOH*_Ni_2_N_3_CNT, and (c) TDOS of OOH*_Ni_2_N_3_CNT.*

strongly bound and can easily desorb on the surface. Such facile desorption of H_2O is beneficial for enhancing the ORR kinetics because it prevents site blockage. In contrast, the spin-density distribution for the H_2O_Ni_2_N_4_CNT system (Figure 6.6b) shows significant delocalization involving the H_2O molecule and the catalytic site. This stronger interaction is consistent with the negative adsorption energy of −1.71 eV, indicating the stable adsorption of H_2O on this surface. This behavior could result in slower desorption kinetics, potentially inhibiting ORR activity by hindering active site availability. Thus, putting all findings together, we concluded that the Ni_2_N_3_CNT DAC with the Ni active site is the most active and favorable catalyst among all other possible configurations considered in this study. Liang et al. developed the Ni_1_N_3_CNT, Ni_1_N_4_CNT, Ni_2_N_3_CNT, and Ni_2_N_4_CNT SAC and DAC experimentally and theoretically and studied the electrocatalytic activity of these systems toward CO_2RR. The researchers found that the DACs exhibited superior performance compared to the SACs in CO_2RR. Specifically, the Ni_2_N_3_CNT configuration demonstrated the highest electrocatalytic activity among all tested systems[47]. In our study, we found that Ni_2_N_3_CNT demonstrates higher ORR activity than other configurations, which is consistent with the preliminary reported experimental results. Sun et al. studied the electrocatalytic activity of the Fe- and Cu-based SAC and DAC experimentally and theoretically toward the ORR and demonstrated that the bimetallic electrocatalyst shows higher catalytic activity than the single-atom electrocatalyst[78]. Additionally, Zhang et al. reported that both the FeN_2 SAC and Fe_2N_6 DAC are ORR electrocatalysts. They reported that the DAC exhibits improved electrocatalytic activity compared to the SAC[79]. These consistent experimental and theoretical results further support the effectiveness of DACs in enhancing electrocatalytic performance. The catalytic performance of the electrocatalysts toward the ORR is significantly interlinked with the selectivity of the ORR pathway. The $4e^-$ reduction pathway can further proceed via two different pathways: (1) dissociative and (2) associative pathways, which depend on how the O-O bond breaks. In the dissociative pathway, after adsorption of the O_2* molecule on the catalytic site, it dissociates into two O* atoms at different catalytic sites before reduction. In the associative mechanism, the O_2* molecule is initially adsorbed on the surface of the catalyst, followed by reduction to form the OOH* species, and then O-O bond cleavage happens to form the O* and OH* species at two different catalytic sites. After the reduction of OOH* into O* and OH*, the associative pathway goes the same as the dissociative pathway. We calculated the adsorption energy of both intermediate species 2O* and OOH* to select the favorable reduction path. Adsorption of the 2O* and OOH* intermediate species was found to be +1.94 and −0.23 eV, respectively, as tabulated in Table 3 and represented in Figure 6.7a,b. We

observed that 2O* species have very weak adsorption strength on the catalytic surface and OOH* species have moderate adsorption on the Ni catalytic active site. Thus, considering the adsorption strength of 2O* and OOH* species, the associative path will be a favorable path for breakage of the O-O bond and for the ORR process on the surface of Ni_2_N_3_CNT. Hence, we have considered the associative pathway here to study the O_2 reduction mechanism on the surface of Ni_2_N_3_CNT with the Ni active catalytic site. To further understand the ORR activity of Ni_2_N_3_CNT, the adsorption energy of each of the intermediate species was calculated, as represented in Figure 6.7a,b and tabulated in Tables 6.4 and 6.5. The whole ORR has been studied on the surface of Ni_2_N_3_CNT at the Ni site by following the associative path of the ORR process. The process started with the adsorption of the O_2* molecule on the Ni site. This step was modeled by placing an O_2* molecule near the Ni site. The optimization of the resulting system, O_2*_Ni_2_N_3_CNT, was done by employing the B3LYP-D3 method. The equilibrium bond length of the O_2* molecule after being adsorbed at the Ni site was found to be elongated up to 1.48 Å. The elongation in the OO bond from 1.23 to 1.48 Å indicates activation of the O_2* molecule after adsorption. The Mulliken charge-transfer analysis depicts that the charge transfer of 0.42 |e| from the Ni_2_N_3_CNT surface to O_2* has taken place, which favors bond elongation and activation of the O_2* molecule. The adsorption energy of the O_2* molecule on the Ni_2_N_3_CNT surface was found to be −1.48 eV, which is negative and moderate, indicating that O_2* adsorption is favorable on the Ni_2_N_3_CNT surface at the Ni site. The adsorption energies of other reaction intermediates involved in the associative path of the reaction such as OOH*, O*, and OH* were calculated by following a similar pattern and methods. The adsorption energies of the OOH*, O*, and OH* species on the surface of Ni_2_N_3_CNT were calculated to be −0.23, −1.96, and −2.09 eV, respectively, as represented in Figure 6.7a,b. The moderate and negative values of the adsorption of OOH*, O*, and OH* indicate that all of the species are favorably adducted on the Ni_2_N_3_CNT surface and energetically favorable for the reaction. The adsorption energy of the H_2O molecule was found to be 0.80 eV. The equilibrium structural properties of the intermediate products in the associative and dissociative paths are summarized in Tables 6.6 and 6.7, respectively. The adsorption energies of the intermediate species involved in the dissociative path of the ORR process were also calculated for comparison and the sake of completeness of the study and are represented in Figure 6.7a and shown in Table 6.5. The equilibrium structure of O_2*_Ni_2_N_3_CNT, 2O*_Ni_2_N_3_CNT, O*_OH*_Ni_2_N_3_CNT, O*_Ni_2_N_3_CNT, OH*_Ni_2_N_3_CNT, and OOH*_Ni_2_N_3_CNT are represented in Figures 6.8a, 6.9a, 6.10a, 6.11a, 6.12a, and 6.13a, respectively. Electron transfer has a significant role in the ORR

process. Hence, the study and analysis of the electronic properties of each intermediate reaction structure are important for a better understanding of the catalytic behavior of the material. The band structure and corresponding TDOS for all of the reaction intermediate structures were computed by employing the same DFT functionals. Here, we considered eight bands around the E_F level to analyze the electronic behavior of the intermediate structures. The band structure plot was done along the Γ−M−K−Γ high symmetric path. The intermediate species O_2*_Ni_2_N_3_CNT, 2O*_Ni_2_N_3_CNT, and O*_Ni_2_N_3_CNT show the semiconducting nature with band gaps of 0.41, 0.75, and 0.50 eV, respectively, shown in Figures 6.8b, 6.9b, and 6.11b, respectively. On the other hand, O*_OH*_Ni_2_N_3_CNT, OH*_Ni_2_N_3_CNT, and OOH*_Ni_2_N_3_CNT exhibit metallic nature, as represented in Figures 6.10b, 6.12b, and 6.13b, respectively. EF values

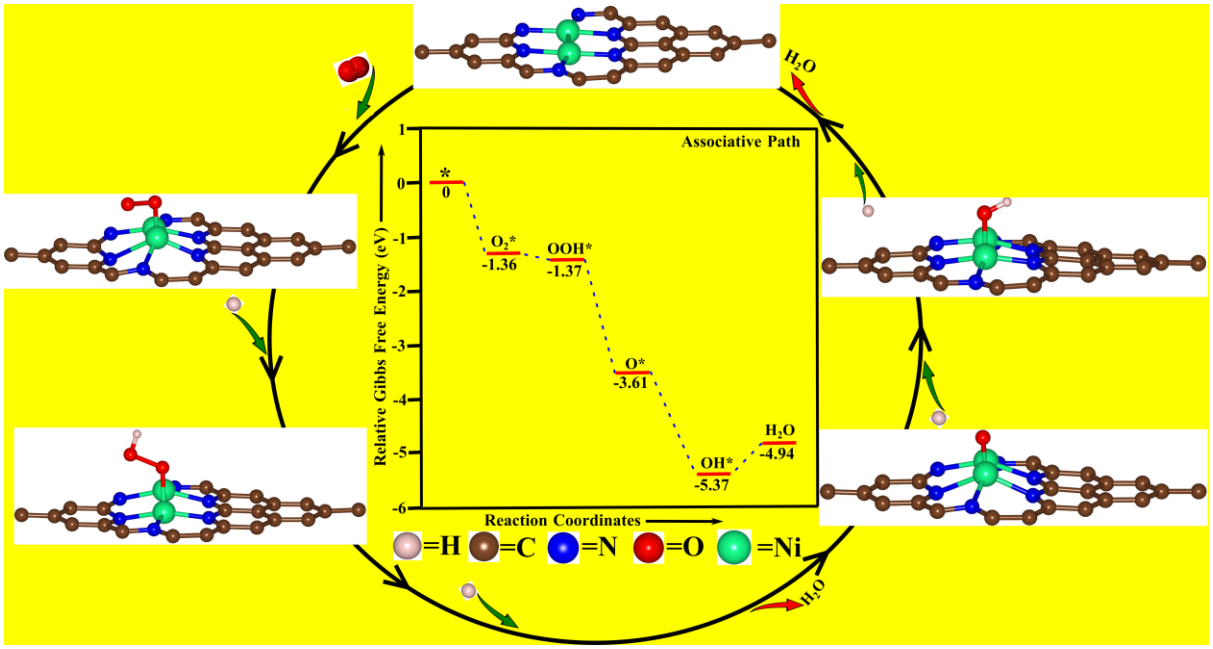

Figure 6.14. *The Gibbs free energy diagram (i.e. free energy vs. reaction coordinates) for the associative ORR pathway on the surface of the Ni_2_N_3_CNT.*

for O_2*_Ni_2_N_3_CNT, 2O*_Ni_2_N_3_CNT, O*_OH*_Ni_2_N_3_CNT, O*_Ni_2_N3_CNT, OH*_Ni_2_N_3_CNT, and OOH*_Ni_2_N_3_CNT are located at −4.67, −5.40, −4.25, −4.16, −2.83, and −3.12 eV, respectively, as shown by the dotted lines in Figures 6.8b, 6.9b, 6.10b, 6.11b, 6.12b, and 6.13b, respectively. The TDOS profiles corresponding to each of the band structure plots of the intermediate species were plotted within the same energy range. The TDOS profile is consistent with the band structure plots and supports the band-gap values. The metallic and semiconducting nature of the intermediate species structures supports electron transfer and facilitates the ORR process. The TDOS plots of O_2*_Ni_2_N_3_CNT, 2O*_Ni_2_N_3_CNT, O*_OH*_Ni_2_N_3_CNT, O*_Ni_2_N_3_CNT, OH*_Ni_2_N_3_CNT, and OOH*_Ni_2_N_3_CNT are

represented in Figures 6.8c, 6.9c, 6.10c, 6.11c, 6.12c, and 6.13c, respectively. Thermodynamic analysis of the whole electrochemical reaction was done by computing the change in free energy (ΔG) for all of the possible intermediate reaction steps according to eq 3. Because the associative path is the favorable path for the O_2* reduction reaction on the

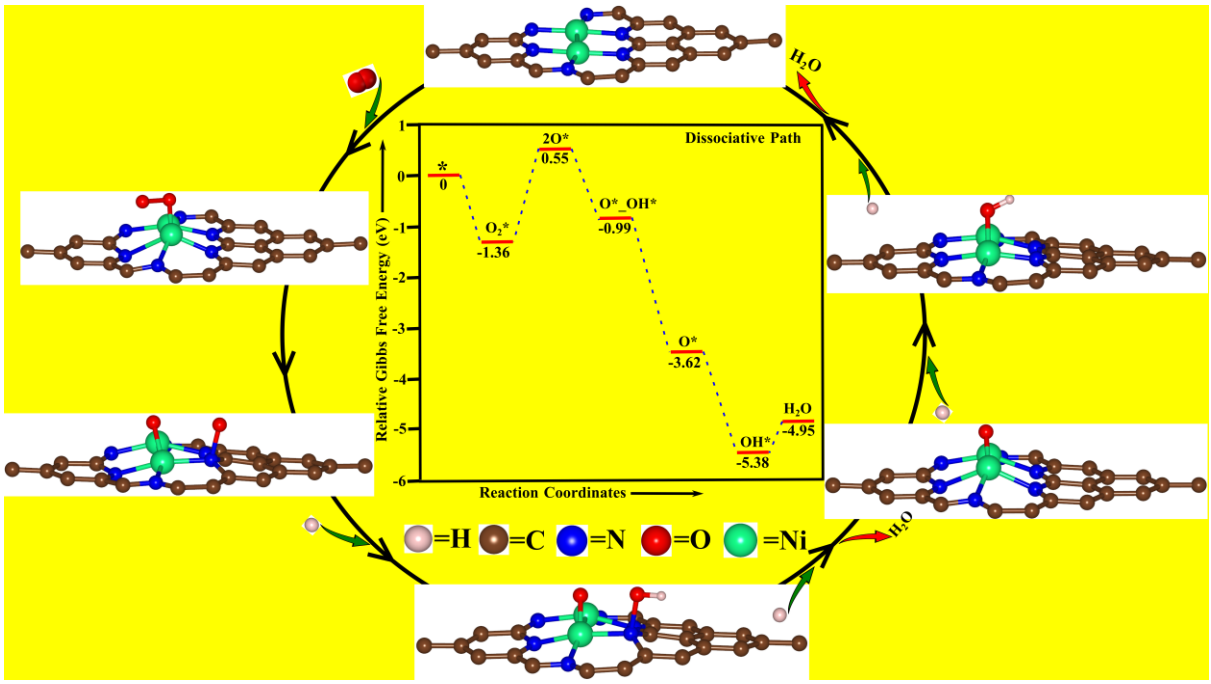

Figure 6.15. *The Gibbs energy diagram for the dissociative ORR pathways on the surface of the Ni_2_N_3_CNT.*

surface of Ni_2_N_3_CNT, the reaction starts with adsorption of the O_2 molecule, i.e., $O_2 + * \rightarrow O_2*$. ΔG during this reaction step was observed to be −1.36 eV. The negative value of ΔG indicates the exothermic nature of the reaction. Hence, this reaction step is a spontaneous and thermodynamically favorable reaction step. This step is followed by hydrogenation of the adsorbed O_2* molecule on the Ni site by a pair of $H^+ + e^-$ reactions. This reaction step is represented as $O_2* + H^+ + e^- \rightarrow OOH*$. ΔG during this reaction step was observed to be −0.01 eV. The exothermic nature of the reaction ensures the favorability of this reaction step. The associative path after hydrogenation of OOH* has three successive reduction steps to reduce the O_2* molecule into water. The subsequent reaction steps are represented as $OOH* + H^+ + e^- \rightarrow O* + H_2O$, $O* + H^+ + e^- \rightarrow OH*$, and $OH* + H^+ + e^- \rightarrow * + H_2O$. ΔG for these reaction steps was calculated to be −2.24, −1.76, and 0.43 eV, respectively. By analyzing the ΔG values for these reaction steps, we observed that the reaction steps of $OOH* + H^+ + e^- \rightarrow O* + H_2O$ and $O* + H^+ + e^- \rightarrow OH*$ are exothermic in nature, hence energetically favorable reaction steps. The last reaction step, $OH* + H^+ + e^- \rightarrow * + H_2O$, has a positive value of ΔG and is hence endothermic in nature. The ΔG values of all of the intermediate reaction steps are summarized in Table 6.9. We have also computed the ΔG values for the dissociative path,

which are shown in Table 6.8. To compile the electrocatalytic reactivity of $Ni_2\_N_3\_CNT$ toward the ORR, we plotted a potential energy surface curve of the associative path of the ORR process based on the ΔG values. The potential energy surface was plotted under the standard conditions U = 0 V, T = 298.3 K, P = 1 bar, and pH = 0. At the standard conditions, the total ΔG during the reaction $O_2 + 4H^+ + 4e^- \rightarrow 2H_2O$ should be approximately close to the value of −4.92 eV. We have drawn the potential energy surface curve by considering the $Ni_2\_N_3\_CNT$ geometry as a reference geometry, which corresponds to 0 eV. The potential energy curve for the associative path depicts that all of the reaction steps are downhill in the potential energy surface except removal of the H_2O molecule, as shown in Figure 6.14. The downhill nature of the reaction steps in the potential energy surface indicates that these reaction steps are energetically favorable on the surface of $Ni_2\_N_3\_CNT$. Moreover, we observed that the total change in ΔG during all of the reaction intermediate steps was found to be −4.94 eV, which is well consistent with the standard change in ΔG. The potential energy surface for the dissociative path was also plotted and is represented in Figure 6.15.

6.5 Conclusions and Future Work: In summary, we have computationally designed Ni_2 DAC and Ni_1 SAC and investigated their potential applications as ORR electrocatalysts. First, we performed structural optimization calculations of the CNT sheet and Ni-based structures (SAC and DAC) by using the DFT-D3 method. We explored the structural and electronic properties of all of the configurations at their equilibrium geometry. The pristine CNT sheet has semimetallic nature, and the Ni-based CNTs have either semiconducting ($Ni_1\_N_4\_CNT$ and $Ni_2\_N_4\_CNT$) or metallic ($Ni_1\_N_3\_CNT$ and $Ni_2\_N_3\_CNT$) nature. Many previous experimental findings indicate that metallic systems exhibit a promising catalytic activity. Consequently, the Ni-based NCNTs are supposed to demonstrate significant efficacy in catalyzing the ORR. To compare the catalytic activity of each possible configuration (SAC and DAC), we computed the adsorption energy of key intermediate species of the ORR such as O_2*, O*, and H_2O at both possible active sites (here, Ni and N sites) of each of the SAC and DAC configurations. We observed that the $Ni_2\_N_3\_CNT$ DAC exhibits superior catalytic activity among all other configurations, with the Ni site as a more electrocatalytically active site, which agrees with the experimental observation. The ORR process follows the $4e^-$ associative reaction pathway on the surface of $Ni_2\_N_3\_CNT$. The adsorption energies of the reaction intermediates O_2*, OOH*, O*, and OH* were calculated to be −1.48, −0.23, −1.96, and −2.09 eV, respectively. The moderate negative adsorption energy of the reaction intermediates depicts that all of the intermediate reaction species are favorably adducted to the

catalytic active site and thermodynamically stable. Furthermore, the potential energy surface for the associative path of the ORR reveals that all of the reaction steps are downhill in nature. Consequently, the $4e^-$ associative path of O_2 reduction is facilitated on the surface of $Ni_2_N_3$_CNT with Ni as an active site. Thus, this theoretical and computational work on Ni-based materials (SAC and DAC) as an ORR electrocatalyst can be useful in developing efficient and highly active electrocatalysts for fuel cells. Electron spin-density calculations were carried out to explain the performance of the subject materials toward the ORR. We acknowledge that our current comparison of electrocatalysts is based solely on adsorption calculations. We agree that incorporating kinetic calculations would provide a more comprehensive evaluation of the performance of the electrocatalysts. In future work, we plan to include kinetic calculations to complement our adsorption studies, which will offer a more detailed understanding of the catalytic processes. Our results demonstrate the potential of subect materials as promising substitutes for Pt-based electrodes and show that they are excellent materials for fuel-cell components.

6.6 References:

[1] T. Ahmad, D. A. Zhang, Critical Review of Comparative Global Historical Energy Consumption and Future Demand: The Story Told So Far, Energy Reports, 6 (2020) 1973–1991.

[2] N. Abas, A. Kalair, N. Khan, Review of Fossil Fuels and Future Energy Technologies, Futures 69 (2017) 31–49.

[3] F. Martins, C. Felgueiras, M. Smitkova, N. Caetano, Analysis of Fossil Fuel Energy Consumption and Environmental Impacts in European Countries, Energies 12 (2019) 964.

[4] F. Perera, Pollution from Fossil-Fuel Combustion Is the Leading Environmental Threat to Global Pediatric Health and Equity: Solutions Exist, Int. J. Environ. Res. Public Health 15 (2018) 16.

[5] S. Sen, S. Ganguly, Opportunities, Barriers and Issues with Renewable Energy Development – A Discussion, Renew. Sustain. Energy Rev. 69 (2016) 1170–1181.

[6] B. N. Stram, Key Challenges to Expanding Renewable Energy, Energy Policy 96 (2016) 728–734.

[7] L. Fan, Z. Tu, S. Hwa, Recent Development of Hydrogen and Fuel Cell Technologies: A Review, Energy Reports 7 (2021) 8421–8446.

[8] Y. Li, H. Dai, Recent Advances in Zinc-air Batteries, Chem. Soc. Rev. 43 (2014) 5257–5275.

[9] Debe, M. K. Electrocatalyst Approaches and Challenges for Automotive Fuel Cells, Nature 2012, 486, 43–51.

[10] Z. Duan, G. Wang, Comparison of Reaction Energetics for Oxygen Reduction Reactions on Pt (100), Pt (111), Pt/Ni (100), and Pt/Ni (111) Surfaces: A First-Principles Study, J. Phys. Chem. C 117 (2013) 6284−6292.

[11] S. Sui, X. Wang, X. Zhou, Y. Su, S. Riffat, C. J. Liu, A Comprehensive Review of Pt Electrocatalysts for the Oxygen Reduction Reaction: Nanostructure, Activity, Mechanism and Carbon Support in PEM Fuel Cells, J. Mater. Chem. A 5 (2017) 1808–1825.

[12] D. Li, H. Lv, Y. Kang, N. M. Markovic, V. R. Stamenkovic, Progress in the Development of Oxygen Reduction Reaction Catalysts for Low-Temperature Fuel Cells, Annu. Rev. Chem. Biomol. Eng. 7 (2016) 509–532.

[13] X. Yu, S. Ye, Recent Advances in Activity and Durability Enhancement of Pt/C Catalytic Cathode in PEMFC Part II: Degradation Mechanism and Durability Enhancement of Carbon Supported Platinum Catalyst, Journal of Power Sources 172 (2007) 145–154.

[14] Y. Shao, G. Yin, Y. Gao, Understanding and Approaches for the Durability Issues of Pt-Based Catalysts for PEM Fuel Cell, Journal of Power Sources 171 (2007), 558–566.

[15] Y. Shao-Horn, W. C. Sheng, S. Chen, P. J. Ferreira, E. F. Holby, D. Morgan, Instability of Supported Platinum Nanoparticles in Low-Temperature Fuel Cells, Topics in Catalysis 46 (2007) 285–305.

[16] R. Lin, X. Cai, H. Zeng, Z. Yu, Stability of High-Performance Pt-based Catalysts for Oxygen Reduction Reactions, Adv. Mater. 30 (2018) 1705332.

[17] F. Reith, S. G. Campbell, A. S. Ball, A. Pring, G. Southam, Platinum in Earth Surface Environments, Earth-Science Rev. 131 (2014) 1–21.

[18] M. Ali, T. Wilberforce, K. Elsaid, Transition Metal Carbides and Nitrides as Oxygen Reduction Reaction Catalyst or Catalyst Support in Proton Exchange Membrane Fuel Cells (PEMFCs), Int. J. Hydrogen Energy 46 (2020) 23529–23547.

[19] Y. Wang, J. Li, Z. Wei, Transition-metal-oxide-based Catalysts for the Oxygen Reduction Reaction, J. Mater. Chem. A 6 (2018) 8194–8209.

[20] A. Singh, S. Pakhira, Unraveling the Electrocatalytic Activity of Platinum Doped Zirconium Disulfide toward the Oxygen Reduction Reaction, Energy Fuels 37 (2023) 567–579.

[21] M. Liu, X. Xiao, Q. Li, L. Luo, M. Ding, B. Zhang, Y. Li, J. Zou, B. Jiang, Recent Progress of Electrocatalysts for Oxygen Reduction in Fuel Cells, J. Colloid Interface Sci. 607 (2022) 791–815.

[22] P. Cui, L. Zhao, Y. Long, L. Dai, C. Hu, Carbon-Based Electrocatalysts for Acidic Oxygen Reduction Reaction, Angew. Chem. Int. Ed. 62 (2023) e20221826.

[23] X. Zhao, P. Pachfule, A. Thomas, Covalent Organic Frameworks (COFs) for Eletrochemical Applications, Chem. Soc. Rev. 50 (2021) 6871–6913.

[24] A. Peigney, C. Laurent, E. Flahaut, R. R. Bacsa, A. Rousset, Specific Surface Area of Carbon Nanotubes and Bundles of Carbon Nanotubes, Carbon 39 (2001) 507–514.

[25] L. Peng, Z. L. Zhang, Z. Q. Xue, Q. D. Wu, Z. N. Gu, D. G. Pettifor, Stability of Carbon Nanotubes: How Small Can They Be? Phys. Rev. Lett. 85 (2000) 3249–3252.

[26] F. Xu, L. X. Sun, J. Zhang, Y. N. Qi, L. N. Yang, H. Y. Ru, F. L. Huang, Thermal Stability of Carbon Nanotubes, J. Therm. Anal. Calorim. 102 (2010) 785–791.

[27] S. Rathinavel, K. Priyadharshini, D. Panda, Materials Science & Engineering B A Review on Carbon Nanotube: An Overview of Synthesis, Properties, Functionalization, Characterization, and the Application, Mater. Sci. Eng. B 268 (2021) 115095.

[28] N. Alexeyeva, K. Tammeveski, Electrochemical Reduction of Oxygen on Multiwalled Carbon Nanotube Modified Glassy Carbon Electrodes in Acid Media, Electrochemical and Solid-State Letters 10 (2007) F18–F21.

[29] J. P. Britto, V. S. K. Santhanam, A. Rubio, A. J. Alonso, M. P. Ajayan, Improved Transfer at Carbon Nanotube Electrodes, Advanced Materials 11 (1999) 154–157.

[30] J. Maruyama, I. Abe, Cathodic Oxygen Reduction at the Interface between Nafion and Electrochemically Oxidized Glassy Carbon Surfaces, Journal of Electroanalytical Chemistry 527 (2002) 65–70.

[31] Z. Chen, D. Higgins, Z. Chen, Nitrogen-Doped Carbon Nanotubes and Their Impact on the Oxygen Reduction Reaction in Fuel Cells, Carbon N. Y. 48 (2010) 3057–3065.

[32] W. Niu, S. Pakhira, K. Marcus, Z. Li, J. L. Mendoza-Cortes, Y. Yang, Apically Dominant Mechanism for Improving Catalytic Activities of N-Doped Carbon Nanotube Arrays in Rechargeable Zinc-Air Battery, Adv. Energy Mater. 8 (2018) 1800480.

[33] Wang, A. Wu, Z. Qiu, A. Li, W. Qin, H. Huang, Applied Surface Science N-CNT Supported Fe/Ce Bimetallic Catalyst for Al-Air Aqueous Batteries, Appl. Surf. Sci. 608 (2023) 155185.

[34] N. Wang, X. Zheng, Y. Buba, H. Wang, X. Wang, Y. Zhao, Electrocatalytic Performance of Cobalt/Nickel Nanoparticles Encapsulated by N-Doped Carbon Nanotubes toward the Oxygen Reduction Reaction, App. Surf. Sci. 615 (2023) 156317.

[35] J. Huang, F. Gao, Q. Liu, P. Gong, H. Li, Y. Jiang, Facilitation of Fenton-Like Reaction of Copper-Nitrogen-Doped Carbon-Based Nanocatalysts by Enhancing Hydroxyl Adsorption on Single-Atom Cu-N_xC_{4-x} Sites, Small 20 (2024) e2309637.

[36] F. Gao, J. Huang, Y. Ruan, H. Li, P. Gong, F. Wang, Q. Tang, Y. Jiang, Unraveling the Structure Transition and Peroxidase Mimic Activity of Copper Sites over Atomically Dispersed Copper-Doped Carbonized Polymer Dots, Angew. Chem. Int. Ed. 62 (2023) e202214042.

[37] Y. Zhou, Q. Zhou, H. Liu, W. Xu, Z. Wang, S. Qiao, H. Ding, D. Chen, J. Zhu, Z. Qi, X. Wu, Q. He, L. Song, Asymmetric Dinitrogen-Coordinated Nickel Single-Atomic Sites for Efficient CO_2 Electroreduction, Nat. Commun. 14 (2023) 3776.

[38] J. Wang, C. X. Zhao, J. N. Liu, Y. W. Song, J. Q. Huang, B. Q. Li, Dual-atom Catalysts for Oxygen Electrocatalysis, Nano Energy 104 (2022) 107927.

[39] J. Zhang, A. Yu, C. Sun, Applied Surface Science Computational Exploration of Dual Atom Catalysts Loaded on Defective Graphene for Oxygen Reduction Reaction, Appl. Surf. Sci. 605 (2022) 154534.

[40] W. Zou, R. Lu, X. Liu, G. Xiao, X. Liao, Z. Wang, Y. Zhao, Theoretical Insights into Dual-Atom Catalysts for the Oxygen Reduction Reaction: The Crucial Role of Orbital Polarization, J. Mater. Chem. A 10 (2022) 9150–9160.

[41] R. Li, D. Wang Superiority of Dual-Atom Catalysts in Electrocatalysis: One Step Further Than Single-Atom Catalysts, Adv. Energy Mater. 12 (2022) 2103564.

[42] T. Tang, Y. Wang, J. Han, Q. Zhang, X. Bai, X. Niu, Z. Wang, J. Gaun, Dual-atom Co-Fe Catalysts for Oxygen Reduction Reaction, Chinese Journal of Catalysis 46 (2023) 48–55.

[43] J. Wang, W. Liu, G. Luo, J. Z. Li, C. Zhao, M. Z. Zhang, Q. Xu, Q. X. Wang, M. c. Zhau, T. Y. Qu, K. Z. Yang, T. Tao, F. Y. Li, Y. Lin, Y. Wu, D. Y. Li, Synergistic Effect of Well-Defined Dual Sites Boosting the Oxygen Reduction Reaction, Energy Environ. Sci. 11 (2018) 3375–3379.

[44] H. W. Ren, X. Tan, F. W. Yang, C. Jia, M. S. Xu, X. K. Wang, C. S. Smith, C. Zhao, Isolated Diatomic Ni-Fe Metal–Nitrogen Sites for Synergistic Electroreduction of CO_2, Angew. Chem. Int. Ed. 58 (2019) 6972–6976.

[45] Y. Li, C. Chen, R. Cao, H. He, K. Zhou, Dual-atom Ag_2/graphene Catalyts for Efficient Electroreduction of CO_2 to CO, Appl. catal. B: Environ. 268 (2020) 118747.

[46] G. Luo, Y. Jing, Y. Li, Rational Design of Dual-Metal-Site Catalysts for Electroreduction of Carbon Dioxide, J. Mater. Chem. A 8 (2020) 15809–15815.

[47] X. Liang, H. Wang, C. Zhang, D. Zhong, T. Lu, Controlled Synthesis of a Ni_2 Dual-Atom Catalyst for Synergistic CO_2 Electroreduction, Applied Catalysis B: Environmental 322 (2023) 122073.

[48] V. V. Porsev, A. V. Bandura, R. A. Evarestov, Ab Initio Modeling of Helically Periodic Nanostructures Using CRYSTAL17: A General Algorithm First Applied to Nanohelicenes, Comput. Mater. Sci. 203 (2022) 111063.

[49] R. Dovesi, V. R. Saunders, C. Roetti, R. Orlando, C. M. Zicovich-Wilson, F. Pascale, B. Civalleri, K. Doll, N. M. Harrison, I. J. Bush, P. D'Arco, M. Llunell, M. Causà, Y. Noël, L. Maschio, A. Erba, M. Rerat, S. Casassa, CRYSTAL17 User's Manual (University of Turin, Turin, 2017). 2018.

[50] R. Dovesi, A. Erba, R. Orlando, C. M. Zicovich-Wilson, B. Civalleri, L. Maschio, M. Rérat, S. Casassa, J. Baima, S. Salustro, B. Kirtman, Quantum-Mechanical Condensed

Matter Simulations with CRYSTAL, Wiley Interdiscip. Rev. Comput. Mol. Sci. 8 (2018) e1360.

[51] S. Grimme, A. Hansen, J. G. Brandenburg, C. Bannwarth, Dispersion-Corrected Mean-Field Electronic Structure Methods, Chemical Reviews, 116 (2016) 5105–5154.

[52] J. Laun, T. Bredow, BSSE-Corrected Consistent Gaussian Basis Sets of Triple-Zeta Valence with Polarization Quality of the Sixth Period for Solid-State Calculations, J. Comput. Chem. 42 (2021) 1064–1072.

[53] J. Laun, T. Bredow, BSSE-corrected Consistent Gaussian Basis Sets of Triple-zeta Valence with Polarization Quality of the Fifth Period for Solid-State Calculations, J. Comput. Chem. 43 (2022) 839–846.

[54] D. Vilela Oliveira, J. Laun, M. F. Peintinger, T. Bredow, BSSE-Correction Scheme for Consistent Gaussian Basis Sets of Double- and Triple-Zeta Valence with Polarization Quality for Solid-State Calculations, J. Comput. Chem. 40 (2019) 2364–2376.

[55] J. Laun, D. Vilela Oliveira, T. Bredow, Consistent Gaussian Basis Sets of Double- and Triple-Zeta Valence with Polarization Quality of the Fifth Period for Solid-State Calculations, J. Comput. Chem. 39 (2018) 1285–1290.

[56] M. F. Peintinger, D. V. Oliveira, T. Bredow, Consistent Gaussian Basis Sets of Triple-Zeta Valence with Polarization Quality for Solid-State Calculations, J. Comput. Chem. 34 (2013) 451–459.

[57] H. J. Monkhorst, J. D. Pack, Special Points for Brillouin-zone Integrations, Phys. Rev. B 13 (1976) 5188–5192.

[58] K. Momma, F. Izumi, VESTA 3 for Three-Dimensional Visualization of Crystal, Volumetric and Morphology Data, J. Appl. Crystallogr. 44 (2011) 1272–1276.

[59] R. Ma, G. Lin, Y. Zhou, Q. Liu, T. Zhang, G. Shan, M. Yang, J. Wang, A Review of Oxygen Reduction Mechanisms for Metal-Free Carbon-Based Electrocatalysts, npj Comput. Mater. 5 (2019) 78.

[60] A. Singh, S. Pakhira, Revealing the Mechanism and Activity of O_2 Reduction Reaction of Co Nanocluster Encapsulated by Carbon Nanotube, Energy and Fuels 38 (2024) 11837–11851.

[61] S. N. Upadhyay, V. B. Sardar, A. Singh, V. Kumar, Pakhira, S. Elucidating the Oxygen Reduction Reaction Mechanism on the Surfaces of 2D Monolayer $CsPbBr_3$ Perovskite, Phys. Chem. Chem. Phys. 24 (2022) 28283–28294.

[62] G. Fazio, L. Ferrighi, D. Perilli, C. Di Valentin, Computational Electrochemistry of Doped Graphene as Electrocatalytic Material in Fuel Cells, Int. J. Quantum Chem. 116 (2016) 1623–1640.

[63] Y. Ji, M. Yang, H. Dong, L. Wang, T. Hou, Y. Li, Monolayer Group IVA Monochalcogenides as Potential and Efficient Catalysts for the Oxygen Reduction Reaction from First-Principles Calculations, J. Mater. Chem. A 5 (2017) 1734–1741.

[64] D. Kan, D. Wang, X. Zhang, R. Lian, J. Xu, G. Chen, Y. Wei, Rational Design of Bifunctional ORR/OER Catalysts Based on Pt/Pd-Doped Nb_2CT_2 MXene by First-Principles Calculations, J. Mater. Chem. A 8 (2020) 3097–3108.

[65] J. K. Nørskov, J. Rossmeisl, A. Logadottir, L. Lindqvist, J. R. Kitchin, T. Bligaard, H. Jónsson, Origin of the Overpotential for Oxygen Reduction at a Fuel-Cell Cathode, J. Phys. Chem. B 108 (2004) 17886–17892.

[66] A. Singh, S. Pakhira, Synergistic Niobium Doped Two-Dimensional Zirconium Diselenide: An Efficient Electrocatalyst for O_2 Reduction Reaction, ACS Phys. Chem. Au 4 (2024) 40–56.

[67] http://www.cccbdb.nist.gov for Computational Chemistry Comparison and Benchmark Data Base, National Institute of Standards and Technology website.

[68] A. R. Urade, I. Lahiri, K. S. Suresh, Graphene Properties, Synthesis and Applications: A Review. Jom 75 (2023) 614–630.

[69] A. H. Castro Neto, F. Guinea, N. M. R. Peres, K. S. Novoselov, A. K. Geim, The Electronic Properties of Graphene, Rev. Mod. Phys. 81 (2009) 109–162.

[70] E. Kaxiras J. D. Joannopoulos, Quantum Theory of Materials, 2nd ed.; Vol. 60. Cambridge University Press, 2019; pp 235–244.

[71] T. Ando, The Electronic Properties of Graphene and Carbon Nanotubes, NPG Asia Mater. 1 (2009) 17–21.

[72] T.C. Dinadayalane, J. Leszczynski, Fundamental Structural, Electronic, and Chemical Properties of Carbon Nanostructures: Graphene, Fullerenes, Carbon Nanotubes, and Their Derivatives, In: Leszczynski, J. (eds) Handbook of Computational Chemistry, Springer, Dordrecht, 2012, pp 793–868.

[73] D. Fathi, A Review of Electronic Band Structure of Graphene and Carbon Nanotubes Using Tight Binding, J. Nanotechnol. 2011 (2011) 471241.

[74] J. Yang, Y. Yuan, G. Chen, First–Principles Study of Potassium Adsorption and Diffusion on Graphene, Mol. Phys. 118 (2020) e1581291.

[75] X. Zhou, J. Gao, Y. Hu, Z. Jin, K. Hu, K. M. Reddy, Q. Yuan, X. Lin, H. J. Qiu, Theoretically Revealed and Experimentally Demonstrated Synergistic Electronic Interaction of CoFe Dual-Metal Sites on N-Doped Carbon for Boosting Both Oxygen Reduction and Evolution Reactions, Nano Lett. 22 (2022) 3392–3399.

[76] W. Ye, S. Chen, Y. Lin, L. Yang, S. Chen, X. Zheng, Z. Qi, C. Wang, R. Long, M. Chen, J. Zhu, P. Gao, L. Song, J. Jiang, Y. Xiong, Precisely Tuning the Number of Fe Atoms in Clusters on N-Doped Carbon toward Acidic Oxygen Reduction Reaction, Chem 5 (2019) 2865–2878.

[77] J. Wang, Z. Huang, W. Liu, C. Chang, H. Tang, Z. Li, W. Chen, C. Jia, T. Yao, S. Wei, Y. Wu, Y. Li, Design of N-Coordinated Dual-Metal Sites: A Stable and Active Pt-Free Catalyst for Acidic Oxygen Reduction Reaction, J. Am. Chem. Soc. 139 (2017) 17281–17284.

[78] H. Sun, M. Wang, S. Zhang, S. Liu, X. Shen, T. Qian, X. Niu, J. Xiong, C. Yan, Boosting Oxygen Dissociation over Bimetal Sites to Facilitate Oxygen Reduction Activity of Zinc-Air Battery, Adv. Funct. Mater. 31 (2021) 2006533.

[79] N. Zhang, T. Zhou, J. Ge, Y. Lin, Z. Du, C. Zhong, W. Wang, Q. Jiao, R. Yuan, Y. Tian, W. Chu, C. Wu, Y. Xie, High-Density Planar-like Fe_2N_6 Structure Catalyzes Efficient Oxygen Reduction, Matter 3 (2020) 509–521

CHAPTER 7

Summary and Perspectives

7.1 Summary: This thesis has systematically explored the theoretical and computational design and analysis of novel materials as efficient electrocatalysts towards O_2 reduction reaction (ORR), a fundamental electrochemical process central to energy conversion technologies such as fuel cells. Through the comprehensive density functional theory (DFT) calculations, we have investigated and explored the electrocatalytic potential of four distinct classes of materials towards ORR:

1) The first study highlights the effect of niobium doping on the electronic and catalytic properties of monolayer $ZrSe_2$. The pristine material exhibited semiconducting behavior, while Nb doping introduced metallic character, improving electronic conductivity. The DFT based investigations with computational hydrogen electrode (CHE) model revealed that the associative pathway for ORR was energetically favorable, suggesting the promise of Nb-$ZrSe_2$ as a non-noble metal ORR catalyst.

2) We have further expanded our understanding by investigating Pt-doped ZrS_2, where we have observed that the Pt doping significantly modifies the electronic structure, reducing the band gap while enhancing catalytic activity. In contrast to the Nb-$ZrSe_2$, our calculations indicates that Pt-ZrS_2 favors the dissociative ORR pathway, highlighting how the nature of the dopant can fundamentally alter reaction mechanisms. The exceptional performance of Pt-ZrS_2 demonstrates the potential of noble metal-doped TMDs as cost-effective alternatives to pure platinum catalysts.

3) Moving beyond TMDs, we have explored Co@SWCNT systems, where the Co nanoparticles are encapsulated within single wall carbon nanotubes. Our calculations reveals that the Co nanoparticles dramatically enhance the electronic conductivity of the system while creating active sites on the external carbon surface for ORR. The Co@SWCNT system exhibits

a strong preference for the $4e^-$ dissociative pathway, with favorable adsorption energies for oxygen intermediates, indicating its promise as a durable and efficient ORR electrocatalyst.

4) In a significant final contribution, we have introduced and studied N-coordinated Ni-based single-atom and dual-atom catalysts on carbon frameworks, drawing from experimental precedents. Using rigorous DFT-D3 calculations, we have found that the $Ni_2_N_3$_CNT configuration not only exhibits superior electronic conductivity and stable adsorption energies but also promotes an energetically downhill associative reaction pathway, making it an exceptional Pt-alternative for ORR catalysis. The synergistic interplay between neighboring Ni centers and the surrounding N-coordination environment provides an enhanced activity through favorable orbital hybridization and electron redistribution.

In all cases, the CHE model and thermodynamic descriptors such as Gibbs free energy and adsorption energies have been systematically utilized to determine the most promising active sites and reaction pathways. The results underscore that strategic heteroatom doping, atomic dispersion, and nanoconfinement are pivotal levers for optimizing catalytic performance of novel materials for ORR. Collectively, these studies have established several key design principles for high-performance ORR electrocatalysts:

a) The introduction of specific dopants into inactive materials (e.g., TMD basal planes) can break surface symmetry, introduce localized states near the Fermi level, and create new catalytic centers that facilitate ORR. Strategic substitutional doping of 2D electrocatalytic materials modulates charge density and introduces favorable adsorption sites for electrochemical reaction intermediates species.

b) The chemical nature and electronic configuration of the dopant not only influences the structural and electronic properties of 2D electrocatalytic materials, but also significantly influences the preferred ORR mechanism (associative vs. dissociative) and determines the thermodynamic favorability of the ORR mechanism (associative vs. dissociative).

c) Encapsulating transition metals such as cobalt inside carbon nanotubes (Co@SWCNT) creates a confined environment that stabilizes the active metal while ensuring high conductivity and enhanced electron transfer, crucial for multistep ORR.

d) The presence of two adjacent metal atoms (as in Ni_2-based systems) introduces cooperative effects that modify adsorption energies and promote multi-electron transfer. Dual-site

mechanisms often outperform single-atom analogs due to improved binding and activation of intermediates.

e) Electronic conductivity and appropriate binding strengths for ORR intermediates are critical factors for catalyst performance.

f) The stability of the catalyst under operational conditions, evidenced by favorable formation energies and minimal structural distortion, is essential for practical applications in fuel cells and other electrochemical systems.

These findings contribute significantly to the fundamental understanding of electrocatalytic materials and provide practical guidance for the rational design of efficient ORR catalysts for energy conversion and storage applications.

7.2 Perspective: While this thesis lays a robust foundation in understanding the catalytic behavior of several novel ORR electrocatalysts, the journey is far from complete. The following are envisioned as future frontiers of this research:

7.2.1 Janus Transition Metal Dichalcogenides (Janus TMDs): Two-dimensional Transition metal dichalcogenides (TMDs), represented as MX_2 (M=Transition metal, X= Chalcogen atom) generally have three atomic layers stacked on top of each other. TMDs consist of a middle transition atomic (M) layer sandwiched by two atomic layers of chalcogen atoms (X). Janus TMDs, represented by MXX' (M=Transition metal, X= first chalcogen atom, X' = Next chalcogen atom) can be constructed from normal TMDs by replacing one atomic layer of chalcogen atom (X) with another chalcogen atom (X'), as represented in Figure 7.1. Janus TMDs have drawn greater attention of researchers because of their specific asymmetric structure with various interesting properties namely tunable bandgap, carrier mobility, magnetism, and dipole[1,2]. The Janus MoSSe was successfully synthesized from the original MoS_2 ($MoSe_2$) monolayer by chemical vapor deposition and thermal selenization by substituting one layer of S(Se) atoms with Se(S)[3,4]. This indicates that Janus TMDs can be synthesized experimentally. In comparison to normal TMDs monolayers, Janus TMDs break the out-of-plane structural symmetry. Janus TMDs show a widespread application in the field of photocatalysis due to symmetry breaking. This structure asymmetry imposes intrinsic strain and electric field inside the crystal which is absent in the non-Janus TMDs. This intrinsic strain and electric field in Janus TMDs, have been found responsible for the higher HER activity of Janus TMDs[3,5]. Yand et al. showed that Janus NbTeSe is an active HER catalyst to split the water[6]. Er et al. proposed theoretically the HER activity of various Janus TMDs and reported

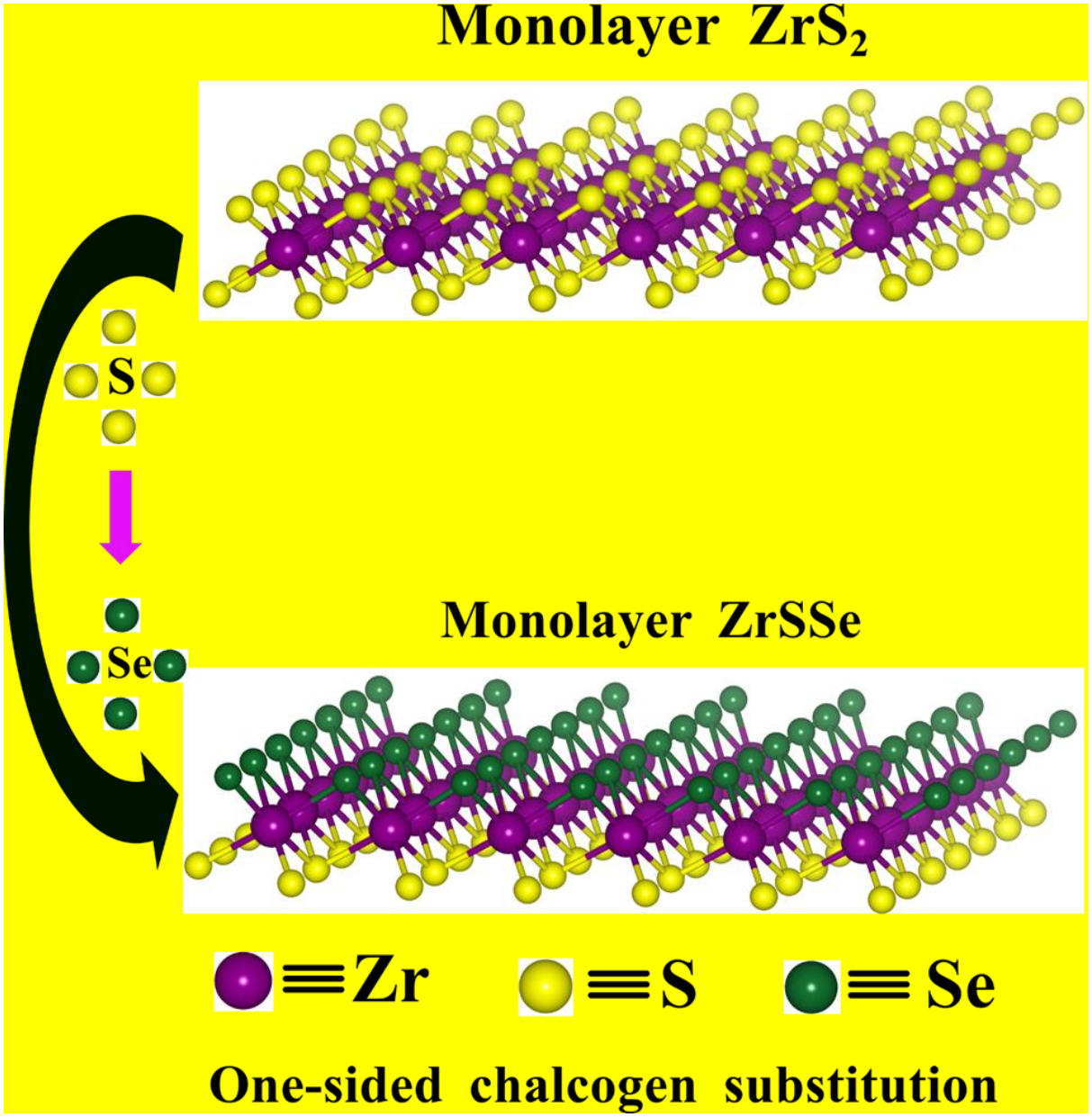

***Figure 7.5**. Illustration of the formation of Janus ZrSSe by replacement of one atomic layer of S atoms in monolayer ZrS_2.*

Janus WSSe can serve as a better catalyst for HER with the presence of S/Se vacancy[5]. Using the first principle calculation Guo and co-workers showed that the Janus ZrSSe, an indirect semiconductor, is mechanically and dynamically stable[7]. Janus ZrSSe may possess photocatalytic activity due to its high asymmetric arrangements. Shom et al. demonstrated that Janus ZrSSe with doping of Nb, Pt can serve as a good catalyst for HER[8]. Motivated by the fine catalytic activity of doped Janus ZrSSe towards HER, an exciting question typically arises: can ZrSSe monolayer be utilized as a catalyst for ORR by doping engineering? Hence, in this work by means of density functional theory (DFT) computations, we propose to systematically investigate the ORR activity of Janus ZrSSe and its doped variants in our future work. To begin,

we constructed the Janus ZrSSe from the original TMDs ZrS_2 by replacing one atomic layer of the sulfur (S) atom with an atomic layer of selenium atom (Se).

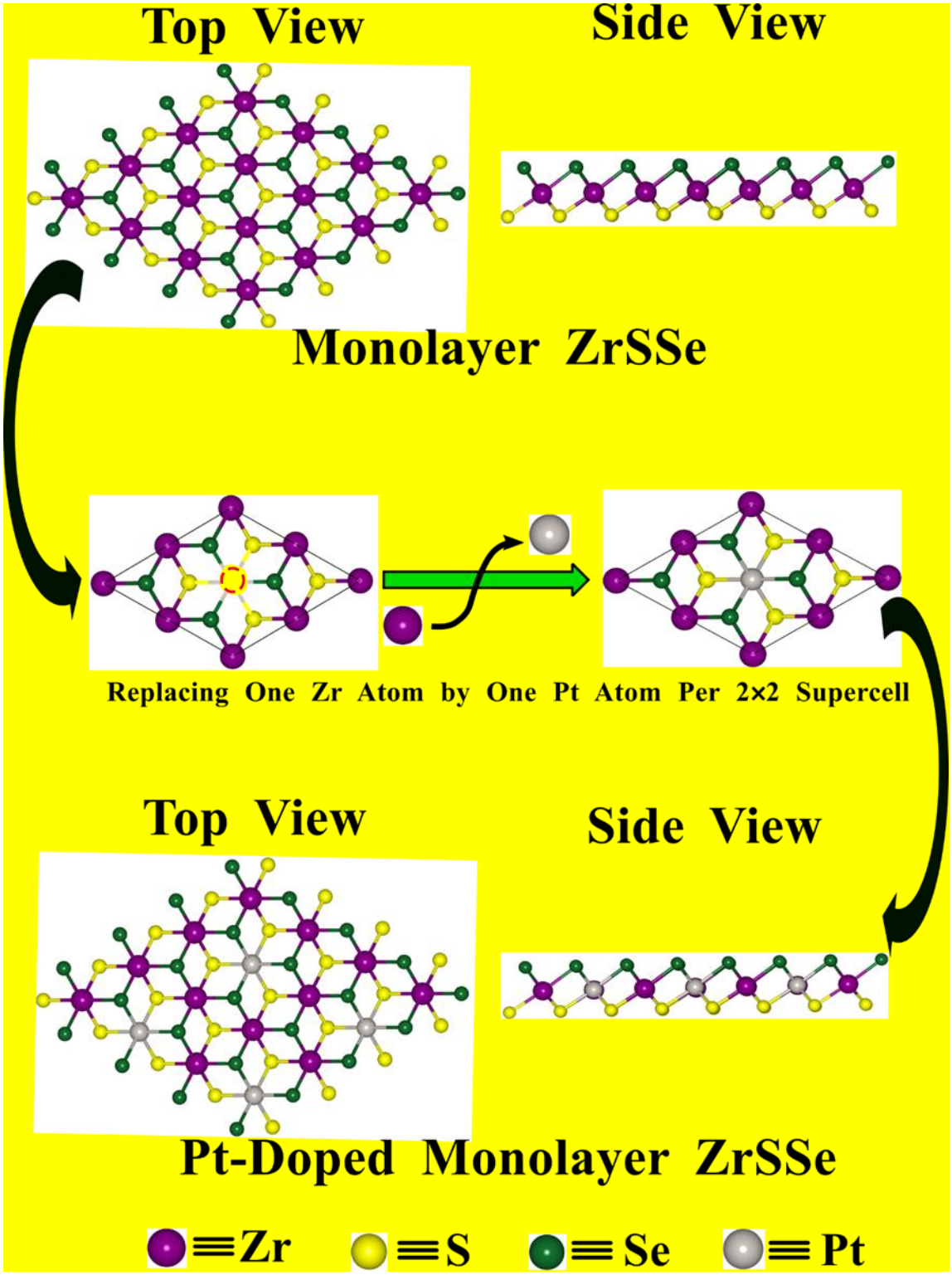

***Figure 7.6**. Systemic process and formation of Pt-ZrSSe model supercell by replacement of Zr atom by Pt atom.*

There is one Zirconium (Zr), one sulfur (S), and One Selenium (Se) atom present per unit cell of ZrSSe. The equilibrium structures of Janus, ZrSSe were obtained by the Density Function

Theory (DFT) method as shown in Figure (1). We then modeled platinum-doped ZrSSe (Pt-ZrSSe) by substituting one Zirconium atom (Zr) with one platinum (Pt) atom per 2×2 supercell of ZrSSe. There are 12 atoms present in the 2×2 supercell of the Pt-ZrSSe, which involves three Zr atoms, one Pt atom, and four S and four Se atoms. The equilibrium structure of Pt-ZrSSe was obtained by the same level of theory. The model of the Pt-ZrSSe is shown in Figure 7.2. The key objectives of our upcoming research include:

1) To perform comprehensive DFT studies on pristine and doped Janus ZrSSe (e.g., dopants like Pt) to examine changes in structural properties, electronic structure, charge density distribution, and orbital contributions relevant to ORR.

2) To investigate and examine the favorable active site for ORR intermediate species on pristine and doped Janus ZrSSe (e.g., dopants like Pt).

3) A detailed analysis of the complete oxygen reduction reaction (ORR) pathways, including both the associative and the dissociative mechanisms, will be conducted at various potential active sites of Janus ZrSSe and doped Janus ZrSSe using the computational hydrogen electrode (CHE) model.

4) Benchmark the catalytic performance of Janus ZrSSe against conventional ZrS_2 and doped ZrS_2 to evaluate the actual enhancement due to Janus architecture.

Through this future investigation, we aim to reveal whether Janus ZrSSe can serve not only as a promising HER catalyst, but also as a highly efficient, non-noble-metal-based material for ORR, thereby opening up a new direction in the design of asymmetric 2D electrocatalysts for sustainable energy technologies.

7.3 References:

[1] Y. Hao, L.C. Xu, J. Pu, L. Wang, L.F. Huang, Stable zigzag edges of transition-metal dichalcogenides with high catalytic activity for oxygen reduction, Electrochim. Acta 338 (2020) 135865.

[2] X. Tang, L. Kou, 2D Janus Transition Metal Dichalcogenides: Properties and Applications, Phys. Status Solidi Basic Res. 259 (2022) 2100562.

[3] A. Y. Lu, H. Zhu, J. Xiao, C. P. Chuu, Y. Han, M. H. Chiu, C. C. Cheng, C. W. Yang, K. H. Wei, Y. Yang, Y. Wang, D. Sokaras, D. Nordlund, P. Yang, D. A. Muller, M. Y. Chou,

X. Zhang, L. J. Li, Janus monolayers of transition metal dichalcogenides, Nat. Nanotechnol. 12 (2017) 744–749.

[4] J. Zhang, S. Jia, I. Kholmanov, L. Dong, D. Er, W. Chen, H. Guo, Z. Jin, V. B. Shenoy, L. Shi, J. Lou, Janus Monolayer Transition-Metal Dichalcogenides, ACS Nano 11 (2017) 8192–8198.

[5] D. Er, H. Ye, N. C. Frey, H. Kumar, J. Lou, V. B. Shenoy, Prediction of Enhanced Catalytic Activity for Hydrogen Evolution Reaction in Janus Transition Metal Dichalcogenides, Nano Lett. 18 (2018) 3943–3949.

[6] X. Yang, A. Banerjee, R. Ahuja, Structural Insight of the Frailty of 2D Janus NbSeTe as an Active Photocatalyst, ChemCatChem 12 (2020) 6013–6023.

[7] T. V. Vu, H.D. Tong, D. P. Tran, N. T. T. Binh, C. V. Nguyen, H. V. Phuc, H.M. Do, N. N. Hieu, Electronic and optical properties of Janus ZrSSe by density functional theory, RSC Adv. 9 (2019) 41058–41065.

[8] N. N. Som, P. K. Jha, Hydrogen evolution reaction of metal di-chalcogenides: ZrS_2, $ZrSe_2$ and Janus ZrSSe, Int. J. Hydrogen Energy 45 (2020) 23920–23927.

****

Supporting Information

Exploring the Active Site and Catalytic Activity of N-Coordinated Ni_2 Dual-Atom Catalysts for Oxygen Reduction Reaction

Ashok Singh[1] and Srimanta Pakhira[1,2*]

[1] Department of Physics, Indian Institute of Technology Indore (IIT Indore), Simrol, Khandwa Road, Indore-453552, Madhya Pradesh, India.

[2] Centre for Advanced Electronics (CAE), Indian Institute of Technology Indore, Simrol, Khandwa Road, Indore-453552, Madhya Pradesh, India.

*Corresponding author: spakhira@iiti.ac.in (or) spakhirafsu@gmail.com

Contents Page

Optimized Structures (.cif format)

The optimized structure of the carbon sheet and Ni_2_N_3_CNT and all the reaction intermediates involved in the oxygen reduction reaction (ORR) are provided below in the .cif format.

1.1 For Carbon Sheet

data_Bg_CNT.out

```
_cell_length_a                    2.450000
_cell_length_b                    2.450000
_cell_length_c                    20.000000
_cell_angle_alpha                 90.000000
_cell_angle_beta                  90.000000
_cell_angle_gamma                 120.000000
_symmetry_space_group_name_H-M    'P 1'
_symmetry_Int_Tables_number       1

loop_
_symmetry_equiv_pos_as_xyz
  'x, y, z'

loop_
  _atom_site_label
  _atom_site_type_symbol
  _atom_site_fract_x
  _atom_site_fract_y
  _atom_site_fract_z
```

C001 C 0.333333 -0.333333 0.000000

C002 C -0.333333 0.333333 0.000000

1.2 For Ni_2_N_3_CNT

data_Bg_Ni_2_N_3_CNT.out

_cell_length_a 10.146960

_cell_length_b 9.663300

_cell_length_c 20.000000

_cell_angle_alpha 90.000000

_cell_angle_beta 90.000000

_cell_angle_gamma 121.645000

_symmetry_space_group_name_H-M 'P 1'

_symmetry_Int_Tables_number 1

loop_

_symmetry_equiv_pos_as_xyz

'x, y, z'

loop_

_atom_site_label

_atom_site_type_symbol

_atom_site_fract_x

_atom_site_fract_y

_atom_site_fract_z

C001	C	0.083637	0.174161	0.033575
C002	C	0.178538	0.100948	0.033566
C003	C	0.346377	0.182876	0.033540
C004	C	0.417726	0.087813	0.033532
C005	C	-0.418772	0.160537	0.033541
C006	C	-0.347422	0.065471	0.033573
C007	C	-0.179598	0.147407	0.033587
C008	C	-0.084716	0.074177	0.033590
C009	C	0.068403	0.408824	0.033539
N010	N	0.151413	0.335534	0.033570
NI011	NI	0.370885	0.497345	0.033490
N012	N	0.441951	0.349962	0.033543
C013	C	-0.401561	0.422551	0.033582
C014	C	-0.328841	0.330540	0.033546
C015	C	-0.168118	0.410153	0.033558
C016	C	-0.094529	0.320061	0.033554
C017	C	0.080382	-0.332637	0.033504
C018	C	0.156086	-0.417855	0.033493
N019	N	0.314336	-0.339423	0.033474
N020	N	-0.315376	-0.412208	0.033661
C021	C	-0.157146	-0.333774	0.033585
C022	C	-0.081447	-0.418999	0.033554
C023	C	0.093457	-0.071705	0.033534
C024	C	0.167056	-0.161791	0.033521

C025 C 0.327793 -0.082187 0.033507

C026 C 0.400529 -0.174188 0.033517

N027 N -0.442977 -0.101607 0.033602

NI028 NI -0.372040 -0.249121 0.033784

N029 N -0.152510 -0.087193 0.033608

C030 C -0.069486 -0.160464 0.033574

2 Equilibrium structures(.cif format) for ORR intermediates

2.1 O_2_ Ni_2_N_3_CNT

data_Bg_O2_Ni_2_N_3_CNT_Ni.out

_cell_length_a 10.012250

_cell_length_b 9.669280

_cell_length_c 20.000000

_cell_angle_alpha 90.000000

_cell_angle_beta 90.000000

_cell_angle_gamma 121.457490

_symmetry_space_group_name_H-M 'P 1'

_symmetry_Int_Tables_number 1

loop_

_symmetry_equiv_pos_as_xyz

'x, y, z'

loop_

_atom_site_label

_atom_site_type_symbol

_atom_site_fract_x

_atom_site_fract_y

_atom_site_fract_z

C001 C 0.077163 0.167259 0.035745

C002 C 0.170645 0.092967 0.035259

C003 C 0.339052 0.176226 0.035692

C004 C 0.412366 0.083855 0.031509

C005 C -0.423066 0.158403 0.030897

C006 C -0.350060 0.064494 0.031089

C007 C -0.181810 0.146819 0.031256

C008 C -0.091668 0.069373 0.031725

C009 C 0.070352 0.406930 0.029401

N010 N 0.148470 0.329458 0.040111

NI011 NI 0.349384 0.460933 0.079480

N012 N 0.432126 0.342244 0.040434

C013 C -0.410170 0.418098 0.035077

C014 C -0.334107 0.327763 0.030404

C015 C -0.171567 0.407443 0.027908

C016 C -0.095060 0.319056 0.028242

C017 C 0.077871 -0.336840 0.025585

C018 C 0.159383 -0.418705 0.022730

N019 N 0.316958 -0.337147 0.016904

N020 N -0.323541 -0.417427 0.035081

C021 C -0.164292 -0.339085 0.031066

C022 C -0.085471 -0.422443 0.027942

C023 C 0.085593 -0.078447 0.030610

C024 C 0.161850 -0.166790 0.027192

C025 C 0.323826 -0.085224 0.027863

C026 C 0.398173 -0.175928 0.024626

N027 N -0.443039 -0.100778 0.030692

NI028 NI -0.381668 -0.254280 0.049086

N029 N -0.163203 -0.093475 0.030938

C030 C -0.078644 -0.166789 0.030222

O031 O -0.493988 -0.373616 0.129728

O032 O 0.350366 -0.395156 0.143579

2.2 OOH_ Ni_2_N_3_CNT

data_Bg_OOH_Ni_2_N_3_CNT_Ni-5002.out

_cell_length_a 10.105950

_cell_length_b 9.679830

_cell_length_c 20.000000

_cell_angle_alpha 90.000000

_cell_angle_beta 90.000000

_cell_angle_gamma 121.753700

_symmetry_space_group_name_H-M 'P 1'

_symmetry_Int_Tables_number 1

```
loop_
_symmetry_equiv_pos_as_xyz
  'x, y, z'

loop_
  _atom_site_label
  _atom_site_type_symbol
  _atom_site_fract_x
  _atom_site_fract_y
  _atom_site_fract_z
C001   C   0.076857   0.167499   0.031779
C002   C   0.170286   0.093287   0.031830
C003   C   0.338381   0.175046   0.032139
C004   C   0.410225   0.080747   0.030577
C005   C  -0.425865   0.153842   0.030783
C006   C  -0.354376   0.059139   0.031454
C007   C  -0.185887   0.141715   0.031753
C008   C  -0.092422   0.067358   0.032503
C009   C   0.063436   0.403344   0.027938
N010   N   0.146163   0.329689   0.030786
NI011  NI  0.368888   0.497764   0.041366
N012   N   0.433759   0.340800   0.033751
C013   C  -0.409266   0.414460   0.034039
```

C014	C	-0.335858	0.323493	0.031409
C015	C	-0.174703	0.403701	0.030028
C016	C	-0.100268	0.314303	0.029547
C017	C	0.072951	-0.339247	0.026918
C018	C	0.150280	-0.423053	0.024566
N019	N	0.307956	-0.343005	0.020843
N020	N	-0.324159	-0.421208	0.036537
C021	C	-0.166332	-0.341631	0.032847
C022	C	-0.089139	-0.425631	0.029502
C023	C	0.084522	-0.079373	0.030379
C024	C	0.159087	-0.168540	0.027731
C025	C	0.320515	-0.088581	0.027908
C026	C	0.394685	-0.179221	0.026541
N027	N	-0.449176	-0.106927	0.031739
NI028	NI	-0.381514	-0.257151	0.055170
N029	N	-0.162342	-0.094852	0.034620
C030	C	-0.079227	-0.167886	0.032374
O031	O	0.462983	-0.401197	0.127219
O032	O	0.371875	-0.332349	0.158817
H033	H	0.383654	-0.352917	0.204941

2.3 O_ Ni_2_N_3_CNT

data_Bg_O_Ni_2_N_3_CNT_Ni.out

```
_cell_length_a                    10.068300
_cell_length_b                    9.663500
_cell_length_c                    20.000000
_cell_angle_alpha                 90.000000
_cell_angle_beta                  90.000000
_cell_angle_gamma                 121.454000
_symmetry_space_group_name_H-M    'P 1'
_symmetry_Int_Tables_number       1

loop_
_symmetry_equiv_pos_as_xyz
  'x, y, z'

loop_
  _atom_site_label
  _atom_site_type_symbol
  _atom_site_fract_x
  _atom_site_fract_y
  _atom_site_fract_z
C001   C   0.077674   0.167444   0.033226
C002   C   0.172388   0.093991   0.032141
C003   C   0.340902   0.176517   0.033452
C004   C   0.413127   0.082576   0.031442
C005   C  -0.422821   0.157160   0.031157
```

C006	C	-0.350600	0.062737	0.033618
C007	C	-0.182833	0.144791	0.031220
C008	C	-0.090521	0.069172	0.029975
C009	C	0.066548	0.404576	0.029439
N010	N	0.146157	0.328756	0.038289
NI011	NI	0.357414	0.480326	0.076653
N012	N	0.434606	0.342309	0.037294
C013	C	-0.408225	0.418436	0.033687
C014	C	-0.333714	0.327012	0.029213
C015	C	-0.172259	0.406292	0.026590
C016	C	-0.097375	0.316890	0.027670
C017	C	0.076868	-0.337418	0.024401
C018	C	0.155495	-0.420850	0.026170
N019	N	0.312966	-0.341545	0.027611
N020	N	-0.320674	-0.416445	0.035361
C021	C	-0.163319	-0.339370	0.028526
C022	C	-0.085742	-0.423319	0.025208
C023	C	0.087688	-0.077748	0.027606
C024	C	0.163114	-0.167004	0.026105
C025	C	0.324693	-0.086993	0.029176
C026	C	0.399028	-0.178426	0.031909
N027	N	-0.443348	-0.102804	0.038885
NI028	NI	-0.365258	-0.242868	0.059527
N029	N	-0.160348	-0.093056	0.027737

C030 C -0.076228 -0.166252 0.026775

O031 O -0.498642 -0.360767 0.127378

2.4 OH_ Ni_2_N_3_CNT

data_Bg_OH_Ni_2_N_3_CNT_Ni-5001.out

_cell_length_a 10.051940

_cell_length_b 9.623200

_cell_length_c 20.000000

_cell_angle_alpha 90.000000

_cell_angle_beta 90.000000

_cell_angle_gamma 121.404000

_symmetry_space_group_name_H-M 'P 1'

_symmetry_Int_Tables_number 1

loop_

_symmetry_equiv_pos_as_xyz

'x, y, z'

loop_

_atom_site_label

_atom_site_type_symbol

_atom_site_fract_x

_atom_site_fract_y

_atom_site_fract_z

C001 C 0.077924 0.167423 0.027967

C002 C 0.171331 0.092775 0.031432

C003 C 0.337625 0.174158 0.037607

C004 C 0.410975 0.080579 0.036638

C005 C -0.424532 0.155777 0.036508

C006 C -0.351373 0.061951 0.036875

C007 C -0.184749 0.143731 0.030985

C008 C -0.091638 0.068926 0.028109

C009 C 0.064115 0.404603 0.024094

N010 N 0.148761 0.330159 0.024600

NI011 NI 0.352771 0.483805 0.052802

N012 N 0.430972 0.342353 0.044461

C013 C -0.410883 0.418471 0.038628

C014 C -0.336819 0.326062 0.033759

C015 C -0.174918 0.405216 0.028434

C016 C -0.099776 0.316015 0.026904

C017 C 0.074641 -0.338936 0.025264

C018 C 0.150357 -0.424592 0.027095

N019 N 0.308963 -0.347655 0.034342

N020 N -0.321729 -0.415540 0.037193

C021 C -0.163084 -0.338580 0.028714

C022 C -0.087807 -0.424512 0.025746

C023 C 0.086381 -0.079494 0.027447

C024	C	0.161544	-0.168694	0.028340
C025	C	0.323400	-0.089621	0.033404
C026	C	0.397516	-0.182168	0.037282
N027	N	-0.444463	-0.105993	0.042640
NI028	NI	-0.367395	-0.248055	0.053064
N029	N	-0.162571	-0.094002	0.025796
C030	C	-0.077536	-0.168139	0.025302
O031	O	0.489128	-0.380246	0.120079
H032	H	-0.463680	-0.433725	0.141554

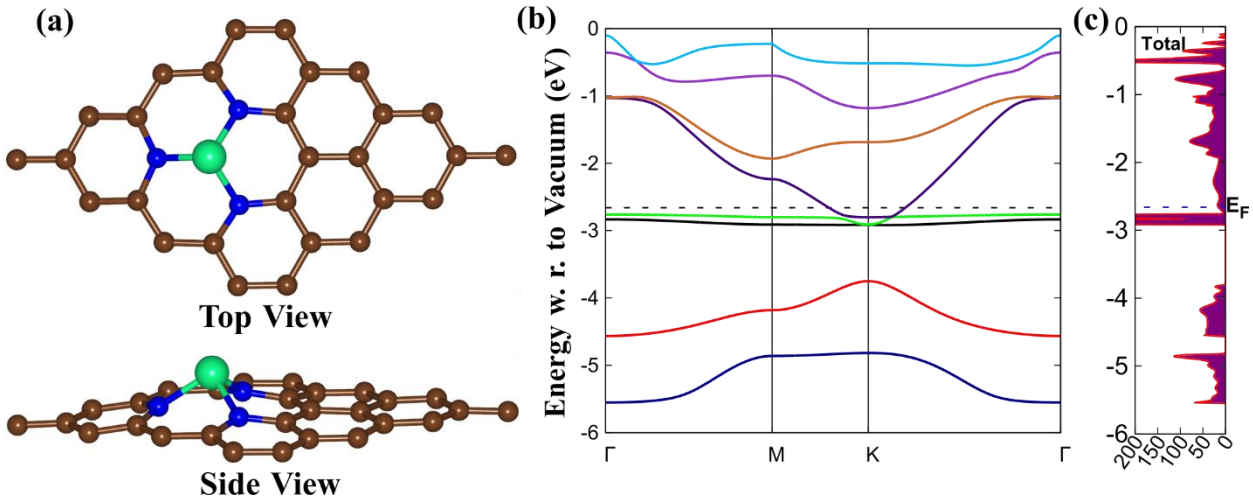

Figure S1. The representation of (a) equilibrium structure (top and side view) of $Ni_1\_N_3\_CNT$, (b) band structure of $Ni_1\_N_3\_CNT$, (c) TDOS of $Ni_1\_N_3\_CNT$.

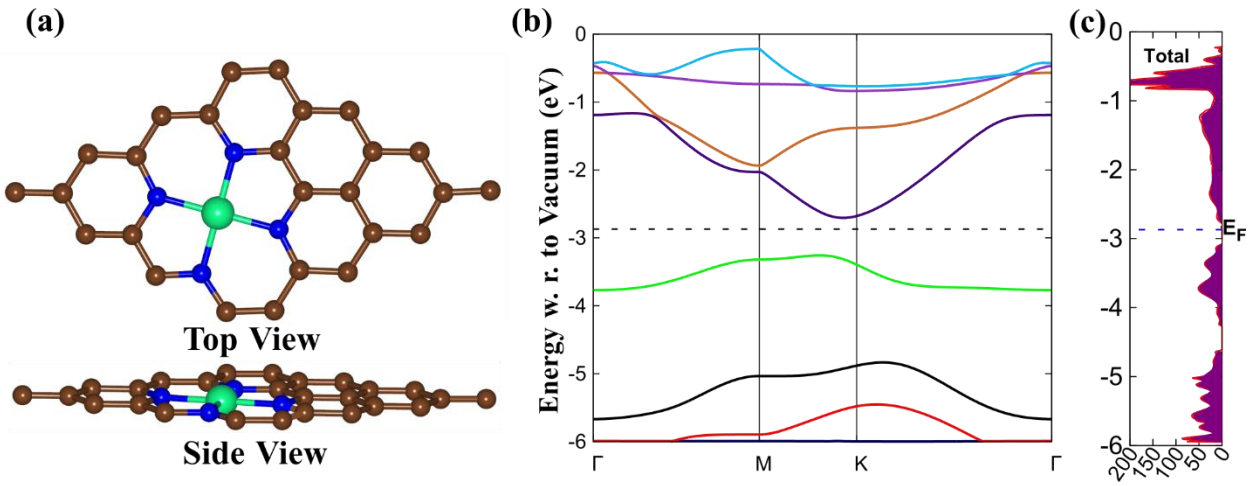

Figure S2. The representation of (a) equilibrium structure (top and side view) of $Ni_1\_N_4\_CNT$, (b) band structure of $Ni_1\_N_4\_CNT$, (c) TDOS of $Ni_1\_N_4\_CNT$.

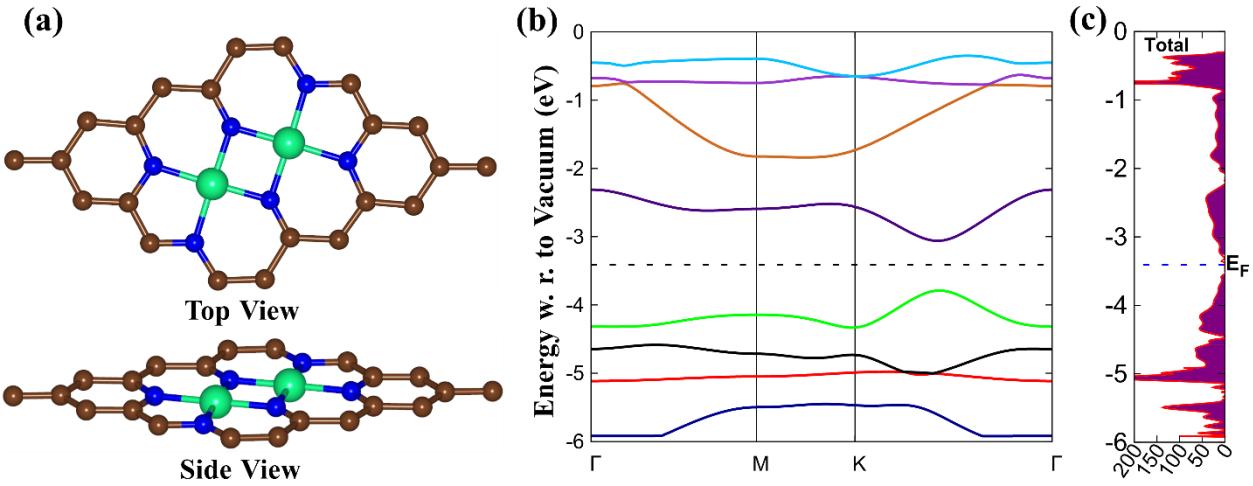

Figure S3. The representation of (a) equilibrium structure (top and side view) of $Ni_2\_N_4\_CNT$, (b) band structure of $Ni_2\_N_4\_CNT$, (c) TDOS of $Ni_2\_N_4\_CNT$.